Design of Heterostructured Photoelectrodes for Water-Splitting

Adeline Blot

▶ **To cite this version:**

Adeline Blot. Design of Heterostructured Photoelectrodes for Water-Splitting. Material chemistry. Sorbonne Université, 2023. English. NNT : 2023SORUS458 . tel-04406110

HAL Id: tel-04406110

https://theses.hal.science/tel-04406110v1

Submitted on 19 Jan 2024

HAL is a multi-disciplinary open access archive for the deposit and dissemination of scientific research documents, whether they are published or not. The documents may come from teaching and research institutions in France or abroad, or from public or private research centers.

L'archive ouverte pluridisciplinaire **HAL**, est destinée au dépôt et à la diffusion de documents scientifiques de niveau recherche, publiés ou non, émanant des établissements d'enseignement et de recherche français ou étrangers, des laboratoires publics ou privés.

Sorbonne Université

Ecole doctorale 397 Physique et Chimie des Matériaux

Laboratoire de Chimie de la Matière Condensée de Paris

Design of Heterostructured Photoelectrodes for Water-Splitting

Par Adeline Blot

Thèse de doctorat de chimie des matériaux

Dirigée par Christel Laberty-Robert et Olivier Durupthy

Présentée et soutenue publiquement le 24 octobre 2023

Devant un jury composé de :

Mr Loïc ASSAUD	Maître de Conférence, Univ. Paris Saclay	Rapporteur
Mme Mireille RICHARD-PLOUET	Directrice de recherche, IMN, CNRS	Rapporteure
Mme Jennifer PERON	Professeure, Univ. Paris Cité	Examinatrice
Mr Olivier DURUPTHY	Professeur, Sorbonne Université	Directeur de Thèse
Mme Christel LABERTY-ROBERT	Professeure, Sorbonne Université	Co-directrice de Thèse

Remerciements

Je souhaite remercier dans un premier temps les membres du jury qui ont accepté de juger mes travaux de thèse avec en tant que rapporteurs Mr Loïc Assaud et Mme Mireille Richard-Plouet. Je remercie également Pr. Jennifer Péron en tant que présidente du jury et qui fut également mon enseignante et encadrante de stage durant ma licence et mon master au sein de l'université Paris Cité. Je voudrai remercier grandement mes co-directeurs de thèse Pr. Christel Laberty-Robert et Pr. Olivier Durupthy auprès desquels j'ai énormément appris. Je vous remercie pour votre grande disponibilité, pour ces moments de rire également et votre bienveillance devant mes erreurs d'inattention. Je remercie égalemet l'iMAT pour le financement de mon projet de thèse.

Je tiens à remercier tout particulièrement la direction, Christian Bonhomme et François Ribot et l'administration du laboratoire qui se montrent toujours présents et accessibles avec Hélène, Corinne, Diana, Nora et Simon et qui m'ont permis de travailler dans un environnement agréable de qualité avec une belle cohésion, grâce aux évements organisés comme les petits déjeuners, la galette des rois.

Je remercie égalament les teams RMES, Nano et MHP avec qui j'ai pu échanger scientifiquement et sur pleins d'autres sujets tout au long de mon projet de thèse. Je souhaite également remercier Patrick Le Griel, Isabelle Genois et Mohamed Selmane de m'avoir formée et répondu à mes questions sur des appareils d'analyse. Je remerrcie également tous les collaborateurs extérieurs sans qui mon projet n'aurait pu aboutir ainsi que chaque échange que nous avons eu, en particulier David Montero, Sophie Nowak, Jean-Marc Krafft, Gwénaël Gouadec et Rémi Losno.

Je voudrai remercier également tous mes co-bureaux avec qui j'ai partagé joie et peine, Florence, Léna, Agathe, Milad, Anthony, Amandine, Adam, Morgan, Kethsovann, Ryma, Maria Letizia, Ambre. Je remercie également tous ceux qui m'ont bien accueillie et qui sont partis depuis, Yang, Runhe, Camille, Mélissa et Kim ainsi que ceux avec qui j'ai partagé de bons moments au laboratoire et en dehors que je n'ai pas encore cité, Edouard, Daniel, Thomas, Hajar Anissa, Natalia, Vivi, Emile, Flo, Laurence et plein d'autres. De manière globale je remercie tous les membres du laboratoire pour ces trois années passées à vos côtés.

Enfin, Je remercie de tout cœur ma famille, mes proches et amis qui m'ont soutenue tout au long de ce parcourt et ont toujours cru en moi.

Acknowledgments

I would like to first thank the members of the jury who agreed to evaluate my thesis work, with Mr. Loïc Assaud and Mrs. Mireille Richard-Plouet serving as referees. I also thank Professor Jennifer Péron, who served as the president of the jury and was also my teacher and internship supervisor during my bachelor's and master's studies at the University of Paris Cité. I want to express my sincere gratitude to my co-supervisors, Professor Christel Laberty-Robert and Professor Olivier Durupthy, from whom I have learned a great deal. Thank you for your availability, moments of laughter, and your kindness in the face of my lapses in attention. I also thank iMAT for funding my thesis project.

I would like to extend special thanks to the leadership of Christian Bonhomme and François Ribot, as well as the laboratory administration, who have always been present and accessible. I appreciate Hélène, Corinne, Diana, Nora, and Simon for creating a pleasant and quality working environment with great cohesion, thanks to events such as breakfasts and the king cake.

I also want to thank the RMES, Nano, and MHP teams, with whom I have had scientific exchanges and discussions on various topics throughout my thesis project. Special thanks to Patrick Le Griel, Isabelle Genois, and Mohamed Selmane for training me and answering my questions about analysis equipment. I also thank all external collaborators without whom my project could not have succeeded, especially David Montero, Sophie Nowak, Jean-Marc Krafft, Gwénaël Gouadec, and Rémi Losno.

I want to express my gratitude to all my office mates with whom I shared joy and sorrow: Florence, Léna, Agathe, Milad, Anthony, Amandine, Adam, Morgan, Kethsovann, Ryma, Maria Letizia, Ambre. I also thank everyone who welcomed me and those who have left since then: Yang, Runhe, Camille, Mélissa, and Kim, as well as those with whom I shared good times in and outside the laboratory that I haven't mentioned yet: Edouard, Daniel, Thomas, Hajar Anissa, Natalia, Vivi, Emile, Flo, Laurence, and many others. Overall, I thank all the members of the laboratory for these three years spent alongside you.

Finally, I sincerely thank my family, close ones, and friends who supported me throughout this journey and always believed in me.

Table of Content

Chapter II part 2: Sol-Gel $BiVO_4$-based photoanode with enhanced stability through the deposit of a TiO_2 passivation layer

Chapter III: Hydrothermal synthesis of nano-size $BiVO_4$ nanoparticles and easy heterostructured Mo:$BiVO_4$/V_2O_5 photoanode generation for photoelectrochemical water oxidation in acidic conditions

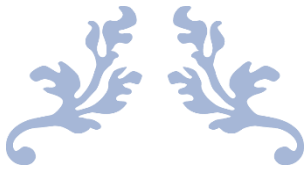

INTRODUCTION

Introduction

Finding sustainable energy solutions (production and storage) is of paramount importance in our efforts to minimize greenhouse gas emissions. One sector that holds significant promise in this regard is hydrogen production. A study conducted by the International Energy Agency (IEA) in 2019, titled "The Future of Hydrogen,"[1] offers a comprehensive and impartial assessment of hydrogen's current status including its potential contributions to achieving a clean, secure, and affordable energy future. Interestingly, this report presents the strategies required to unlock this potential. As a leading authority covering all energy sources and technologies, the IEA is ideally positioned to settle global policy on hydrogen through collaboration with governments, industry, and academia. But, this report shows that hydrogen production is intrinsically linked to societal concerns and political choices. Government initiatives, including public funding, play a critical role for the creation of innovative solutions. As well as seeking economies of scale, research plays a central role in lowering production costs and enhancing performance.

Hydrogen have a rich history of energy applications, including its contribution to the Apollo moon missions. Despite its long history, demand for hydrogen keep on increasing, having more than tripled since 1975. However, the majority of hydrogen production still relies on fossil fuels, resulting in around 830 million tonnes of carbon dioxide (CO_2) emissions every year. Today, its production and use highlight two others characteristics: i/ hydrogen's potential for emission-free use and ii/ its ability to be generated from a variety of low-carbon energy sources.

Figure 1 depicts the distribution of hydrogen production and use. Hydrogen can be produced from fossil fuels, biomass, or through water electrolysis. Its high energy content per unit of mass makes it an attractive transport fuel. The water electrolysis reaction is the only known process that splits the water molecule to produce H_2, with dioxygen (O_2) as the only by-product. However, currently, less than 0.1% of global hydrogen production comes from water electrolysis, primarily serving markets requiring high-purity hydrogen, such as electronics and polysilicon production. Natural gas remains the dominant source of hydrogen production, followed by coal and a smaller portion from oil and electricity. The hydrogen production through electrolysis requires an energy source to apply an electrical bias to split the water molecules, which entails significant production costs. Overcoming this obstacle is essential if we are to achieve global production that is competitive with oil. This challenge has led to the

colour classification of hydrogen production based on its production process (origin of reactants and energy source). Colours such as "black," "grey," or "brown" indicate hydrogen produced from coal, natural gas, and lignite, respectively. "Blue" is commonly used for hydrogen production from fossil fuels with a reduction in CO_2 emissions thanks to carbon capture or storage. "Green" refers to hydrogen produced from renewable electricity using electrolysers.

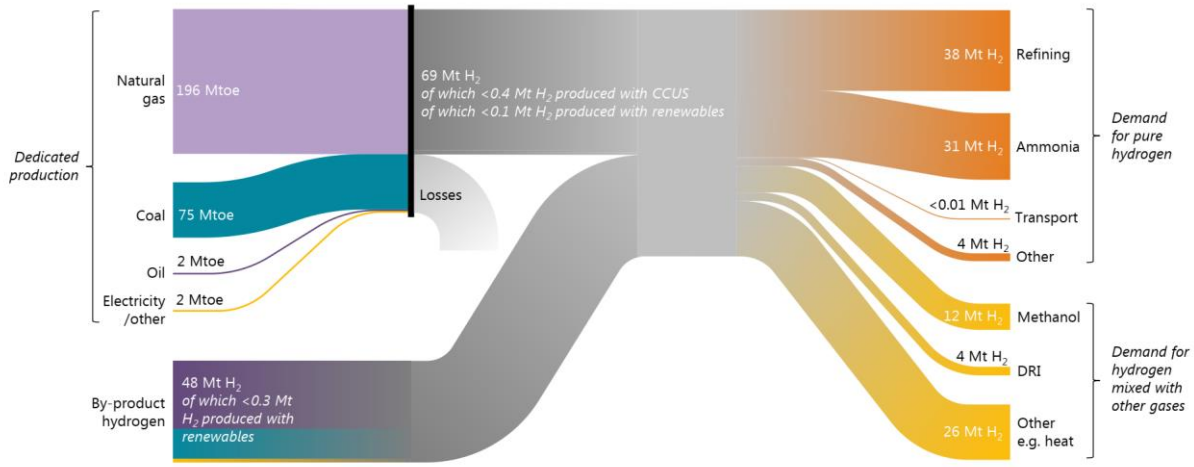

Figure 1: Today's Hydrogen product chain, from @ IEA 2019.[1]

Another aspect highlighted by the IEA concerning the long-term use of hydrogen is the maximization of its usage beyond existing industrial applications. New sectors of interest have emerged, increasing the demand for renewable hydrogen. The transport, buildings, and power sectors hold the potential to utilize hydrogen if production and utilization costs align favourably with other alternatives.

Nevertheless, beyond all considerations on the cost and the origin of the energy source for electrolysis of water, the composition of electrolyser device itself presents challenges, as many current devices rely on noble metals for both the cathode and anode components, potentially leading to future shortage. Consequently, new electrodes compositions are actively searched to maintain a high reactivity with more available metals.

The scientific community has explored sustainable hydrogen production as a means of storing solar energy, inspired by artificial photosynthesis. Solar energy, among various sustainable sources, stands out as an abundant and virtually limitless resource, with an estimated power capacity nearly 10,000 times greater than global power consumption (17.7 TW). Converting solar energy into chemical energy (within the dihydrogen bond) through photoelectrochemical (PEC) water splitting is an attractive strategy for meeting the growing demand for energy while considering the availability of raw material through the use of easily available semiconductors.

The choice of materials for solar water splitting also considers factors such as price, potential impact on the environment and abundance on Earth. One of the advantages of PEC water splitting systems is their ability to reduce applied bias by absorbing solar light energy. A variety of semiconductors allow the built of devices with two photon absorbers, one for the photocathode (where water is reduced to H_2) and one for the photoanode (where water is oxidised to O_2), creating a fully functional closed system without the need for external bias. However, such a device introduces new constraints, notably the need for a single electrolyte that ensure the durability and efficiency of the photocathode and photoanode. While efficient copper-based photocathode materials have been proposed, they typically function in acidic aqueous electrolytes. This presents a significant challenge in the search for compatible materials for photoanodes. The oxidation of water to produce one mole of oxygen requires twice as many charge carriers as the production of the same amount hydrogen, which has an impact on overall efficiency. Furthermore, employing acidic aqueous electrolytes to support efficient photoelectrochemical water oxidation is detrimental to the overall efficiency and durability of the PEC water-splitting system.

In this thesis, we explore different strategies aimed at developing an efficient and durable photoanode that is compatible with an electrolyte in a weakly acidic environment. The choice of the photoanode material was set to bismuth vanadate for prior studies in the laboratory and in the literature demonstrate its efficiency in alkaline and neutral medium. The manuscript reporting the research work in order to improve that photoanode according to our requirements is structured as follows:

The chapter I provides a general introduction to photoelectrochemical water-splitting. It outlines the photoelectrochemical water-splitting process, discusses its thermodynamic constraints, and introduces advanced research focused on efficient photoanode generation using the semiconductor bismuth vanadate ($BiVO_4$). The chapter explains both intrinsic and environmental limitations, highlighting the challenges of comparing materials, particularly dependent on the electrolyte's pH and composition. Additionally, the critical challenges posed by this material for generating a photoelectrochemical tandem-cell device with a photocathode under acid conditions are discussed.

Chapter II concerns the development of an efficient $BiVO_4$ electrode and it is divided into two parts. The first part focuses on the development of an efficient photoanode based on $BiVO_4$ through a scalable and accessible synthesis method, combining Sol-gel chemistry and the dip-coating deposition technique. An in-depth study was carried out into the impact of the

electrolyte and chemical modifications to $BiVO_4$ and its electrode/electrolyte interface on the efficiency of water oxidation and its durability. In the second part of Chapter II, we focus on improving the durability of the photoanode. To this end, we study the approach of depositing a titanium dioxide passivation layer on the surface of $BiVO_4$-photoanode. In this part, two deposition methods were explored: atomic layer deposition and the sol-gel process coupled with dip-coating process. Our objective was to determine how the thickness and crystallinity of the passivation layer affect the performances of the $BiVO_4$ photoanode.

Chapter III introduces a novel approach to generating $BiVO_4$ photoanode with controlled thickness. This approach involves a two-step process in which $BiVO_4$ nanoparticles are first synthesized and then deposited on the electrode substrate using dip-coating. This method offers the advantage of structural and morphological control of $BiVO_4$ prior to deposition, as well as the possibility of creating heterojunctions. New hydrothermal synthesis methods are developed to generate nano-sized $BiVO_4$ particles. Interestingly, we developed a one-step deposition method to create n-n heterojunction, inspired by the "brick and mortar" approach. This method involves dispersing Mo-doped $BiVO_4$ nanoparticles in a V_2O_5 gel, allowing a film to be deposited in a single dip-coating step. This approach enables the synthesis of a heterostructured photoanode with strong particle/particle contact facilitated by V_2O_5, which acts as a binding agent.

Finally, a general conclusion and outlook are given, bringing together the results and the areas that could be developed to improve and produce photoanodes compatible with photocathodes in acid conditions.

(1) IEA. *The Future of Hydrogen*; OECD, 2019. https://doi.org/10.1787/1e0514c4-en.

CHAPTER I

Exploring Photoelectrochemical Water Splitting: Thermodynamic Constraints and Advances in Bismuth Vanadate Photoanodes

CHAPTER I

Table of Content

Exploring Photoelectrochemical Water Splitting: Thermodynamic Constraints and Advances in Bismuth Vanadate Photoanodes

1. Introduction

Solar energy compared to different sustainable energy sources stands out as an abundant and limitless resource. With an estimated power capacity of 173,000 Terawatts (TW), which is nearly 10,000 times greater than the global power consumption of 17.7 TW, its conversion into electricity is very interesting.[1,2] Nonetheless, solar energy's uneven distribution and intermittent nature pose significant challenges in meeting our energy needs. However, scientists have turned to nature for inspiration, leading to the development of artificial synthesis methods where solar energy can be converted into bonding energy stored in chemical bonds. This approach is very promising for addressing the challenges associated with solar energy purpose.[1] The molecule of dihydrogen is a very interesting molecule to consider for energy storage into a chemical bond. It is a carbon-free source with a high energy storage density. It has been determined that the energy provided to split the water molecule corresponds to a positive increase of the Gibbs free energy by 237 kJ mol^{-1}.[3]

The reaction can be written as:

$$H_2O\,(l) \rightarrow H_2\,(g) + \frac{1}{2}\,O_2(g) \qquad \Delta G = 237\ \text{KJ}\,mol^{-1} \qquad (1)$$

Performing the water-splitting reaction allows to store electric energy into a chemical form within the H_2 molecule. The energy per electron required to split a water molecule, also described as the thermodynamic voltage corresponds to the standard potential E°(O_2/H_2O) of 1.23 V vs NHE.[4]

A classical electrolyser cell consists mainly of anode, cathode, membrane/separator, frames, sealing and bipolar plates (Figure 1). The cathode serves for the reduction of water (Hydrogen Evolution Reaction – HER) and the anode for water oxidation (Oxygen Evolution Reaction, OER). The devices are classified into three categories, comprising the use of liquid electrolytes:

- Alkaline Water Electrolysis (AWE), electrolysis in an acid ionomer environment
- Polymer Electrolyte Membrane Electrolysis (PEM)/Solid Polymer Electrolysis (SPE)

- Solid Oxide Electrolyte with Steam electrolysis (High temperature electrolysis -HTEL or SOEL).[5]

Generally, for all systems, cathode materials with the most efficiency are based on noble metal Pt, or Pd. Ni-based materials can be found for the anode in AWE or SOEL, and IrO_2 for PEM. Most of the systems operate with heat, with a minimum of 40 °C to 1000°C. All these systems are well described in the literature as shown by the study by Rashid *et al*.[5] However, water electrolysis in a standard water-splitting device requires an overpotential for the two half-reactions to occur. The cathode requires a potential more negative than $E°(H^+ / H_2) = 0\ V_{RHE}$ to produce hydrogen. At the anode, an overpotential of more than 0.2 V must be applied because OER involves twice as many electrons as HER. Consequently, the activation energy is much higher for OER.

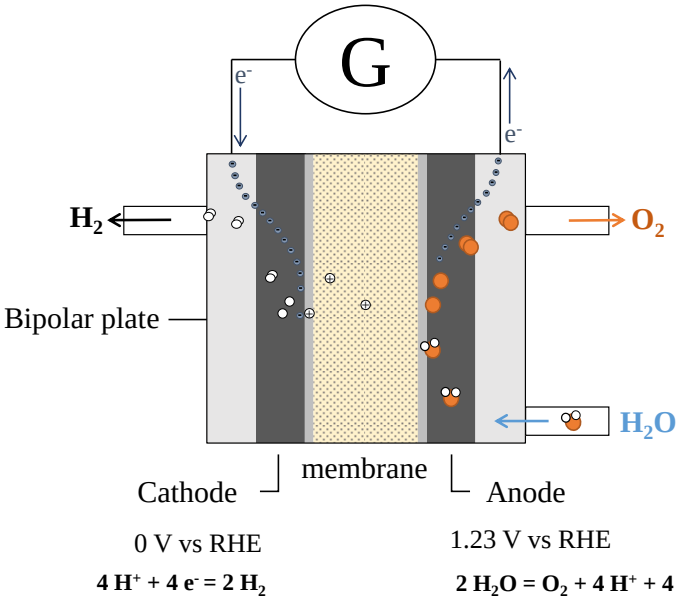

Figure 1: Classical electrolyser, *@ reproduced from L'Esprit sorcier/CEA*

Combining solar harvesting and dihydrogen production through photoelectrochemical (PEC) water splitting is a very attractive strategy for simultaneously meeting growing energy demands and supply challenges.[6,7] One of the advantages of PEC water-splitting systems is that they enable a reduction in applied bias through the absorption of photon energy.

Various types of photoelectrochemical cells can be employed. These cells consist of two electrodes, similar to traditional electrolysis, with a cathode and an anode, but they also include at least one photoelectrode, which absorbs energy from the solar spectrum. This absorption of energy may initiate half-cell reactions at each electrode, leading to the decomposition of water

into H_2 and O_2.[6] To achieve this, the photoelectrode must absorb light and generate photoexcited electron/hole pairs. Subsequently, these charge carriers have to separate from each other. The photogenerated holes migrate to the interface between the photo-anode and the electrolyte, where they oxidize water molecules into O_2, while the photogenerated electrons flow through the external circuit to reduce protons, resulting in the formation of H_2 at the cathode as described with equation (2) and (3):

$$2\,H_2O + 4\,h^+ \rightarrow 4\,H^+ + O_2 + 4\,e^- \quad (2)$$

$$4\,H^+ + 4\,e^- \rightarrow 2\,H_2 \quad (3)$$

2. Semiconductor behaviour in electrolyte

In PEC water-splitting, the materials used for each electrode are semiconductors which are immersed in an electrolyte solution containing the redox couple (A/A^-), with A/A^- corresponding to O_2/H_2O for the water oxidation half-reaction or H^+/H_2 for the water reduction. A difference between the Fermi level (E_f) of the semiconductor and the electrochemical potential of the electrolyte $-qE°_{(A/A^-)}$ where E° is the Nernst potential of the redox pair (A/A^-) exists (Figure 2.A).

This difference in potential has to be equalized for the system to reach equilibrium.[2,8] To accomplish this, charge carriers, such as electrons, must flow across the interface between the semiconductor and the electrolyte, creating a potential gradient known as band bending. Band bending represents a distortion of the energy levels in the valence and conduction bands of the semiconductor near the interface.[2,6,8] For a photoelectrochemical water splitting device, in the presence of a n-type semiconductor the Fermi level is shifted close to the conduction band (CB) and the potential of O_2/H_2O redox couple. On the opposite, for a p-type semiconductor, the Fermi level is shifted close to the valence band (VB) and the potential of the H^+/H_2 as redox couples. Other factors can induce band bending, notably the application of a potential between the working electrode and the reference one. Due to band bending, the main potential drop occurs inside the semiconductor, facilitating charge separation in the space charge layer (SCL). This corresponds to the region of the semiconductor where the potential gradient is established as shown in Figure 2.[8] N-type semiconductor are generally employed as photoanode material due to the flow of positive charges from the bulk to the electrolyte solution.

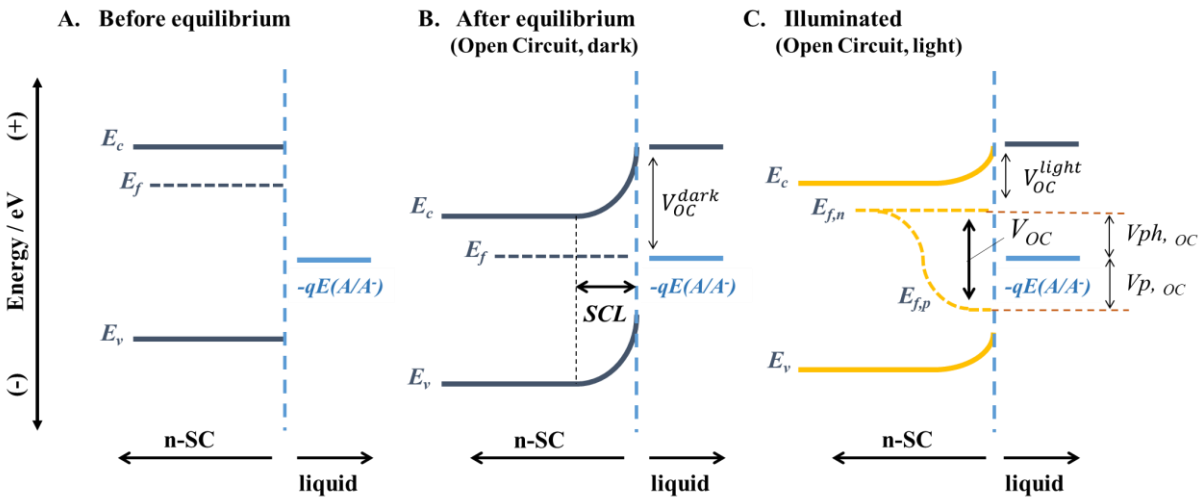

Figure 2: Band diagram of n-type semiconductor (n-SC)/liquid interface presented in three cases : (A) before equilibrium (B) after equilibrium in the dark where V_{OC}^{dark} is kown as the barrier height and correspond to the theoretical maximum energy that can be extracted from a separated electron-hole pair at the n-SC/liquid junction, (C) illuminated, in non-equilibrium conditions where E_f is split into two quasi-Fermi levels $E_{f,n}$ and $E_{f,p}$ with the open circuit voltage V_{oc} which further splits into open-circuit photovoltage $V_{ph,\,oc}$ and the open-circuit hole voltage $V_{p,\,oc}$. Inspired from ref [7,9]

As Figure 2 presents the example of a n-type semiconductor in an open circuit, electrons and holes pairs recombine easily in the flat band region. In contrast, they separate efficiently at the SCL without illumination, where the Fermi level E_f is perfectly aligned with the liquid electrochemical potential $-qE°_{(A/A^-)}$ (Figure 2.B). Under light, the equilibrium changes due electron-hole pairs generation within the n-type semiconductor immersed in an electrolyte solution. The E_f at equilibrium is splitting into two quasi-Fermi levels which describe the electrochemical potential of a hole or an electron. Each population can be separately describe thanks to the Fermi-Dirac statistics .[7,9] The difference between electron and hole quasi-Fermi levels ($E_{f,n}$ and $E_{f,p}$) is defined as the open-circuit voltage, V_{oc}.[9] This directly affects the band bending, making it smaller. The reduction of the band bending upon illumination is then calculated as follows:

$$V_{ph,OC} = V_{RHE,OC}^{dark} - V_{RHE,OC}^{light} \quad (4)$$

Because, under light, the movement of charges influences the positions of the conduction and valence bands, the photovoltage is assimilated to a change in electrostatic potential and is associated with the open-circuit voltage of the cell, $V_{p,\ oc}$:

$$V_{p,oc} = V_{oc} - V_{ph,\ oc} = E_{f,p}^{light} - E_f^{dark} \quad (5)$$

Even if a semiconductor has suitable band edge positions to enable PEC water-splitting reactions, higher photovoltages are still required to drive the reaction.[7] This phenomenon is attributed to kinetic processes that influence photovoltages and lead to the recombination of electron-hole pairs.

These recombination phenomena are described by Walter et al. and the corresponding current density are summarized below:

- Recombination in the bulk of the solid (J_{br}),
- Recombination in the depletion region (J_{dr}),
- Tunnel through the electric potential barrier near the surface (J_t),
- Thermionic emission (J_{et}) by thermally overcoming the interfacial potential barrier,
- Recombination at defects at the semiconductor/electrolyte interface (J_{ss}).

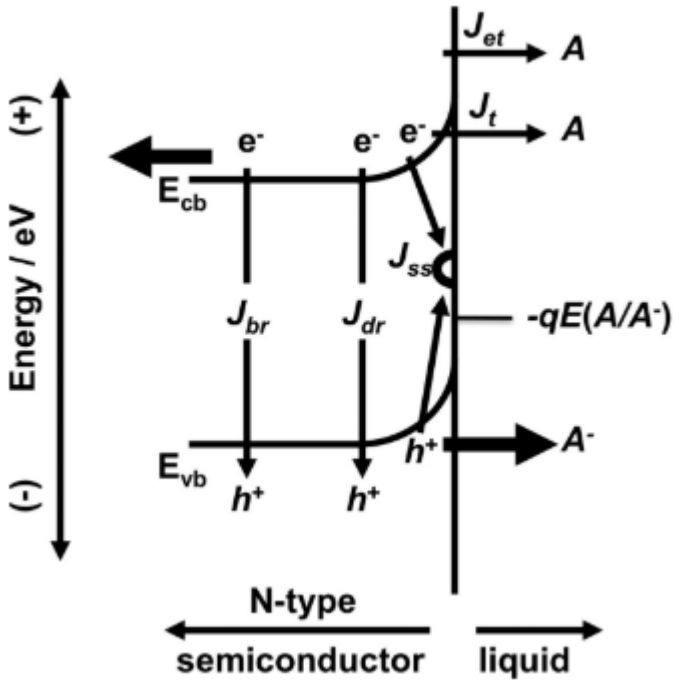

Figure 3: Recombination pathways for photoexcited carriers in a semiconductor photoelectrochemical cell (thin arrows). The electron-hole pairs can recombine through a current density associated to five type of recombination. Electron collection by the back contact and hole collection by the redox couple contribute positively to device efficiency (thick black arrows). Extracted from Walter et al[7], which is a reproduction of the work from Lewis et al, ref.[10]

In summary, considering all these recombination processes and losses, a semiconductor can only effectively drive water photoelectrolysis when recombination is adequately suppressed. The efficiency of charge carrier separation and the kinetics of the reaction becomes crucial factors in achieving efficient water-splitting.[2]

3. Photoelectrochemical Cells

a. Simple PEC cell

Different types of tandem cells have been proposed in the literature to effectively split the water molecule using the solar spectrum. As reported by Jiang *et al.* and Walter *et al.*, photoelectrochemical water splitting devices can be constructed using a variety of configurations, including single band gap devices and dual band gap devices.[2,7] The material used as photoelectrodes are n- or p-type semiconductors.[11,12]

Figure 4, describes a simple PEC cell with a single band gap device based on n-SC photoanode. This electrode is electrically connected to a metal counter electrode, platinum for example. In this device, the three main processes are i) light absorption, ii) separation and iii) transport of charge carrier and iii) redox reactions at the surface.

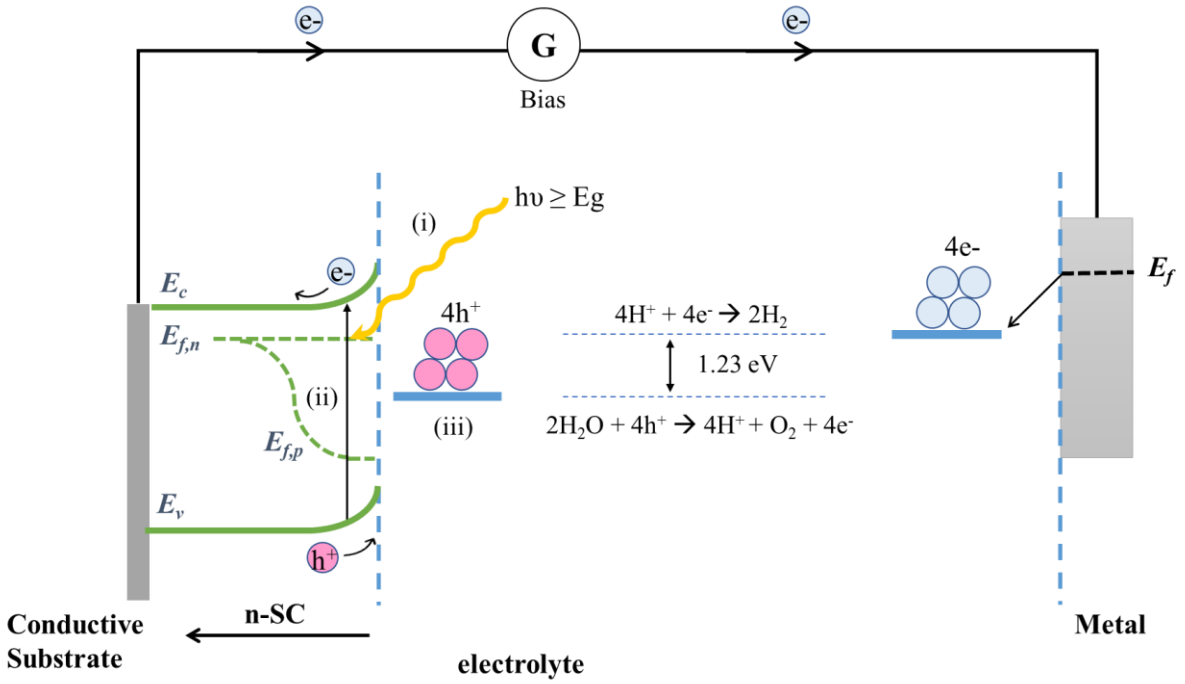

Figure 4: Scheme of simple PEC with n-SC photoanode connected to a metal counter electrode in acidic/neutral condition under non equilibrium (illumination) adapted from ref.[2]

b. PEC performance evaluation

To determine the performance of a PEC cell, we use the concept of energy conversion efficiency. It is commonly quantified by the standard solar-to-hydrogen conversion efficiency (STH), which represents the ratio between the total energy generated and the total energy input by sunlight irradiation under AM 1.5G conditions with an intensity of 100 mW cm^{-2}. It is determined with the equation (4):

$$\eta_{STH} = \frac{\text{Total energy generated}}{\text{Total energy input}} = \frac{\Delta G \times r_{H_2}}{P_{sun} \times S} \quad (6)$$

with ΔG is the Gibbs free energy (237 kJ mol^{-1}), r_{H_2} is the rate of H_2 production (mol s^{-1}), P_{sun} is the incident light (100 mW cm^{-2}) and S is the illuminated surface of the electrode (cm^2).

In cases where an external bias is applied to the PEC system, the electrical energy contributed by the bias must be considered. Therefore, the applied bias photon-to-current efficiency (ABPE) is often used to estimate the efficiency after subtracting the electrical energy:

$$ABPE = \frac{J_{ph}(V_{redox} - \Delta E_{app}) \times \eta_{FE}}{P_{light}} \quad (7)$$

with V_{redox} the redox potential of water-splitting (1.23 V_{RE}), ΔE_{app} the actual bias potential difference between the working and counter electrode (V), η_{FE} the Faradic efficiency, P_{light} is the incident power of the solar simulated light (100 mW cm^{-2}) and J_{ph} the generated photocurrent density (mA cm^{-2})

In a tree-electrodes system, the ΔE_{app} is calculated from the applied potential E, assuming that the overpotential for HER is negligible at the counter electrode:

$$\Delta E_{app} = E^{\circ}\ (O_2/H_2O) - E \quad (8)$$

The hypothetical ABPE corresponds to the half-cell, STH and is independent of the properties of the counter cathode meaning that half-cell STH efficient is different from the ABPE one in a two-electrode system.[8]

The Faradic efficiency (η_{FE}) provides information on the selectivity of OER at the photoanode in competition with the photocorrosion phenomenon. It is defined as the ratio of the actual evolved gas divided by the theoretical evolved gas based on the measured photocurrent.[2] In the case of oxygen evolution, the amount of O_2 can be quantified by gas chromatography, mass spectroscopy and an O_2 gas sensor, using an oxygen electrode of the fluorescence detector.

$$\eta_{FE} = \frac{\text{Experimental gas evolution}}{\text{Theoretical gas evolution}} = \frac{O_2 \text{ measured}}{\text{Gas evolution based on the photocurrent}}$$

$$= \frac{O_2 \text{ measured} \times e \times 4 \times N_A}{J_{photo} \times S \times T} \times 100 \quad (9)$$

with the gas evolution unit (moles), J_{photo} the photocurrent density (A cm^{-2}) measured during the time T (s), *S* the illuminated surface of the photoelectrode (cm^2), *e* the charge of an electron (1.602 10^{-19} C) and N_A the Avogadro constant (6.02 10^{23} mol^{-1}).

The incident photon-to-current conversion efficiency (IPCE) is an accessible method to evaluate external quantum efficiency (also called apparent quantum efficiency). The IPCE is defined of the ratio of J_{photo} at a static potential vs. the incident photon of a monochromatic incident light:

$$IPCE = \frac{\left(\frac{J_{photo}(\lambda)}{e}\right) \times \left(\frac{hc}{\lambda}\right)}{P(\lambda)} \times 100\ \% = \frac{J_{photo}(\lambda)}{P(\lambda)} \times \frac{1240}{\lambda} \quad (10)$$

with $J_{photo}(\lambda)$ the photocurrent density at the wavelength λ (nm) of incident light (mA cm^{-2}), *e* the charge of an electron (1.602 10^{-19} C), *h* Planck's constant (6.626 10^{-34} J s), *c* light celerity (3 10^8 m s^{-1}), $P(\lambda)$ the incident power of the specific wavelength λ (mW cm^{-2}).

c. PEC tandem cell configurations

As presented in Figure 5, single band gap devices can be represented by the Type I and Type II. As described by Jiang *et al*, the simplest Type I (Figure 5.a) contains one semiconducting light absorber, a photoanode or photocathode.[2] Single band gap devices require a semiconductor with a minimum band gap of 1.6 to 1.7 eV to generate the necessary voltage for water-splitting.[7] However, a band gap greater than 2 eV is generally preferred due to voltage-loss mechanisms and overpotential generally required to promote HER and OER.[2,8] As part of this strategy, heterostructures composed of multiple semiconductors are being investigated to enhance device performance by efficiently absorbing a greater proportion of the solar spectrum and modifying charge transport. This modification is achieved by generating a band bending between the semiconductors at the heterojunction, as demonstrated with Type II (Figure 5.b).

Nevertheless, this strategy has certain drawbacks, in particular the risk of generating recombination sites at grain boundaries. Some configurations combine the single-band gap device with a photovoltaic cell to compensate for external bias by converting solar energy directly into electricity. However, while this approach eliminates the need for external bias, it

does not address the question of the choice of counter electrodes, which are generally composed of expensive noble metals, whether they serve as anodes or cathodes.

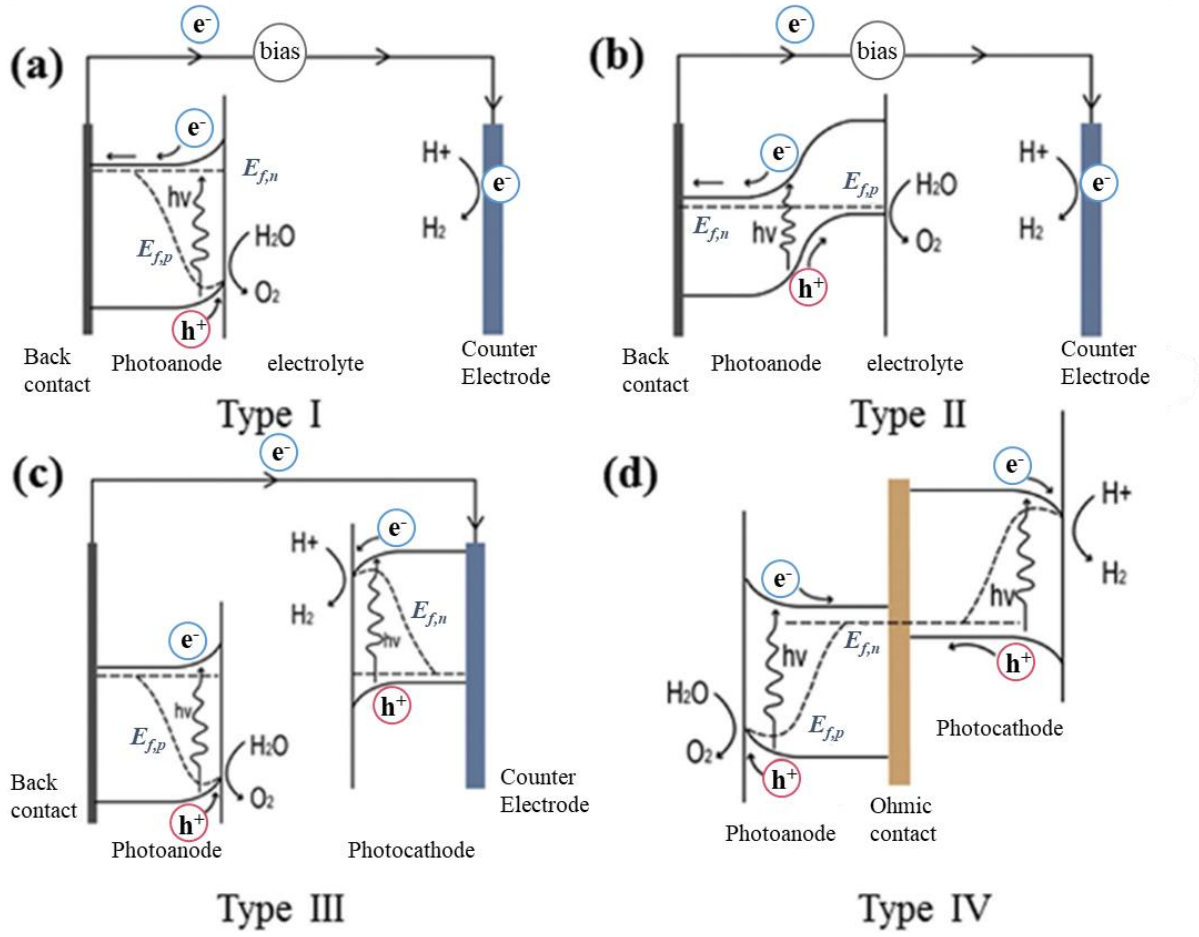

Figure 5: Various PEC water splitting device configurations: (a) type I single light absorber; (b) type II heterojunction photoelectrode; (c) type III wired PEC tandem cell; (d) type IV wireless PEC tandem cell. Modified from ref.[2]

Compared with single-band gap devices, dual-band gap PEC cells can produce dihydrogen without the need for an external bias, using photoelectrodes made from metal oxides that are more readily available and cost-effective. This makes them a promising final strategy. Additionally, they offer the advantage of exploring combinations of semiconductors with smaller band gaps, enabling complementary absorption and enhanced stability characteristics.[7] For example, catalysts integrated at the semiconductor/liquid interfaces can improve reaction kinetics and overcome voltage losses. Without external bias, two configuration exists, the type III and the type IV (Figure 5.c,d). Type III corresponds to a photocathode and a photoanode linked by a conductive metal wire. The type IV configuration have a unique photoelectrode

composed of the photoanode in one side and the photocathode in the other side with an electron collector in between. This last configuration avoids the use of wires to connect each photoelectrode. Both devices require the photoanode's conduction band minimum to be more negative than the valence band of the photocathode.[13] Maintaining the required photovoltages, reducing losses at semiconductor/liquid junctions, and achieving high photocurrent density in tandem configurations are crucial challenges. Additionally, it is essential to guarantee the stability of materials and to consider cost factors when practical applications are considered. To create an efficient PEC cell in Type III or IV configuration, general criteria must be met and are essential for this application.

In general, the photoelectrodes should have:

- appropriate band alignment to allow HER or OER on its surface,

Indeed for OER, the valence band (VB) should have a higher potential than the oxidation potential value, $E°(O_2/H_2O)$ and for HER, the VB must be lower than $E°(H^+/H_2)$.[8]

- good absorption in the solar spectrum,

The band gap should allow the absorption of wavelength from the visible light region since it constitutes the primary portion of the solar spectrum, meaning that it should be lower than 3.1 eV, equivalent to 400 nm.[8]

- fast and efficient charge separation and transport.

Low reaction kinetics and charge recombination are the primary obstacles to achieving high PEC performance. Since PEC water-splitting occurs in aqueous media, the process is also significantly influenced by the efficient transfer of charges. It involves their interaction at the surface with the electrolyte, as well as the effective separation of photogenerated excitons within the space charge layer.

- high stability in the electrolyte.[1,14,15]

The pH of the electrolyte can affect the chemical stability and act as a favourable factor for the degradation of photoelectrodes through photocorrosion. It can be described as a competitive reaction at the OER where the electron/hole pairs created by the absorption of solar energy, react to produce active species that contribute to the degradation of the electrode. Photocorrosion occurs mainly on the surface of the photoanode when it is exposed to illumination in the presence of the electrolyte, and this effect is further intensified when a voltage bias is applied.[7,16]

As for photocathode materials, copper oxide Cu_2O based photoelectrodes have shown very promising results in the literature under acidic conditions.[2,17] With its lower band-gap of 1.4 eV, it could be coupled with efficient photoanode.[2,7] To obtain a Type III or IV configuration, the main bottleneck remains the photoanode material because generating O_2 in the OER requires doubling the charges in the HER.

4. Photoanode materials choice

Various semiconductors have been reported as potential photoanode materials. The band gap (Eg) for a semiconductor is between 1 and 5 eV.[2,18] In figure 6, only few n-type semiconductor present absorption in the visible range of the solar spectrum. Among them, (TiO_2 (Eg = 3 eV) or WO_3 (Eg = 2.7 eV)), $BiVO_4$ exhibits the lowest band gap (Eg ~ 2.4 eV) a well aligned valence band for OER and is cheaper than current anodes in a classical electrolyser.[11,19] Moreover, compared to other common oxygen evolution photocatalysts like WO_3 and Fe_2O_3, $BiVO_4$ has a CB edge at 0.02 V_{RHE}. As a result, less bias potential is needed to bring the photoexcited electrons above the reduction potential of water (0.0 V_{RHE}).[11] Indeed, to drive the water-splitting reaction, the electrons must have energy higher than the water's reduction potential of 0.0 V_{RHE}. When coupled with a photocathode, an efficient electron transfer from $BiVO_4$ photoanode to the photocathode can potentially reduce the bias voltage required to drive the overall water-splitting reaction. This would reach a self-sustaining reaction solely driven by light absorption.[11] Interestingly, even if Fe_2O_3 presents a lowest band gap and a theoretical photocurrent of 12 mA cm^{-2}, it is strongly limited by the bulk recombination of electrons and holes due to a short carrier diffusion length (less than 10 nm). For $BiVO_4$ semiconductor, its theoretical STH efficiency is about 9.2 % with a maximum of photocurrent of 7.5 mA cm^{-2} under standard AM 1.5 solar light irradiation.[15,20,21] However, in practical experiments, achieving such high photocurrents is challenging, despite the various strategies employed, such as doping, surface passivation, and nanostructuring, to enhance its photoactivity.[4,22]

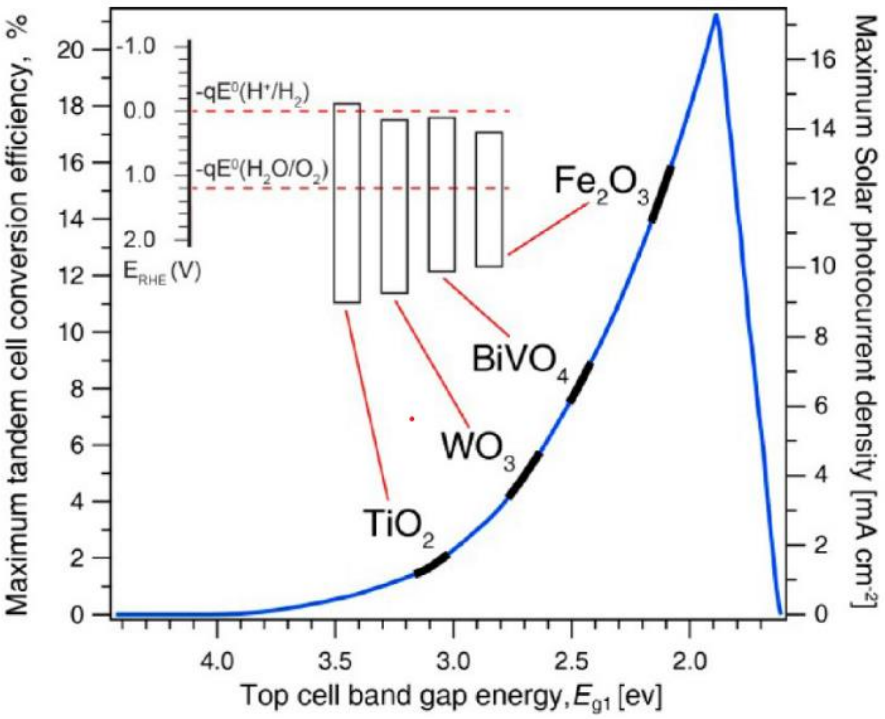

Figure 6: Maximum solar-to-hydrogen conversion efficiency and solar photocurrent as a function of the top cell band gap energy in a tandem cell with the loss assumptions identical to Figure 2. The band gap energies and efficiency range for commonly used semiconductor oxide photoanodes are also shown. Extracted from the work of Prévot & Sivula[13]

a. Bismuth vanadate metal oxide

$BiVO_4$ has the ability to crystallize in three different structures:[19,23,24]

- the tetragonal zircon (t-z) structure corresponding to the kinetic phase,
- the tetragonal scheelite (t-s) structure with intermediate stability,
- the monoclinic scheelite (m-s) structure which is the thermodynamic phase.[24]

In Figure 7.a, for each structure, the vanadium coordination polyhedra is a tetrahedron,VO_4 and the bismuth is surrounded by eight oxygen atoms, BiO_8 from eight different VO_4 units.[18,25,26] The different space groups are detailed in Figure 8.[19,24,26,27] The m-s polymorph is the most interesting phase for photoelectrochemical application due to its ability to absorb more light of the solar spectrum as it exhibits the lowest band gap of 2.4-2.5 eV compared to 2.6 eV and 2.8 eV for t-s and t-z polymorph, respectively. It has been reported that distortion in the

crystalline structure of $BiVO_4$ ensures interactions between Bi 6s and O 2p orbitals.[28,29] These phenomena justify the lowest band gap value for m-s polymorphs and its better photoactivity as explained by the work of J. K. Cooper *et al.*[29] In their work, they have determined the energy level diagram of $BiVO_4$ m-s (Figure 7.b).This distortions usually exposed for $BiVO_4$ m-s have also been observed for $BiVO_4$ t-s, as in the work of S. Hilliard *et al.*[30] and Tokunaga *et al.*[19] Even if it is a promising photoanode material, $BiVO_4$ presents major outcomes that prevent high photocurrents from being obtained. It has intrinsic low electron – hole pairs mobility, slow water oxidation kinetics and has also the limitation of holes diffusion length around 70 – 100 nm.[31–33] It was revealed that the low electron mobility in the material, was a consequence of the overlap of V 3d with Bi 6p. To overcome this limitation, W^{6+} or Mo^{6+} doping has been proposed as it improves the electronic conductivity of the material.

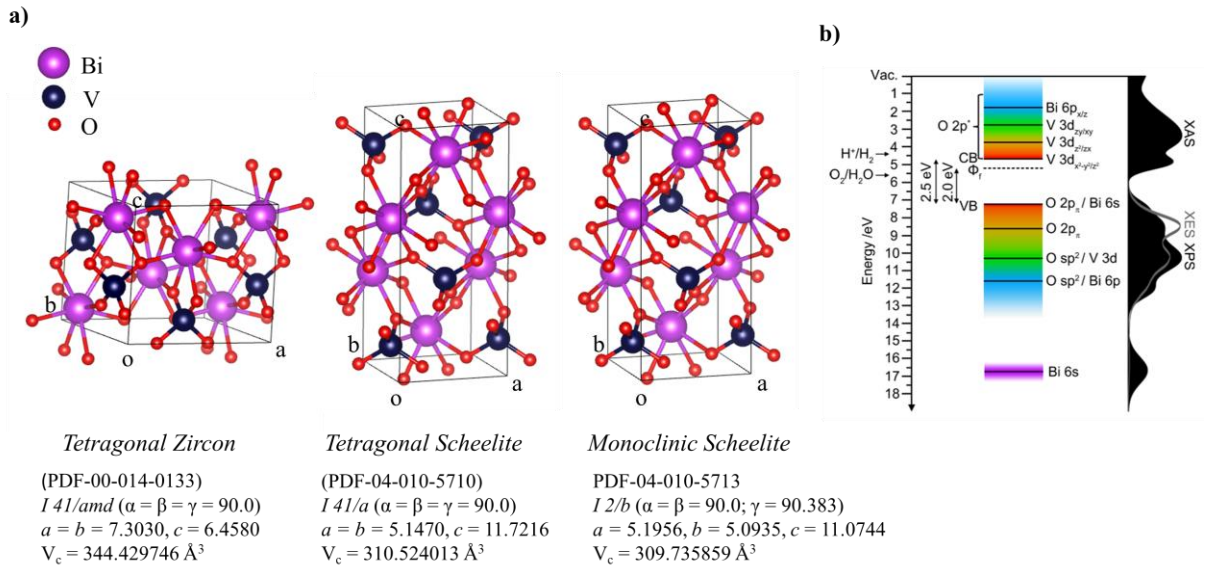

Figure 7: a) crystalline structure visualisation of $BiVO_4$ Tetragonal Zircon PDF 00-014-0133, Tetragonal Scheelite PDF 04-010-5710, Monoclinic Scheelite PDF 04-010-5713; Vc corresponds to unit-cell volume b) electronic structure of $BiVO_4$ m-s calculated by Cooper J. K; et al[29]

b. $BiVO_4$ photoanode design

In the past decades, various shapes of $BiVO_4$ particles have been produced for photocatalytic applications. The synthesis methods employed were mostly hydrothermal syntheses, resulting in a wide range of morphologies including square-like, octahedral, spherical, porous, nanoplates , spherical, dendrite, flower-like.[34–39] All these synthesis strategies result in micron-sized particles. To use $BiVO_4$ particles as photoanode material, they must form a good contact with the substrate, typically fluorine doped tin-oxide (FTO) which collects electrons. It should also takes in consideration the limiting holes diffusion length around 70 – 100 nm, which then requires the use of nanometric-sized $BiVO_4$ particles.[33] To combine these requirements, various synthesis/deposition process were developed as electrodeposition [40], spin-coating or dip-coating [30,41], spray pyrolysis [42] or chemical vapor deposition (CVD) [43]. The choice of synthesis impacts the structure and microstructure of the $BiVO_4$ nanoparticles film on the substrate. It aims at enhancing the overall PEC water oxidation. As mentioned earlier, in the PEC water oxidation half-reaction, electron transfer at the semiconductor/electrolyte interface competes with the recombination of electron/hole photocharges in the bulk and on the surface.[8] To improve the OER performance, the general strategy involves an optimization of each steps of the water oxidation process including: i/ the enhancement of light absorption and charge transfer efficiency and ii/ the optimization of charge separation. Additionally, the chemical stability of the electrode should be addressed in the dedicated electrolyte. In the review of Gaikwad *et al.*, they classified electrode optimization strategies into three main categories, those that address modifications to the "bulk" materials of the electrode, electrode surface engineering which corresponds to the surface in contact with the electrolyte and the fabrication of heterojunction referred as interface engineering.[1] In table 1, the evolution of photocurrent density as function of the strategy applied between pristine $BiVO_4$ photoanode and the modified one is reported with the measurement's conditions at 1.23 V_{RHE} under standardize simulated light illumination (100 mW cm^{-2}; AM 1.5 G). Then, the best results in the literature with mix strategies are presented in the last part of the table.

Strategy	**Electrode design**	**Synthesis method**	**Electrolyte**	**Performance (pristine $BiVO_4$) at 1.23 V_{RHE}**	**Performances (after modifications) at 1.23 V_{RHE}**	**Ref.**
Bulk Morphology faceted	FTO/$BiVO_4$ (040)	seed-assisted hydrothermal synthesis + electrochemical treatment in borate buffer (pH 9.5)	1 M potassium borate buffer (pH 9.5)	**0.25 mA cm^{-2}** Onset potential ~ 0.4 V_{RHE} /	**2.5 mA cm^{-2}** Onset potential ~ 0.25 V_{RHE} /	44
Bulk Morphology: facets exposition	FTO/$BiVO_4$ (001)	Oriented $BiVO_4$ solid state reaction + Laser ablation Randomly oriented $BiVO_4$: sol-gel drop-casting	0.5 M potassium phosphate buffer (pH 7)	**0.25 mA cm^{-2}** Onset potential ~ 0.7 V_{RHE} IPCE 7 % @ 350 nm	**3.9 mA cm^{-2}** Onset potential ~ 0.55 V_{RHE} IPCE ~ 74 % @ 350 nm	45
Bulk Defect engineering (O vacancies)	FTO/$BiVO_4$	Spray pyrolysis + Photocharging in electrolyte	0.1 M phosphate borate buffer (pH 10)	**1,2 mA cm^{-2}** Onset potential ~ 0.7 V_{RHE} IPCE ~ 30 % @ 430 nm	**4.3 mA cm^{-2}** Onset potential ~ 0.25 V_{RHE} IPCE ~ 90 % @ 430 nm	46
Bulk Mo-doping	FTO/Mo:$BiVO_4$	DLI-CVD	0.5 M potassium phosphate buffer (pH ~ 7)	**1.5 mA cm^{-2}** Onset potential ~ 0.5 V_{RHE} IPCE ~ 25 % @ 430 nm	**2.4 mA cm^{-2}** Onset potential ~ 0.3 V_{RHE} IPCE ~ 40 % @ 430 nm	43
Bulk Mo-doping	FTO/Mo:$BiVO_4$	Spin-coating $BiVO_4$ seeds + subsequently growth of Mo:$BiVO_4$ with substitution of V / Mo at various temperature	0.2 M potassium phosphate buffer (pH~7)	**0.6 mA cm^{-2}** Onset potential ~ 0.75 V_{RHE} IPCE ~ 22 % @ 420 nm	**3.18 mA cm^{-2}** Onset potential ~ 0.55 V_{RHE} IPCE ~ 50 % @ 420 nm	47

Interface Type II heterojunction n-n junction	FTO/WO_3/$BiVO_4$	WO_3: wet chemical reduction reaction $BiVO_4$: spin coating	0.5 M potassium sulphate, K_2SO_4 (pH 7.1)	**0.30 mA cm^{-2}** Onset potential ~ 0.6 V_{RHE} IPCE ~ 10 % @ 430 nm	**2.83 mA cm^{-2}** Onset potential ~ 0.4 V_{RHE} IPCE ~ 45 % @ 430 nm	48
Interface Type II heterojunction n-n junction	FTO/TaON/$BiVO_4$	$BiVO_4$: Electrodeposition of BiOI and conversion to $BiVO_4$ by impregnation-calcination process + Immersion in TaON suspension TaON: Ta_2O_5 particles heated under NH_3	0.1 M potassium phosphate buffer (pH 7)	**1.5 mA cm^{-2}** Onset potential ~ 0.4 V_{RHE} /	**2.6 mA cm^{-2}** Onset potential ~ 0.25 V_{RHE} /	49
Interface Type II heterojunction p-n junction	FTO/BiOI/$BiVO_4$ (nanoporous)	$BiVO_4$: Electrodeposition of BiOI and conversion to $BiVO_4$ by impregnation-calcination process + Eelectrodeposition of BiOI	0.5 M potassium phosphate buffer (pH 7)	**1.23 mA cm^{-2}** / IPCE ~ 13 % @ 430 nmIPCE ~	**3.27 mA cm^{-2}** / IPCE ~ 44 % @ 430 nmIPCE ~	50
Interface Type II heterojunction p-n junction	FTO/$AgVO_3$/$BiVO_4$	$BiVO_4$: spin-coating $AgVO_3$: SILAR process deposition	0.1 M sodium sulphate, Na_2SO_4 (pH 6.4)	**0.25 mA cm^{-2}** Onset potential ~ 0.9 V_{RHE} IPCE = 7 % @ 420-450 nm	**1.5 mA cm^{-2}** Onset potential ~ 0.7 V_{RHE} /	51

Surface funct. Metal carbide co-catalyst	FTO/$BiVO_4$/ $Ti_3C_2T_x$	Nanoporous RA-$BiVO_4$: Electrodeposition of BiOI and conversion to $BiVO_4$ by impregnation-calcination process + reannealing (RA) in Ar $Ti_3C_2T_x$: etching process of Ti_3AlC_2 + spin-coating	1.0 M phosphate borate buffer (pH 9.3)	**2.1 mA cm^{-2}** Onset potential ~ 0.4 V_{RHE} IPCE ~ 29 % @ 430 nm	**3.45 mA cm^{-2}** Onset potential ~ 0.4 V_{RHE} IPCE = 58 % @ 430 nm	52
Surface funct. Co-catalyst	FTO/$BiVO_4$/Co (salophen)	$BiVO_4$: Electrodeposition of BiOI and conversion to $BiVO_4$ by impregnation-calcination process +room temperature soaking for Co(salophen)	1.0 M Phosphate buffer (pH 7)	**1.48 mA cm^{-2}** Onset potential ~ 0.42 V_{RHE} Stability ~ 3 h IPCE ~ 40 % @430 nm	**4.27 mA cm^{-2}** Onset potential ~ 0.2 V_{RHE} Stability ~ 3 h IPCE ~ 89 % @430 nm	53
Surface funct. Metal oxide/hydroxide-based cocatalysts	FTO/$BiVO_4$/β-FeOOH	$BiVO_4$: Electrodeposition of BiOI and conversion to $BiVO_4$ by impregnation-calcination process + solution impregnation method (β-FeOOH)	0.2 M Na_2SO_4 (pH 7)	**1 mA cm^{-2}** Onset potential ~ 0.62 V_{RHE} IPCE ~ 10 % @420 nm	**4.3 mA cm^{-2}** Onset potential ~ 0.42 V_{RHE} Stability ~ 2 h IPCE = 55% @420 nm	54
Surface funct. Passivation layer	FTO/$BiVO_4$/Al_2O_3	$BiVO_4$: Electrodeposition of BiOI and conversion to $BiVO_4$ by impregnation-calcination process Al_2O_3: plasma-enhance ALD	0.5 M sodium sulphate, Na_2SO_4 (pH 6)	**1.34 mA cm^{-2}** Onset potential ~ 0.3 V_{RHE} /	**1.2 mA cm^{-2}** Onset Potential ~ 0.6 V_{RHE} /	55

Surface funct. Passivation layer Coupled with catalyst	FTO/$BiVO_4$/TiO_2/Ni	$BiVO_4$: spin-coating + ALD of TiO_2 Sputtering of Ni	0.1 M potassium hydroxide, KOH (pH 13)	**~ 0.5 mA cm^{-2}** Onset potential ~ 0.7 V_{RHE} Stability for minutes	**1.3 mA cm^{-2}** Onset potential ~ 0.6 V_{RHE} Stability for hours (4 h)	56

COMBINED STRATEGIES						
Bulk + Interface + Surface funct. Doping/n-n junction/ co-catalyst	FTO/WO_3/Mo:$BiVO_4$/Co-Pi	WO_3: wet chemical reduction reaction $BiVO_4$: spin coating Co-Pi: photo-assisted electrodeposition	0.5 M potassium sulphate, K_2SO_4 (pH 7.1)	**0.30 mA cm^{-2}** Onset potential ~ 0.6 V_{RHE} IPCE ~ 10 % @ 430 nm	**5.38 mA cm^{-2}** Onset potential ~ 0.4 V_{RHE} IPCE ~ 75 % @ 430 nm	48
Bulk + Interface Doping/p-n junction	FTO/$AgVO_3$/Mo:$BiVO_4$	Mo:$BiVO_4$: spin-coating $AgVO_3$: SILAR process deposition	0.1 M sodium sulphate, Na_2SO_4 (pH 6.4)	**0.25 mA cm^{-2}** Onset potential ~ 0.9 V_{RHE} IPCE = 7 % @ 420-450 nm	**1.93 mA cm^{-2}** Onset potential ~ 0.6 V_{RHE} IPCE = 53 % @ 420-450 nm	51
Interface + Surface funct. n-n junction/ co-catalyst	FTO/TaON/$BiVO_4$/Co-Pi	Electrodeposition of BiOI and conversion to $BiVO_4$ by impregnation-calcination process + Immersion in TaON suspension TaON: Ta_2O_5 particles heated under NH_3 Co-Pi: photo-assisted electrodeposition	0.1 M potassium phosphate buffer (pH 7)	**1.5 mA cm^{-2}** Onset potential ~ 0.4 V_{RHE} /	**3.6 mA cm^{-2}** Onset potential ~ 0.25 V_{RHE} /	49

Bulk + Interface Graded layers, doping, and n-n junction	FTO/WO_3/W:$BiVO_4$/$BiVO_4$	WO_3: Sol-gel and spin-coating $BiVO_4$ and W:$BiVO_4$: spin coating	0.5 M, sodium sulphate, Na_2SO_4 (pH 6)	**0.4 mA cm^{-2}** Onset potential ~ 0.75 V_{RHE} /	**2.6 mA cm^{-2}** Onset potential ~ 0.6 V_{RHE} /	57
Bulk + Surface funct. Lattices/ passivation	FTO/*b*-$BiVO_4$/TiO_{2-x} (b = Black)	$BiVO_4$: Electrodeposition of BiOI and conversion to $BiVO_4$ by impregnation-calcination process TiO_2: ALD Hydrogen plasma treatment	0.5 potassium phosphate buffer (pH 7)	**1.9 mA cm^{-2}** Onset potential ~ 0.4 V_{RHE} IPCE ~60 % @ 450 nm	**6.12 mA cm^{-2}** Onset potential ~ 0.2 V_{RHE} IPCE ~ 90 % @ 450 nm Stability ~ 100 h	58
Surface Naporous film + co-catalyst	FTO/$BiVO_4$/$Fe_xNi_{1-x}OOH$	$BiVO_4$: Electrodeposition of BiOI and conversion to $BiVO_4$ by impregnation-calcination process $Fe_xNi_{1-x}OOH$: pH-modulated immersion method	0.5 M potassium borate, K_3BO_3 buffer (pH 9.5)	**2.1 mA cm^{-2}** Onset potential ~ 0.4 V_{RHE} IPCE ~29 % @ 420 nm	**5.8 mA cm^{-2}** Onset potential ~ 0.45 V_{RHE} IPCE ~ 90 % @ 420 nm	59
Bulk + Interface Doping with graded layers + co-catalyst + textured FTO substrate	FTO/W:$BiVO_4$/Co-Pi	W:$BiVO_4$: spray pyrolysis With concentration gradient of W (textured FTO) Co-Pi: electrodeposition	0.1 M potassium phosphate buffer (pH 7)	Gradient doped FTO/W:$BiVO_4$ without Co-Pi: ***J* = 1.1 mA cm^{-2}** Onset potential ~ 0.6 V_{RHE}	**3.6 mA cm^{-2}** Onset potential ~ 0.3 V_{RHE}	21

Table 1: Some best photoanode reported in literature with the strategies employed (Surface funct. = surface functionalization)

- The **Bulk** modification strategy corresponds to morphology engineering, defect engineering and doping.

As the recombination of electrons and holes is strongly dependent on the structural and surface properties of the photoanode composition, a high crystallinity, in general, has a positive effect on the photocurrent. This is due to a decrease in crystalline defects and surface trap states.[8]
Looking at morphology engineering, the size, shape and facet orientation directly affect the charge transfer dynamics. Using this strategy, S. Wang *et al*. showed a tenfold improvement of the photocurrent density and reached a value of 2.5 mA cm^{-2} at 1.23 V_{RHE} (Figure 8.a) by exposing the (040) facet of $BiVO_4$.[44] They prepared $BiVO_4$ films on an FTO glass substrate with the (040) side exposed to the electrolyte, using a seed-assisted hydrothermal method coupled with electrochemical treatment in 1 M potassium borate electrolyte (pH 9.5). S.H. Han *et al.* demonstrated the advantages of pristine $BiVO_4$ with a preferred [001] growth orientation compared to randomly oriented $BiVO_4$ particles.[45] They achieved a photocurrent density of 3.9 mA cm^{-2} compared to (J = 0.25 mA cm^{-2}) (Figure 8.b), as better charge transport properties and surface reactivity is achieved with this orientation.
Introducing oxygen vacancies in $BiVO_4$ has led to a significant increase in the photocurrent compare to pristine $BiVO_4$. To realize this, various methods have been reported for generating oxygen vacancies. In their review, S. Wang *et al.* report the use of thermal treatment in reduction/inert atmospheres, heteroatom doping, chemical reduction, electrochemical reduction, photo-treatment in PEC cell, precursor/solution film treatment for creating oxygen vacancies.[60] Trześniewski *et al.* modified the surface of $BiVO_4$ using a process called photocharging.[46] They immersed the $BiVO_4$ photoanode, prepared by spray pyrolysis, in a potassium borate electrolyte (pH 10) while exposed to illumination. This results in a photocurrent density of 4.3 mA cm^{-2} with a low onset potential of 0.25 V_{RHE} (Figure 8.c).
Doping $BiVO_4$ with Mo conduces to improvement in electronic conductivity and then limit the electron/hole recombination. Yengantiwar *et al.* used the direct liquid injection chemical vapor deposition (DLI-CVD) technique to produce well-adherent and dense films of $BiVO_4$ and doped Mo:$BiVO_4$ to enhance OER.[43] They achieved a photocurrent density of 2.4 mA cm^{-2} compared to 1.5 mA cm^{-2} for pristine $BiVO_4$ in (Figure 8.d). Yin *et al.* achieved a highly efficient $BiVO_4$ photoanode by incorporating an excess of Mo during the doping process.[47] They deposited subsequently sealed electrode with $BiVO_4$ seeds in an autoclave containing the Bi and Mo precursors or Bi and V precursors at various temperatures. This process significantly improves

the electrode's PEC performance by creating porosity, which increase electrode/electrolyte interface. As a result, they obtained a photocurrent density of 3.18 mA cm^{-2} (Figure 8.e).

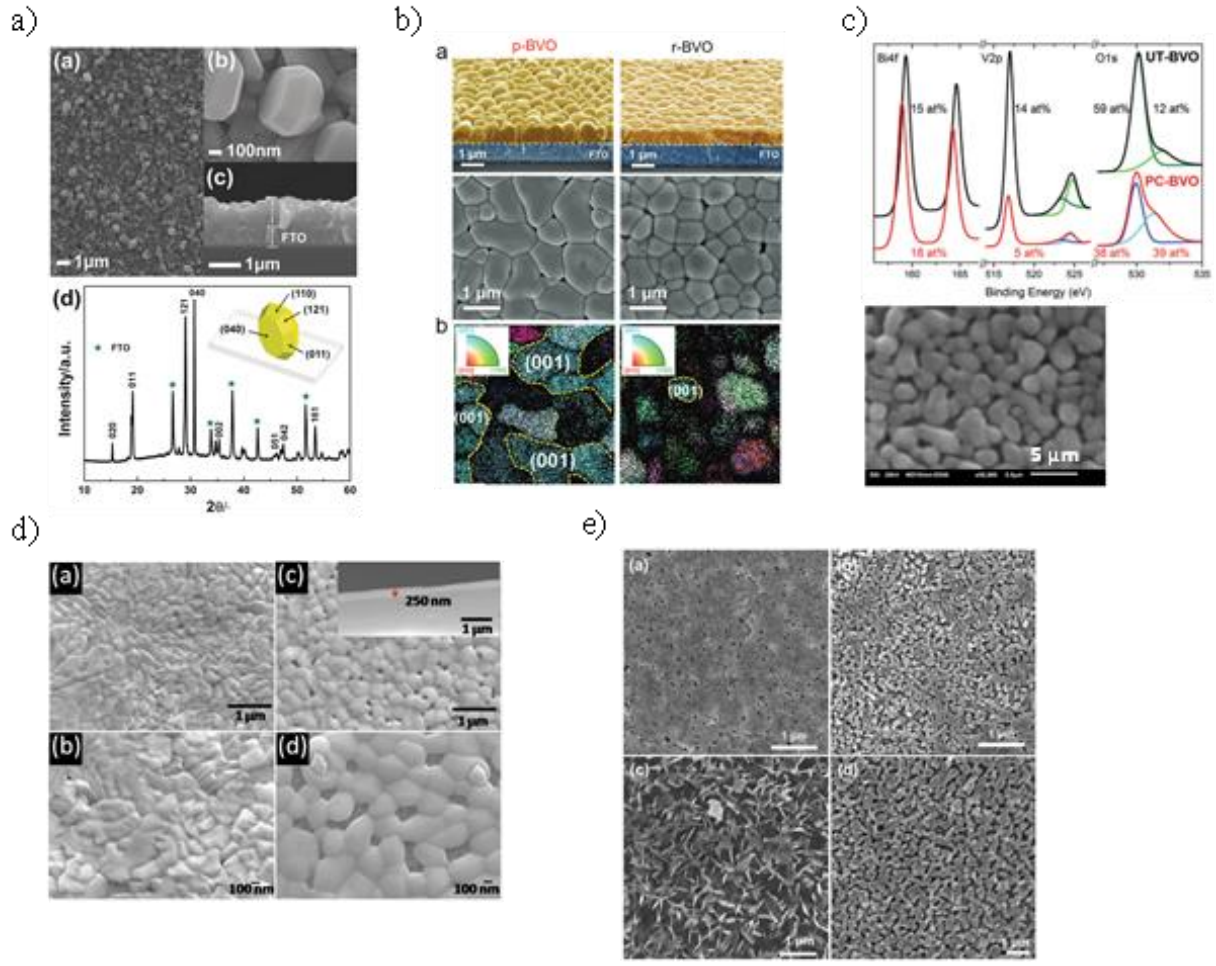

Figure 8: a) Seed assisted hydrothermal $BiVO_4$ synthesis: Low-magnification, (b) high-magnification, (c) cross-sectional FEG-SEM images, and (d) XRD pattern of $BiVO_4$. Inset: illustration of the crystal contacted with FTO substrates for $BiVO_4$ [44] **b) Laser ablation (LA) growth of $BiVO_4$** and crystallographic orientation analysis of the pristine-$BiVO_4$ (p-BVO) photoanode. (a) Film morphologies and (b) inverse pole figure (grain orientation) mapping images for p-BVO (thickness of 800 nm, 30-min deposition) and conventional sol–gel-derived $BiVO_4$ (r-BVO, thickness E 800 nm, 12 coating cycles) [45] **c) photocharging of $BiVO_4$ synthesized by spray pyrolysis**: XPS spectra of $BiVO_4$ photoanodes before and after photocharging in 0.1 M potassium borate buffer, pH 10, under AM1.5G simulated illumination and SEM imaging after photocharging pH 10 [46] **d) Mo-doped $BiVO_4$ synthesis by DLI-CVD**: FE-SEM image of (a, b) Pristine $BiVO_4$ and (c, d) 8% Mo:$BiVO_4$ nanocrystalline thin film. Inset shows cross-section SEM image of 30 min deposited 8% Mo:$BiVO_4$ film [43] **e) Synthesis of VMo-$BiVO_4$ by re-substitution process**: SEM images of (a) $BiVO_4$, (b) V-$BiVO_4$, (c) Mo-$BiVO_4$ and (d) V/Mo-$BiVO_4$ films [47]

- **Interface modifications** corresponds to the combination of $BiVO_4$ with another material to generate interesting heterojunctions for PEC water-splitting such as p-n junction or type II junction.

The addition of another metal oxide semiconductor in contact with $BiVO_4$ can create interesting junctions that facilitate the charge transport and solar absorption. Indeed, to have high redox capacity, a single semiconductor requires a higher energy which is directly linked to the band gap value.[61] However, semiconductors with wider band gaps are less sensitive to light in the solar spectrum.[61] The formation of heterojunctions between two or more semiconductors can improve reaction kinetics and charge separation. The various type of heterojunctions involving $BiVO_4$ semiconductors are well described in the work of Zhong. *et al.*[61,62] Based on the alignment of band structure, heterojunctions are categories in three main categories: straddling band gap (type I), staggered band gap (type II) and broken band gap (type III) as represented in Figure 9.[20] Generally, the type II heterojunction composed of n-n and p-n junctions is considered the most effective configuration to efficiently separate the charge carrier and inhibit electron/hole recombination.[1,61,63] In contrast, type I heterojunctions with $BiVO_4$ does not support the water reduction reaction at the cathode (semiconductor 1 in Figure 9 – type I) due to electron migration from semiconductor 1 to $BiVO_4$. In type III heterojunctions, the charges cannot be separated effectively.

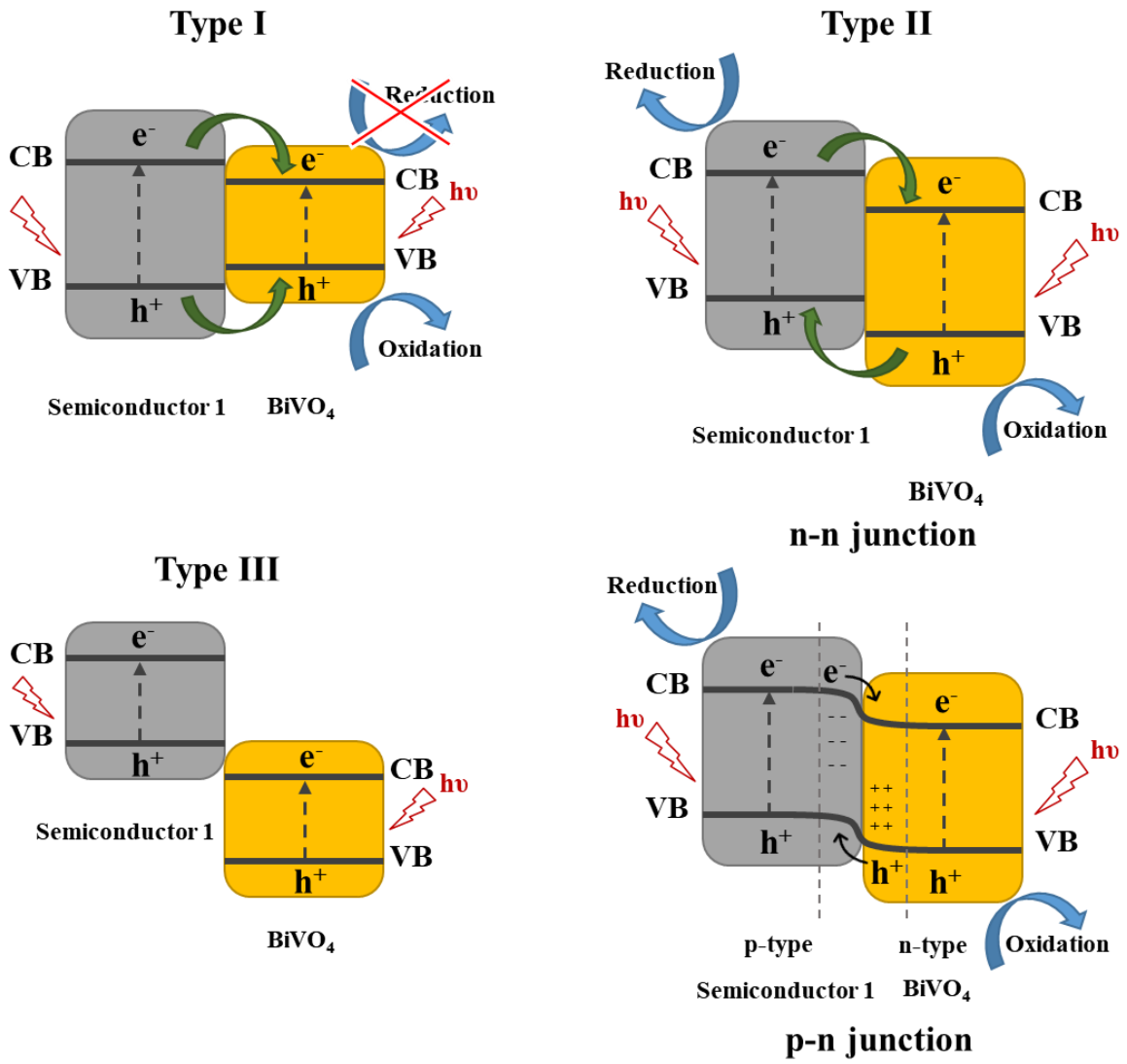

Figure 9: Scheme of heterojunctions types I, II (n-n junction and p-n junction), and III. Inspired from ref [61]

Recent studies have identified n-type semiconductor WO_3 as an intriguing candidate for coupling with $BiVO_4$. Its CB and VB edges are more positive than the corresponding band edges of $BiVO_4$, allowing the formation of a Type II n-n heterojunction.[1,48,64] The group of Q. Zheng *et al.* generated a $WO_3/BiVO_4$ photoanode and obtained a photocurrent density of 2.8 mA cm^{-2} with an IPCE of ~ 45 % at 430 nm.[48] Through additional modifications such as doping and surface functionalization by depositing Co-Pi co-catalyst for hole collection at the surface, they were able to reach a photocurrent of 5.38 mA cm^{-2} (Figure 10.a). L. Na *et al*. has improved 1.75 times the PEC efficiency of pristine $BiVO_4$ synthesised by spin coating by creating a heterojunction with another n-type semiconductor tantalum oxonitride

TaON/$BiVO_4$.[49] Their photoanode reached a photocurrent of 2.6 mA cm^{-2} compared with pristine $BiVO_4$, which has a value of 1.5 mA cm^{-2}. In addition, the low onset potential is 0.2 V_{RHE}. Further improvement at the surface with photoelectron deposition of Co-Pi co-catalyst resulted in the obtention of 3.6 mA cm^{-2} (Figure 10.b).[49]

Interestingly, type II p-n heterojunctions generate a built-in electric field that facilitates the efficient separation of photogenerated electrons and holes leading to improved PEC efficiency. This results in a fast flow of electrons and holes in opposite directions. The electrons being transferred to the CB of the n-type semiconductor and holes to the VB of the p-type semiconductor. K-H. Ye *et al.* designed a photoanode composed of BiOI and nanoporous $BiVO_4$, BiOI/$BiVO_4$ p-n junction.[50] They increased the active surface area and the limited bulk recombination by controlling the nanoparticles' thickness and porosity (Figure 10.c). They improved the photocurrent density and reached a photocurrent of 3.27 mA cm^{-2} compared to the one observed with pristine $BiVO_4$ of 1.23 mA cm^{-2}. Gao and co-workers fabricated a heterostructure with the p-type $AgVO_3$ semiconductor and $BiVO_4$.[51] They obtained a photocurrent of 1.5 mA cm^{-2} which is 6 times higher than that of pure $BiVO_4$. Further, they increased their photocurrent density and reached a value of 1.93 mA cm^{-2}, reducing significantly the onset potential of their pristine $BiVO_4$ photoanode by Mo-doping (Figure 10.d).[51]

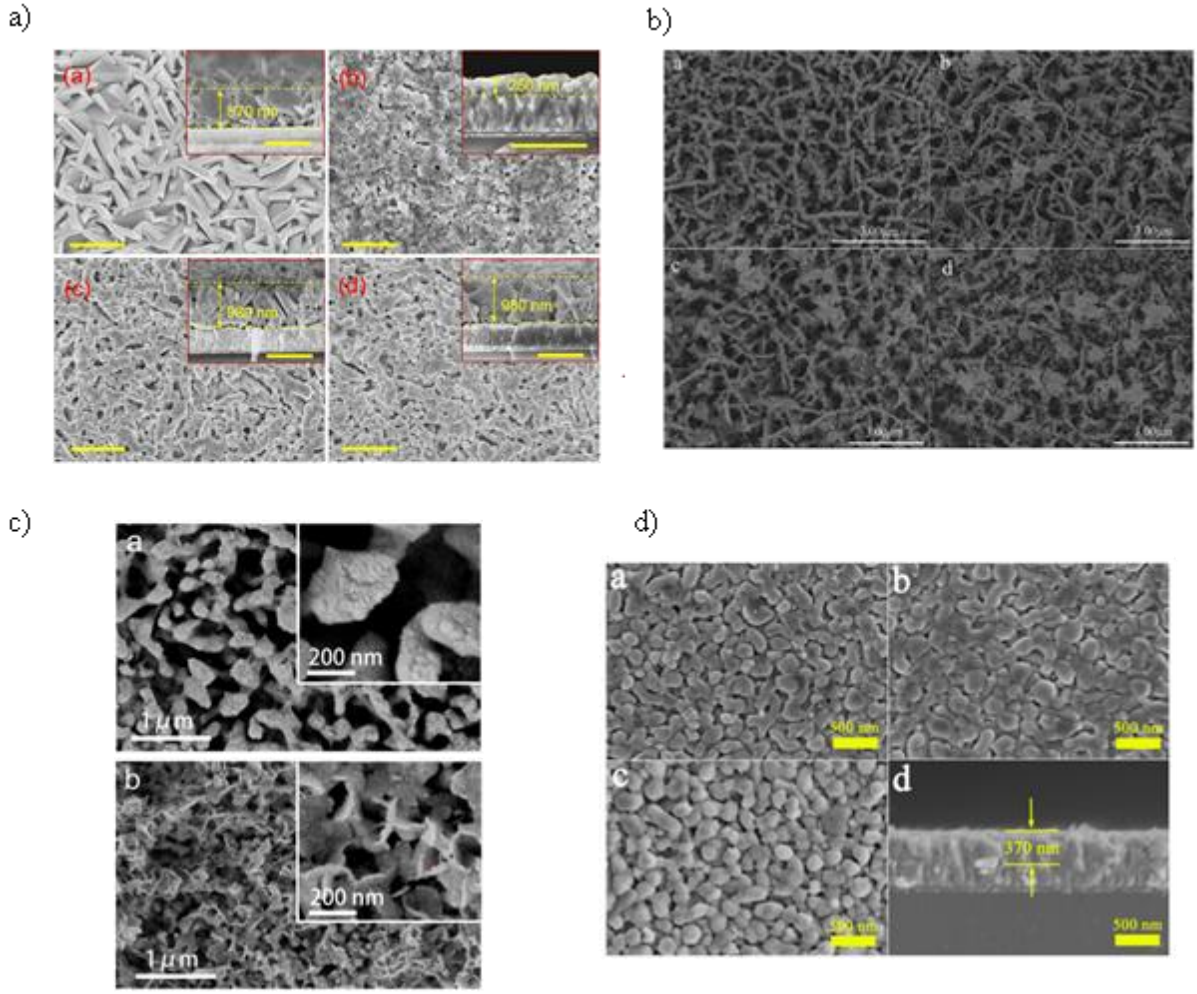

Figure 10 a) $WO_3/BiVO_4$ photoanode SEM images of the (a) WO_3, (b) $BiVO_4$, (c) $WO_3/BiVO_4$, and (d) WO_3/Mo-$BiVO_4$ photoanodes. The inserts are the corresponding cross-sectional SEM images. All the scale bars are 1 µm. [48]. b) **TaON/$BiVO_4$ photoanode**, SEM images of different electrodes. (a) $BiVO_4$, (b) 1-TaON/ $BiVO_4$, (c) 2-TaON/$BiVO_4$, (d) 3-TaON/$BiVO_4$. [49] c) **BiOI/$BiVO_4$ p-n junction photoanode**, top-view SEM images of (a) $BiVO_4$ and (b) BiOI/$BiVO_4$ [50] d) **$AgVO_3$/Mo:$BiVO_4$ photoanode**, SEM images of (a) $BiVO_4$, (b) 5% Mo-$BiVO_4$, (c) $AgVO_3$/5% Mo-$BiVO_4$, and (d) cross-sectional SEM of 5% Mo-$BiVO_4$ [51]

Recent discoveries showed that residual electrostatic interactions in the bulk of the semiconductor hinder the efficient transfer of photogenerated electrons and holes to other catalysts, limiting the full potential of the electrode. To address these limitations, some researches explore new heterojunction designs with Z-Scheme heterojunction.[62,63]

- **Surface functionalization** consists in adding at the electrode/electrolyte interface, a co-catalyst or a passivating layer.

The role of co-catalysts is to collect the holes accumulated at the surface, enhancing the OER kinetics. An overall improvement of the PEC water oxidation process is then observed. Rapid holes collection also helps to minimize photocorrosion reactions and ensures better stability over time. Additionally, by accelerating the OER kinetics, co-catalysts contribute to reducing the onset potential (causing a cathodic shift). Typically, carbon-based and earth-abundant elements such as Fe, Ni, and Co-based co-catalysts have been studied, including iron oxide/hydroxide, nickel oxide/hydroxide or cobalt phosphate/borate.[27,48] Recently, a metal carbide $Ti_3C_2T_x$ flakes has been used as co-catalyst by D. Yan *et al.* in $BiVO_4$/ $Ti_3C_2T_x$ photoanode with $BiVO_4$ film re-annealed after synthesis in argon (Figure 11.a). [52] Ti_3C_2Tx flakes enhanced the charge transfer of photogenerated carriers resulting in higher photocurrent density with a value of 3.45 mA cm^{-2} compared to 2.1 mA cm^{-2} for $BiVO_4$ photoanode. An improvement of the onset potential of ~ 0.4 V_{RHE} is also observed. Y. Liu *et al.* have used a cobalt salophen complex and have observed an increase of photocurrent by a factor 2.9 reaching a value of 4.27 mA cm^{-2} compared to 1.48 mA cm^{-2} for pristine $BiVO_4$.[53] A cathodic shift of their onset potential is also observed.[53] Interestingly, B. Zhang *et al.* have designed a $BiVO_4$/β-FeOOH photoanode.[54] They functionalized the $BiVO_4$ electrode surface with an ultrathin iron hydroxide layer, containing oxygen vacancies which promotes holes transport and separation. Doing this, an increase of the number of surface-active sites is observed (Figure 11.b) and they obtained a remarkable photocurrent of 4.3 mA cm^{-2}; this value is 4 times higher than the one observed for pristine, $BiVO_4$.

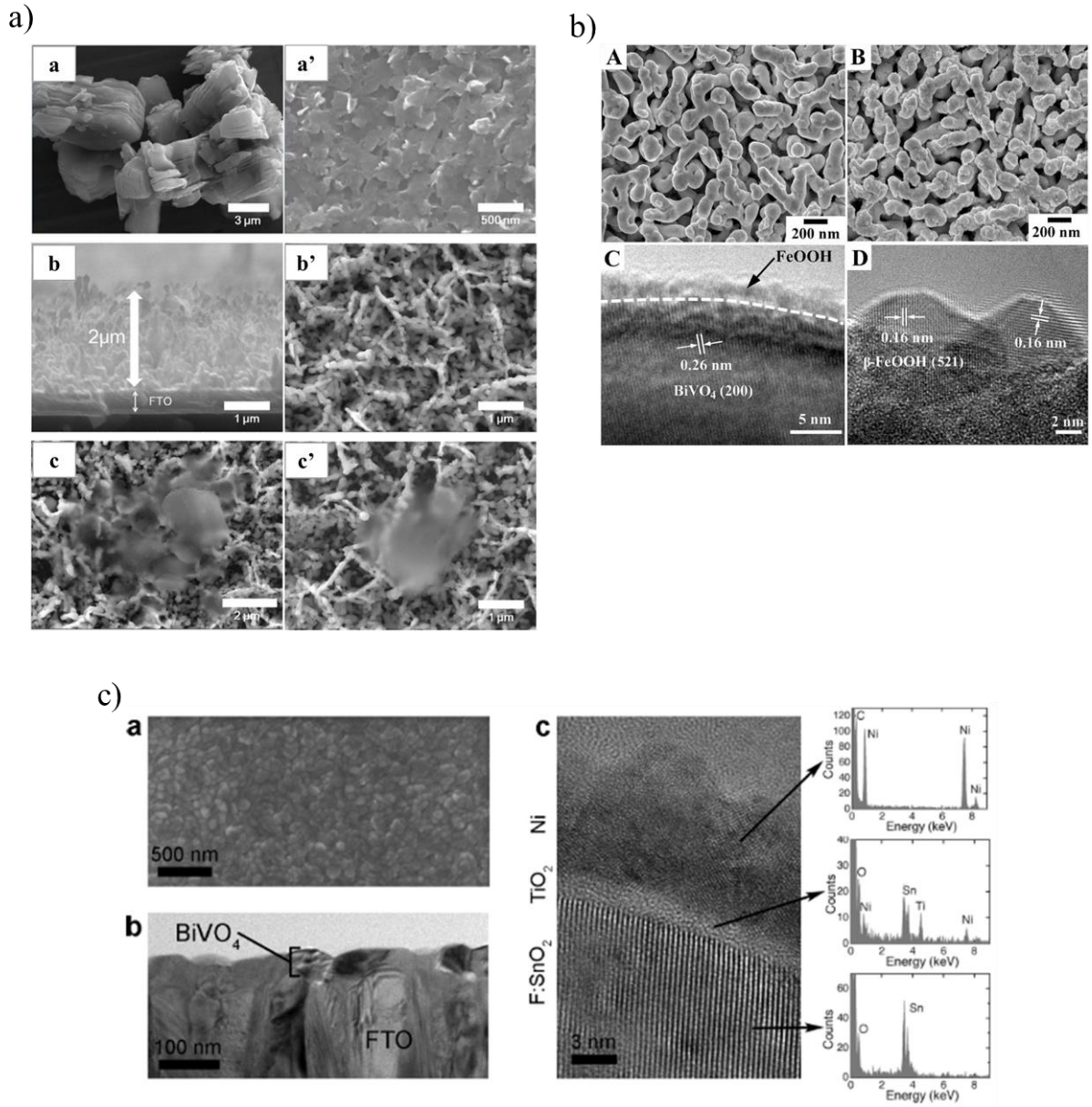

Figure 11: a) $BiVO_4/Ti_3C_2T_X$ photoanode: SEM images of a) a') $Ti_3C_2T_x$ b) b') $BiVO_{4\ a}$ and c)c') BiVO4/$Ti_3C_2T_x$ [52] **b) $BiVO_4$/β-FeOOH photoanode:** SEM images of A) $BiVO_4$ and B) $BiVO_4$/β-FeOOH, C),D) High-Resolution TEM images of $BiVO_4$/β-FeOOH photoanode [54] **c) $BiVO_4/TiO_2$/ Ni photoanode:** SEM images of a) $BiVO_4$ surface, b) $BiVO_4$ cross-section c) High-Resolution cross-section TEM images of TiO_2/Ni dual-layer on FTO [56]

One particular aspect to consider when a co-catalyst is deposited at the surface of an electrode is the possible undesired "shunting effect". It has been reported that depending on the underlayer film microstructure, a catalyst in contact with both photoactive material and FTO substrate is likely to directly contribute to recombination phenomena at the contact between the catalyst and FTO, as it is represented in the scheme Figure 12.[65,66]

Some groups have focused their efforts on developing passivation layers. While these layers may have negligible contributions to OER, they serve to protect and significantly enhance the durability of the photoanode in both the electrolyte and under light. Controlling the thickness of the passivation layer is essential to limit the reduction in photocurrent density. In a recent study, X. Wan *et al.* used plasma enhanced ALD to generate an ultrathin Al_2O_3 layer ~ 1 nm (10 ALD cycles) combined with a chemical treatment for passivation and to minimize the decrease in photocurrent density.[55] M.T. McDowell *et al.* propose to couple an ultrathin TiO_2 passivation layer with Ni on $BiVO_4$ photoanode to compensate the decrease in photocurrent (figure 11.c).[56] To obtain NiOOH co-catalyst, they disperse Ni particles onto the ultrathin TiO_2 layer. In contact with the electrolyte solution, the Ni particle transforms into NiOOH. A stable photocurrent of ~ 1.3 mA cm^{-2} is achieved during 4 hours. This is very interesting compared to bare $BiVO_4$ where its photocurrent density decreases after few minutes.

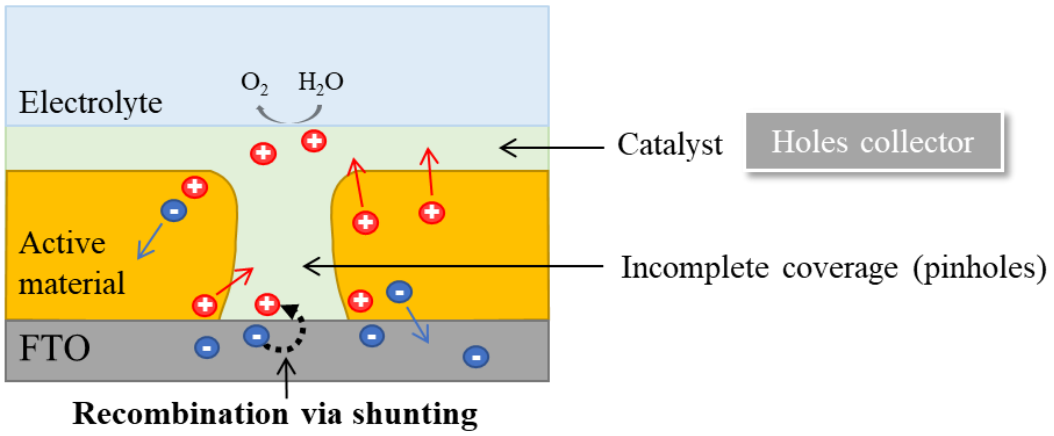

Figure 12: Scheme of recombination via shunting adapted from ref [65,66].

Finally, to significantly improve the photocurrent density and the durability of the photoanode, a combination of multiple strategies is often the most effective approach. As described in the section "Combined Strategies" of the Table 1, it has been possible to reach high photocurrent density above 4 mA cm^{-2}. In these cases, the synthesis process plays a crucial role on the $BiVO_4$ structure and morphology. For instance, one of the most widespread synthesis methods is the production of a nanoporous $BiVO_4$ photoanode developed by T. W. Kim and K-S. Choi. [40] BiOI is electrodeposited onto the FTO substrate, then impregnated with a V precursor and calcined to convert it into $BiVO_4$. To achieve a good surface coverage of the electrode, the synthesis of $BiVO_4$ from precursors dissolved in solvents coupled with spin-coating deposition technique is often used.

c. Electrolyte impact

Another noticeable parameter that influence the photoanode performance, but is often not explicitly addressed in the majority of reviews on the subject, is the electrolyte buffer and its pH. $BiVO_4$-based photoanodes exhibit better efficiency and long-term stability for the OER in alkaline electrolyte solutions. In alkaline conditions, the reaction equations change to:

$$4\,OH^- + 4\,h^+ = 2\,H_2O + O_2$$

$$4\,H_2O + 4\,e^- = 4\,OH^- + 2\,H_2$$

In an alkaline solution, the kinetics of the OER are much faster, resulting in a rapid formation of hydroxide ions in the electrolyte. These hydroxide ions can then effectively act as hole scavengers, facilitating the movement of charge carriers and reducing recombination of electron/hole pairs on the semiconductor surface. This leads to improved charge separation and increased photocurrent density, which is essential for an efficient photoelectrochemical water-splitting process.[16]

Since the OER reaction kinetics are faster in the presence of hydroxides, long-term stability is less of a concern.

However, in neutral and acidic conditions, the competitive reactions against OER are more significant than in alkaline environments, due to the weaker OER kinetics. It has been seen an increase of photocorrosion when the surface of the photoanode is directly illuminated due to the accumulation of holes generated at the electrode/electrolyte interface. They recombined easily with new photogenerated electrons and react with the electrolyte to generate very reactive species, notably radicals that contribute to the degradation of the photoanode itself and the decrease of photocurrent value over time. Favaro *et al.* have observed light induced surface reactions at the $BiVO_4$/potassium phosphate buffer (pH 7) interface.[67] They found that, as a result of photocorrosion, a passivation layer is formed by the precipitation of $BiPO_4$ and is then dissolved in the dark.

In the majority of reported reviews on PEC water-splitting, the photocurrent obtained in various studies are compared without considering the influence of electrolyte pH on the OER kinetics and without explicitly mentioning the presence of sodium sulphite in the electrolyte. Indeed, Na_2SO_3 plays the role of a sacrificial hole scavenger. In the presence of Na_2SO_3, the redox reaction does not imply the water-splitting reaction but the evolution of sulphites into sulphates which requires 2 times fewer holes to react compared to OER, as detailed in the following equation:

$$H_2O + SO_3^{2-} + 2\,h^+ = SO_4^{2-} + 2H^+$$

$$2H^+ + 2e^- = H_2$$

S. Zhang *et al.* investigated the dissolution behaviour in near-pH-neutral electrolytes with borate (pH 9), phosphate (pH 7) and citrate (used as hole scavenger).[16] In borate solutions, they observed a simultaneous dissolution of Bi and V, whereas in phosphate solutions, Bi and V dissolved at different potential range and rates. Bi dissolution is slowed down at more anodic potentials whereas V dissolution kept increasing with the formation of a Bi-rich surface layer constituted of $BiPO_4$. These results offer a new vision on the electrolyte buffer choice as the durability of the photoanode is linked to a balance between the intrinsic dissolution rate of Bi and V and the fast consumption of holes for OER. This last few years, a large variety of $BiVO_4$-based photoanode have been proposed and tested in neutral condition. Though, only few papers have designed photoanodes for PEC water-splitting in acidic conditions. Therefore, an improvement in the reaction kinetics in an acidic medium becomes essential. Additionally, as previously mentioned, some of the best photocathodes found in the literature exhibit high efficiency in acidic conditions. To enable the combination of this work with efficient photoanodes, it is necessary to adapt $BiVO_4$-based photoanodes for use in acidic conditions, where the OER is less favourable. In such conditions, the stability of the photoanode and the OER reaction kinetics become critical parameters.

5. Opportunity for $BiVO_4$ photoelectrodes and challenges

This thesis addresses issues related to the design of efficient $BiVO_4$-based photoanodes for PEC water-oxidation in acidic conditions (pH 6) since OER kinetics are not ease at this pH. Additionally, the separation and consumption of photocharges for electrochemical reactions significantly impact the photoanode's durability. Limiting photocorrosion phenomena is an even more competitive challenge than improving OER. Surprisingly, no studies have looked at the limiting parameters and long-term durability under these specific conditions. In addition, the synthesis methods have to be designed to be easily scalable and reproducible. These challenges were addressed by exploring two approaches: a one-step process using Sol-Gel chemistry coupled with the dip-coating technique and a two-step process involving first the generation of nanoparticles followed by their deposition onto an FTO substrate by dip-coating. The dip-coating deposition technique is well-developed in the laboratory and offers several advantages. It is versatile and can be used for a wide range of materials, including metallic-oxide coatings from sol-gel solutions, as well as biomolecules, polymers, metallic nanoparticles, ceramics, colloids and hybrids as metal-organic frameworks.[68–70] The dip-coating process involves immersing a substrate into the solution or dispersion, and then either draining the solution away or withdrawing the substrate, depending on the instrument used. During this process, the solvent evaporates, resulting in the formation of a homogeneous film. It can also be used to create more complex materials with thickness gradients.[69,71,72] The main parameter that affects the thickness of the deposited film is the withdrawal rate. However, other parameters, such as the temperature of the solution, the atmosphere, density, viscosity, and particle concentration for colloids, can also be controlled.[73] Depending on the application and solution-based precursor, several coating repetitions can be performed.[74] In contrast, other deposition methods can be used and may have certain drawbacks as listed below.

- **Spin-coating** generates homogeneous films but is inefficient for 2D film production due to excessive precursor wastage, and it's an out-of-equilibrium technique.[75] Viscosity and particle concentration control sintering properties.[76] Rotational speed must match nanoparticle size in colloidal suspension.[77] If particles are too large, they may be ejected due to centripetal force.[74] In dip-coating, additives can enhance colloidal suspension stability but may alter nanoparticle sintering properties.[78,79]

- **Drop-casting** is less controllable and is primarily used for depositing colloidal nanoparticles or when the "coffee-ring effect" and thickness variation are significant. It's not scalable like dip-coating and less reproducible.[80,81]
- **Blade coating** using a doctor blade, is an advanced “drop-cast” method for depositing colloidal nanoparticles with less waste and can coat large-scale substrates uniformly.[74,82] Blade speed is crucial, but thinner drops may lead to less uniform thickness compared to dip-coating, and the film quality relies on the blade gap and shape.[83,84]
- **Spray coating** deposits fine aerosol on a substrate, followed by drying and potential repetition. Constraints include isolated droplets, uneven surfaces, and pinholes.[74]

In the Chapter 2, we addressed the enhancement of PEC water oxidation in acidic media and its durability using a one-step approach for the synthesis of $BiVO_4$ electrode. We implemented a modified synthesis protocol previously developed by S. Hilliard *et al.* which demonstrated high reproducibility and yielded films with an average thickness of ~110 nm.[30] These films were produced using a sol-gel process coupled with the dip-coating technique, resulting in dense $BiVO_4$ and Mo-doped $BiVO_4$ films. Two strategies were employed to enhance charge transport, separation, and OER kinetics. First, the bulk was modified with Mo-doping in $BiVO_4$, and second, the surface was functionalized with Co-Pi as a co-catalyst. In-depth electrochemical analysis, along with the use of a hole-accepting agent as an electrolyte, provided a better understanding of the limiting phenomena of the photoanode. Mo-doping was found to be favourable for increasing charge transport under direct illumination conditions. However, low OER kinetics led to the accumulation of positive charges, contributing to charge recombination and photocorrosion phenomena.

The electrochemical response of Mo:$BiVO_4$/Co-Pi, featuring Co-Pi as a co-catalyst, was examined from the initial generation of electron-hole pairs. This investigation revealed changes in surface chemistry linked to Co (II) oxidation in presence of phosphates and its partial recovery. This modification greatly improved chemical stability, as demonstrated by the retention of photoanode thickness after 5 hours of continuous electrochemical analysis via chronoamperometry.

The durability of the photoanode was addressed by applying a passivation layer consisting of a thin TiO_2 layer deposited onto the surface of $BiVO_4$ or Mo:$BiVO_4$ photoanodes. The impact of TiO_2 thickness and crystallinity on its ability to protect the underlying $BiVO_4$ layer was evaluated for two types of synthesized films. While ALD is the reference deposition method

for ultrathin passivation layers, we also developed a modified Sol-Gel chemistry coupled with dip-coating protocol based on J. Sum *et al.* for generating ultrathin TiO_2 films.[85] Among these approaches, ultrathin TiO_2 deposited via dip-coating demonstrated the most promising results for passivation, minimizing the decrease in PEC water-oxidation efficiency when compared to ALD-deposited TiO_2 films.

In the Chapter 3, the development of structure and size-controlled nanoparticles through hydrothermal syntheses enabled the creation of a Mo:$BiVO_4$/V_2O_5 heterostructured photoanode. This approach combines two strategies: bulk modification achieved by incorporating Mo^{6+} into the structure and interface modification by establishing a type II n-n heterojunction between $BiVO_4$ and V_2O_5. The fabrication of this heterostructured photoanode was accomplished in a single deposition step. Following the synthesis of Mo:$BiVO_4$, a V_2O_5 gel was utilized as a "solvent" to disperse the Mo:$BiVO_4$ nanoparticles, forming a film through dip-coating on an FTO substrate inspired of “brick and mortar” approach. The unique 2D structure of V_2O_5 plays a crucial role as a binder between the Mo:$BiVO_4$ nanoparticles, significantly improving particle-to-particle contact. This study marks the first exploration in acidic conditions of the $BiVO_4$/V_2O_5-based photoanode’s OER performance under standardized illumination conditions, without the addition of a hole scavenger in the electrolyte, such as Na_2SO_3, making it directly comparable to other heterojunctions.

6. References

(1) Gaikwad, M. A.; Suryawanshi, U. P.; Ghorpade, U. V.; Jang, J. S.; Suryawanshi, M. P.; Kim, J. H. Emerging Surface, Bulk, and Interface Engineering Strategies on $BiVO_4$ for Photoelectrochemical Water Splitting. *Small* **2022**, *18* (10), 1–35. https://doi.org/10.1002/smll.202105084.

(2) Jiang, C.; Moniz, S. J. A.; Wang, A.; Zhang, T.; Tang, J. Photoelectrochemical Devices for Solar Water Splitting-Materials and Challenges. *Chem. Soc. Rev*. 2017, pp 4645–4660. https://doi.org/10.1039/c6cs00306k.

(3) Hisatomi, T.; Kubota, J.; Domen, K. Recent Advances in Semiconductors for Photocatalytic and Photoelectrochemical Water Splitting. *Chem. Soc. Rev*. 2014, pp 7520–7535. https://doi.org/10.1039/c3cs60378d.

(4) Yang, W.; Ramanujam Prabhakar, R.; Tan, J.; Tilley, D. S.; Moon, J. Strategies for Enhancing the Photocurrent, Photovoltage, and Stability of Photoelectrodes for Photoelectrochemical Water Splitting. *Chem. Soc. Rev* **2019**, *48*, 4979–5015. https://doi.org/10.1039/c8cs00997j.

(5) Rashid, M. M.; Mesfer, M. K. Al; Naseem, H.; Danish, M. Hydrogen Production by Water Electrolysis: A Review of Alkaline Water Electrolysis, PEM Water Electrolysis and High Temperature Water Electrolysis. *Int. J. Eng. Adv. Technol.* **2015**, No. 3, 2249–8958.

(6) Kumar, M.; Meena, B.; Subramanyam, P.; Suryakala, D.; Subrahmanyam, C. Recent Trends in Photoelectrochemical Water Splitting: The Role of Cocatalysts. *NPG Asia Materials*. 2022. https://doi.org/10.1038/s41427-022-00436-x.

(7) Walter, M. G.; Warren, E. L.; McKone, J. R.; Boettcher, S. W.; Mi, Q.; Santori, E. A.; Lewis, N. S. Solar Water Splitting Cells. *Chem. Rev.* **2010**, *110* (11), 6446–6473. https://doi.org/10.1021/cr1002326.

(8) Amano, F. Photoelectrochemical Oxygen Evolution. In *Solar-to-Chemical Conversion: Photocatalytic and Photoelectrochemical Processes*; Wiley, 2021; pp 163–187. https://doi.org/10.1002/9783527825073.ch7.

(9) Miao, B.; Iqbal, A.; Bevan, K. H. Utilizing Band Diagrams to Interpret the Photovoltage and Photocurrent in Photoanodes: A Semiclassical Device Modeling Study. *J. Phys. Chem. C* **2019**, *123* (47), 28593–28603. https://doi.org/10.1021/acs.jpcc.9b07536.

(10) Lewis, N. S. Chemical Control of Charge Transfer and Recombination at Semiconductor Photoelectrode Surfaces. *Inorganic Chemistry*. 2005, pp 6900–6911. https://doi.org/10.1021/ic051118p.

(11) Tayebi, M.; Lee, B. K. Recent Advances in $BiVO_4$ Semiconductor Materials for Hydrogen Production Using Photoelectrochemical Water Splitting. *Renew. Sustain. Energy Rev.* **2019**, *111* (May), 332–343. https://doi.org/10.1016/j.rser.2019.05.030.

(12) Fang, W.; Shangguan, W. A Review on Bismuth-Based Composite Oxides for Photocatalytic Hydrogen Generation. *International Journal of Hydrogen Energy*. 2019, pp 895–912. https://doi.org/10.1016/j.ijhydene.2018.11.063.

(13) Prévot, M. S.; Sivula, K. Photoelectrochemical Tandem Cells for Solar Water Splitting. *Am. Chem. Soc.* **2013**, *117*, 17879–17893. https://doi.org/dx.doi.org/10.1021/jp405291g.

(14) Chen, D.; Xie, Z.; Tong, Y.; Huang, Y. Review on $BiVO_4$-Based Photoanodes for Photoelectrochemical Water Oxidation: The Main Influencing Factors. *Energy and Fuels*. 2022, pp 9932–9949. https://doi.org/10.1021/acs.energyfuels.2c02119.

(15) Tolod, K. R.; Hernández, S.; Russo, N. Recent Advances in the $BiVO_4$ Photocatalyst for Sun-

Driven Water Oxidation: Top-Performing Photoanodes and Scale-up Challenges. *Catalysts* **2017**, *7* (1). https://doi.org/10.3390/catal7010013.

(16) Zhang, S.; Ahmet, I.; Kim, S. H.; Kasian, O.; Mingers, A. M.; Schnell, P.; Kölbach, M.; Lim, J.; Fischer, A.; Mayrhofer, K. J. J.; Cherevko, S.; Gault, B.; Van De Krol, R.; Scheu, C. Different Photostability of $BiVO_4$ in near-PH-Neutral Electrolytes. *ACS Appl. Energy Mater.* **2020**, *3* (10), 9523–9527. https://doi.org/10.1021/acsaem.0c01904.

(17) Siavash Moakhar, R.; Hosseini-Hosseinabad, S. M.; Masudy-Panah, S.; Seza, A.; Jalali, M.; Fallah-Arani, H.; Dabir, F.; Gholipour, S.; Abdi, Y.; Bagheri-Hariri, M.; Riahi-Noori, N.; Lim, Y. F.; Hagfeldt, A.; Saliba, M. Photoelectrochemical Water-Splitting Using CuO-Based Electrodes for Hydrogen Production: A Review. *Advanced Materials*. John Wiley and Sons Inc August 1, 2021, p 2007285. https://doi.org/10.1002/adma.202007285.

(18) Kim, J. H.; Lee, J. S. Elaborately Modified $BiVO_4$ Photoanodes for Solar Water Splitting. *Advanced Materials*. 2019, pp 1806938 (30)-1806938 (35). https://doi.org/10.1002/adma.201806938.

(19) Tokunaga, S.; Kato, H.; Kudo, A. Selective Preparation of Monoclinic and Tetragonal $BiVO_4$ with Scheelite Structure and Their Photocatalytic Properties. *Chem. Mater.* **2001**, *13* (12), 4624–4628. https://doi.org/10.1021/cm0103390.

(20) Huang, Z. F.; Pan, L.; Zou, J. J.; Zhang, X.; Wang, L. Nanostructured Bismuth Vanadate-Based Materials for Solar-Energy-Driven Water Oxidation: A Review on Recent Progress. *Nanoscale* **2014**, *6* (23), 14044–14063. https://doi.org/10.1039/c4nr05245e.

(21) Abdi, F. F.; Han, L.; Smets, A. H. M.; Zeman, M.; Dam, B.; Van De Krol, R. Efficient Solar Water Splitting by Enhanced Charge Separation in a Bismuth Vanadate-Silicon Tandem Photoelectrode. *Nat. Commun.* **2013**, *4*. https://doi.org/10.1038/ncomms3195.

(22) Ahn, H. J.; Kwak, M. J.; Lee, J. S.; Yoon, K. Y.; Jang, J. H. Nanoporous Hematite Structures to Overcome Short Diffusion Lengths in Water Splitting. *J. Mater. Chem. A* **2014**, *2* (47), 19999–20003. https://doi.org/10.1039/c4ta04890c.

(23) Bhattacharya, A. K.; Mallick, K. K.; Hartridge, A. Phase Transition in BiVO4. *Mater. Lett.* **1997**, *30*, 7–13.

(24) Li, G.; Bai, Y.; Zhang, W. F. Difference in Valence Band Top of $BiVO_4$ with Different Crystal Structure. *Mater. Chem. Phys.* **2012**, *136* (2–3), 930–934. https://doi.org/10.1016/j.matchemphys.2012.08.023.

(25) Saison, T.; Chemin, N.; Chanéac, C.; Durupthy, O.; Mariey, L.; Maugé, F.; Brezová, V.; Jolivet, J. P. New Insights into $BiVO_4$ Properties as Visible Light Photocatalyst. *J. Phys. Chem. C* **2015**, *119* (23), 12967–12977. https://doi.org/10.1021/acs.jpcc.5b01468.

(26) Park, Y.; Mc Donald, K. J.; Choi, K. S. Progress in Bismuth Vanadate Photoanodes for Use in Solar Water Oxidation. *Chem. Soc. Rev* **2013**, *42* (6), 2321–2337. https://doi.org/10.1039/c2cs35260e.

(27) Lee, D. K.; Choi, K. S. Enhancing Long-Term Photostability of $BiVO_4$ Photoanodes for Solar Water Splitting by Tuning Electrolyte Composition. *Nat. Energy* **2018**, *3* (1), 53–60. https://doi.org/10.1038/s41560-017-0057-0.

(28) Walsh, A.; Yan, Y.; Huda, M. N.; Al-Jassim, M. M.; Wei, S. H. Band Edge Electronic Structure of $BiVO_4$: Elucidating the Role of the Bi s and V d Orbitals. *Chem. Mater.* **2009**, *21* (3), 547–551. https://doi.org/10.1021/cm802894z.

(29) Cooper, J. K.; Gul, S.; Toma, F. M.; Chen, L.; Glans, P. A.; Guo, J.; Ager, J. W.; Yano, J.; Sharp, I. D. Electronic Structure of Monoclinic $BiVO_4$. *Chem. Mater.* **2014**, *26* (18), 5365–5373. https://doi.org/10.1021/cm5025074.

(30) Hilliard, S.; Friedrich, D.; Kressman, S.; Strub, H.; Artero, V.; Laberty-Robert, C. Solar-Water-Splitting $BiVO_4$ Thin-Film Photoanodes Prepared By Using a Sol–Gel Dip-Coating Technique. *ChemPhotoChem* **2017**, *1* (6), 273–280. https://doi.org/10.1002/cptc.201700003.

(31) Tan, H. L.; Amal, R.; Ng, Y. H. Alternative Strategies in Improving the Photocatalytic and Photoelectrochemical Activities of Visible Light-Driven $BiVO_4$: A Review. *J. Mater. Chem. A* **2017**, *5* (32), 16498–16521. https://doi.org/10.1039/c7ta04441k.

(32) Abdi, F. F.; Van De Krol, R. Nature and Light Dependence of Bulk Recombination in Co-Pi-Catalyzed $BiVO_4$ Photoanodes. *J. Phys. Chem. C* **2012**, *116* (17), 9398–9404. https://doi.org/10.1021/jp3007552.

(33) Rettie, A. J. E.; Lee, H. C.; Marshall, L. G.; Lin, J. F.; Capan, C.; Lindemuth, J.; McCloy, J. S.; Zhou, J.; Bard, A. J.; Mullins, C. B. Combined Charge Carrier Transport and Photoelectrochemical Characterization of $BiVO_4$ Single Crystals: Intrinsic Behavior of a Complex Metal Oxide. *J. Am. Chem. Soc.* **2013**, *135* (30), 11389–11396. https://doi.org/10.1021/ja405550k.

(34) Yabuta, M.; Takeda, A.; Sugimoto, T.; Watanabe, K.; Kudo, A.; Matsumoto, Y. Particle Size Dependence of Carrier Dynamics and Reactivity of Photocatalyst $BiVO_4$ Probed with Single-Particle Transient Absorption Microscopy. *J. Phys. Chem. C* **2017**, *121* (40), 22060–22066. https://doi.org/10.1021/acs.jpcc.7b06230.

(35) Wu, M.; Jing, Q.; Feng, X.; Chen, L. $BiVO_4$ Microstructures with Various Morphologies: Synthesis and Characterization. *Appl. Surf. Sci.* **2018**, *427*, 525–532. https://doi.org/10.1016/j.apsusc.2017.07.299.

(36) Ressnig, D.; Kontic, R.; Patzke, G. R. Morphology Control of $BiVO_4$ Photocatalysts: PH Optimization vs. Self-Organization. *Mater. Chem. Phys.* **2012**, *135* (2–3), 457–466. https://doi.org/10.1016/j.matchemphys.2012.05.008.

(37) Rather, R. A.; Mehta, A.; Lu, Y.; Valant, M.; Fang, M.; Liu, W. Influence of Exposed Facets, Morphology and Hetero-Interfaces of $BiVO_4$ on Photocatalytic Water Oxidation: A Review. *International Journal of Hydrogen Energy*. 2021, pp 21866–21888. https://doi.org/10.1016/j.ijhydene.2021.04.060.

(38) Malathi, A.; Madhavan, J.; Ashokkumar, M.; Arunachalam, P. A Review on $BiVO_4$ Photocatalyst: Activity Enhancement Methods for Solar Photocatalytic Applications. *Applied Catalysis A: General*. 2018, pp 47–74. https://doi.org/10.1016/j.apcata.2018.02.010.

(39) Zulkifili, A. N.; Fujiki, A.; Kimijima, S. Flower-like BiVO4 Microspheres and Their Visible Light-Driven Photocatalytic Activity. *Appl. Sci.* **2018**, *8*, 1–10. https://doi.org/10.3390/app8020216.

(40) Kim, T. W.; Choi, K. S. SI_Nanoporous $BiVO_4$ Photoanodes with Dual-Layer Oxygen Evolution Catalysts for Solar Water Splitting. *Science (80-.).* **2014**, *343* (6174), 990–994. https://doi.org/10.1126/science.1246913.

(41) Toma, F. M.; Cooper, J. K.; Kunzelmann, V.; McDowell, M. T.; Yu, J.; Larson, D. M.; Borys, N. J.; Abelyan, C.; Beeman, J. W.; Yu, K. M.; Yang, J.; Chen, L.; Shaner, M. R.; Spurgeon, J.; Houle, F. A.; Persson, K. A.; Sharp, I. D. Mechanistic Insights into Chemical and Photochemical Transformations of Bismuth Vanadate Photoanodes. *Nat. Commun.* **2016**, *7* (May), 1–11. https://doi.org/10.1038/ncomms12012.

(42) Liang, Y.; Tsubota, T.; Mooij, L. P. A.; Van De Krol, R. Highly Improved Quantum Efficiencies for Thin Film $BiVO_4$ Photoanodes. *J. Phys. Chem. C* **2011**, *115* (35), 17594–17598. https://doi.org/10.1021/jp203004v.

(43) Yengantiwar, A.; Palanivel, S.; Archana, P. S.; Ma, Y.; Pan, S.; Gupta, A. Direct Liquid Injection Chemical Vapor Deposition of Molybdenum-Doped Bismuth Vanadate

Photoelectrodes for Efficient Solar Water Splitting. *J. Phys. Chem. C* **2017**, *121* (11), 5914–5924. https://doi.org/10.1021/acs.jpcc.6b12710.

(44) Wang, S.; Chen, P.; Yun, J. H.; Hu, Y.; Wang, L. An Electrochemically Treated $BiVO_4$ Photoanode for Efficient Photoelectrochemical Water Splitting. *Angew. Chemie - Int. Ed.* **2017**, *56* (29), 8500–8504. https://doi.org/10.1002/ANIE.201703491.

(45) Han, H. S.; Shin, S.; Kim, D. H.; Park, I. J.; Kim, J. S.; Huang, P.-S. S.; Lee, J.-K. K.; Cho, I. S.; Zheng, X. Boosting the Solar Water Oxidation Performance of a $BiVO_4$ Photoanode by Crystallographic Orientation Control. *Energy Environ. Sci.* **2018**, *11* (5), 1299–1306. https://doi.org/10.1039/c8ee00125a.

(46) Trzes´niewski, B. J.; Trzes´niewski, T.; Digdaya, I. A.; Nagaki, T.; Ravishankar, S.; Herraiz-Cardona, I.; Vermaas, D. A.; Longo, A.; Gimenez, S.; Smith, W. A. Near-Complete Suppression of Surface Losses and Total Internal Quantum Efficiency in BiVO4 Photoanodes. *Energy Environ. Sci.* **2017**, *10*, 1517. https://doi.org/10.1039/c6ee03677e.

(47) Yin, X.; Qiu, W.; Li, W.; Li, C.; Wang, K.; Yang, X.; Du, L.; Liu, Y.; Li, J. High Porosity Mo Doped $BiVO_4$ Film by Vanadium Re-Substitution for Efficient Photoelectrochemical Water Splitting. *Chem. Eng. J.* **2020**, *389*, 124365. https://doi.org/10.1016/j.cej.2020.124365.

(48) Zeng, Q.; Li, J.; Li, L.; Bai, J.; Xia, L.; Zhou, B. Synthesis of WO_3/$BiVO_4$ Photoanode Using a Reaction of Bismuth Nitrate with Peroxovanadate on WO_3 Film for Efficient Photoelectrocatalytic Water Splitting and Organic Pollutant Degradation. *Appl. Catal. B Environ.* **2017**, *217*, 21–29. https://doi.org/10.1016/j.apcatb.2017.05.072.

(49) Li, N.; Jiang, Y.; Wang, X.; Hu, C.; Jiang, W.; Li, S.; Xia, L. Efficient Charge Separation and Transfer of a TaON/ $BiVO_4$ Heterojunction for Photoelectrochemical Water Splitting †. *R. Soc. Chem.* **2021**, *11*, 13269. https://doi.org/10.1039/d1ra00974e.

(50) Ye, K. H.; Chai, Z.; Gu, J.; Yu, X.; Zhao, C.; Zhang, Y.; Mai, W. BiOI-$BiVO_4$ Photoanodes with Significantly Improved Solar Water Splitting Capability: P-n Junction to Expand Solar Adsorption Range and Facilitate Charge Carrier Dynamics. *Nano Energy* **2015**, *18*, 222–231. https://doi.org/10.1016/j.nanoen.2015.10.018.

(51) Gao, L.; Long, X.; Wei, S.; Wang, C.; Wang, T.; Li, F.; Hu, Y.; Ma, J.; Jin, J. Facile Growth of $AgVO_3$ Nanoparticles on Mo-Doped $BiVO_4$ Film for Enhanced Photoelectrochemical Water Oxidation. *Chem. Eng. J.* **2019**, *378*, 122193. https://doi.org/10.1016/j.cej.2019.122193.

(52) Yan, D.; Fu, X.; Shang, Z.; Liu, J.; Luo, A. A $BiVO_4$ Film Photoanode with Re-Annealing Treatment and 2D Thin $Ti_3C_2T_X$ Flakes Decoration for Enhanced Photoelectrochemical Water Oxidation. *Chem. Eng. J.* **2018**, *361*, 853–861. https://doi.org/10.1016/j.cej.2018.12.146.

(53) Liu, Y.; Jiang, Y.; Li, F.; Yu, F.; Jiang, W.; Xia, L. Molecular Cobalt Salophen Catalyst-Integrated $BiVO_4$ as Stable and Robust Photoanodes for Photoelectrochemical Water Splitting. *J. Mater. Chem. A* **2018**, *6* (23), 10761–10768. https://doi.org/10.1039/c8ta01304g.

(54) Zhang, B.; Wang, L.; Zhang, Y.; Ding, Y.; Bi, Y. Ultrathin FeOOH Nanolayers with Abundant Oxygen Vacancies on $BiVO_4$ Photoanodes for Efficient Water Oxidation. *Angew. Chemie* **2018**, *130* (8), 2270–2274. https://doi.org/10.1002/ange.201712499.

(55) Wan, X.; Xu, Y.; Wang, X.; Guan, X.; Fu, Y.; Hu, C.; Hu, H.; Rong, N. Atomic Layer Deposition Assisted Surface Passivation on Bismuth Vanadate Photoanodes for Enhanced Solar Water Oxidation. *Appl. Surf. Sci.* **2022**, *573*, 151492. https://doi.org/10.1016/j.apsusc.2021.151492.

(56) McDowell, M. T.; Lichterman, M. F.; Spurgeon, J. M.; Hu, S.; Sharp, I. D.; Brunschwig, B. S.; Lewis, N. S. Improved Stability of Polycrystalline Bismuth Vanadate Photoanodes by Use of Dual-Layer Thin TiO_2/Ni Coatings. *J. Phys. Chem. C* **2014**, *118* (34), 19618–19624. https://doi.org/10.1021/jp506133y.

(57) Choi, J.; Sudhagar, P.; Kim, J. H.; Kwon, J.; Kim, J.; Terashima, C.; Fujishima, A.; Song, T.; Paik, U. WO_3/W:$BiVO_4$/$BiVO_4$ Graded Photoabsorber Electrode for Enhanced Photoelectrocatalytic Solar Light Driven Water Oxidation. *Phys. Chem. Chem. Phys.* **2017**, *19* (6), 4648–4655. https://doi.org/10.1039/c6cp08199a.

(58) Tian, Z.; Zhang, P.; Qin, P.; Sun, D.; Zhang, S.; Guo, X.; Zhao, W.; Zhao, D.; Huang, F. Novel Black $BiVO_4$/TiO_2−x Photoanode with Enhanced Photon Absorption and Charge Separation for Efficient and Stable Solar Water Splitting. *Adv. Energy Mater.* **2019**, *9* (27), 1–8. https://doi.org/10.1002/aenm.201901287.

(59) Zhang, B.; Huang, X.; Zhang, Y.; Lu, G.; Chou, L.; Bi, Y. Unveiling the Activity and Stability Origin of $BiVO_4$ Photoanodes with FeNi Oxyhydroxides for Oxygen Evolution. *Angew. Chemie - Int. Ed.* **2020**, *59* (43), 18990–18995. https://doi.org/10.1002/anie.202008198.

(60) Wang, S.; Wang, X.; Liu, B.; Guo, Z.; Ostrikov, K.; Wang, L.; Huang, W. Vacancy Defect Engineering of $BiVO_4$ Photoanodes for Photoelectrochemical Water Splitting. *Nanoscale* **2021**, *13* (43), 17989–18009. https://doi.org/10.1039/d1nr05691c.

(61) Zhong, X.; Li, Y.; Wu, H.; Xie, R. Recent Progress in $BiVO_4$-Based Heterojunction Nanomaterials for Photocatalytic Applications. *Materials Science and Engineering B: Solid-State Materials for Advanced Technology*. Elsevier Ltd March 1, 2023. https://doi.org/10.1016/j.mseb.2023.116278.

(62) Li, S.; Xu, W.; Meng, L.; Tian, W.; Li, L. Recent Progress on Semiconductor Heterojunction-Based Photoanodes for Photoelectrochemical Water Splitting. *Small Sci.* **2022**, *2* (5), 2100112. https://doi.org/10.1002/smsc.202100112.

(63) He, D.; Wang, Q.; Zhang, W.; Liu, X.; Cui, X. $BiVO_4$ Heterojunctions as Efficient Photoanodes for Photoelectrochemical Water Oxidation: A Minireview. *ChemPhotoChem* **2023**. https://doi.org/10.1002/cptc.202300080.

(64) Chae, S. Y.; Lee, C. S.; Jung, H.; Joo, O. S.; Min, B. K.; Kim, J. H.; Hwang, Y. J. Insight into Charge Separation in WO_3/$BiVO_4$ Heterojunction for Solar Water Splitting. *ACS Appl. Mater. Interfaces* **2017**, *9* (23), 19780–19790. https://doi.org/10.1021/acsami.7b02486.

(65) Irani, R.; Plate, P.; Höhn, C.; Bogdanoff, P.; Wollgarten, M.; Höflich, K.; Van De Krol, R.; Abdi, F. F. The Role of Ultra-Thin MnO: X Co-Catalysts on the Photoelectrochemical Properties of BiVO4 Photoanodes. *J. Mater. Chem. A* **2020**, *8* (11), 5508–5516. https://doi.org/10.1039/d0ta00939c.

(66) Qiu, J.; Hajibabaei, H.; Nellist, M. R.; Laskowski, F. A. L.; Oener, S. Z.; Hamann, T. W.; Boettcher, S. W. Catalyst Deposition on Photoanodes: The Roles of Intrinsic Catalytic Activity, Catalyst Electrical Conductivity, and Semiconductor Morphology. *ACS Energy Lett.* **2018**, *3* (4), 961–969. https://doi.org/10.1021/acsenergylett.8b00336.

(67) Favaro, M.; Abdi, F. F.; Lamers, M.; Crumlin, E. J.; Liu, Z.; Van De Krol, R.; Starr, D. E. Light-Induced Surface Reactions at the Bismuth Vanadate/Potassium Phosphate Interface. *J. Phys. Chem. B* **2018**, *122* (2), 801–809. https://doi.org/10.1021/acs.jpcb.7b06942.

(68) Grosso, D. How to Exploit the Full Potential of the Dip-Coating Process to Better Control Film Formation. *J. Mater. Chem.* **2011**, *21* (43), 17033–17038. https://doi.org/10.1039/c1jm12837j.

(69) Faustini, M.; Ceratti, D. R.; Louis, B.; Boudot, M.; Albouy, P. A.; Boissière, C.; Grosso, D. Engineering Functionality Gradients by Dip Coating Process in Acceleration Mode. *ACS Appl. Mater. Interfaces* **2014**, *6* (19), 17102–17110. https://doi.org/10.1021/am504770x.

(70) García Márquez, A.; Demessence, A.; Platero-Prats, A. E.; Heurtaux, D.; Horcajada, P.; Serre, C.; Chang, J. S.; Férey, G.; De La Peña-O'Shea, V. A.; Boissière, C.; Grosso, D.; Sanchez, C. Green Microwave Synthesis of MIL-100(Al, Cr, Fe) Nanoparticles for Thin-Film Elaboration. *Eur. J. Inorg. Chem.* **2012**, No. 32, 5165–5174. https://doi.org/10.1002/ejic.201200710.

(71) Bindini, E.; Naudin, G.; Faustini, M.; Grosso, D.; Boissière, C. Critical Role of the Atmosphere in Dip-Coating Process. *J. Phys. Chem. C* **2017**, *121* (27), 14572–14580. https://doi.org/10.1021/acs.jpcc.7b02530.

(72) Perlich, J.; Schwartzkopf, M.; Körstgens, V.; Erb, D.; Risch, J. F. H.; Müller-Buschbaum, P.; Röhlsberger, R.; Roth, S. V.; Gehrke, R. Pattern Formation of Colloidal Suspensions by Dip-Coating: An in Situ Grazing Incidence X-Ray Scattering Study. *Phys. Status Solidi - Rapid Res. Lett.* **2012**, *6* (6), 253–255. https://doi.org/10.1002/pssr.201206114.

(73) Berteloot, G.; Daerr, A.; Lequeux, F.; Limat, L. Dip Coating with Colloids and Evaporation. *Chem. Eng. Process. Process Intensif.* **2013**, *68*, 69–73. https://doi.org/10.1016/j.cep.2012.09.001.

(74) Butt, M. A. Thin-Film Coating Methods: A Successful Marriage of High-Quality and Cost-Effectiveness—A Brief Exploration. *Coatings* **2022**, *12* (8). https://doi.org/10.3390/coatings12081115.

(75) Pichumani, M.; Bagheri, P.; Poduska, K. M.; González-Viñas, W.; Yethiraj, A. Dynamics, Crystallization and Structures in Colloid Spin Coating. *Soft Matter* **2013**, *9* (12), 3220–3229. https://doi.org/10.1039/c3sm27455a.

(76) Chou, K. Sen; Huang, K. C.; Lee, H. H. Fabrication and Sintering Effect on the Morphologies and Conductivity of Nano-Ag Particle Films by the Spin Coating Method. *Nanotechnology* **2005**, *16* (6), 779–784. https://doi.org/10.1088/0957-4484/16/6/027.

(77) Zhao, Y.; Marshall, J. S. Spin Coating of a Colloidal Suspension. *Phys. Fluids* **2008**, *20* (4). https://doi.org/10.1063/1.2896601.

(78) Vrij, A. V. Polymers At Interfaces And The Interactions in Colloidal Dispersions. *Pure Appl. Chem.* **1976**, *48* (4), 471–483. https://doi.org/10.1351/pac197648040471.

(79) Liufu, S.; Xiao, H.; Li, Y. Adsorption of Poly(Acrylic Acid) onto the Surface of Titanium Dioxide and the Colloidal Stability of Aqueous Suspension. *J. Colloid Interface Sci.* **2005**, *281* (1), 155–163. https://doi.org/10.1016/j.jcis.2004.08.075.

(80) Deegan, R. D.; Bakajin, O.; Dupont, T. F. Capillary Flow as the Cause of Ring Stains from Dried Liquid Drops. *Nature* **1997**, *389*, 827–829.

(81) Kaliyaraj Selva Kumar, A.; Zhang, Y.; Li, D.; Compton, R. G. A Mini-Review: How Reliable Is the Drop Casting Technique? *Electrochem. commun.* **2020**, *121* (September), 106867. https://doi.org/10.1016/j.elecom.2020.106867.

(82) Xiao, Y.; Zuo, C.; Zhong, J. X.; Wu, W. Q.; Shen, L.; Ding, L. Large-Area Blade-Coated Solar Cells: Advances and Perspectives. *Adv. Energy Mater.* **2021**, *11* (21), 1–20. https://doi.org/10.1002/aenm.202100378.

(83) Yang, H.; Jiang, P. Large-Scale Colloidal Self-Assembly by Doctor Blade Coating. *Langmuir* **2010**, *26* (16), 13173–13182. https://doi.org/10.1021/la101721v.

(84) Nang Dinh, N.; Minh Quyen, N.; Chung, D. N.; Zikova, M.; Truong, V. Van. Highly-Efficient Electrochromic Performance of Nanostructured TiO_2 Films Made by Doctor Blade Technique. *Sol. Energy Mater. Sol. Cells* **2011**, *95* (2), 618–623. https://doi.org/10.1016/j.solmat.2010.09.028.

(85) Sum, J.; Durupthy, O.; Krins, N.; Laberty-Robert, C. Regeneration of Electrocatalyst through Li-Ion Insertion. *J. Electrochem. Soc.* **2022**, *169* (3), 030522. https://doi.org/10.1149/1945-7111/ac5ad4.

CHAPTER II PART 1

Conception of a heterostructured Mo doped-$BiVO_4$/Co-Pi photoanode for solar-driven water oxidation in acidic conditions

CHAPTER II PART 1

Table of Content

Conception of a heterostructured Mo doped-$BiVO_4$/Co-Pi photoanode for solar-driven water oxidation in acidic conditions

ABSTRACT

In the quest for efficient photoelectrolysis devices for solar-driven water splitting, designing a high-performing photoanode that operates compatibly with the electrolyte buffer of the photocathode remains a challenge. One promising solution is the development of an efficient and durable photoanode in acidic conditions. Despite the potential benefits, the limiting factors affecting performance under such conditions have not been well understood. In this study, we present a scalable Mo doped-$BiVO_4$/Co-Pi photoanode incorporating cobalt-phosphate (Co-Pi) as co-catalyst. Our research led to a great breakthrough by achieving a 2.4 mA cm^{-2} photocurrent density at 1.23V_{RHE} (pH 6) in standardized illumination conditions as well as a significant improvement of the photoanode's durability (over 5 hours). Furthermore, our investigation explores the evolution of the photoanode chemistry within the material after doping, and at the surface after Co-Pi deposition at various stage of the PEC process. This analysis highlighted the recovery of Co-Pi in cyclic voltammetry.

1. Introduction

Photoelectrochemical (PEC) water-splitting is a highly promising approach for producing dihydrogen through oxidation-reduction reactions, eliminating the overpotential in conventional electrolysis.[1] The design of tandem cells constituted of a photocathode and a photoanode is a solution for dihydrogen production without external bias input.[1–5] Nevertheless, the bottleneck resides in the photoanode material where oxidation of water (OER) requires a double amount of photocharges compared to hydrogen reduction (HER) for one O_2 molecule production.[1,4] Among the number of semiconductors having favourable valence band edge for OER , bismuth vanadate is the most promising due to its low bang gap around 2.4 eV, and a conduction band edge (0.02 V_{RHE}) the closest above HER potential (0.0 V_{RHE}).[1,4,6–10] Theoretically with a 2.4 eV band gap, 11 % of the standard AM 1.5 G solar spectrum can be absorbed, which corresponds to 9.2 % of solar-to-hydrogen (STH) conversion efficiency with a maximum photocurrent of 7.5 mA cm^{-2}.[11,12]

However, the main constraints for achieving high STH conversion with $BiVO_4$-based photoanodes are related to: poor electron-hole charge transport, slow water oxidation kinetics, in addition to stability issues in the electrolyte buffer.[6,11,13] To overcome these limitations many efforts have been made to optimize the photoanode, resulting in the classification of three main strategies: surface engineering, bulk modification, and interface engineering.[5,6,14–18] Efficient copper-based photocathodes are employed in acidic pH conditions. On the opposite, $BiVO_4$ photoanode stability in acidic conditions is a significant challenge when developing PEC devices in this pH range.[4,19] In acidic conditions the kinetics of OER are slower compared to neutral and alkaline electrolyte where the amount of hydroxides ions is higher.[20] As indicated in table S1, there is limited research conducted in acidic media, leading to a lack of visibility into the predominant factors affecting the overall photoanode efficiency. S. Hilliard *et al.* have demonstrated that sol-gel chemistry coupled with dip-coating was an interesting and easily scalable method for generating $BiVO_4$ photoanodes with well sintered particles.[21] They achieved a photocurrent density of 2.1 $mA.cm^{-2}$ at 1.23 V_{RHE} in 1M potassium phosphate buffer (pH 7) under 350 $mW.cm^{-2}$ Their photoanode consisted of a 10-layer $BiVO_4$ film deposited on FTO with a thickness of approximately 75 nm.[21] To reach this photocurrent density, the power of the simulated light was 3.5 times higher than standardise conditions.

In this study, we addressed two questions: whether there is a limitation associated with low thickness in the photocurrent value under standardized conditions and how to improve $BiVO_4$ photoanode efficiency for OER in acidic conditions. To do so, we evaluated the PEC performances of a Mo:$BiVO_4$/Co-Pi photoanode achieved through bulk modification by doping and surface functionalization with cobalt-phosphate (Co-Pi) co-catalyst.

2. Materials and methods

a. Synthesis of the $BiVO_4$-based photoanode

$BiVO_4$ and Mo:$BiVO_4$ films: To synthesize multilayer $BiVO_4$ and doped Mo:$BiVO_4$ photoanodes, sol-gel chemistry has been coupled with the dip-coating deposition technique as represented in Figure S2. The syntheses are based on a previous work developed by S. Hilliard.[21]. For the undoped $BiVO_4$ precursor solution, 1.08 mmol of bismuth (III) nitrate pentahydrate (ACS reagent ≥ 98.0 %) and 1.08 mmol of vanadium (IV) oxide acetylacetonate (ACS reagent ≥ 95.0 %) are dissolved in a mixture of 130.8 mmol acetylacetone (ACS reagent ≥ 99.0 %) and 28.1 mmol acetic acid. For the doped Mo: $BiVO_4$ precursor solution, 1 %mol of the vanadium precursor is replaced by molybdenum (VI) dioxide bis(acetylacetone) (ACS reagent ≥ 95.0 %) given 1.069 mmol of vanadium precursor and 0.0108 mmol of Mo^{6+} precursor. They are first put in an ultrasonic bath for 10 minutes at 35 °C before being magnetically stirred overnight. For the deposition, a commercial glass of F-doped SnO_2 (FTO) 80 nm/ Glass substrate from (SOLEMS: YSUB/ASAHI120/1) with effective resistivity measured between 200 – 250 **Ω** is used as an electrode substrate. The films are produced by dip coating (Ossila Dip-Coater) and controlling the relative humidity (RH) (< 5%). Firstly, an ultrathin layer is obtained at a deposition rate of 1 mm s^{-1} to help anchor the subsequent layers. After each deposited layer, the non-conductive side of the substrate is wiped with ethanol and acetone and the electrode is annealed at 400 °C for 1 – 2 minutes. 6 layers of the precursor solution are deposited at 8 mm s^{-1} resulting in an average of 18 nm/layer. Finally, the films are crystallized by a calcination step at 450°C for 1 h in air.

Cobalt-phosphate (Co-Pi) co-catalyst layer: Co-Pi is electrodeposited at the surface of the Mo:$BiVO_4$ photoanode by using an electrolyte containing Co precursors. A solution S_A of a 0.1 M phosphate buffer electrolyte is made from potassium phosphate monobasic, KH_2PO_4 (ACS reagent ≥ 99.0 %) and potassium hydroxide, KOH (ACS reagent ≥ 90.0 %). A Solution S_B is prepared by dissolving 29.5 mmol of Cobalt (II) nitrate hexahydrate, $Co(NO_3)_2.6H_2O$ (ACS reagent ≥ 98.0 %) in 35 mL of Milli-Q water. S_B is then poured into S_A. Electrodeposition is carried out at 1.713 V_{RHE} constant voltage for deposition times ranging from 1 min to 10 min, without stirring in a 3-electrode cell. The photoanode is the working electrode, an enrolled platinum wire is the counter electrode and the reference is an Ag/AgCl. KCl saturated electrode.

b. Characterization

X-Ray diffraction (XRD): X-ray diffractograms were acquired in Bragg–Brentano geometry using a Bruker Discover D8 apparatus, equipped with a Cu anode (1.54 Å) and a LynxEye XE-T detector, over a 2θ range from 5° to 70° with a step size of 0.02°.

UV-Visible spectroscopy: UV/visible light absorption measurements were performed with an Agilent Technologies Cary Series 5000 UV/visible/near-infrared spectrometer using a double beam with a background of FTO defined.

Fluorescence: X-ray fluorescence measurements are performed on an Epsilon 3XL energy dispersive spectrometer (@Malvern-Panalytical). Bismuth (Lα) and Molybdenum (Kα) are measured with a voltage of 50 kV, an intensity of 6 µA for 300 s, for vanadium (Kα) during 60 s, a voltage of 12 kV and an intensity of 25 µA is applied. For all three elements, a calibration is established using standard solutions of 1 $g.L^{-1}$ deposited for different volumes on polycarbonate membranes. The powdered samples are then prepared in exactly the same way. For samples on substrates, a prolene membrane (highly transparent to X-rays) is used to deposit the sample. When the sample is thin, there are no matrix effects and the signal intensity is directly proportional to the mass of the element present in the analysed area (0.5 cm^2).

FEG-SEM EDX imaging: Field emission gun-scanning electron microscopy (FEG-SEM) and energy-dispersive X-ray spectroscopy (EDX) were carried out using a Hitachi SU-70 equipped with Oxford X-Max beam with 50 mm^2 X-Max silicon drift EDS detector with a 50 mm^2 tungsten filament operated at 10 – 15 kV. High-resolution transmission electron microscopy (HR-TEM) was done using a JEOL JEM-2010.

Photoelectrochemical performances: The PEC performance of $BiVO_4$ photoanodes was checked performed with an AMETEK Solartron Analytical Modulab potentiostat coupled with a Newport Xenon lamp in a pH 6 potassium phosphate buffer conducting linear sweep voltammetry (LSV) under AM 1.5 G illumination (100 mW/cm^2) under both front side (through the film/electrolyte interface) and back side (through the FTP back-contact). The LSV were measured from -0.2 V to 0.74 V vs. Ag/AgCl. KCl sat. reference electrode ($E^0_{Ag/AgCl}$ = 0.197 V vs. NHE) using a scan rate of 10 mV s^{-1}. All current density curves were referenced to the reversible hydrogen electrode (RHE), using the Nernstian relation of:

$$V_{RHE} = E\ vs.\ Ag/AgCl\ +\ 0.197\ +\ 0.059 \times pH$$

The photocurrent was stable for at least 5 scans and reproducible. The 3rd scans acquired with illumination for all investigated electrodes are collected. Chronoamperometry measurement under alternative irradiation was performed using the potentiostatic mode at a fixed potential of 1.23 V_{RHE}. The geometric active area of the $BiVO_4$, working electrode, was defined by Hi-Bond polyamide scotch tape (HB830-19) and measured 0.28 cm^2. Electrical contacts were made by conductive copper scotch (3M Scotch 1245) which was adhered directly to the FTO exposed portion of the photoelectrode. The electrolyte used during electrochemical and photoelectrochemical tests was a 1M potassium phosphate buffer of pH 6.07 and a 1M potassium phosphate buffer enriched with 1M Na_2SO_3 pH 6.77.

XPS Fitting Procedure: XPS analyses were performed using an Omicron Argus X-ray photoelectron spectrometer, equipped with a monochromated Al Kα radiation source (hν = 1486.6 eV) and a 280 W electron beam power. The emission of photoelectrons from the sample was analyzed at a take-off angle of 45° under ultra-high vacuum conditions (≤10−9 mBar). Spectra were carried out with 100 eV pass energy for the survey scan and 20 eV pass energy for the C 1s, O 1s, N 1s, Bi 4f, V 2p, Mo 3d, P 2p and Co 2p regions. Binding energies were calibrated against the C 1s (C-C) binding energy at 284.8 eV and element peak intensities were corrected by Scofield factors. The peak areas were determined after subtraction of a (LINEAR – SHIRLEY – U 2 TOUGAARD) background. The spectra were fitted using Casa XPS v.2.3.15 software (Casa Software Ltd, U.K.) and applying a Gaussian/Lorentzian ratio g/l equal to 70/30.

Ellipsometry were performed on a J;A Woollam Ellipsometer to determine de thickness and the band-gap (Eg) of each sample. The method is described in supporting information.

Electrochemically active surface area: The comparison of the double layer capacitance (C_{DL}) of the samples brings information on the electrochemically active surface area (EASA). C_{DL} was determined following the methodology described in the supporting information.

ICP-AES: Inductive coupled plasma-atomic emission spectrometry was conducted on a Spectrogreen spectrometer. The samples are diluted by a factor of 10 in a solution HNO_3 1% prepared with ultrapure milliQ water and pure HNO_3 68 %. For each wavelength, three measurements were done.

3. Results and Discussion

a. Characterisation of $BiVO_4$-based photoanode

To investigate the effect of a thickness improvement, the synthesis developed by Hillard *et al.* was reproduced.[21] The $BiVO_4$ photoanode obtained is crystallized in the scheelite structure with both polymorphs tetragonal scheelite and monoclinic scheelite, exhibits well sintered particles. The film has a thickness of 60 nm (Figure S3 a, b, c). Here, Eg is calculated by applying a Tauc-plot on UV-Visible absorbance spectra and is about 2.63 eV (Figure S3.d).

The modification to increase the electrode thickness highlighted several parameters affecting the quality of the photoanode. A high withdrawal speed during dip-coating resulted in thicker, more surface-sensitive layers. Strict control of atmosphere and cleanliness during the primary layers depositions impacts sintering, germ growth and porosity (Figure S4).

i. Pristine $BiVO_4$ photoanode

Figure 1 depicts the characterization of $BiVO_4$ calcined at 450°C for 1 hour. In figure 1.a, the XRD pattern of pristine $BiVO_4$ electrode reveals the presence of a shoulder on the peaks at 35° and 46° in 2θ/°. The characteristic doublets (200), (020) and (204), (024) at these degrees correspond respectively to the monoclinic scheelite (m-s) structure and are not completely isolated from the single peak of the tetragonal scheelite structure (t-s).[8] This means that the contribution of the two scheelite polymorphs coexists, as demonstrated by Pamar *et al.*[22] FEG-SEM imaging exhibits a dense film with well sintered nanoparticles of size ranging from 30 to 430 nm with a majority of particles between 50 and 150 nm (Figure 1.b, d). In figure 1.c, cross-section image provides a thickness of 110 nm in agreement with the one determined by ellipsometry analysis. (Table S6) The Eg of the semiconductor is evaluated to be 2.65 eV. (Figure 1.e, method, Figure S5).

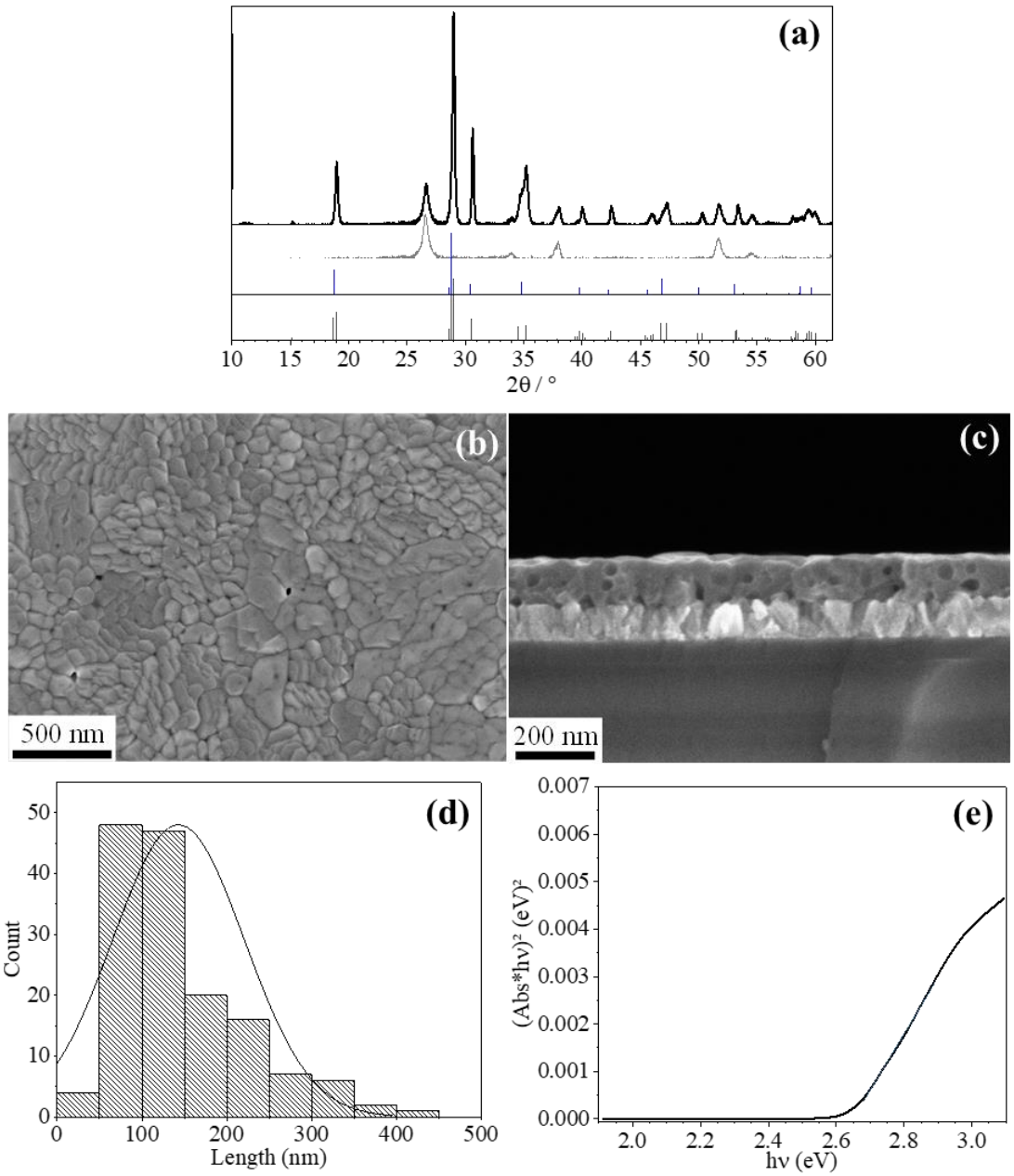

Figure 1: pristine $BiVO_4$ characterisation: a) XRD pattern of pristine $BiVO_4$ (black curve), grey curve annealed FTO substrate (grey curve), PDF-04-010-5710 $BiVO_4$ tetragonal scheelite (blue straight-line) and PDF-04-010-5713 $BiVO_4$ monoclinic scheelite (black straight-line); b)FEG-SEM surface imaging; c) FEG-SEM cross-section imaging e) Bang-gap determination by ellipsometry

ii. Mo:$BiVO_4$ photoanode

Mo:$BiVO_4$ photoanode exhibits a similar diffractogram to pristine $BiVO_4$. In figure 2.a, the crystalline structure comprises the two scheelite polymorphs. The morphology of the film closely resembles that of pure $BiVO_4$ with a thickness of 110 nm as determined by SEM-FEG analyses. The film is dense with low porosity and excellent sintering. To quantify the percentage of Mo^{6+} effectively incorporate into the $BiVO_4$ photoanode, X-Ray fluorescence was conducted with detection limits (LOD) and quantifications Limits (LOQ) of 0.013 µg and 0.44 µg for Bi, and 0.008 µg, and 0.026 µg for both atoms Mo and V. The Mo:$BiVO_4$ photoanode is doped at 0.56 mol% giving the chemical formula $BiV_{0.994}Mo_{0.006}O_4$ (Table S7). The photoanode's Eg calculated is 2.63 eV, which is very close to that of pristine $BiVO_4$ (Figure 2.e). The details are referred in table S5.

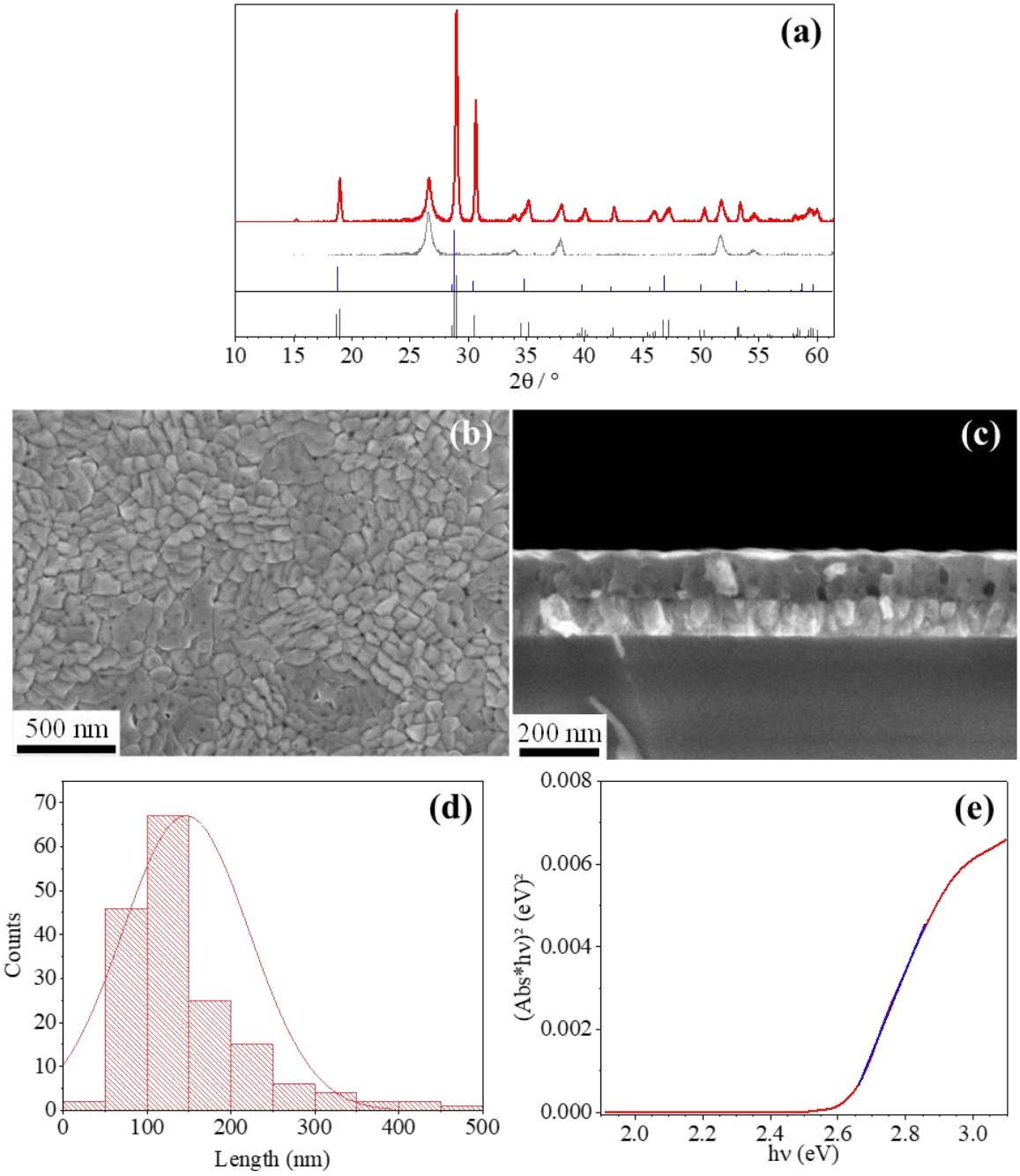

Figure 2: Mo:$BiVO_4$ characterisation: a) XRD pattern of pristine $BiVO_4$ (black curve), grey curve annealed FTO substrate (grey curve), PDF-04-010-5710 $BiVO_4$ tetragonal scheelite (blue straight-line) and PDF-04-010-5713 $BiVO_4$ monoclinic scheelite (black straight-line); b)FEG-SEM surface imaging; c) FEG-SEM cross-section imaging e) Bang-gap determination by ellipsometry

The chemical state of the Bi, V, Mo and O atoms are investigated by XPS. The fitted spectra are presented in Figure 7 and the indexed acquisition of the first survey spectra is detailed in Figure S8. Pristine $BiVO_4$ and Mo:$BiVO_4$ exhibit the characteristic spin-orbit splitting for Bi

and V atoms with Bi $4f_{5/2}$, Bi $4f_{7/2}$ and V $2p_{1/2}$, V $2p_{3/2}$ signals. XPS spectrum of Mo confirms the presence of Mo 3d in the doped sample. The O 1s, corresponding to the binding energy for the lattice oxide, is detected at 529.82 eV for $BiVO_4$ and 529.43 eV for Mo:$BiVO_4$. The presence of V(V) oxide is also observed at 530.59 eV and 530.41 eV for $BiVO_4$ and Mo:$BiVO_4$ respectively. This corresponds to the oxidation state of V in VO_4^{3-}.

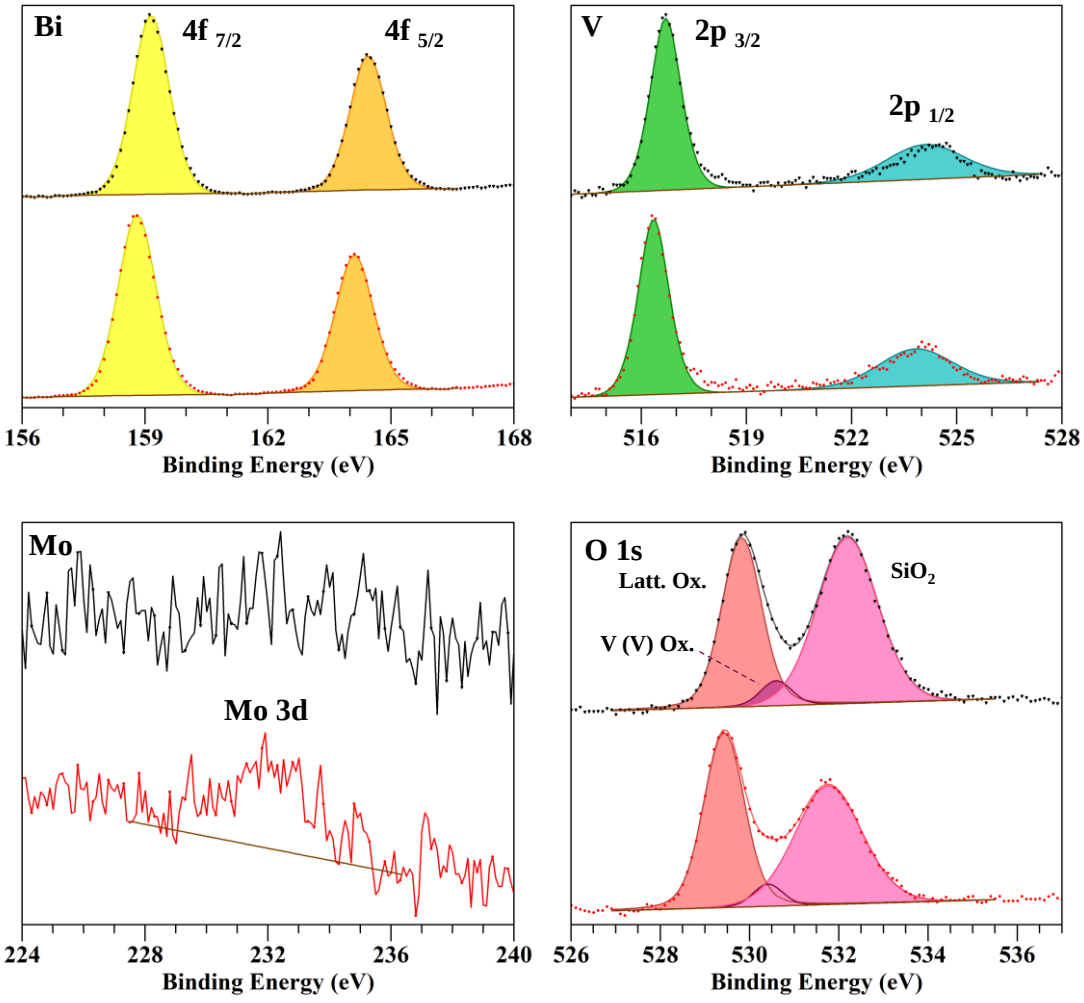

Figure 3: Room-temperature XPS spectra of air-exposed samples. Colour code: black spectra corresponding to pristine $BiVO_4$ and red spectra corresponding to Mo:$BiVO_4$.

The values of the binding energy for Bi 4f and V 2p are summarized in Table 1, with the delta value. The fitted curves for C 1s and Si 2p are shown in the Figure S9 and their binding energy values are grouped in Table S10. If we consider the difference in delta energy Bi $4f_{7/2}$ and Bi $4f_{5/2}$, no significant difference was observed for doped and undoped samples. However, the small decrease in the delta V 2p could correspond to the replacement of V atoms by Mo.

Table 1: Binding energy in eV of Bi 4f $_{7/2}$, Bi 4f $_{5/2}$, V 2p $_{3/2}$, and V 2p $_{1/2}$ in the electrodes of $BiVO_4$ and Mo:$BiVO_4$; Δ (Bi 4f) = E(Bi 4f $_{5/2}$) – E (Bi 4f $_{7/2}$), Δ (V 2p) = E(V 2p $_{1/2}$) – E (V 2p $_{3/2}$) .

Samples	Bi 4f $_{7/2}$	Bi 4f $_{5/2}$	Δ (Bi 4f)	V 2p $_{3/2}$	V 2p $_{1/2}$	Δ (V 2p)
$BiVO_4$	158.80	164.11	5.30	516.35	523.83	7.48
Mo:$BiVO_4$	159.14	164.44	5.30	516.70	524.10	7.40

b. PEC Performances Evaluation of pristine $BiVO_4$

The PEC performances are evaluated in a 1M potassium phosphate buffer (pH 6) with direct illumination of 100 mW cm^{-2} of the photoanode surface. Figure S11 illustrates a scheme of the PEC set up. For the synthesis of $BiVO_4$ (60 nm), the linear sweep voltammetry showed an onset potential at 0.7 V_{RHE} with light and a photocurrent density of 0.7 mA cm^{-2} at 1.23 V_{RHE} (Figure S12.a). Subsequently, chronoamperometric measurements were conducted at a fixed potential of 1.23 V_{RHE} with chopped on-off illumination intervals of 90 seconds in the same electrolyte buffer.(Figure S12.b). These measurements revealed a fast decrease of the photocurrent plateau from ~ 0.15 mA cm^{-2} to 0.025 mA cm^{-2} after 2 h.

i. Pristine $BiVO_4$ photoanode efficiency

The PEC measurements of $BiVO_4$ (110 nm) are realised in the same conditions as for $BiVO_4$ (60 nm) with the additional inclusion of PEC analysis with back illumination. Figure 4 summarizes all the data. The photoanode analysis reveals a maximum photocurrent density of 1.2 mA cm^{-2} at 1.23 V_{RHE} for front illumination with an onset potential of 0.6 V_{RHE}, lower than $BiVO_4$ (60 nm) (Figure 4.a). The dependence of photocurrent density on the electrode's side of irradiation provides insight into electron or hole transport limitations within the material's bulk. Generally, under back-side irradiation, high density of charge carriers is photogenerated close to the FTO back-contact, allowing the electrons to be instantaneously injected into the external circuit. This presents an advantage for materials suffering from poor electron transport, such as $BiVO_4$.[23] However, our sample reveals comparable values under both back and front side irradiation (Figure 4.a). As the thickness of our electrode layer does not exceed ~ 100 nm, which corresponds to the diffusion length of photocharges in $BiVO_4$, this limitation becomes negligible.[23] In addition, a thickness of 110 nm resulted in an increase in photocurrent density

of 0.5 mA cm^{-2} compared to the $BiVO_4$ photoanode (60 nm). This suggests that below a certain thickness, the PEC performance of the $BiVO_4$ photoanode is limited.

The stability of the electrode was assessed through chronoamperometric measurements conducted over a 5-hour period. In Figure 4.b, pure $BiVO_4$ produced a photocurrent density of ~ 0.8 mA cm^{-2} at 1.23 V_{RHE} after 45 minutes of analysis and decreased to 0.3 mA cm^{-2} after 2 hours. After 5 hours, the electrode exhibits a very low photocurrent of 0.03 mA cm^{-2}. The presence of sharp charges recombination peaks indicates that improving the separation and transport rate of electrons within the material could lead to higher photocurrent values. Additionally, the gradual decrease in photocurrent value over time reveals competitive reactions occurring in parallel with OER and contributing to the degradation of the photoanode itself. Doping the photoanode will have an impact on both bulk properties and surface chemistry.

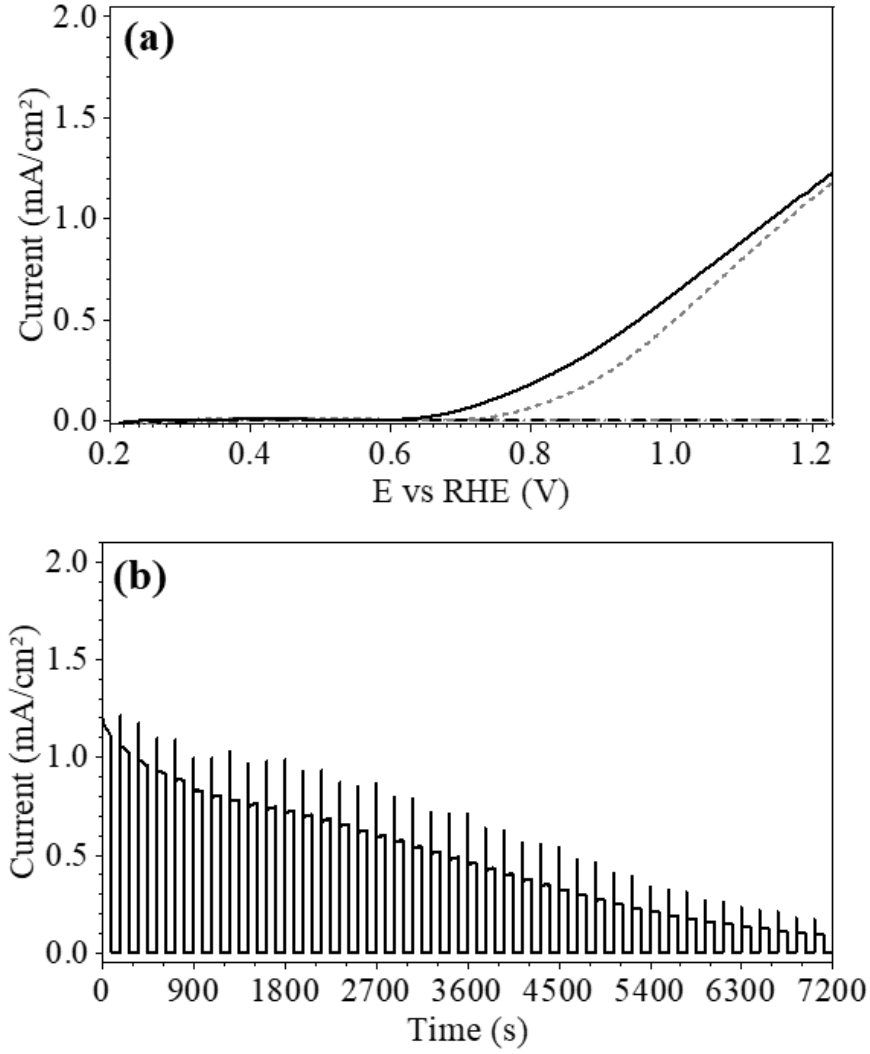

Figure 4: Photoelectrochemical measurements in 1M potassium phosphate buffer (pH 6) under simulated illumination at 100 mW cm^{-2} a) Linear voltage sweeps measured at Mo:$BiVO_4$ thin films with/without illumination in front-side (black curves) and in back-side (grey dots); b) chronoamperometric measurement $BiVO_4$ thin films at 1.23 V_{RHE} with chopped on/off front-side illumination of 90 s for 2 h.

ii. Mo:$BiVO_4$ photoanode efficiency

Mo:$BiVO_4$ photoanode was synthesized to modify the charge carrier dynamic and then limit the electron-hole recombination. [22,24–26] Figure 5.a. shows the current-voltage curves of Mo:$BiVO_4$. In front illumination, the photocurrent of the Mo:$BiVO_4$ at 1.23 V_{RHE} increases by a factor of 1.42 compared to pristine $BiVO_4$, reaching a value of 1.7 mA cm^{-2}. However, under back illumination, the photocurrent of the Mo:$BiVO_4$ photoanode at 1.23 V_{RHE} decreased by a factor of 2.66, accompanied by an anodic shift of the onset potential by 150 mV. The doped photoanode shows a considerably higher photocurrent than pure $BiVO_4$ under front illumination, indicating that Mo^{6+} doping overcomes the "dead-layer" effects that affect pure $BiVO_4$. This increase in photocurrent density is not attributed to changes in specific areas since the electrochemically active surface area of $BiVO_4$ and Mo:$BiVO_4$ is comparable (Figure S13). Instead, the better performance under front-side rather than back-side illumination provides proofs of the electron transport enhancement produced by Mo^{6+} incorporation in $BiVO_4$. The poor electron transport in the bulk of the material is no longer an obstacle to photocurrent production. Nevertheless, because of the doping, the OER efficiency is reduced for back-lighting. In this situation the flow of holes is limited. Chronoamperometric measurements during 2 hours in Figure 5 showed a photocurrent density of ~ 1.2 mA cm^{-2} at 1.23 V_{RHE} after 45 min which corresponds to the maximum photocurrent of pristine $BiVO_4$. After 2 h, the photocurrent density decreased to reach 0.6 mA cm^{-2} Finally at the end of the 5-hour period, as $BiVO_4$ photoanode, the current continues to decrease until it reaches 0.04 mA cm^{-2}.

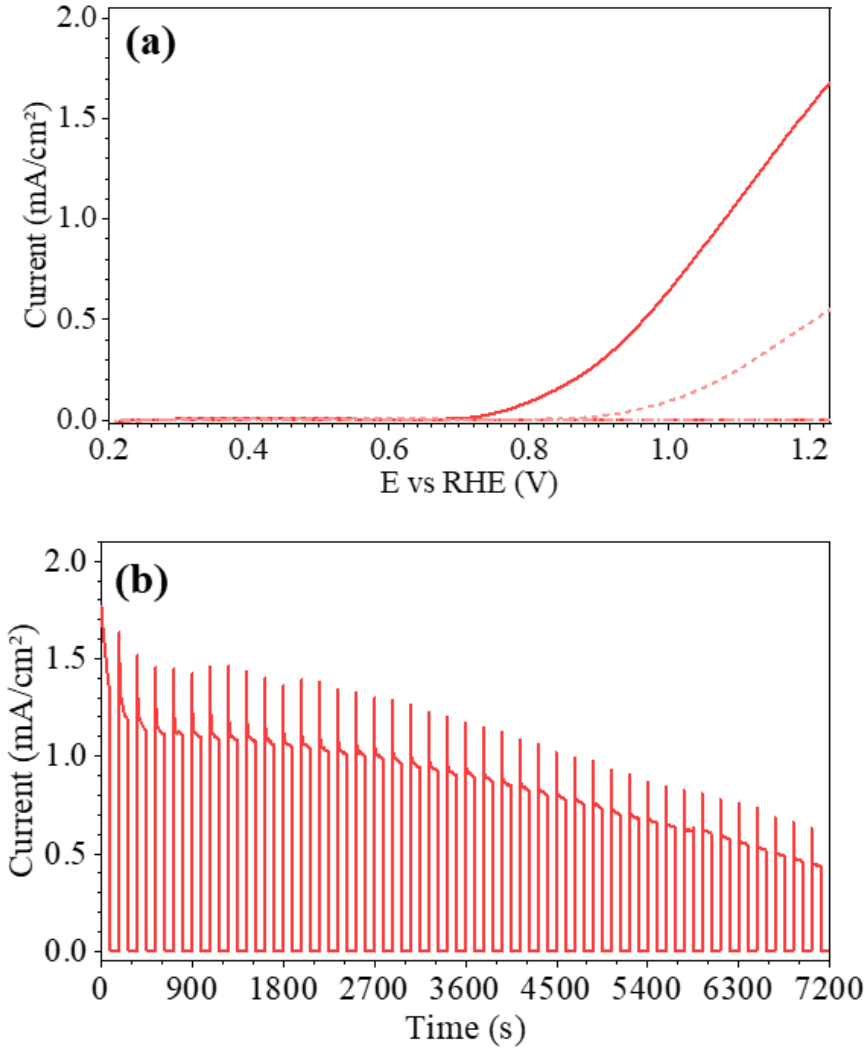

Figure 5: Photoelectrochemical measurements in 1M potassium phosphate buffer (pH 6) under simulated illumination at 100 mW cm^{-2} a) Linear voltage sweeps measured at Mo:$BiVO_4$ thin films with/without illumination in front-side (red curves) and in back-side (pink dots); b) chronoamperometric measurement on Mo:$BiVO_4$ thin films at 1.23 V_{RHE} with chopped on/off front-side illumination of 90 s for 2 h.

FEG-SEM post-mortem analysis after 5 hours of chronoamperometric measurements reveals a significant electrode degradation for $BiVO_4$ and Mo:$BiVO_4$ (Figure 6). The thickness of the photoactive material is generally thinner in front irradiation than in back irradiation and the presence of pores between (10-30) nm shows the degradation and corrosion of the photoanode. (Figure S14). The degradation rate seems reduced with backlighting, which may comfort the hypothesis that the rate of holes consumption accumulated at the interface between the electrode/electrolyte plays a key role in the type of reaction that is happening at the interface.

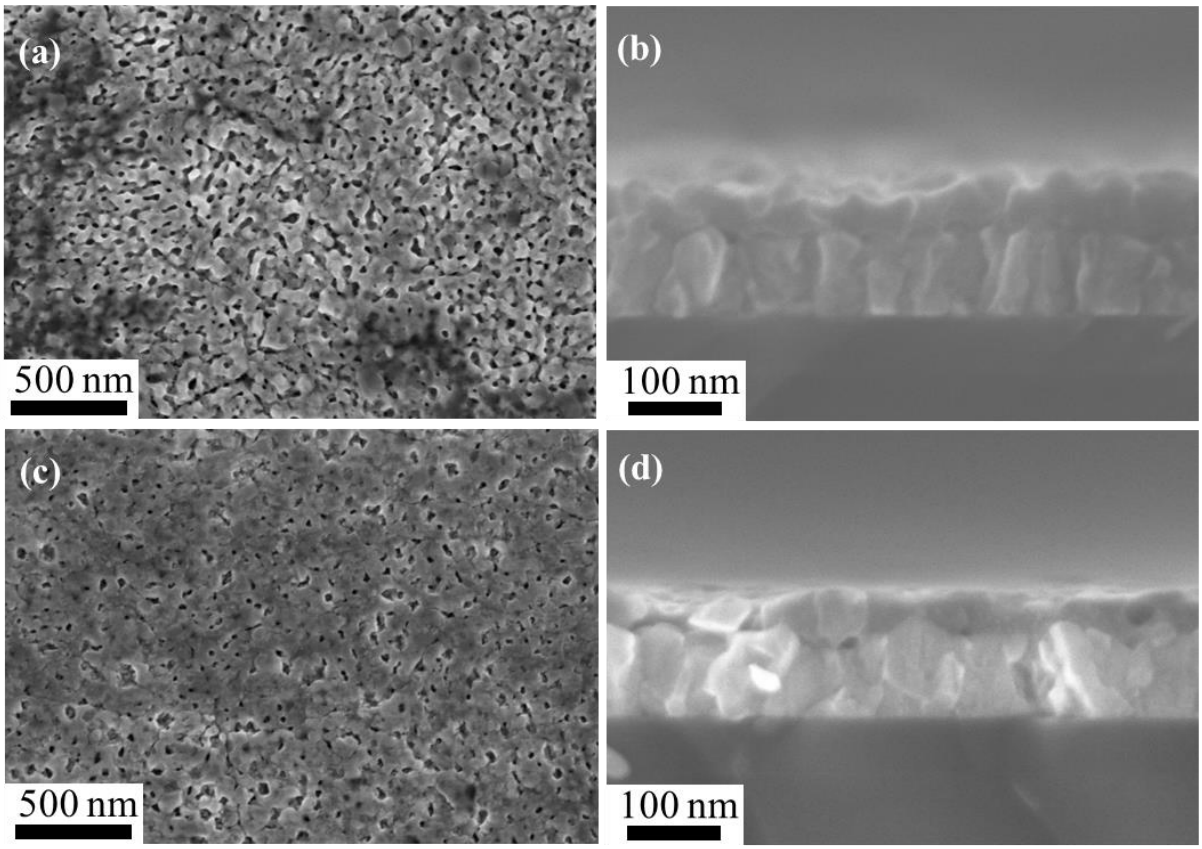

Figure 6: FEG-SEM post-mortem imaging of $BiVO_4$ (110 nm) a) surface; b) cross-section and Mo:$BiVO_4$ a) surface; b) cross-section.

c. Photocorrosion Study

To investigate electrode degradation, we studied its chemical stability in the electrolyte under both dark and illuminated conditions, as illustrated in Figure 7. After immersing the electrode in potassium phosphate electrolyte (pH 6) without exposure to light for 5 hours, the electrode's morphology remains unchanged (Figure 7.a, b) However, when subjected to simulated light at 100 mW cm^{-2} (AM 1.5 G) for an additional 5 hours, we observed partial dissolution of the electrode (Figure 7.c). This dissolution is attributed to photocorrosion phenomena [27,28], involving the preferential dissolution of V and the formation of $BiPO_4$ under illumination.[13,29,30]

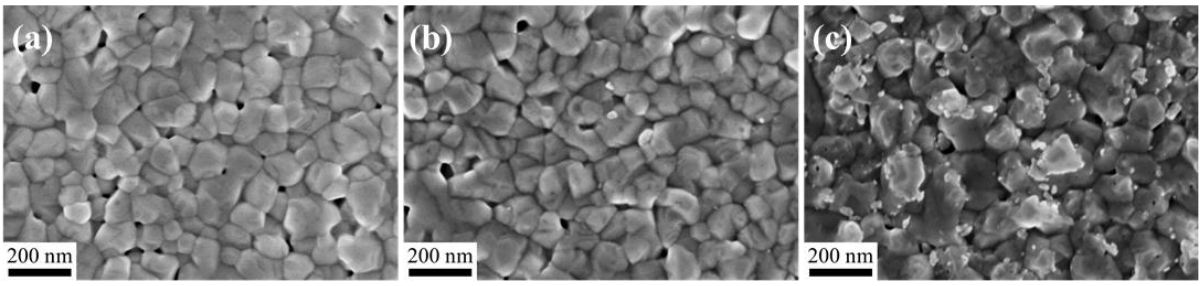

Figure 7: FEG-SEM imaging of Mo:$BiVO_4$ a) after synthesis without any external perturbation, b) immersed in 1M potassium phosphate electrolyte (pH 6) in dark conditions during 5 h, c) immersed in 1M potassium phosphate electrolyte (pH 6) in dark conditions during 5 h with 100 mW $cm^{-2}$of simulated light.

Post-mortem analysis and chronoamperometric curves of $BiVO_4$ and Mo:$BiVO_4$ photoanodes suggest that the chemistry at the interface implying holes for OER is a critical parameter on the photocurrent density and durability. Charge carrier recombination, indicated by the sharp peak beginning each cycle of 90 s illumination, is a key factor in electrochemistry.

To assess the overall potential efficiency of the photoanode, additional 1 M sodium sulphite (Na_2SO_3) is introduced to the phosphate electrolyte as a sacrificial agent, slightly raising the pH to 6.8 (Figure 8). In Figure 8.a, the optimized OER photocurrent of Mo:$BiVO_4$ which reached 1.7 mA cm^{-2} at 1.23 V_{RHE} increased to 3.6 mA cm^{-2} in presence of Na_2SO_3. Additionally, the onset potential presented a cathodic shifts of ~ 0.4 mV upon the addition of the sacrificial agent. These results highlight the direct impact of surface chemistry on the onset potential. The significant increase of photocurrent density in presence of sulphites confirms that recombination phenomena are a major limiting factor. Furthermore, the corresponding chronoamperometry curve revealed better stability and fewer electron-hole recombination, as demonstrated by the little variation of the steady-state current. The addition of SO_3^{2-} ions allows twice-lower electron-hole pair to be generated compared to the OER reaction. The stability obtained for an easier reaction confirms that photogenerated holes drives the anodic corrosion (Figure 8.b). Also, we hypothesized that the presence of Mo^{6+} doping can influence the stability of vanadium's oxidation state within the material or passivate the surface state. Doping $BiVO_4$ with Mo^{6+} alters the properties of the material's bulk by increasing the donor density, which enhances electron conductivity and simultaneously moderates the accumulation of holes.

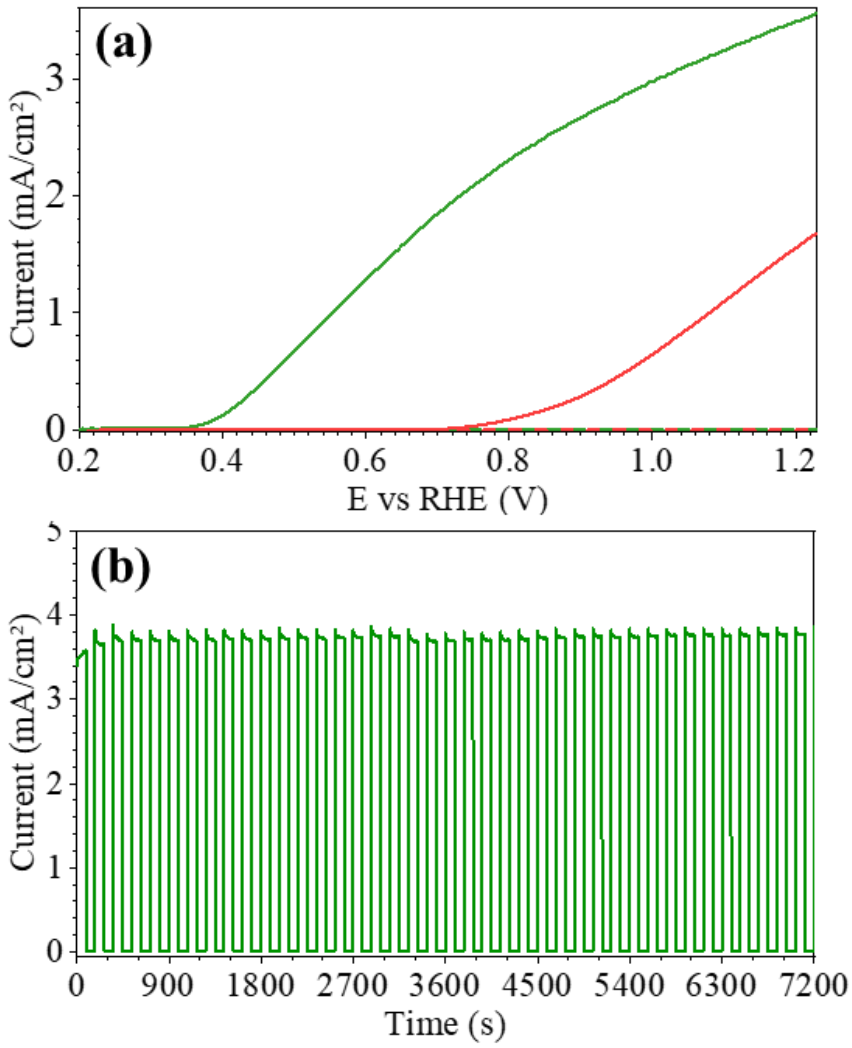

Figure 8: Photoelectrochemical measurements in 1 M potassium phosphate buffer with 1 M additional Na_2SO_3 (pH 6.8) under front simulated illumination at 100 mW cm^{-2} a) Linear voltage sweeps measured at Mo:$BiVO_4$ thin films front irradiation; b) chronoamperometric measurement on Mo:$BiVO_4$ thin films at 1.23 V_{RHE} with chopped on/off illumination of 90 s for 2 h.

After 5 hours of chronoamperometric measurement, the photocurrent value remains the same. (Figure S15). FEG-SEM post-mortem analysis showed that the particles are still well sintered and dense. A tiny change in the surface is detectable, corresponding to the slight residual peak in charge recombination observed in chronoamperometry (Figure S16).

Therefore, passivating layers including OER catalysts are indispensable to protect the $BiVO_4$ and Mo:$BiVO_4$ surface from photocorrosion. This have already shown stable operation for 1100 and 500 h.[30,31]

d. Surface engineering with Co-Pi layer addition

To provide an efficient photoanode, a sacrificial agent cannot be a solution in time because the sulphite's concentration will decay. Otherwise, surface engineering can be a long-lasting solution. To confirm this, the doping efforts were diverted towards surface co-catalyst addition to reduce recombination centres, modify the surface chemistry and then limit then photocorrosion. However, P.Plate *et al*. and Irani *et al.* have highlighted two opposing contributions with this approach depending on the coverage of the co-catalyst at the surface of the active material.[32,33] They have shown that an increase of the photocurrent density is generally linked to the band bending effect, which reduces surface recombination, as demonstrated onto the MnOx co-catalyst.[33] However, as the co-catalyst is a hole collector, if the active material is deposited onto the electron collector (FTO), a direct contact of the co-catalyst layer with the FTO occurs due to the presence of pinholes from incomplete coverage. Accordingly, electron-holes can recombine at the interface of the FTO / co-catalyst on these defects. This will impact the photocurrent density. To identify if Mo:$BiVO_4$ thin films could potentially create pinholes in contact of a co-catalyst layer, cyclic voltammetry measurements of the oxidation and reduction of the couple Fe^{3+}/Fe^{2+} from ferri/ferrocyanide is studied according to the work of Irani *et al.* [33] (more details in supporting information S17).

The absence of oxidation and reduction peaks of Fe^{3+}/Fe^{2+} on Mo:$BiVO_4$ thin films put in evidence the complete FTO coverage and absence of pinholes (Figure S16). In these conditions, the contribution of a co-catalyst should only be beneficial for OER.

Co-Pi co-catalyst was deposited on Mo:$BiVO_4$ photoanode by electrodeposition. Various times of deposition were applied to determine the best conditions for enhancement of the photoanode efficiency. The Figure 8 showed the surface of the photoanode after 5 min of electrodeposition. Small particles are observed on the surface, where the co-catalyst is deposited but the film does not cover homogeneously the photoanode surface. (Figure 8.b).

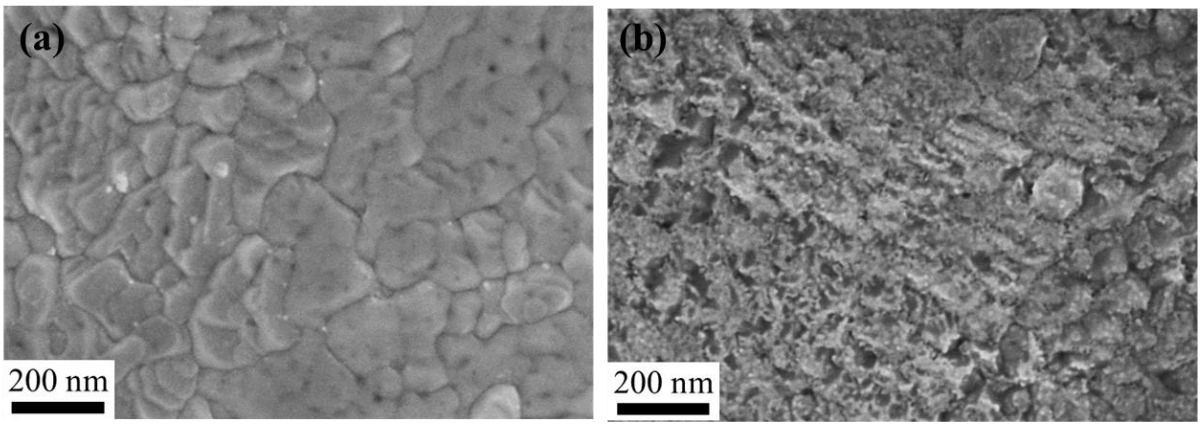

Figure 8: FEG-SEM surface imaging of a) bare Mo:$BiVO_4$ thin film, b) Mo:$BiVO_4$ after 5 min Co-Pi electrodeposition.

Looking at the photocurrent density obtained after the addition of the co-catalyst layer (Figure 9.a), the best result is obtained for 5 minutes of deposition with a photocurrent density of 1.9 mA cm^{-2} at 1.23 V_{RHE} measured in linear sweep mode. In comparison with Mo:$BiVO_4$ current-voltage curve, a cathodic shift of 0.1 mV is observed (Figure 9.b). As previously mentioned, this describes a better surface reactivity of holes. In addition, a change in the shape of the photocurrent density appeared with the co-catalyst, resulting in a small bump directly after the onset potential. Concerning the chronoamperometry curve of Mo:$BiVO_4$/Co-Pi (Figure 9.c), the photocurrent is higher as attended and similar to that of Mo:$BiVO_4$ co-catalyst photoelectrode for the first 2 hours. However, after 2 hours, the surface evolved in such a way that approximately 0.6 mA cm^{-2} of current is still being generated. However, most of this is lost due to surface degradation if we consider the plateau current value of 0.1 mA cm^{-2} (Figure S18).

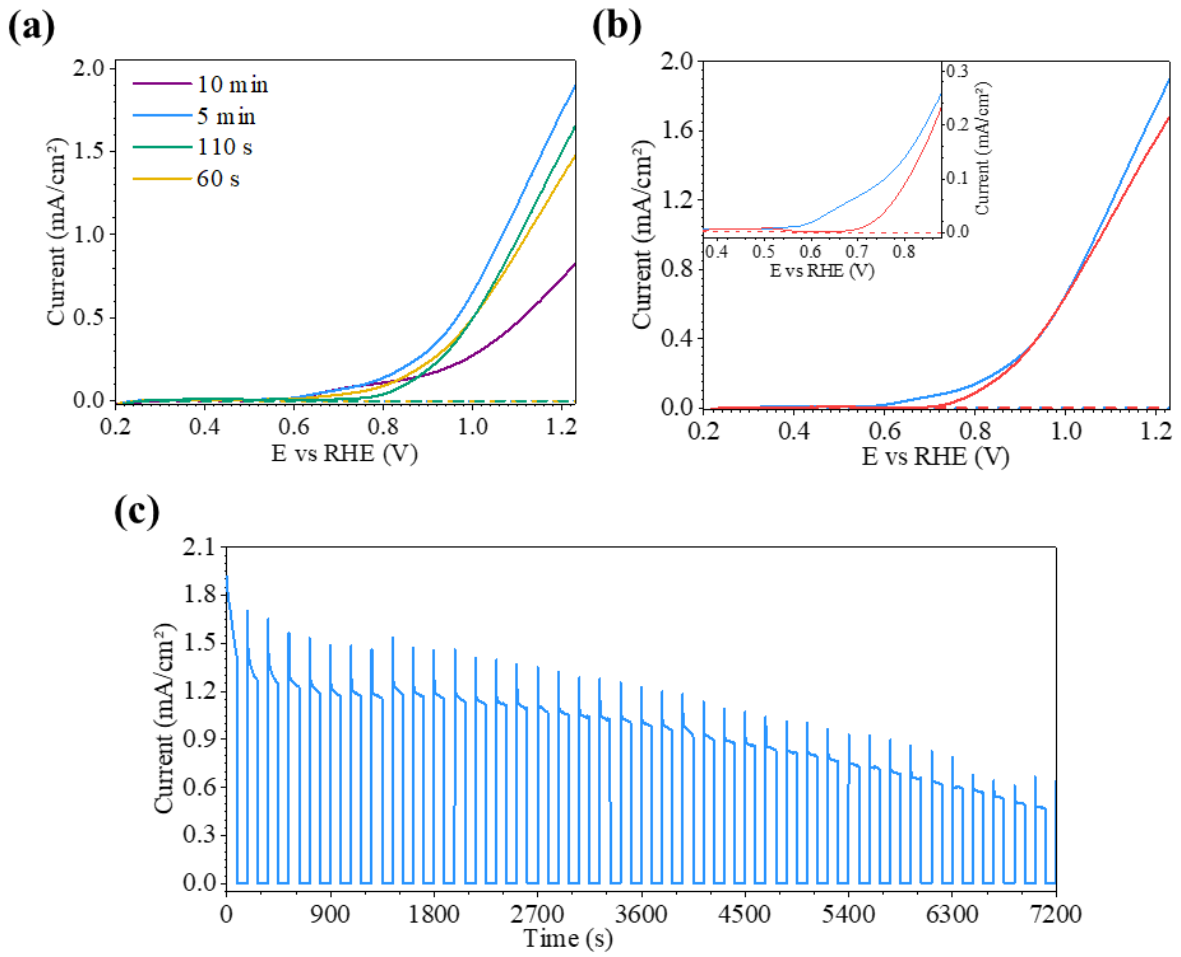

Figure 9: Photoelectrochemical measurements in 1M potassium phosphate buffer (pH 6) under front-side simulated illumination at 100 mW cm^{-2} a) Linear voltage sweeps measured at Mo:$BiVO_4$/Co-Pi thin films with/without illumination on sample with 60 s, 110 s, 5 min, 10 min Co-Pi electrodeposition time; b) Linear voltage sweeps comparison of Mo:$BiVO_4$ (in red) and Mo:$BiVO_4$/Co-Pi with 5 min electrodeposition time c) chronoamperometric measurement on Mo:$BiVO_4$/Co-Pi with 5 min electrodeposition at 1.23 V_{RHE} with chopped on/off illumination of 90 s for 2 h.

FEG-SEM post-mortem analysis revealed porosity on the photoanode with pore size between 10 to 35 nm (Figure 10.a). But, cross-section imaging revealed a thickness that was maintained throughout the PEC measurements (Figure 10.b). We believe that the improvement in photoanode stability is linked to the collection of holes and the increase in the OER rate thanks to the co-catalyst. This modification limits their accumulation on the surface of the electrode, thus avoiding the presence of reactive species that contribute to photocorrosion on the electrode surface. Thea porosity at the photoanode surface, could be linked to the inhomogeneous Co-Pi coating, which affects the shape of the photocurrent after several hours.

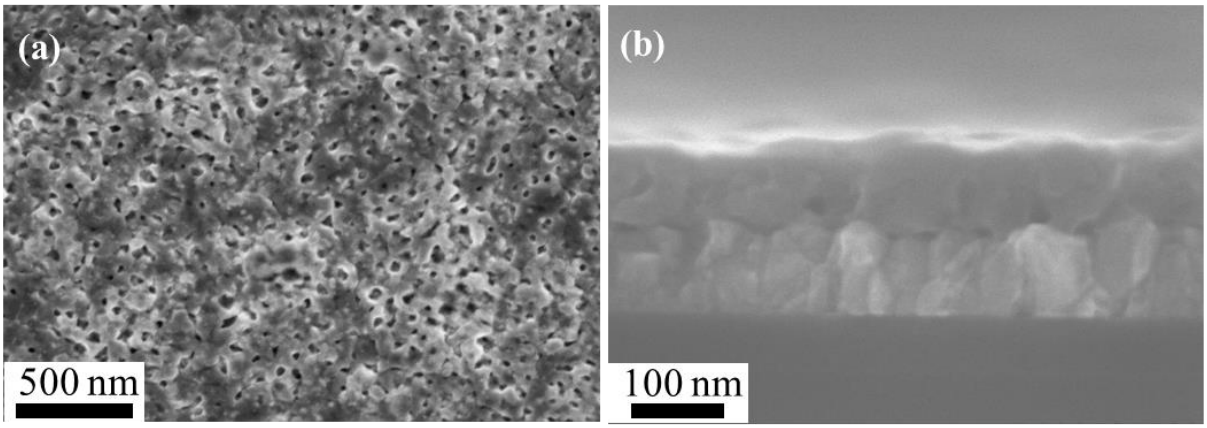

Figure 10: FEG-SEM Post-Mortem imaging of Mo:$BiVO_4$/Co-Pi photoanode of a) surface b) cross-section

The change of shape in linear sweep voltammetry on the sample with Co-Pi co-catalyst suggests that electrochemical reactions are produced in the bump potential range. To further understand these evolution, cyclic voltammetry is used in complement of XPS. This combination of analyses is selected to compare the surface chemistry before any PEC experiments and at different time during the PEC experiment with cyclic voltammetry (CV).

In Figure 11.a, the CV-curves are measured in 1 M potassium phosphate buffer (pH 6) under front illumination. The first cycle distinguished itself from the following ones. Indeed, the oxidation bump at 0.56 mV was bigger and the maximum of photocurrent density was lower during the first scan from 0.2 mV to 1.3 mV. From the 2nd cycle, all the curves presented an identical shape. Also, changing the mode of analysis by adding a scan in reduction, greatly increases the photocurrent density at 1.23 V_{RHE} to reach 2.4 mA cm^{-2}. It enhanced the PEC efficiency by a factor of 1.34. These results confirm that a modification of the electrode occurs during the reaction of the first electron-hole pairs photogenerated at the surface in presence Co-Pi co-catalyst. In the work of M.W. Kanan *et al*, they studied the stability of Co-Pi catalyst and determine "a self-repair cycle" using cyclic voltammetry.[34] They proposed a mechanism in which "Co (II) " in Co-Pi in the presence of holes is oxidized to "Co (III)" and then to "Co (IV)" from which O_2 is produced. Then, Co (II) is formed.

In Figure 11.b and c, XPS analysis before any experiment and just after the first linear scanning with illumination confirms the evolution of the surface layer of Mo:$BiVO_4$ photoanode. After electrodeposition, the presence of different oxidation states of Co in the Co-Pi layer is

identified. The fit on the XPS spectra in figure 11b corresponds to Co 2p in Co_3O_4 showing the presence of both Co(II) and Co(III). After the first linear voltage sweeps under illumination, the Co binding energy peak seems to partially disappear and a new contribution is observed at 807 eV. On the other hand, the atoms of phosphorous, P 2p remains unchanged. These results confirm the Co-Pi dynamic demonstrated by the group of M.W. Kanan, where Co (II) is oxidized and the phosphorous stayed in the form of HPO_4^- during all the process.

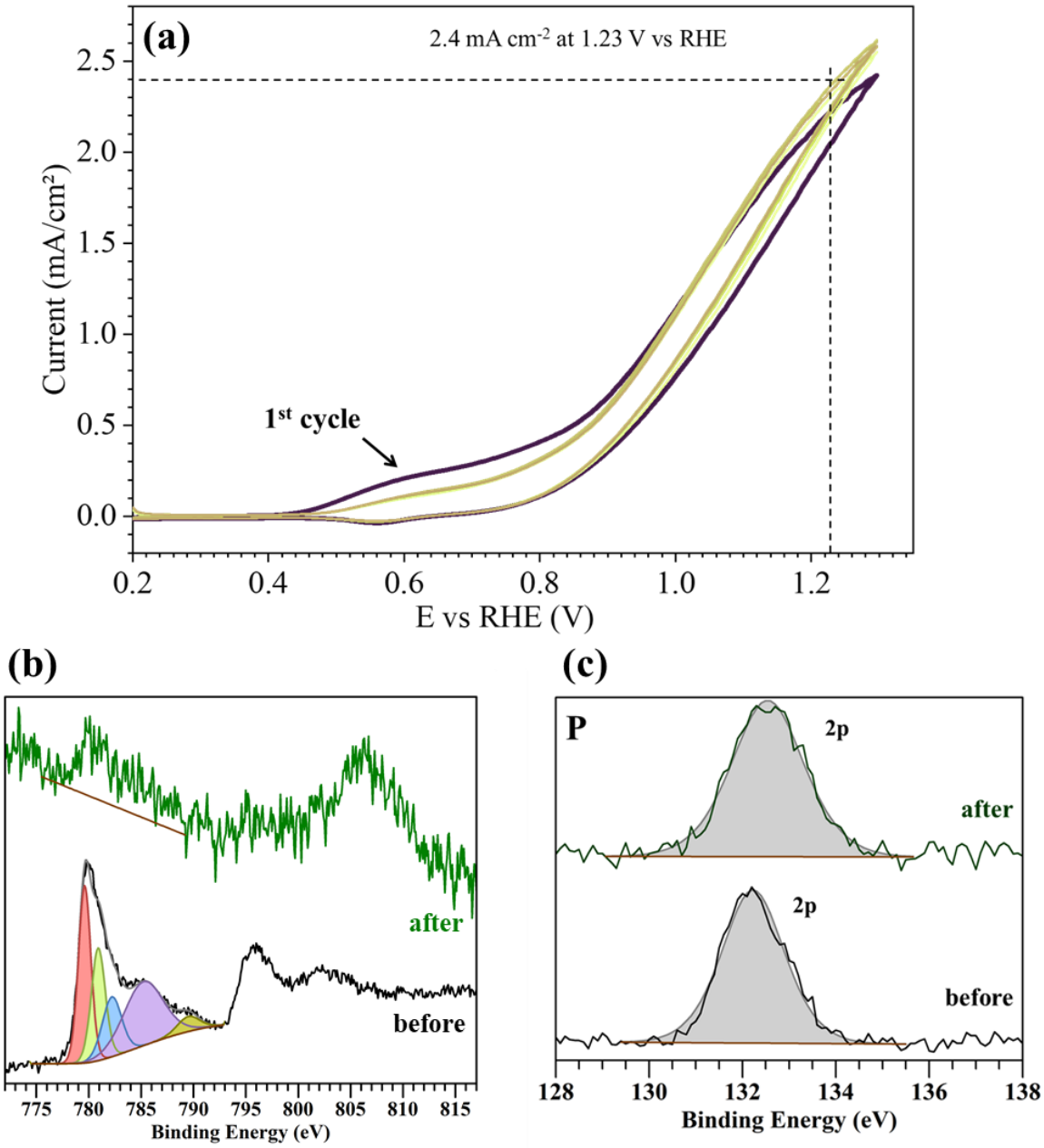

Figure 11: a) Cyclic voltammetry of $BiV_{0.994}Mo_{0.06}O_4$/Co-Pi in 1M potassium phosphate buffer (pH 6) under 100 mW cm^{-2} illumination. XPS study of $BiV_{0.994}Mo_{0.06}O_4$/Co-Pi after electrodeposition (black curve) and after first illumination of linear sweep voltammetry measurements (green) with the binding energy of b) Co atom and c) P atom.

In addition, EASA was assessed before and after the first PEC analysis under front-illumination to justify the improved photocurrent density. In Figure S19, evaluation of the EASA from C_{DL} identification under dark conditions shows an insignificant change in its value, showing that EASA does not affect photocurrent density in all samples. Furthermore, the electrolyte buffer after several CV measurements was subjected to ICP-AES to determine whether or not the Co^{2+} recovery was total or partial. Interestingly, the photocurrent density was decreasing slowly over the 10th cycle. The analysis revealed the presence of 429 ng of cobalt ions in the electrolyte solution with a surface exposition of 0.281 cm^2 for the Mo:$BiVO_4$/Co-Pi (Table 2). This analysis revealed that the "self-repair" property of Co-Pi is not complete despite the significant improvement in photocurrent.

Table 2: ICP-AES of the 1M potassium phosphate buffer before and after PEC analysis.

Name	Type value	Co 228.616 nm	Co 238.892 nm	Co 230.786 nm	Co 237.862 nm
Electrolyte before analysis 1 mL diluted by 10	Average 3 meas. (cps)	221	170	71	128
	SD	42	9	24	17
	RSD	19.20%	5.53%	33.00%	13.00%
	Concentration (ppb)	-0.4	-0.9	-0.8	-0.3
Electrolyte after analysis 1 mL diluted by 10	Average 3 meas. (cps)	2099	2078	1322	1187
	SD	60	72	26	21
	RSD	2.86%	3.47%	1.93%	1.77%
	Concentration (ppb)	9.9	9.5	9.6	9.9
TOTAL	**Average mass in 1 mL (ng)**				**97**
	Average mass in 4.4 mL of eleyctrolyte used (ng)				**429**
slope (cps/ppb)	(Av. Co 1 ppm /Av. Zero) / 1000	181.618	182.475	120.096	103.303

To identify if this amount of Cobalt detected in ionic form could be linked to a partial recovery of the catalyst in Co (II) after several cyclic voltammetry, we determined the mass of cobalt oxidized associated to the difference in photocurrent density from the oxidation/reduction scans at 0.6 V_{RHE} in the bump potential range. We approximate the time where Co^{2+} is oxidize as Co^{3+} to the time of scanning from 0.44 V to 0.62 V. As the scan rate is 10 mV s^{-1} *t* is defined as 18 s.

For the first cycle, the difference in photocurrent is defined as ~ 0.25 mA cm^{-2}. As the illuminated surface is equalled to 0.281 cm^2, we calculated a current *i* of *0.07025* mA

As, $i = \frac{Q}{t}$

with i the current (A), Q the electric charge (C) and t the time (s), the number of electrons (N_e) can be calculated as: $N_e = \frac{Q}{e}$ and e the charge of an electron (C). The N_e calculated value is

7.8933 $10^{15.}$ electrons. If we consider that each electron is used in the oxidation of Co (II) into Co (III), we deposit 772 ng of Co. This mass is superior to the mass measured by ICP in the electrolyte after the CVs. If we calculate with the exact same process the Co regenerate from the following cycles, the difference in photocurrent is ~ 0.13 mA cm^{-2} that corresponds to a current *i* of *0.037* mA. It gives a deposition of 405 ng of Co. This result shows that an incomplete recovery of Co(II) during the electrocatalysis is operating. However, the quantity of CO(II) deposited during each cycle does have an impact on the OER.

4. Conclusion

Dense $BiVO_4$ and Mo:$BiVO_4$ photoanodes were successfully synthesized using sol-gel dip-coating techniques, resulting in a scheelite structure composed of monoclinic and tetragonal polymorphs with an average thickness of 110 nm. Our study reveals that under acidic conditions, the performance of pure $BiVO_4$ photoanode is constrained by three main factors: i/ limited electron transfer within the material , ii/ lower kinetics for OER and iii/ the accumulation of holes at the electrode/electrolyte interface. These issues lead to the recombination of electron-hole pairs photogenerated and photocorrosion, significantly impacting the overall photoanode efficiency and sustainability for OER. Bulk modification through doping enhances electron mobility within the material, resulting in an increase of the photocurrent density from 1.2 mA cm^{-2} to 1.7 mA cm^{-2}. With the addition of Na_2SO_3 as sacrificial agent, Mo:$BiVO_4$ photoanodes exhibit a high photocurrent density reaching up to 3.6 mA cm^{-2} with high stability during 5 h. It demonstrates the potential of enhancing photocurrent density and durability by quickly consuming photogenerated holes for OER. Surface engineering involving the addition a Co-Pi co-catalyst overlayer on Mo:$BiVO_4$ photoanode improves the OER kinetics by a cathodic shift in the onset potential and enhances the photocurrent density to 1.9 mA cm^{-2} at 1.23 V_{RHE} in conditions close to the use in a final device. Furthermore, it notably enhances the long-term stability of the photoanode, preserving its thickness for over 5 hours. Nevertheless, a detailed examination during different stages of cyclic voltammetry experiments revealed an incomplete recovery of Co(II) within the cyclic voltammetry process, also the scanning in reduction has shown better photocurrent density in presence of Co-Pi co-catalyst compared to the linear sweeps emphasizing the incomplete self-repair property. When compared to other $BiVO_4$-based photoanodes designed for OER under acidic conditions, our photoanode currently exhibits one of the highest OER efficiency to date (see Table S1). Future possibilities may include surface modification with more durable

catalysts, such as those based on iron (Fe) or nickel (Ni), to further enhance photocurrent density.

5. References

(1) Amano, F. Photoelectrochemical Oxygen Evolution. In *Solar-to-Chemical Conversion: Photocatalytic and Photoelectrochemical Processes*; Wiley, 2021; pp 163–187. https://doi.org/10.1002/9783527825073.ch7.

(2) Kumar, M.; Meena, B.; Subramanyam, P.; Suryakala, D.; Subrahmanyam, C. Recent Trends in Photoelectrochemical Water Splitting: The Role of Cocatalysts. *NPG Asia Materials*. 2022. https://doi.org/10.1038/s41427-022-00436-x.

(3) Walter, M. G.; Warren, E. L.; McKone, J. R.; Boettcher, S. W.; Mi, Q.; Santori, E. A.; Lewis, N. S. Solar Water Splitting Cells. *Chem. Rev.* **2010**, *110* (11), 6446–6473. https://doi.org/10.1021/cr1002326.

(4) Jiang, C.; Moniz, S. J. A.; Wang, A.; Zhang, T.; Tang, J. Photoelectrochemical Devices for Solar Water Splitting-Materials and Challenges. *Chem. Soc. Rev*. 2017, pp 4645–4660. https://doi.org/10.1039/c6cs00306k.

(5) Tayebi, M.; Lee, B. K. Recent Advances in $BiVO_4$ Semiconductor Materials for Hydrogen Production Using Photoelectrochemical Water Splitting. *Renew. Sustain. Energy Rev.* **2019**, *111* (May), 332–343. https://doi.org/10.1016/j.rser.2019.05.030.

(6) Tolod, K. R.; Hernández, S.; Russo, N. Recent Advances in the $BiVO_4$ Photocatalyst for Sun-Driven Water Oxidation: Top-Performing Photoanodes and Scale-up Challenges. *Catalysts* **2017**, *7* (1). https://doi.org/10.3390/catal7010013.

(7) Cooper, J. K.; Gul, S.; Toma, F. M.; Chen, L.; Glans, P. A.; Guo, J.; Ager, J. W.; Yano, J.; Sharp, I. D. Electronic Structure of Monoclinic $BiVO_4$. *Chem. Mater.* **2014**, *26* (18), 5365–5373. https://doi.org/10.1021/cm5025074.

(8) Tokunaga, S.; Kato, H.; Kudo, A. Selective Preparation of Monoclinic and Tetragonal $BiVO_4$ with Scheelite Structure and Their Photocatalytic Properties. *Chem. Mater.* **2001**, *13* (12), 4624–4628. https://doi.org/10.1021/cm0103390.

(9) Li, G.; Bai, Y.; Zhang, W. F. Difference in Valence Band Top of $BiVO_4$ with Different Crystal Structure. *Mater. Chem. Phys.* **2012**, *136* (2–3), 930–934. https://doi.org/10.1016/j.matchemphys.2012.08.023.

(10) Kim, J. H.; Lee, J. S. Elaborately Modified $BiVO_4$ Photoanodes for Solar Water Splitting. *Advanced Materials*. 2019, pp 1806938 (30)-1806938 (35). https://doi.org/10.1002/adma.201806938.

(11) Tan, H. L.; Amal, R.; Ng, Y. H. Alternative Strategies in Improving the Photocatalytic and Photoelectrochemical Activities of Visible Light-Driven $BiVO_4$: A Review. *J. Mater. Chem. A* **2017**, *5* (32), 16498–16521. https://doi.org/10.1039/c7ta04441k.

(12) Antony, R. P.; Zhang, M.; Zhou, K.; Loo, S. C. J.; Barber, J.; Wong, L. H. Synergistic Effect of Porosity and Gradient Doping in Efficient Solar Water Oxidation of Catalyst-Free Gradient Mo:$BiVO_4$. *ACS Omega* **2018**, *3* (3), 2724–2734. https://doi.org/10.1021/acsomega.7b01794.

(13) Zhang, S.; Ahmet, I.; Kim, S. H.; Kasian, O.; Mingers, A. M.; Schnell, P.; Kölbach, M.; Lim,

J.; Fischer, A.; Mayrhofer, K. J. J.; Cherevko, S.; Gault, B.; Van De Krol, R.; Scheu, C. Different Photostability of $BiVO_4$ in near-PH-Neutral Electrolytes. *ACS Appl. Energy Mater.* **2020**, *3* (10), 9523–9527. https://doi.org/10.1021/acsaem.0c01904.

(14) Gaikwad, M. A.; Suryawanshi, U. P.; Ghorpade, U. V.; Jang, J. S.; Suryawanshi, M. P.; Kim, J. H. Emerging Surface, Bulk, and Interface Engineering Strategies on $BiVO_4$ for Photoelectrochemical Water Splitting. *Small* **2022**, *18* (10), 1–35. https://doi.org/10.1002/smll.202105084.

(15) Chen, D.; Xie, Z.; Tong, Y.; Huang, Y. Review on $BiVO_4$-Based Photoanodes for Photoelectrochemical Water Oxidation: The Main Influencing Factors. *Energy and Fuels*. 2022, pp 9932–9949. https://doi.org/10.1021/acs.energyfuels.2c02119.

(16) Rohloff, M.; Anke, B.; Wiedemann, D.; Ulpe, A. C.; Kasian, O.; Zhang, S.; Scheu, C.; Bredow, T.; Lerch, M.; Fischer, A. Synthesis and Doping Strategies to Improve the Photoelectrochemical Water Oxidation Activity of $BiVO_4$ Photoanodes. *Zeitschrift für Phys. Chemie* **2020**, *234* (4), 655–682. https://doi.org/10.1515/zpch-2019-1476.

(17) Zhong, X.; Li, Y.; Wu, H.; Xie, R. Recent Progress in $BiVO_4$-Based Heterojunction Nanomaterials for Photocatalytic Applications. *Materials Science and Engineering B: Solid-State Materials for Advanced Technology*. Elsevier Ltd March 1, 2023. https://doi.org/10.1016/j.mseb.2023.116278.

(18) Martinez Suarez, C.; Hernández, S.; Russo, N. $BiVO_4$ as Photocatalyst for Solar Fuels Production through Water Splitting: A Short Review. *Appl. Catal. A Gen.* **2015**, *504*, 158–170. https://doi.org/10.1016/j.apcata.2014.11.044.

(19) Siavash Moakhar, R.; Hosseini-Hosseinabad, S. M.; Masudy-Panah, S.; Seza, A.; Jalali, M.; Fallah-Arani, H.; Dabir, F.; Gholipour, S.; Abdi, Y.; Bagheri-Hariri, M.; Riahi-Noori, N.; Lim, Y. F.; Hagfeldt, A.; Saliba, M. Photoelectrochemical Water-Splitting Using CuO-Based Electrodes for Hydrogen Production: A Review. *Advanced Materials*. John Wiley and Sons Inc August 1, 2021, p 2007285. https://doi.org/10.1002/adma.202007285.

(20) Fornaciari, J. C.; Weng, L. C.; Alia, S. M.; Zhan, C.; Pham, T. A.; Bell, A. T.; Ogitsu, T.; Danilovic, N.; Weber, A. Z. Mechanistic Understanding of PH Effects on the Oxygen Evolution Reaction. *Electrochim. Acta* **2022**, *405*. https://doi.org/10.1016/j.electacta.2021.139810.

(21) Hilliard, S.; Friedrich, D.; Kressman, S.; Strub, H.; Artero, V.; Laberty-Robert, C. Solar-Water-Splitting $BiVO_4$ Thin-Film Photoanodes Prepared By Using a Sol–Gel Dip-Coating Technique. *ChemPhotoChem* **2017**, *1* (6), 273–280. https://doi.org/10.1002/cptc.201700003.

(22) Parmar, K. P. S.; Kang, H. J.; Bist, A.; Dua, P.; Jang, J. S.; Lee, J. S. Photocatalytic and Photoelectrochemical Water Oxidation over Metal-Doped Monoclinic $BiVO_4$ Photoanodes. *ChemSusChem* **2012**, *5* (10), 1926–1934. https://doi.org/10.1002/cssc.201200254.

(23) Rettie, A. J. E.; Lee, H. C.; Marshall, L. G.; Lin, J. F.; Capan, C.; Lindemuth, J.; McCloy, J. S.; Zhou, J.; Bard, A. J.; Mullins, C. B. Combined Charge Carrier Transport and Photoelectrochemical Characterization of $BiVO_4$ Single Crystals: Intrinsic Behavior of a Complex Metal Oxide. *J. Am. Chem. Soc.* **2013**, *135* (30), 11389–11396. https://doi.org/10.1021/ja405550k.

(24) Talasila, G.; Sachdev, S.; Srivastva, U.; Saxena, D.; Ramakumar, S. S. V. Modified Synthesis of $BiVO_4$ and Effect of Doping (Mo or W) on Its Photoelectrochemical Performance for Water Splitting. *Energy Reports* **2020**, *6*, 1963–1972. https://doi.org/10.1016/j.egyr.2020.07.024.

(25) Liang, Y.; Tsubota, T.; Mooij, L. P. A.; Van De Krol, R. Highly Improved Quantum Efficiencies for Thin Film $BiVO_4$ Photoanodes. *J. Phys. Chem. C* **2011**, *115* (35), 17594–17598. https://doi.org/10.1021/jp203004v.

(26) Seabold, J. A.; Zhu, K.; Neale, N. R. Efficient Solar Photoelectrolysis by Nanoporous Mo:$BiVO_4$ through Controlled Electron Transport. *Phys. Chem. Chem. Phys.* **2014**, *16* (3), 1121–1131. https://doi.org/10.1039/c3cp54356k.

(27) Zhang, S.; Rohloff, M.; Kasian, O.; Mingers, A. M.; Mayrhofer, K. J. J.; Fischer, A.; Scheu, C.; Cherevko, S. Dissolution of $BiVO_4$ Photoanodes Revealed by Time-Resolved Measurements under Photoelectrochemical Conditions. *J. Phys. Chem. C* **2019**, *123*, 23410–23418. https://doi.org/10.1021/acs.jpcc.9b07220.

(28) Toma, F. M.; Cooper, J. K.; Kunzelmann, V.; McDowell, M. T.; Yu, J.; Larson, D. M.; Borys, N. J.; Abelyan, C.; Beeman, J. W.; Yu, K. M.; Yang, J.; Chen, L.; Shaner, M. R.; Spurgeon, J.; Houle, F. A.; Persson, K. A.; Sharp, I. D. Mechanistic Insights into Chemical and Photochemical Transformations of Bismuth Vanadate Photoanodes. *Nat. Commun.* **2016**, *7* (May), 1–11. https://doi.org/10.1038/ncomms12012.

(29) Favaro, M.; Abdi, F. F.; Lamers, M.; Crumlin, E. J.; Liu, Z.; Van De Krol, R.; Starr, D. E. Light-Induced Surface Reactions at the Bismuth Vanadate/Potassium Phosphate Interface. *J. Phys. Chem. B* **2018**, *122* (2), 801–809. https://doi.org/10.1021/acs.jpcb.7b06942.

(30) Lee, D. K.; Choi, K. S. Enhancing Long-Term Photostability of $BiVO_4$ Photoanodes for Solar Water Splitting by Tuning Electrolyte Composition. *Nat. Energy* **2018**, *3* (1), 53–60. https://doi.org/10.1038/s41560-017-0057-0.

(31) Kuang, Y.; Jia, Q.; Ma, G.; Hisatomi, T.; Minegishi, T.; Nishiyama, H.; Nakabayashi, M.; Shibata, N.; Yamada, T.; Kudo, A.; Domen, K. Ultrastable Low-Bias Water Splitting Photoanodes via Photocorrosion Inhibition and in Situ Catalyst Regeneration. *Nat. Energy* **2017**, *2* (1), 1–9. https://doi.org/10.1038/nenergy.2016.191.

(32) Plate, P.; Höhn, C.; Bloeck, U.; Bogdanoff, P.; Fiechter, S.; Abdi, F. F.; Van De Krol, R.; Bronneberg, A. C. On the Origin of the OER Activity of Ultrathin Manganese Oxide Films. *ACS Appl. Mater. Interfaces* **2021**, *13* (2), 2428–2436. https://doi.org/10.1021/acsami.0c15977.

(33) Irani, R.; Plate, P.; Höhn, C.; Bogdanoff, P.; Wollgarten, M.; Höflich, K.; Van De Krol, R.; Abdi, F. F. The Role of Ultra-Thin MnO: X Co-Catalysts on the Photoelectrochemical Properties of BiVO4 Photoanodes. *J. Mater. Chem. A* **2020**, *8* (11), 5508–5516. https://doi.org/10.1039/d0ta00939c.

(34) Kanan, M. W.; Surendranath, Y.; Nocera, D. G. Cobalt–Phosphate Oxygen-Evolving Compound. *Chem. Soc. Rev* **2009**, *38* (1), 109–114. https://doi.org/10.1039/b802885k.

Conception of a heterostructured Mo doped-$BiVO_4$/Co-Pi photoanode for solar-driven water oxidation in acidic conditions

Supporting Information Chapter II part 1

Table S1: Photoelectrochemical OER performances of $BiVO_4$-based photoanodes in acidic conditions.

Strategy	**Electrode design**	**Synthesis method**	**Electrolyte**	**Performance (pristine $BiVO_4$) at 1.23 V_{RHE}**	**Performances (after modifications) at 1.23 V_{RHE}**	**Ref.**
Interface Type II heterojunction p-n junction	FTO/$AgVO_3$/$BiVO_4$	$BiVO_4$: spin-coating $AgVO_3$: SILAR process deposition	0.1 M sodium sulphate, Na_2SO_4 (pH 6.4)	**0.25 mA cm^{-2}** Onset potential ~ 0.9 V_{RHE} IPCE = 7 % @ 420-450 nm	**1.5 mA cm^{-2}** Onset potential ~ 0.7 V_{RHE} /	1
Surface funct. Passivation layer	FTO/$BiVO_4$/Al_2O_3	$BiVO_4$: Electrodeposition of BiOI and conversion to $BiVO_4$ by impregnation-calcination process Al_2O_3: plasma-enhance ALD	0.5 M sodium sulphate, Na_2SO_4 (pH 6)	**1.34 mA cm^{-2}** Onset potential ~ 0.3 V_{RHE} /	**1.2 mA cm^{-2}** Onset potential ~ 0.6 V_{RHE} /	2
Surface funct. Co-based MOF	FTO/$BiVO_4$/ZIF-67	$BiVO_4$: Spin-coating Room temperature dip coating (ZIF-67)	0.1 M sodium sulphate, Na_2SO_4 (pH 6)	**1 mA cm^{-2}** Onset potential ~ 0.3 V_{RHE} IPCE ~ 10 % @ 480 nm	**2.2 mA cm^{-2}** Onset potential ~ 0.26 V_{RHE} IPCE ~ 23 % @ 480 nm	3
Bulk Morphology engineering	FTO/IO/Mo:$BiVO_4$/	Colloidal crystal template via infiltration	0.5 M sodium sulphate, Na_2SO_4 (Ph 6.6)	**0.5 mA cm^{-2} at 1 $V_{Ag/AgCl}$** IPCE ~ 10 % @ 430 nm	**2 mA cm^{-2} at 1 $V_{Ag/AgCl}$** IPCE ~ 50 % @ 430 nm	4

Bulk In doping	FTO/ In:$BiVO_4$	Drop casting	0.1 M sodium sulphate, Na_2SO_4 (pH 6.8)	**0.5 mA cm^{-2}** IPCE ~ 20 % @ 420 nm	**1.56 mA cm^{-2}** Stability 1 h IPCE ~ 45 % @ 420 nm	5

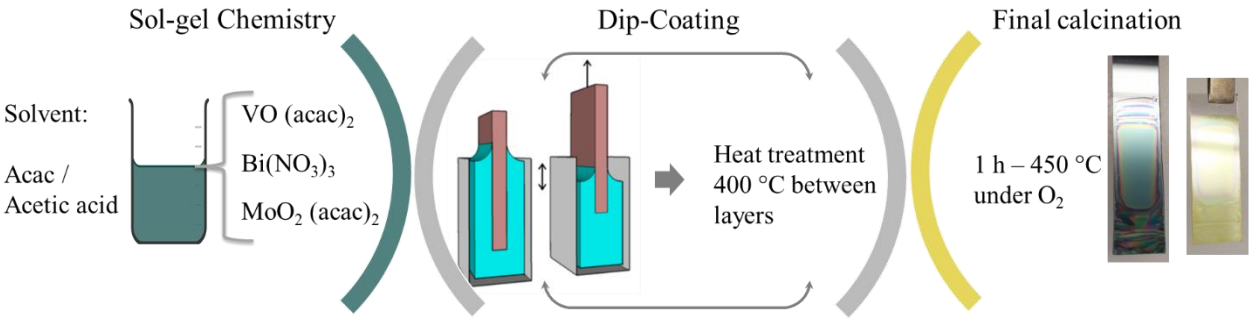

Figure S2: Scheme of the synthesis process (dip-coating scheme extract from Bindini *et Al.* [6])

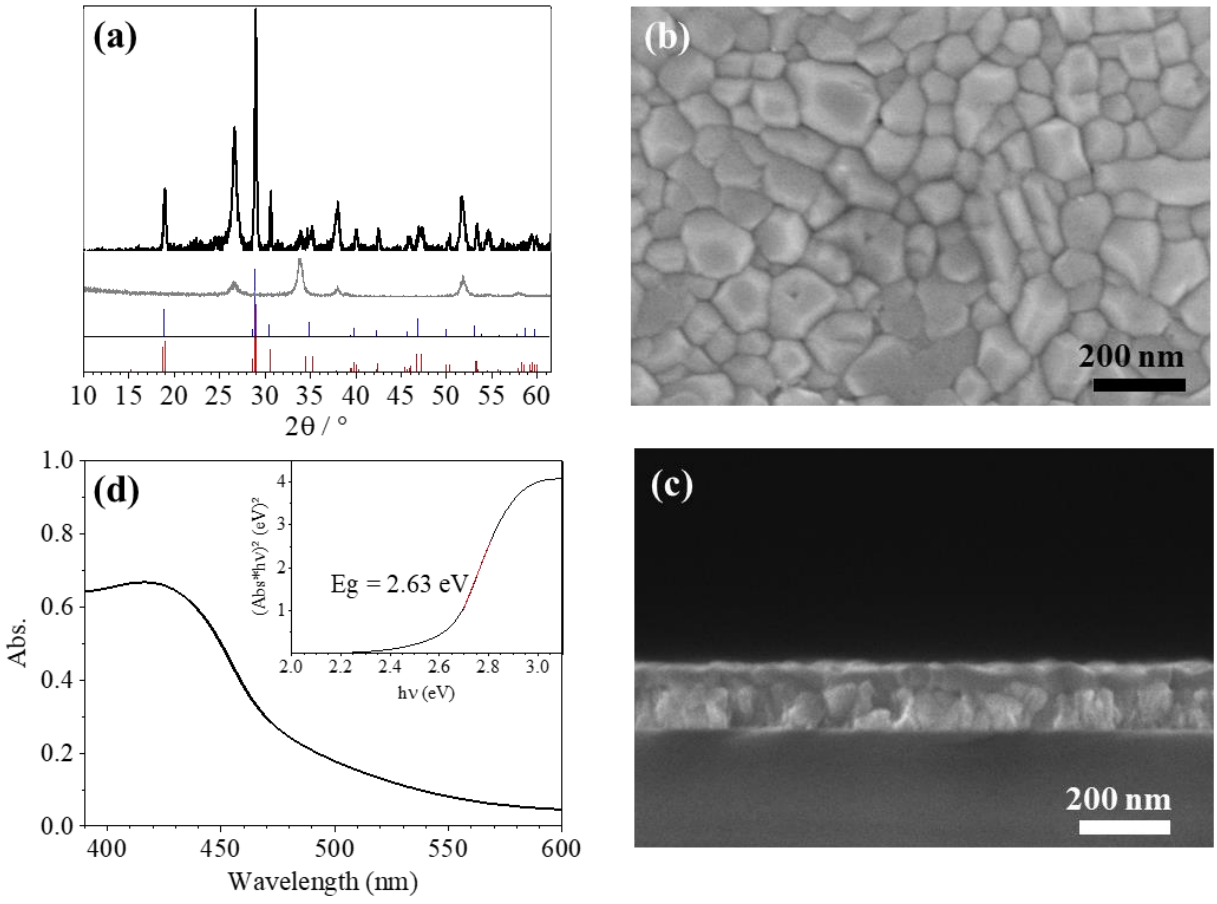

Figure S3: $BiVO_4$ reproduced from Hillard et al. protocol. a) XRD pattern of $BiVO_4$ (black curve), grey curve annealed FTO substrate (grey curve), PDF-04-010-5710 $BiVO_4$ tetragonal scheelite (blue straight-line) and PDF-04-010-5713 $BiVO_4$ monoclinic scheelite (red straight-line); b) UV-Visible absorption spectra and Eg; c) FEG-SEM surface imaging; d) FEG-SEM cross-section imaging;

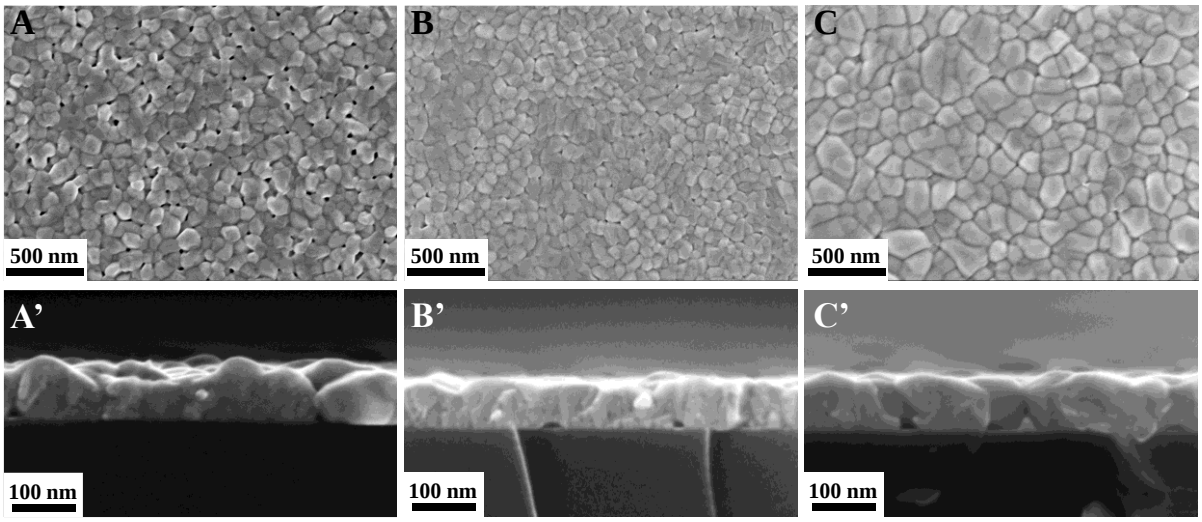

Figure S4: SEM-FEG imaging of Mo:$BiVO_4$ synthesized on Silica substrate surface and cross-section at A) A') RH < 35 %, B) B') RH < 20 %, C)C') RH <10 %.

Method for band gap determination by ellipsometry

Thickness and Eg can be determined by ellypsometry. The band gap of pure $BiVO_4$ was measured from the extinction coefficient k from the ellipsometry measurement by applying the Tauc-Plot methodology. The Model used are Gen-Osc or B-Spline, and the closest to the experimental curves "psy" and "delta". The fitted curves and parameters (MSE, Roughness, Thickness, refractive index n) are detailed below. With the extraction of the "k" parameter for each wavelength we applied a direct Tauc-Plot on the theses value.

With equation (1):

$$hv\ (eV) = \frac{h_{Planck} \times v}{\lambda} \times \frac{1}{e} \qquad (1.a)$$

with: h_{Planck} the constant of Planck (in J.s), v the celerity of light (in nm), λ the wavelength (in nm) and e the elementary charge of a single electron (in Coulombs).

$$hv\ (eV) = \frac{6.626\ e^{34} \times 3\ e^{17}}{\lambda\ (nm)} \times \frac{1}{1.602\ e^{-19}} \qquad (1.b)$$

We transform the wavelength into energy. Then with the formula (3) we obtain an absorbance from the "k" parameter:

$$Abs = \frac{4\ \times \pi \times k}{\lambda\ (nm)} \qquad (2)$$

As $BiVO_4$ is considered a semiconductor with a direct Eg [7] we fitted:

$$(Abs\ \times hv)^2 = f\ (\ hv) \qquad (3)$$

A linear polynomial fit on the linear region of the curves allows us to determine the x-intercept in a typical y = ax + b first-degree polynomial that corresponds to the Eg value

Example with pristine $BiVO_4$ in Figure S4

a)

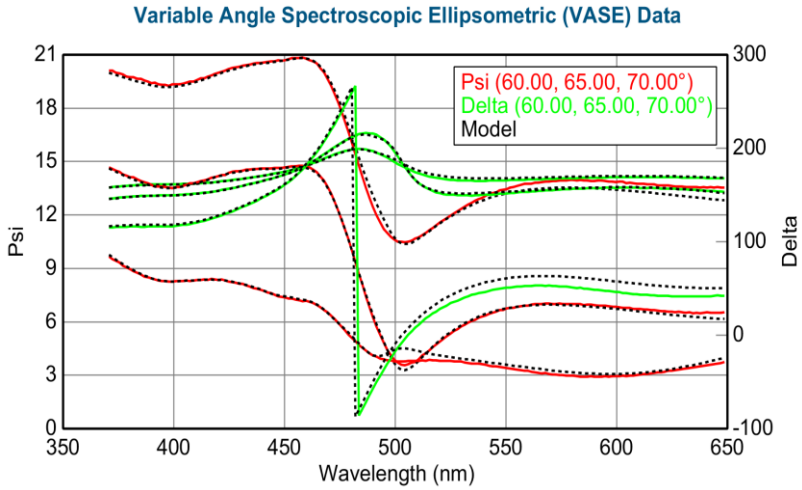

b)

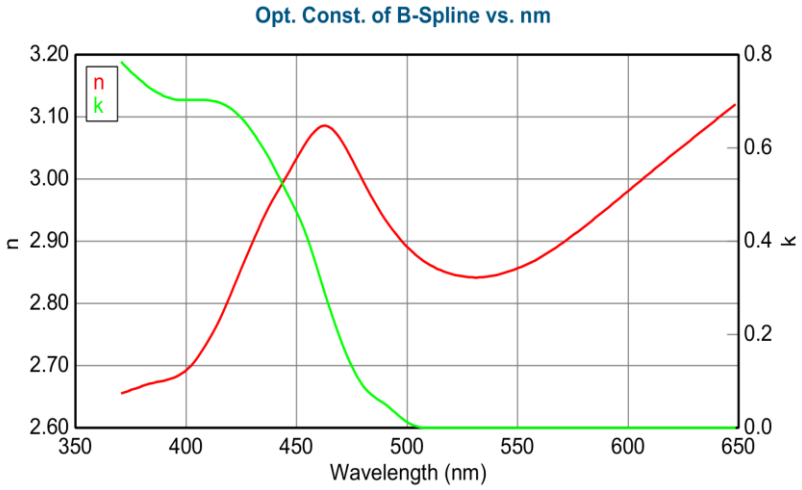

Figure S5: Characterization of pristine $BiVO_4$ deposited on FTO substrate by dip-coating with a) the variable psy and delta measured and the fitting model, b) the refractive "n" and the extinction coefficient "k" in function of the wavelength (nm).

Table S6: Ellipsometry characterization of $BiVO_4$ and Mo:$BiVO_4$ layers deposited by dip-coating.

Sample	**$BiVO_4$**		**Mo:$BiVO_4$**	
MODEL	**B-spline**		**B-spline**	
PARAMETER	**Value**	**Error bar**	**Value**	**Error bar**
MSE	**8.433**		**4.345**	
Thickness # 2 (nm)	0.28	0.517	1.49	0.125
Angle Offset	**104**	1.149	**90.69**	0.397
n of Si_JAW @ 632.8 nm	-1.877	0.0573	-0.664	0.0655
n of coated layer @ 632.8 nm	1.48569		1.48569	

Table S7: X-ray fluorescence determination of the %mol of Mo, Bi, and V element. Determination of the amount of Mo^{6+} in the film

	Mo	**V**	**Bi**
masse (µg)	0.11	5.16	22.82
n (µmol)	0.0012	0.1013	0.1092
% mol	0.56	47.85	51.59

Element	**LOD (limit of detection) in µg**	**LOQ (limit of quantification) in µg**
Bi	0.013	0.044
Mo	0.008	0.026
V	0.008	0.026

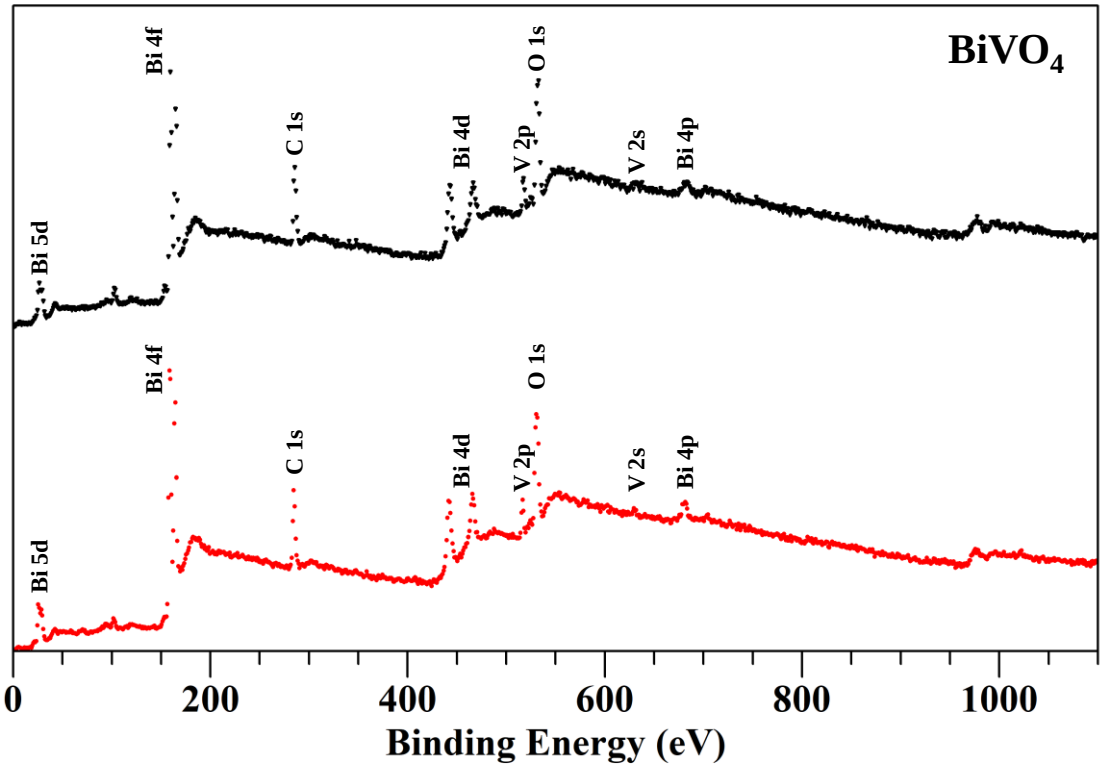

Figure S8: Room-Temperature XPS survey spectra of $BiVO_4$ in black dots and $BiV_{0.994}Mo_{0.06}O_4$ in red dots.

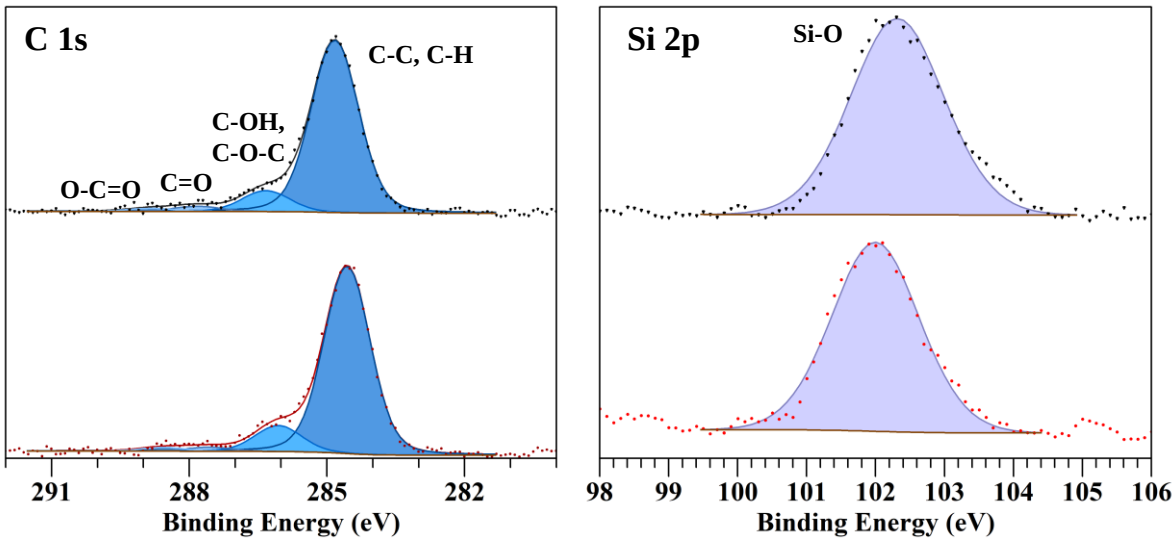

Figure S9: Room-temperature XPS spectra of air exposed samples with the signal of C1s and Si 2. Colour code: black spectra corresponding to pristine $BiVO_4$ and red spectra corresponding to $BiV_{0.994}Mo_{0.06}O_4$.

Table S10: Binding energy in eV of C 1s, and Si 2p in the electrodes of $BiVO_4$ and $BiV_{0.994}Mo_{0.06}O_4$.

Element	C 1s				Si 2p
	C-C, C-H	C-OH, C-O-C	C=O	O-C=O	Si-O
$BiVO_4$	284.56	286.06	287.56	288.56	102.00
$BiV_{0.994}Mo_{0.06}O_4$	284.56	286.06	287.56	288.56	102.31

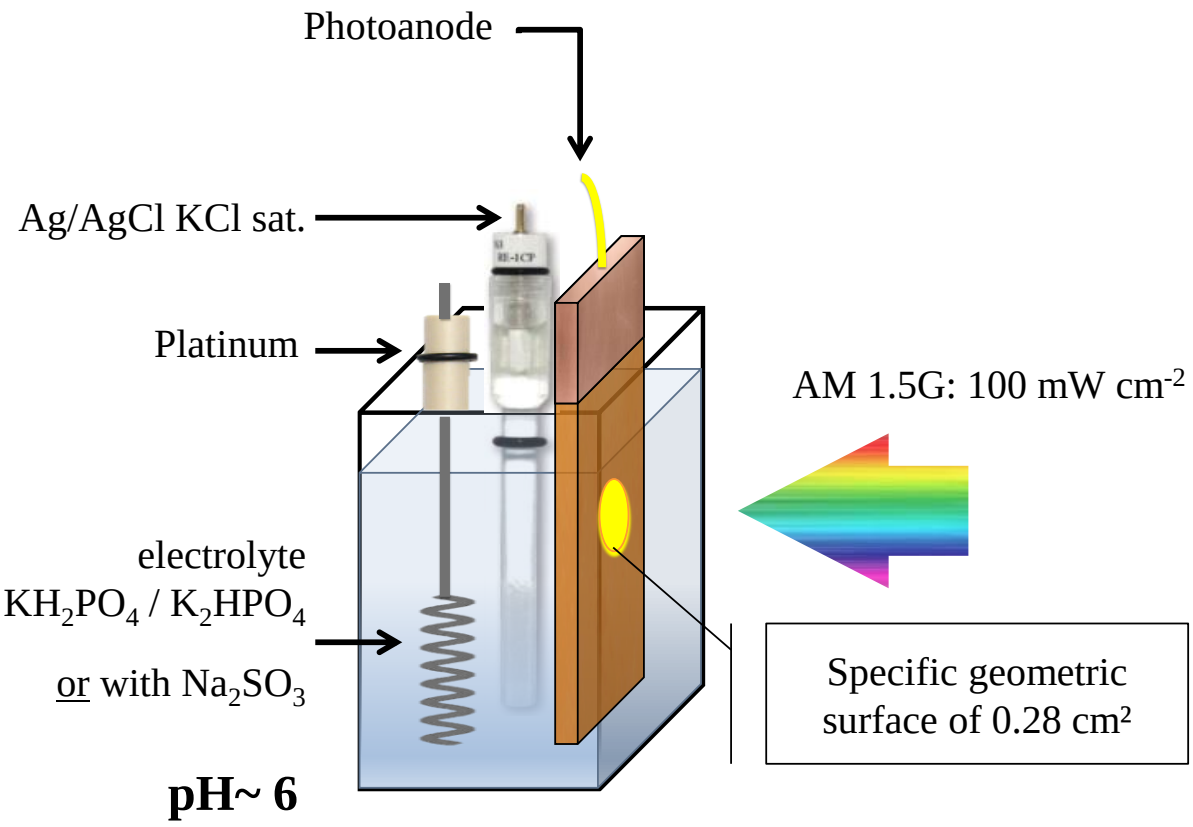

Figure S11: Photoelectrochemical set-up

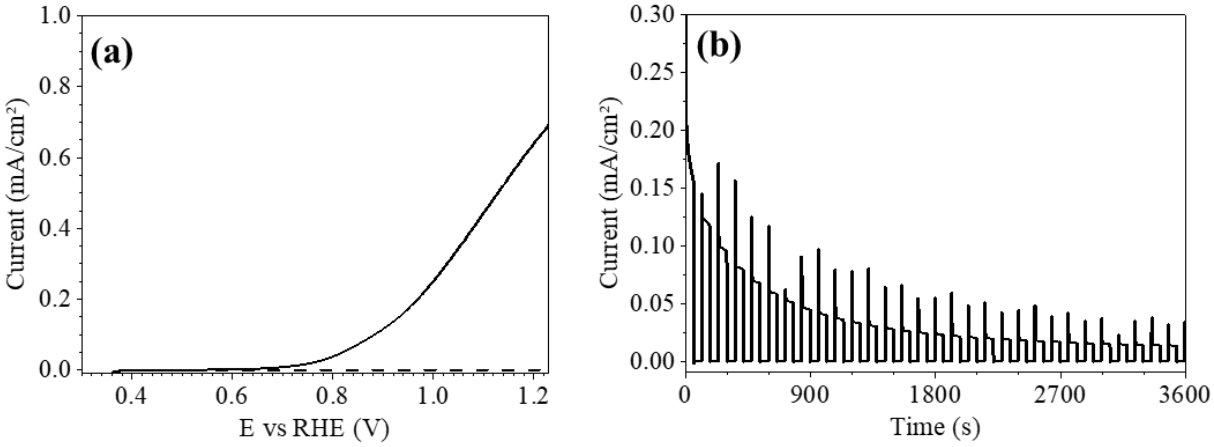

Figure S12: Photoelectrochemical measurements in 1M potassium phosphate buffer (pH 6) under front simulated illumination at 100 mW cm^{-2} a) Linear voltage sweeps measured at $BiVO_4$ (60 nm) thin films light on (black line) light off (large dots) b) chronoamperometric measurement at 1.23 V_{RHE} with chopped on/off illumination of 90 s for 1 h.

. Method for the Electrochemical Active Surface Area determination

The comparison of the double layer capacitance (C_{DL}) of the samples brings information on the electrochemically active surface area (EASA) with the formula (4). The specific capacitance (C_s) describes the capacitance of an ideal flat surface of the catalyst. Due to its value dependency of the pH media, the material and measurement conditions, as reported by McCrory et al. for alkaline solution they identify a variation of ~ 0.11 mF cm^{-2} in benchmark publications. [8,9]

$$EASA = \frac{C_{DL}}{C_s} \quad (4)$$

To compare our samples, we evaluated the electrochemically active surface area as a function of the capacitance value of the double layer. To calculate de C_{DL}, cyclic voltammetry (CV) is performed in 1M potassium phosphate buffer (pH 6) in dark conditions (without any illumination) in the non-faradaic region of the electrodes corresponding to [0.21; 0.41] V_{RHE}. We applied 10 cycles for a specific scan rate and extracted the 8^{th} CV curve which corresponds to the cycle where the curves are nearly identical. We realised these measurements for the scan rates: 5, 10, 20, 50, 100 mV s^{-1}. CV were performed in a 3 electrodes configuration identical to LSV or chronoamperometric measurements. The surface isolated on these samples corresponds to the best part of the deposited film were the photoelectrochemical measurements are studied.

For one sample, the 8^{th} curve was plotted in function of the voltage. Then C_{DL} was assessed from the slope of the linear regression between the current density differences ($\Delta j/2 = (ja-jc)/2$) in the middle of the potential window of CV curves versus the scan rates.

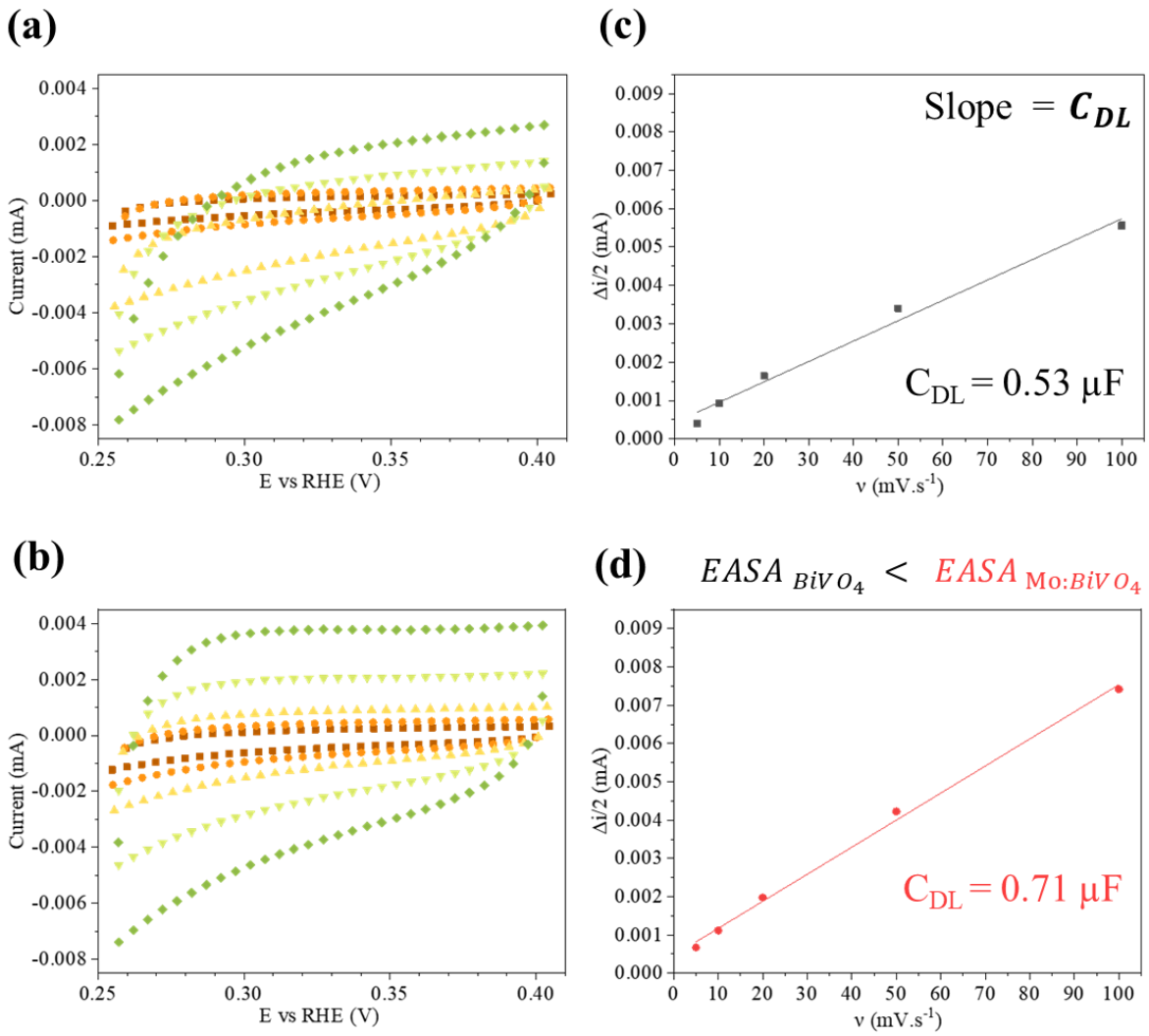

Figure S13: Cyclic voltammetry of scan rates: 5, 10, 20, 50, 100 mV s^{-1} of a) pristine $BiVO_4$, b) Mo:$BiVO_4$, linear regression of Δj/2 in function of the scan rate of c) pristine $BiVO_4$, d) Mo:$BiVO_4$.

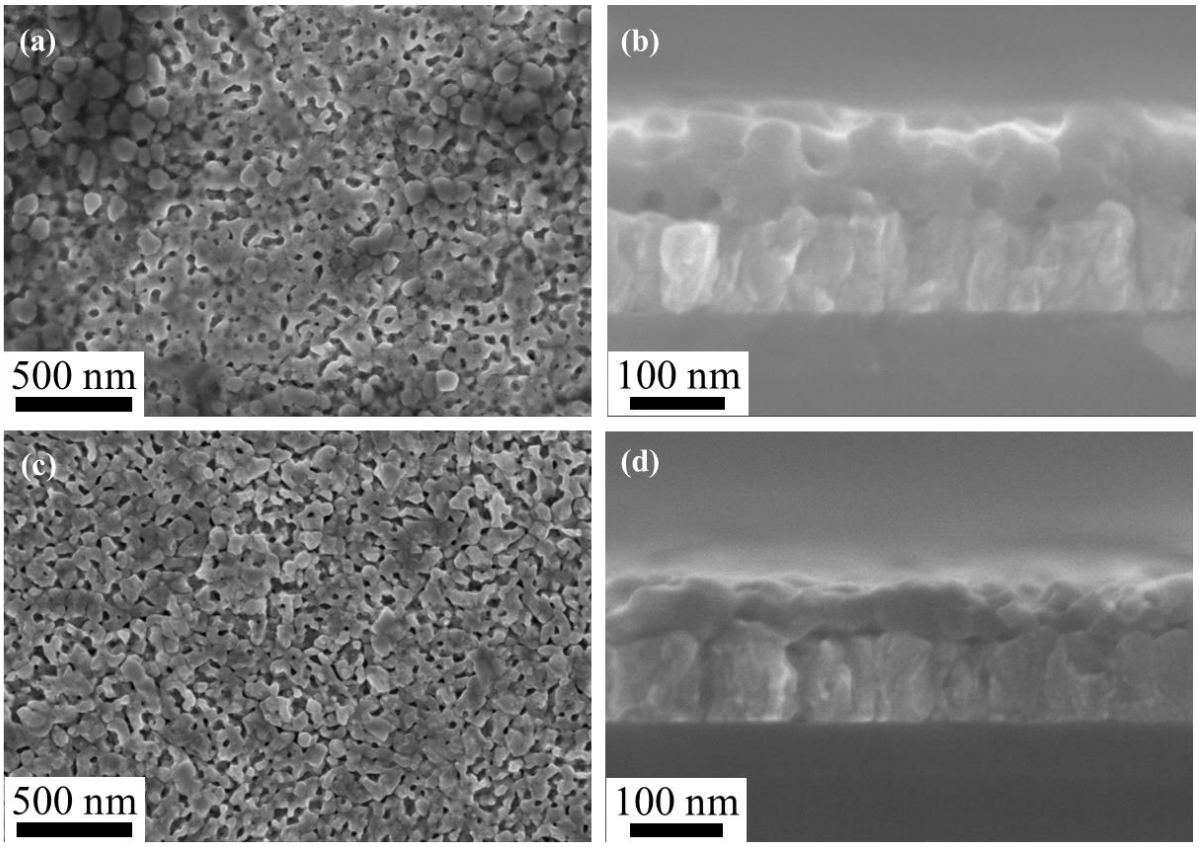

Figure S14: FEG-SEM post-mortem after PEC analysis under back-illumination of a) $BiVO_4$ surface, b) $BiVO_4$ cross-section c) Mo:$BiVO_4$ surface, d) Mo:$BiVO_4$ cross-section.

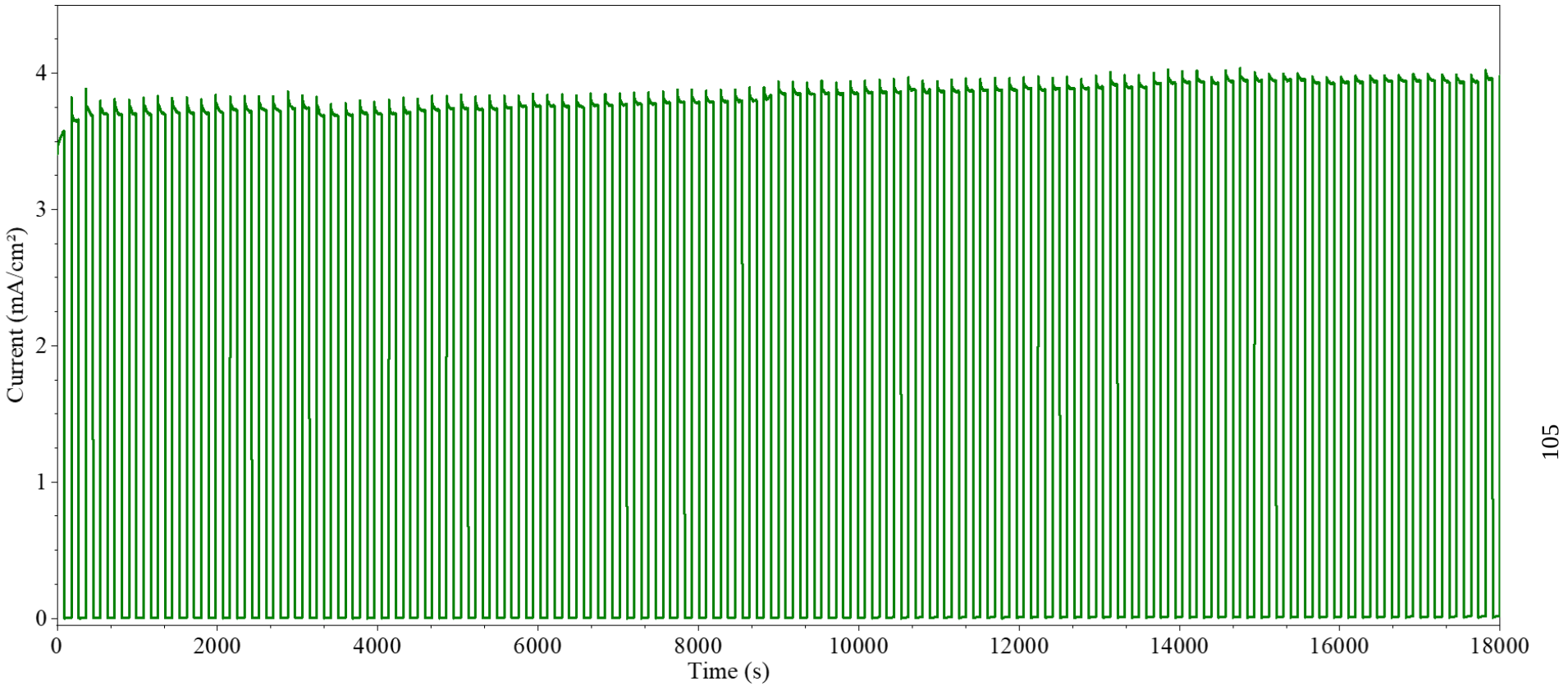

Figure S15: Chronoamperometric measurement on Mo:$BiVO_4$ thin film at 1.23 V vs RHE with chopped on/off irradiation of 90 sec. during 5 h in front irradiation at 1M potassium phosphate buffer with additional 1M Na_2SO_3 (pH 6.8) as sacrificial agent.

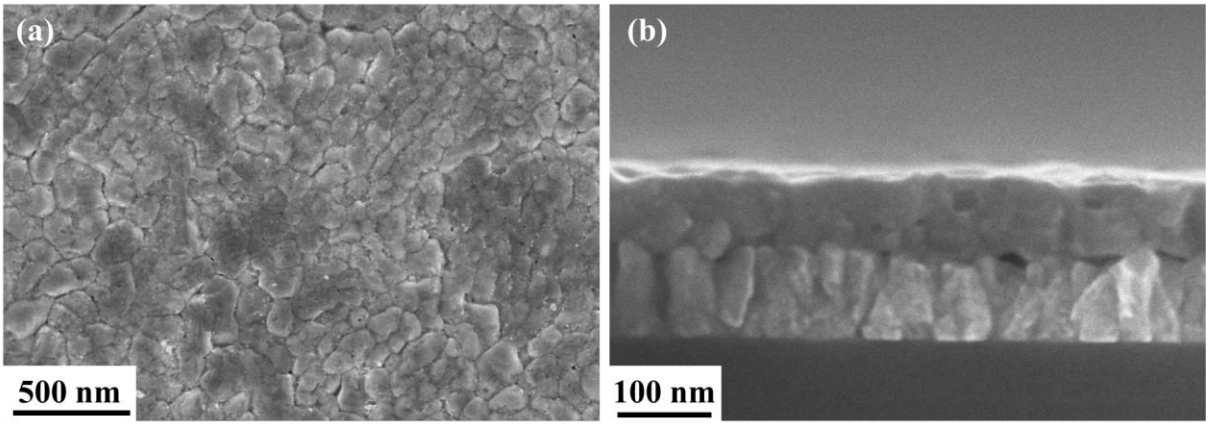

Figure S16: FEG-SEM Post-mortem imaging of Mo:$BiVO_4$ thin film after photoelectrochemical tests at 1M potassium phosphate buffer with additional 1M Na_2SO_3 (pH 6.8) as sacrificial agent.

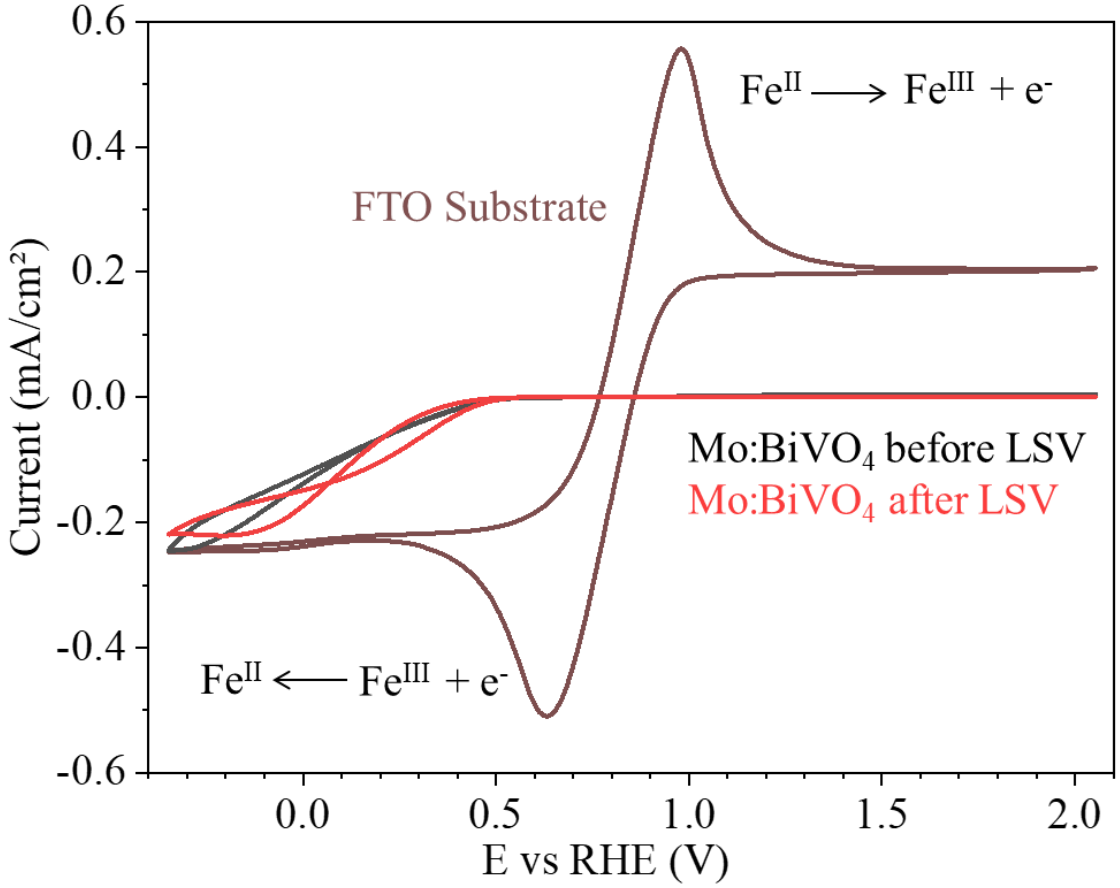

Figure S17: Oxidation and reduction F^{3+}/Fe^{2+} study by cyclic voltammetry on naked FTO, Mo:$BiVO_4$ before any photoexcitation (in black) and after several linear sweep voltammetry measurements in dark and light modes (in red)

The Figure S17 corresponds to the cyclic voltammetry measurements of the couple Fe^{3+} / Fe^{2+} oxidation and reduction for bare FTO and for Mo:$BiVO_4$ after the synthesis before any perturbation or stimulus and after several linear sweep voltammetry measurements in dark and light conditions.

The electrolyte solution is composed of 50 mM ferri/ferrocyanide (potassium ferricyanide III, ACS reagent 99.0 %, potassium hexacyanoferrate II trihydrate, ACS reagent ≤ 100 %) with 0.1 M supporting potassium chloride (ACS reagent 99.0-100.5 %) electrolyte.

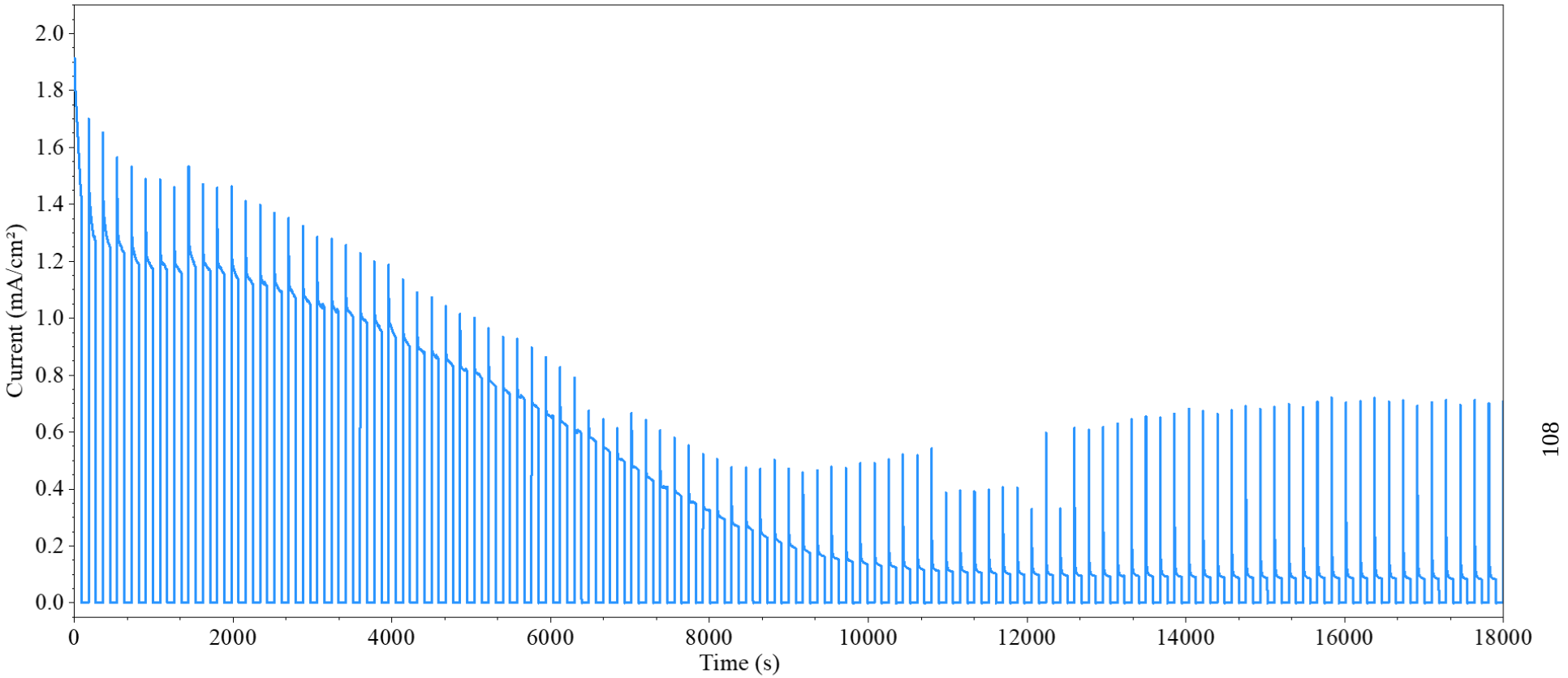

Figure S18: Chronoamperometric measurement on $BiV_{0.994}Mo_{0.06}O_4$/Co-Pi thin film at 1.23 V vs RHE with chopped on/off irradiation of 90 sec. during 5 h in front irradiation at 1M potassium phosphate buffer (pH 6)

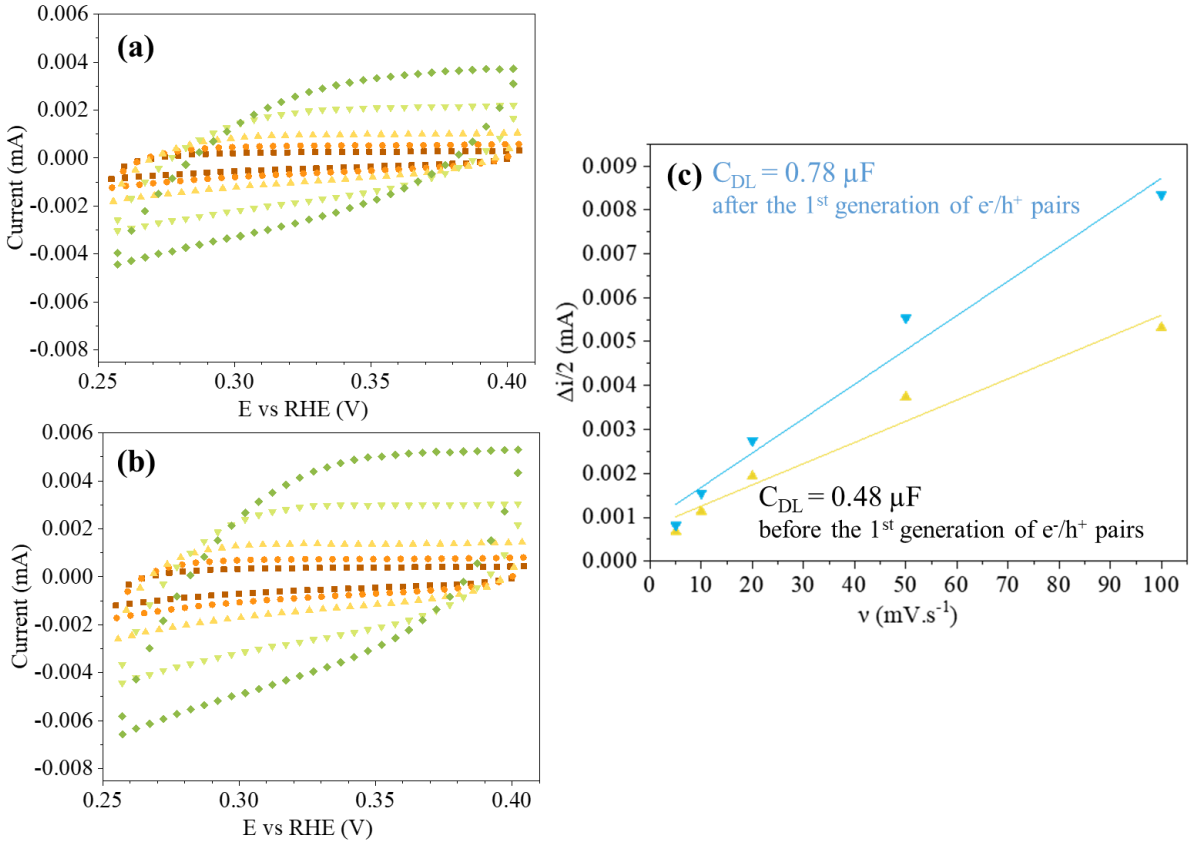

Figure S19: Cyclic voltammetry in the dark with scan rates: 5, 10, 20, 50, 100 mV s^{-1} of a) Mo:$BiVO_4$/Co-Pi before any LSV measurement, b) Mo:$BiVO_4$/Co-Pi after the first LSV measurement under front-illumination at 100 mW cm^{-2}, d) linear regression of Δj/2 in function of the scan rate.

References

(1) Gao, L.; Long, X.; Wei, S.; Wang, C.; Wang, T.; Li, F.; Hu, Y.; Ma, J.; Jin, J. Facile Growth of $AgVO_3$ Nanoparticles on Mo-Doped $BiVO_4$ Film for Enhanced Photoelectrochemical Water Oxidation. *Chem. Eng. J.* **2019**, *378*, 122193. https://doi.org/10.1016/j.cej.2019.122193.

(2) Wan, X.; Xu, Y.; Wang, X.; Guan, X.; Fu, Y.; Hu, C.; Hu, H.; Rong, N. Atomic Layer Deposition Assisted Surface Passivation on Bismuth Vanadate Photoanodes for Enhanced Solar Water Oxidation. *Appl. Surf. Sci.* **2022**, *573*, 151492. https://doi.org/10.1016/j.apsusc.2021.151492.

(3) Ahn, C. H.; Deshpande, N. G.; Lee, H. S.; Cho, H. K. Energy Transfer-Induced Photoelectrochemical Improvement from Porous Zeolitic Imidazolate Framework-Decorated $BiVO_4$ Photoelectrodes. *Small Methods* **2021**, *5* (2), 1–10. https://doi.org/10.1002/smtd.202000753.

(4) Zhou, M.; Bao, J.; Xu, Y.; Zhang, J.; Xie, J.; Guan, M.; Wang, C.; Wen, L.; Lei, Y.; Xie, Y. Photoelectrodes Based upon Mo:$BiVO_4$ Inverse Opals for Photoelectrochemical Water Splitting. *ACS Nano* **2014**, *8* (7), 7088–7098. https://doi.org/10.1021/nn501996a.

(5) Zhong, X.; He, H.; Yang, M.; Ke, G.; Zhao, Z.; Dong, F.; Wang, B.; Chen, Y.; Shi, X.; Zhou, Y. In^{3+}-Doped $BiVO_4$ Photoanodes with Passivated Surface States for Photoelectrochemical Water Oxidation. *J. Mater. Chem. A* **2018**, *6* (22), 10456–10465. https://doi.org/10.1039/c8ta01377b.

(6) Bindini, E.; Naudin, G.; Faustini, M.; Grosso, D.; Boissière, C. Critical Role of the Atmosphere in Dip-Coating Process. *J. Phys. Chem. C* **2017**, *121* (27), 14572–14580. https://doi.org/10.1021/acs.jpcc.7b02530.

(7) Walsh, A.; Yan, Y.; Huda, M. N.; Al-Jassim, M. M.; Wei, S. H. Band Edge Electronic Structure of $BiVO_4$: Elucidating the Role of the Bi s and V d Orbitals. *Chem. Mater.* **2009**, *21* (3), 547–551. https://doi.org/10.1021/cm802894z.

(8) Connor, P.; Schuch, J.; Kaiser, B.; Jaegermann, W. The Determination of Electrochemical Active Surface Area and Specific Capacity Revisited for the System MnOx as an Oxygen Evolution Catalyst. *Zeitschrift für Phys. Chemie* **2020**, *234* (5), 979–994. https://doi.org/10.1515/zpch-2019-1514.

(9) McCrory, C. C. L.; Jung, S.; Peters, J. C.; Jaramillo, T. F. Benchmarking Heterogeneous Electrocatalysts for the Oxygen Evolution Reaction. *J. Am. Chem. Soc.* **2013**, *135* (45), 16977–16987. https://doi.org/10.1021/ja407115p.

CHAPTER II PART 2

Sol-Gel $BiVO_4$-based photoanode with enhanced stability through the deposit of a TiO_2 passivation layer

CHAPTER II PART 2

Table of Content

Sol-Gel $BiVO_4$-based photoanode with enhanced stability through the deposit of a TiO_2 passivation layer

ABSTRACT

Developing efficient $BiVO_4$-based photoanodes for aqueous photoelectrochemical water oxidation poses sustainability challenges. One strategy to enhance sustainability involves passivation, with ultrathin TiO_2 layers proposed as effective barrier. Herein, we investigate the influence of TiO_2 thickness and crystallinity on photoanode durability under mild acidic conditions (pH 6). We employ two deposition methods: Atomic Layer Deposition (ALD) for TiO_2 layers (15-10 nm), emphasizing the need for high crystallinity and reduced thickness. Subsequently, we introduce a scalable alternative method, combining sol-gel chemistry and dip-coating, to create thinner TiO_2 layers (3-5 nm). Our photoanode maintains a stable photocurrent density of ~ 0.3 mA cm^{-2} for 1 hour without a cocatalyst. These findings provide valuable insights into enhancing the durability of $BiVO_4$-based photoanodes and the role of thickness and crystallinity of TiO_2 passivation layer.

1. Introduction

Photoelectrochemical water-splitting is a very promising solution to directly convert solar energy into chemical energy through dihydrogen production.[1] However, the oxygen evolution reaction (OER) is today the limiting step for full device, especially at pH conditions close to neutral.[2] Among various n-type semiconductors with well-aligned conduction and valence bands allowing OER, bismuth vanadate exhibits the best intrinsic properties as photoanode material.[3,4] Its low band gap of 2.4 eV allows wider absorption in the visible range compared to other metal oxides such as TiO_2 or WO_3. The theoretical maximum photocurrent density associated with $BiVO_4$ is 7.5 mA cm^{-2} with ~ 9.2 % solar-to-hydrogen (STH) efficiency.[2,5–7] Reaching this photocurrent density remains a challenge because of intrinsic and environmental limitations.[1] Indeed, $BiVO_4$ has poor charge carrier mobility with a short hole diffusion length (70 – 100 nm)[8] and low kinetic for OER.[9] Many efforts has gone into improving the efficiency of the electrode in order to achieve its full potential of STH conversion yield.[10–14] Photoelectrochemical (PEC) performance has mainly been studied in alkaline electrolytes because hydroxide ions facilitate OER and these few years in neutral conditions. [4,10,12,14,15] To

allow the design of a tandem cell with only solar and water input, the electrolyte buffer should be compatible with both photoanode and photocathode working conditions. Most efficient photocathodes are used in acidic conditions where OER kinetics is low.[1,16] In acidic buffer, the electrode sustainability is strongly compromised due to photocorrosion and recombination of charge carriers.[17,18] Competing with OER, the photogenerated electron-hole pairs may also react with their environment (material/electrolyte) to produce active species that degrade the electrode. Photocorrosion occurs on the surface of the photoanode immersed in the electrolyte under illumination and is enhanced by a bias voltage.[18,19]

To improve $BiVO_4$-based photoanode durability, passivation layers deposition at the interface electrode/electrolyte appears as a very interesting solution.[4,20–22] To do so, these layers must be stable in the electrolyte and the operating conditions (light exposure, wide range of potential).[23] Recently, a number of materials used as passivation layers including catalysts have been studied to limit electrode degradation. The use of NiO_x reduces surface recombination and improves the band bending.[24] ZnO layer containing O vacancies on the surface of $WO_3/BiVO_4$/ZnO photoelectrode facilitates the hole trapping and limits the surface recombination.[25] Furthermore, an Al_2O_3 layer has recently been applied to $BiVO_4$ photo electrodes with promising results for a longer operating time, but recombination are still present.[22] In this context, TiO_2 was proved interesting as a passivation layer because of its stability in a wide pH range.[26] In many works, Atomic layer deposition (ALD) is used to cover the electrode surface with precise thickness control. Accordingly, the group of Usman *et al*. improved their photocurrent density by depositing of 1.3 nm of TiO_2.[21] However, their protective properties appear to be low regarding the transient photocurrent measurements with time. McDowell *et al.* developed a ~ 1 nm thick protective layer of TiO_2 combined with the deposition of a co-catalyst layer based on Ni such as (NiOOH): $BiVO_4/TiO_2$/Ni.[27] They observed an improvement in the photoelectrode durability in a strongly alkaline solution. Yet, the effective passivation property of this extremely thin amorphous TiO_2 layer is questionable, as the benefits are only demonstrated in presence of Ni Ni cocatalyst. Also, the general lack of post-mortem imaging does not allow certification of the chemical stability of the active film at the electrode/electrolyte interface. D. Lee *et al.* designed an efficient $BiVO_4/TiO_2$/FeOOH/NiOOH photoanode in a strongly alkaline solution (pH 12) using an electrodeposition technique with a 6 nm thick layer of TiO_2.[28] Without the addition of a Fe and Ni based co-catalyst, they generated a photocurrent density of 1 mA cm^{-2} at 1.23 V_{RHE}, 1.25 times less than that of pristine $BiVO_4$. However, they were unable to determine the crystallinity of TiO_2 due to the limitations of instrumentation using classical X-ray diffraction.

These studies are still not performed in acidic media that is much less favourable to the PER reaction.

The influence of TiO_2 crystallinity and deposition thickness on its passivation ability in a $BiVO_4$ photoanode, without the use of a hole collector, is still unclear. Generally, well-crystallized materials exhibit better electron-hole mobility. Herein, we explore the impact of the TiO_2 thickness and its crystallinity on photoanode's durability in PEC experiments under weakly acidic conditions (pH 6). This study marks the first investigation of TiO_2 as a passivation layer under such conditions, which holds great promise for efficient photoelectrochemical devices comprising $BiVO_4$-based photoanodes and Cu_2O-based photocathodes.[16] Initially, ALD was used to generate a TiO_2 passivation with a thickness of 15 to 10 nm. Subsequently, we propose an easy-to-scale alternative for designing thin TiO_2 passivation layers with a thickness of 3 to 5 nm using a modified protocol involving sol-gel chemistry coupled with dip-coating deposition.[29]

2. Materials and methods

TiO_2 passivation layers were deposited on pristine $BiVO_4$ or Mo-doped $BiVO_4$ photoanodes. For coatings realised by ALD, the $BiVO_4$-based underlayer presents a thickness of 50 – 60 nm. For TiO_2 deposited by dip-coating, the underlayer consists of Mo:$BiVO_4$ with a thickness of 110 nm. Table 1 shows the identification of each sample and the characteristics of its photoactive underlayer. For each sample, a reference of $BiVO_4$ photoanode with the same thickness as the TiO_2 -coated sample was used to compare the PEC performances.

Table 1: Reference of the samples studied

Name	TiO_2 deposition technique and thickness	Underlayer and thickness	Reference
ALD-15-TiO_2/$BiVO_4$	ALD ~ **15 nm**	$BiVO_4$ ~ 60 nm	$BiVO_4$ (60 nm)
ALD-10-TiO_2/$BiVO_4$	ALD ~ **10 nm**	$BiVO_4$ ~ 60 nm	$BiVO_4$ (60 nm)
ALD-10-TiO_2/Mo:$BiVO_4$	ALD ~ **10 nm** +Heat treatment 450 °C ~ 2 h	Mo:$BiVO_4$ ~ 60 nm	Mo:$BiVO_4$ (60 nm)
Dip-1-TiO_2/Mo:$BiVO_4$	Sol-gel/Dip-coating ~ **5 nm** + Heat treatment 450 °C ~ 2 h	Mo:$BiVO_4$ ~ 110 nm	Mo:$BiVO_4$ (110 nm)
Dip-2-TiO_2/Mo:$BiVO_4$	Sol-gel/Dip-coating ~ **3 nm** + Heat treatment 450 °C ~ 2 h	Mo:$BiVO_4$ ~ 110 nm	Mo:$BiVO_4$ (110 nm)

a. Synthesis of $BiVO_4$-based photoanodes

The synthesis of $BiVO_4$ photoanodes is based on previous works developed by S. Hilliard.[30] Precursors are dissolved by ultrasound in a mix solvent of acetylacetone: acetic acid in a 4.7:1 molar ratio. They are first put in an ultrasonic bath for 10 minutes at 35 °C before being magnetically stirred overnight. The exact amount of each precursor used for the photoanode synthesis is gathered in Table S1. The film deposition is performed the day after the preparation of the solution. A commercial glass of F-doped SnO_2 (FTO) 80 nm/ Glass substrate from (SOLEMS: YSUB/ASAHI120/1) with effective resistivity measured in the 200 – 250 **Ω** range is used as an electrode substrate. $BiVO_4$ photoanodes are produced by dipping FTO substrates in sol solution using an Ossila Dip-Coater at ambient temperature. Several layers are deposited to achieve the adequate thickness. After each layer, the non-conductive side of the substrate is wiped with ethanol and acetone, then annealed at 400 °C for 1 – 2 minutes. A final 1 h calcination at 450 °C under O_2 is applied to achieve good crystallinity and consolidation on the substrate. The dip-coating parameters are summarized in Table S2.

b. Atomic layer deposition of TiO_2

Deposition of TiO_2 by ALD: Atomic layer deposition was used to produce TiO_2 thin films of 15 and 10 nm adapted from Coutancier *et al.*[31] The depositions were done by the onto ~ 50 nm $BiVO_4$ surface. The ALD-TiO_2 thin films were prepared in a BENEQ TFS-200 ALD reactor. Titanium (IV) i-propoxide ($Ti(OiPr)_4$, TTIP, and deionized water were used as Ti and O precursors, respectively. All chemicals were used without further purification. Nitrogen (N_2, 99.99%, Air Liquide) was used as both carrier and purging gas. TTIP was heated in a hot solid source system Beneq HS300 at TTTIP =85 °C, while other precursors were kept at room temperature. Experiments were performed at T_{dep} = 200 °C, and the pressure in the reaction chamber was kept in the range of 1−2 mbar. Prior to ALD treatment, $BiVO_4$/ FTO and Mo:$BiVO_4$ photoanodes were ultrasonically cleaned successively in acetone, ethanol, and deionized water. TiO_2 has a low growth rate (growth per cycle, GPC ∼0.36 Å/cycle). The growth cycle of titanium oxide, {TiO_2}, corresponds to:

{TiO_2} = {[TTIP]/N_2/H_2O/N_2 = [0.5/0.05/0.5/0.5]/5/2/5 s}

The ALD cycling was repeated an appropriate number of times to obtain the desired thicknesses.

c. Sol-gel - dip-coating deposition of TiO_2

Synthesis of TiO_2 by sol-gel / dip-coating on Silicon substrate and Mo:$BiVO_4$ photoanodes: For the deposition of thin TiO_2 layers by sol-gel synthesis coupled with dip-coating deposition technique, a first solution S_a of $TiCl_4$: EtOH 1:5 volumetric ratio (v:v) is prepared. Then 1.6 g from S_a is poured into another flask where 5 g of absolute ethanol and 0.4 g of Milli-Q water is added giving solution S_B ($[Ti^{4+}]$ = 0.2 M). Then, S_B was then diluted with EtOH:H_2O 1:2 (v:v) to obtain a final $[Ti^{4+}]$ concentration of 0.125 M. For dip-coating, deposition begins when the relative humidity in the deposition chamber is below 10 %. An intermediate heat treatment of 1 – 2 minutes at 350 °C is applied before the final calcination of 1 h at 450 °C under O_2. To study thickness as a function of the thickness, a supplementary layer is realised by dipping the sample in the same sol.

For Mo:$BiVO_4$ photoanodes, 2.5 mm s^{-1} withdrawal speed is used to achieve one layer of TiO_2 (named 1-TiO_2/Mo:$BiVO_4$ sample) and 0.8 mm s^{-1} withdrawal speed is used to obtain two layers of TiO_2 with an intermediate heat treatment of 1-2 min at 350 °C between each layer of TiO_2 (named 2-TiO_2/Mo:$BiVO_4$).

d. Characterization methods

FEG-SEM EDX imaging: Field emission gun-scanning electron microscopy (FEG-SEM) and energy-dispersive X-ray spectroscopy (EDX) were carried out using a Hitachi SU-70 equipped with Oxford X-Max beam with 50 mm^2 X-Max silicon drift EDS detector with a 50mm^2 tungsten filament operated at 10 – 15 kV. High-resolution transmission electron microscopy (HR-TEM) was done using a JEOL JEM-2010.

X-Ray diffraction (XRD): X-ray diffractograms were acquired in Bragg–Brentano geometry using a Bruker Discover D8 apparatus, equipped with a Cu anode (1.54 Å) and a LynxEye XE-T detector, over a 2θ range from 5° to 70° with a step size of 0.02°.

Grazing Incident X-ray diffraction (GIXRD) was conducting on a 5-circle diffractometer (Rigaku SmartLab) with Cu K_alpha radiation from a rotating anode and a NaI scintillation detector. The grazing incidence was kept constant at 0.5° during the scans, over a 2θ range from 10° to 65.°

Raman spectroscopy was conducted on a LabRam HR 800 Horiba-Jobin Yvon spectrometer with green wavelength at 514.5 nm: grid with 600 lines or 1800 lines per mm, objective x50 uis2 (NA 0,75), x100 uis2 (NA 0,9) of Olympus, spot size of [1-2] µm analysed.

Photoelectrochemical performances: The PEC performance of $BiVO_4$ photoanodes was checked performed with an AMETEK Solartron Analytical Modulab potentiostat coupled with a Newport Xenon lamp in a 1 M potassium phosphate buffer (pH 6) conducting linear sweep voltammetry (LSV) under AM 1.5 G illumination (100 mW cm^{-2}) under front side (through the film/ interface) with a reference electrode ($E^0_{Ag/AgCl}$ = 0.197 V vs. RHE) and a platinum enrolled wire as a counter electrode and 10 mV s^{-1}scan rate. All current density curves were referenced to the reversible hydrogen electrode (RHE), using the Nernstian relation of:

$$VRHE = E\ vs\ Ag/AgCl + 0.197 + 0.059 \times pH$$

Chronoamperometry measurement under alternative irradiation of 90 s was performed using the potentiostatic mode at a fixed potential of 1.23 V_{RHE}. The geometric active area of the $BiVO_4$, working electrode, was defined by Hi-Bond polyamide scotch tape (HB830-19) and measured 0.28 cm^2. Electrical contacts were made by conductive copper scotch (3M Scotch 1245) which was adhered directly to the FTO exposed portion of the photoelectrode.

Ellipsometry: Ellipsometry was performed on a J;A Woollam Ellipsometer for the overall thickness and the band-gap (Eg) determination of photoanodes and for the thickness determination of TiO_2 deposited by sol-gel / dip-coating technique on silicon wafers. As it is very thin, the thickness of the SiO_2 layer after calcination on the uncoated part of the wafer is measured for each sample before measuring the TiO_2 thickness. The model used for the fit is a Cauchy. $BiVO_4$-based photoanode band-gap determined by ellipsometry was measured from the extinction coefficient k by applying the Tauc-Plot methodology.[32] The model used is a Gen-Osc, and fits to be the closest of the experimental curves “psy” and “delta”. The fitted curves and parameters (MSE, Roughness, Thickness, refractive index n) are detailed in the supporting information.

UV/visible light absorption measurements were performed with an Agilent Technologies Cary Series 5000 UV/visible/near-infrared spectrometer using a double beam with a background of FTO defined to determine the band-gap (Eg) of 10 nm TiO_2 deposited by ALD using a direct Tauc-Plot calculation.

X-ray reflectivity (XRR) using a PANalytical Empyrean equipment using Cu Kα radiations was employed to determine TiO_2 thin films thickness deposited by ALD on silicon wafers.

3. Results and Discussion

a. TiO_2 deposited by ALD characterization

ALD is an interesting technique of deposition for a well and homogeneous surface covering from very thin to thick films.[33] Two thicknesses were generated by ALD on $BiVO_4$ – based photoanodes:15 nm and 10 nm, estimated from XRR. Description of the samples are summarized in Table 1. The typical pristine $BiVO_4$ surface and cross-section imaging are presented in Figure S3. First, $BiVO_4$ film after calcination for 1 h at 450°C is dense and homogeneous showing a very good particle/particle contact. After the deposition of TiO_2, some nanometric defects as white dots appear on the surface (Figure 1). These defects are distributed over the entire surface for the 15 nm TiO_2 deposit (Figure 1.a) but appear to be more localized with the 10 nm TiO_2 deposit (Figure 1.b). Elemental FEG-SEM EDX analysis of portions of homogeneous surfaces on the ALD-10-TiO_2/$BiVO_4$ sample (with 10 nm TiO_2) certifies the presence of Ti with an atomic % of Ti atoms of 1.4 at%, Bi and V atoms of 3 at% and 3.5 at%, respectively, according to the spectra in Figure S4. The surface is well-covered for 10 nm also, as attended when ALD is employed.

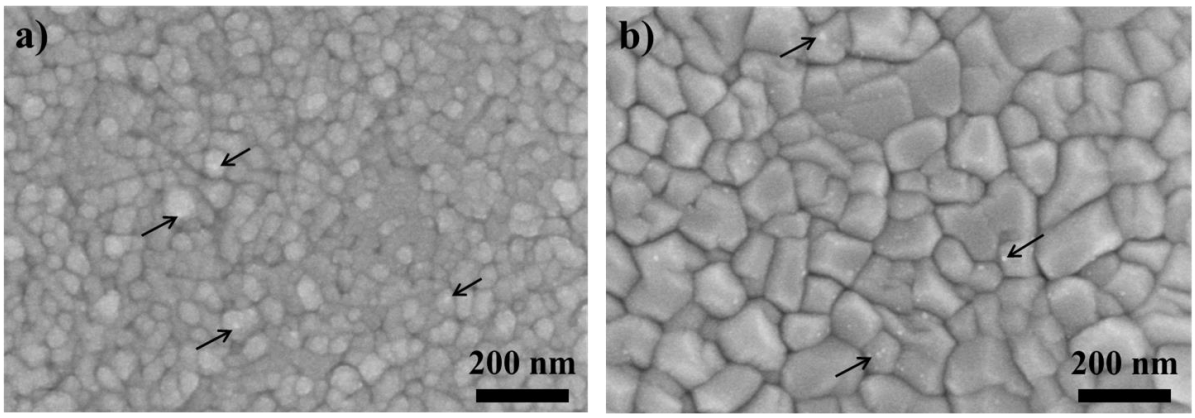

Figure 1: FEG-SEM surface imaging after TiO_2 deposition by ALD a) ALD-15-TiO_2/$BiVO_4$ and b) ALD-10-TiO_2/$BiVO_4$. Some TiO_2 larger nanoparticles are spotted by arrows.

From UV-vis spectra (Figure S6), the band-gap is estimated as 2.52 eV for ALD-15-TiO_2/$BiVO_4$ (Figure S5) and 2.63 eV for both 10 nm thick TiO_2 references: $BiVO_4$ (60 nm) and Mo:$BiVO_4$ (60 nm). As GIXRD identifies only the electrode surface (Figure 2.a), it is then possible to identify the crystalline structure of the thin films deposited on the $BiVO_4$ surface. The presence of a TiO_2 crystalline phase was only observed for ALD-15-TiO_2/$BiVO_4$. In Figure 2.a, the presence of a slight bump at 25° corresponds to the most intense peak of TiO_2 in anatase polymorph (101) at $2\theta = 25.3°$. The $BiVO_4$ underlayer is crystalized in both the tetragonal scheelite and monoclinic scheelite polymorphs. Their contributions are visible at 35° and 47° in 2θ. Raman spectroscopy (Figure 2.b) onto the surface of ALD-15-TiO_2/$BiVO_4$ shows the characteristic band of anatase at 142 cm^{-1} in addition to the $BiVO_4$ band at 122 cm^{-1}. It confirms the presence of TiO_2-Anatase detected by GIXRD. However, the failure to detect a crystalline structure on ALD-10-TiO_2/$BiVO_4$ highlights the amorphous nature of the film. An ALD-10-TiO_2/Mo:$BiVO_4$ sample was then annealed at 450 °C for 2 h in air to force the TiO_2 crystallisation. After this annealing post-treatment, a peak at 143 cm^{-1} appeared in Raman spectroscopy (Figure 2.c), confirming the crystallization of TiO_2 into anatase.

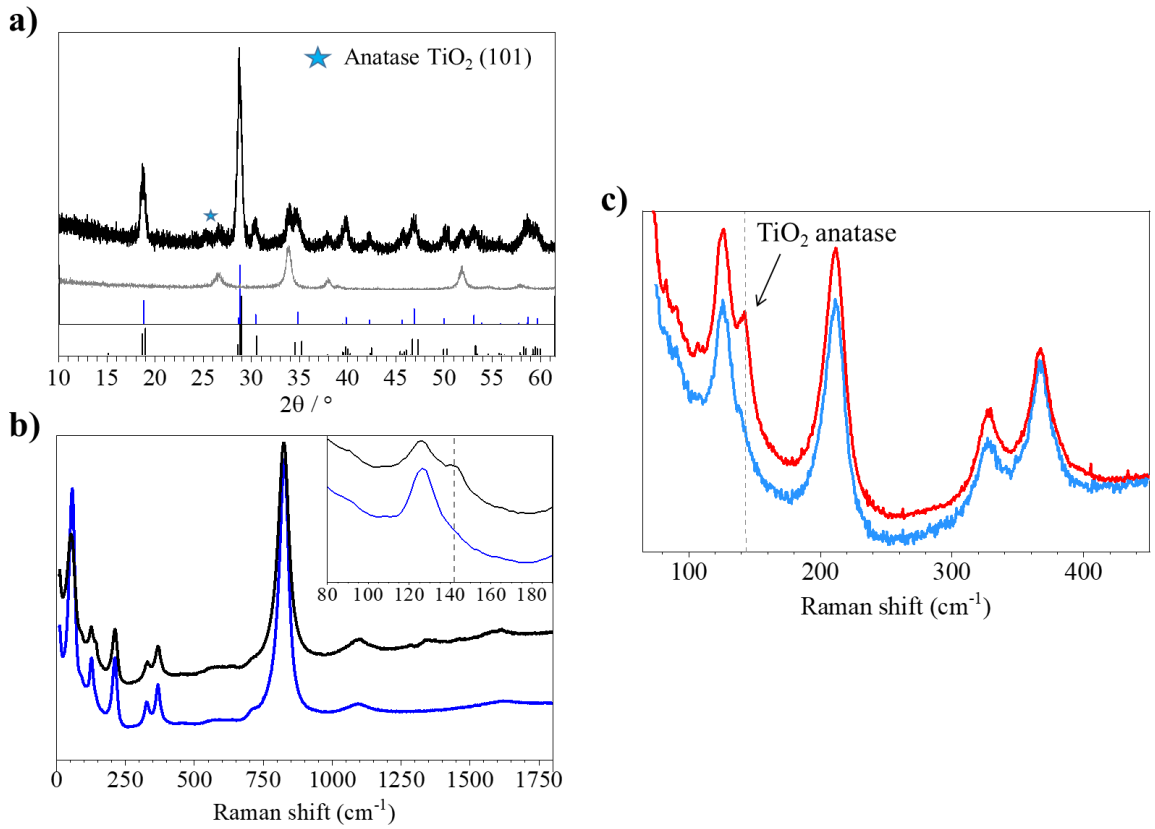

Figure 2: GIXRD pattern of black curve ALD-15-TiO_2/$BiVO_4$, grey curve annealed FTO substrate, blue straight-line PDF-04-010-5710 $BiVO_4$ tetragonal scheelite and black straight-line PDF-04-010-5713 $BiVO_4$ monoclinic scheelite, c) Raman spectroscopy of pristine $BiVO_4$ (in blue) and $BiVO_4$/TiO_2 15 nm (in black), d) Raman spectroscopy of pristine Mo:$BiVO_4$ (in light blue) and ALD-10-TiO_2/Mo:$BiVO_4$ calcinated 2 h at 450 °C (in red).

These results indicate that a maximum thickness of 15 nm must be reached to crystallise TiO_2 by ALD, without the need for annealing post-treatment. Below this threshold, thermal post-treatment becomes mandatory to obtain thin crystalline TiO_2 films.

b. TiO_2 deposited by sol-gel / dip-coating

The fabrication of TiO_2 by Sol-Gel chemistry coupled with the dip-coating deposition process is an easy way and well-known method developed by J. Sum *et al.*[29] A primary study of the thickness obtained as function of the withdrawal speed on silicon substrates is summarized in Figure 3.a. It was necessary to selection the two dip-coating deposition rate of 2.5 mm s^{-1} and 0.8 mm s^{-1} for TiO_2 deposition onto Mo:$BiVO_4$ (110 nm) photoanodes (table 1). These two rates allow to compare the passivating performances of a 5 nm and a 3 nm TiO_2 thick films (Table S7).

The thin 5 nm layer of TiO_2 deposited on a silicon wafer was observed by SEM-FEG surface imaging (Figure 3.b) and complementary EDX analysis revealed the presence of 2.64 at% Ti. A limitation of detection in Raman spectroscopy for ultrathin TiO_2 layers (~ 2- 3 nm) was observed on samples realised on a silicon wafer substrate. To avoid this limitation, a 3rd electrode, Dip-3-TiO_2/Mo:$BiVO_4$ with an average thickness of 5 nm was made, see Table S7. In this sample, after calcination, the presence of anatase TiO_2 crystallized was confirmed because of the appearance of a peak at 144 cm^{-1} (Figure 3.c).

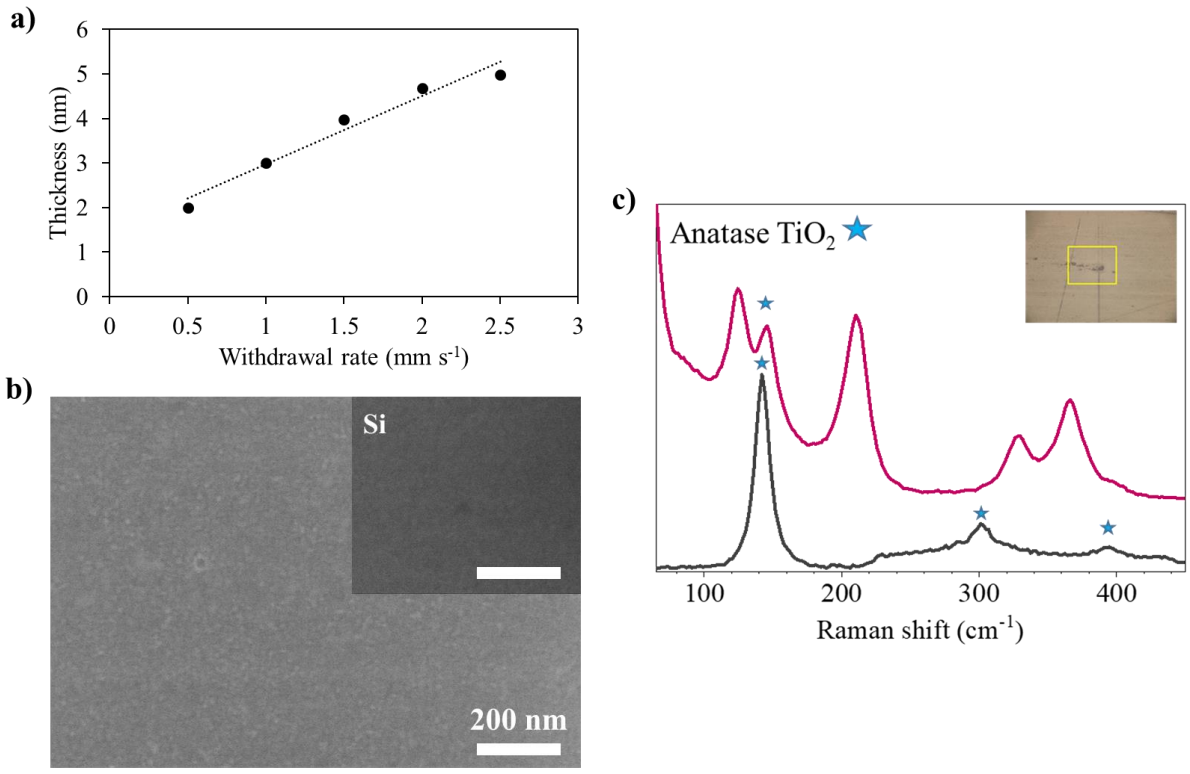

Figure 3: a) TiO_2 thickness measured by ellipsometry plotted in function of the withdrawal rate. The films are made on Si substrate in 1 layer by dip-coating, b) FEG-SEM surface imaging of 5 nm TiO_2 deposited by dip-coating on Si substrate, c) Raman spectroscopy of TiO_2 ~ 50 nm deposited on Si (black curve) as reference for Dip-3-TiO_2/Mo:$BiVO_4$ (in pink)

4. TiO_2 passivating performance evaluation on PEC water-oxidation

a. TiO_2 deposited by ALD

Photoelectrochemical measurements were performed in a 1 M potassium phosphate buffer (pH 6) with direct illumination of the photoanode surface. Linear sweep voltammetry result for pristine $BiVO_4$ shows an onset potential at 0.7 V_{RHE} under illumination (100 mW cm^{-2}) and a photocurrent of ~ 0.7 mA cm^{-2} at 1.23 V_{RHE} (Figure 4.a). Chronoamperometric measurements were measured at a fixed potential with chopped simulated illumination of 90 s. In figure 4.b, the decrease in photocurrent density during the chronoamperometric measurement is evidence of the instability of the pristine $BiVO_4$ photoanode over time. Moreover, the signal indicates electron-hole pairs recombination with the presence of a sharp peak at the beginning of each 90 s illumination After 15 nm TiO_2 deposition by ALD, the evolution of the photocurrent density measured under dark and light conditions are similar (Figure 4.c). Chronoamperometric measurement is realised at 1.76 V_{RHE} which corresponds to the onset potential measured in the linear sweep voltage curve (Figure 4.d). This ensured to measure a photocurrent density with the lowest bias regarding to water oxidation potential of 1.23 $V_{RHE.}$ As expected, the photocurrent density value at 1.76 V_{RHE} is low (~0.015 mA cm^{-2}) compared to the one measured on the pristine photoanode (Figure 4.d). The significant reduction in photocurrent density is attributed to the TiO_2 layer and may be related to its thickness, thus preventing the majority of photogenerated holes from reacting with the electrolyte solution. Interestingly, despite the very low photocurrent density, its constant stability over time and the disappearance of the sharp peak in Figure 4.d suggest the promising advantages of adding TiO_2 as a passivation layer to improve electrode durability.

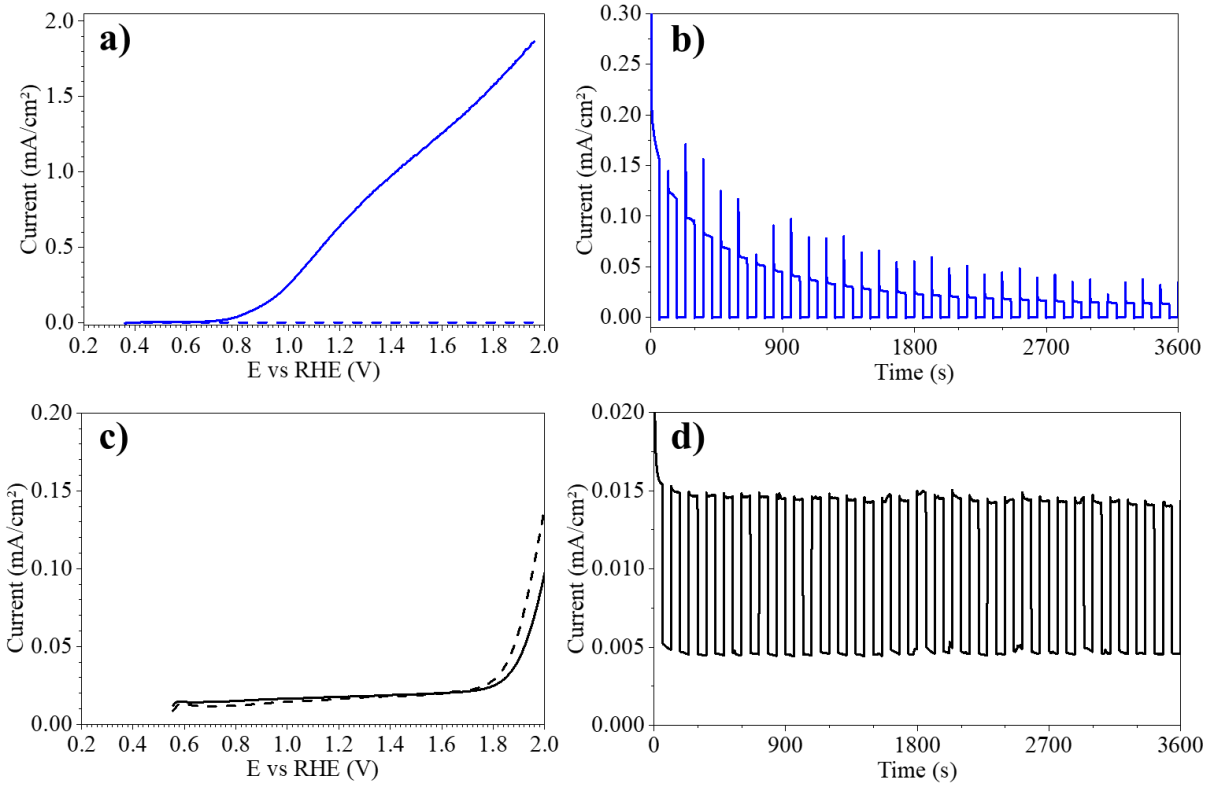

Figure 4: Photoelectrochemical measurements in 1M potassium phosphate buffer (pH 6) under 100 mW cm^{-2} with Linear voltage sweeps measured at a) pristine $BiVO_4$ (60 nm) thin films (blue) b) ALD-15-TiO_2/$BiVO_4$; Chronoamperometric measurements with chopped on/off irradiation of 90 s during 1 h at c) pristine $BiVO_4$ (60 nm) at 1.23 V_{RHE} and d)) ALD-15-TiO_2/$BiVO_4$ at 1.76 V_{RHE}.

In Figure 5, FEG-SEM imaging of post-mortem photoanodes reveals photocorrosion of pure $BiVO_4$: a reduction in thickness is observed with the deposition of larger particles on the surface. These secondary products may correspond to $BiPO_4$, as detailed in the literature (Figure 5.a,b).[34] In contrast, the surface and cross-section imaging of the ALD-15-TiO_2/$BiVO_4$ electrode is identical to that before PEC analysis, confirming the benefit of a crystalline TiO_2 layer against photocorrosion. (Figure 5.c,d).

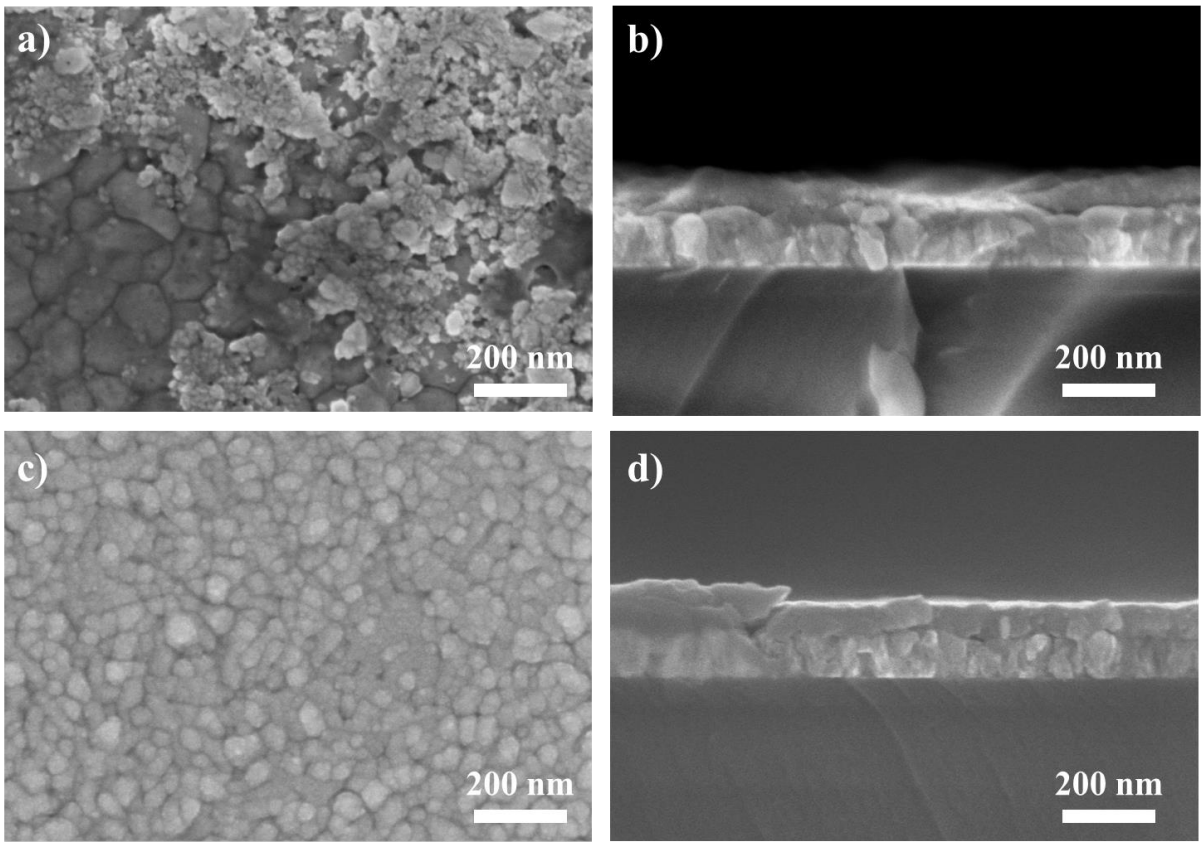

Figure 5: Post-Mortem FEG-SEM imaging after photoelectrochemical analysis of a) typical pristine $BiVO_4$ (60 nm) surface, b) cross-section of pristine $BiVO_4$ (60 nm), c) ALD-15-TiO_2/$BiVO_4$ surface, d) ALD-15-TiO_2/$BiVO_4$ cross-section.

In order to minimise the reduction in photocurrent density, the thickness of the protective layer was reduced to 10 nm and was applied on two samples. The impact of crystallinity on the passivation properties and OER efficiency is compared. PEC analysis on ALD-10-TiO_2/$BiVO_4$ with amorphous TiO_2 reveals an onset potential of 0.7 V_{RHE}, identical to the one observed for pristine $BiVO_4$ (60 nm) (Figure 6.a). Nevertheless, the photocurrent density at 1.23 V_{RHE} remains extremely low with a value of 0.014 mA cm^{-2}. In Figure 6.b, the chronoamperometric measurement shows a sharp recombination peak at each cycle of illumination and a decrease in time of the photocurrent density value (value read at the plateau). This means that the amorphous TiO_2 layer fails to efficiently passivate the surface, preventing a significant number of holes from reacting with the electrolyte buffer. For the sample ALD-10-TiO_2/Mo:$BiVO_4$ calcinated during 2 h at 450°C, a better photocurrent stability over time is observed on the chronoamperometric curve. An average value of 0.06 mA cm^{-2} is measured with a loss of 0.02 mA cm^{-2} corresponding to the recombination peak (see Figure 6.c). The photocurrent density appears stable for 1 h. This new photocurrent density value obtained after annealing

post-treatment, is more than 4-times higher than before annealing. In comparison (Figure S8.a), pristine Mo:$BiVO_4$ (60 nm) gave a photocurrent density of 1.23 mA cm^{-2} at 1.23 V_{RHE} which is 20 times higher than the one measured on annealed ALD-10-TiO_2/Mo:$BiVO_4$. However, the following chronoamperometric measurement revealed a very rapid decrease in electrode efficiency with a photocurrent density ranging from 0.25 mA cm^{-2} to 5 µA cm^{-2} after 1 h (Figure S8.b). These results demonstrate that a good crystallinity is required to passivate the surface of the electrode and allow reactions between the positive charge carrier and the electrolyte.

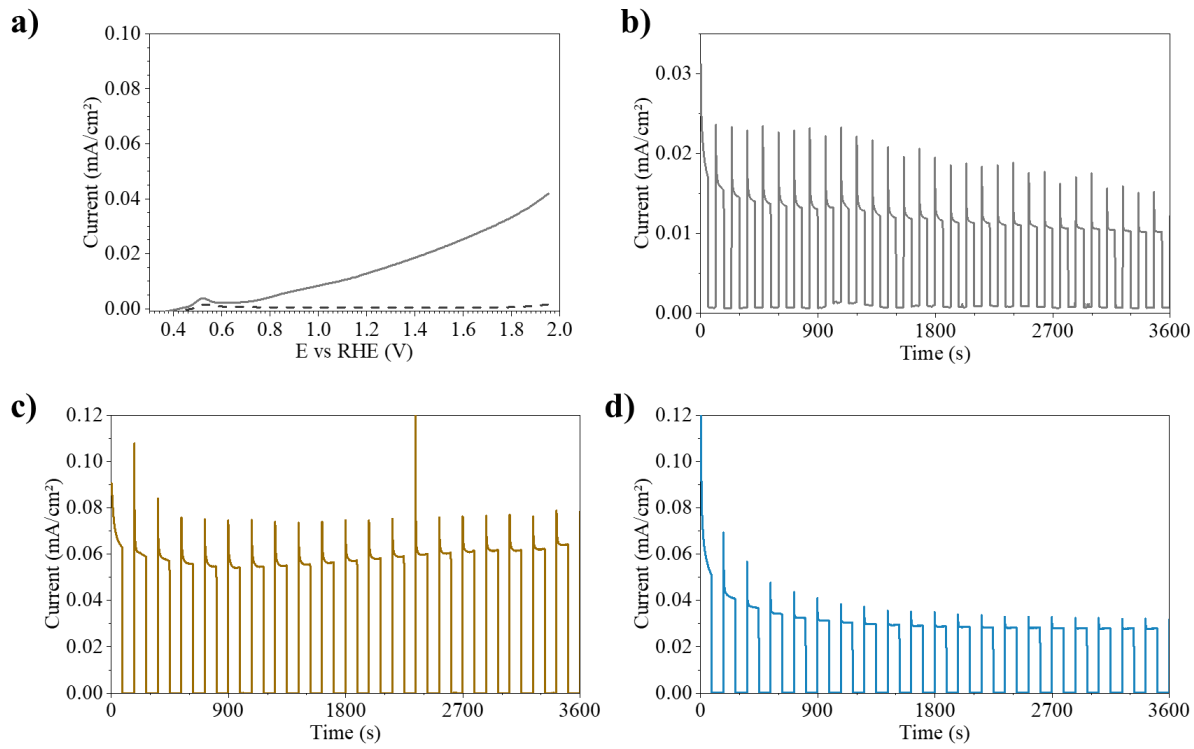

Figure 6: Photoelectrochemical measurements in 1M potassium phosphate buffer (pH 6) under 100 mW cm^{-2} a) Linear voltage sweeps measured at ALD-10-TiO_2/$BiVO_4$ photoanode (grey); Chronoamperometric measurements with chopped on/off irradiation of 90 s during 1 h at 1.23 V_{RHE} on b) ALD-10-TiO_2/$BiVO_4$, c) ALD-10-TiO_2/Mo:$BiVO_4$ annealed 2 h at 450°C, d) ALD-10-TiO_2/Mo:$BiVO_4$ annealed 3 h at 450°C.

An additional hour of calcination at 450°C was applied to ALD-10-TiO_2/Mo:$BiVO_4$ to see if the overall crystallinity could be improved, particularly in cases where amorphous TiO_2 coexists with crystalline anatase TiO_2. In Figure 6.d, the photocurrent shows greater stability, maintaining an average value of 0.03 mA cm^{-2} at the plateau. The recombination peaks are half a large as those previously observed. Unfortunately, with the annealing post-treatment, the increased resistivity of the FTO/glass substrate must be considered in the PEC performance of

the photoanode. An increase of 100 Ω h^{-1} at 450 °C was measured on the commercial FTO/glass substrate used. The increase in the resistivity impacts the value of the photocurrent density. However, the recombination peak reduction can be attributed to a general improvement in the crystallinity of the photoanode enhancing charge transfer.

Post-mortem FEG-SEM surface imaging of ALD-10-TiO_2/$BiVO_4$ annealed during 3 h at 450 °C is presented in Figure 7. These images show incomplete protection of the photoanode against photocorrosion, as pores have developed on the electrode surface in specific areas (Figure 7.a). This favours the penetration of the electrolyte into the bulk and contributes to the degradation of the photoanode, as shown by the presence of transverse pores throughout the film. (Figure 7.d).

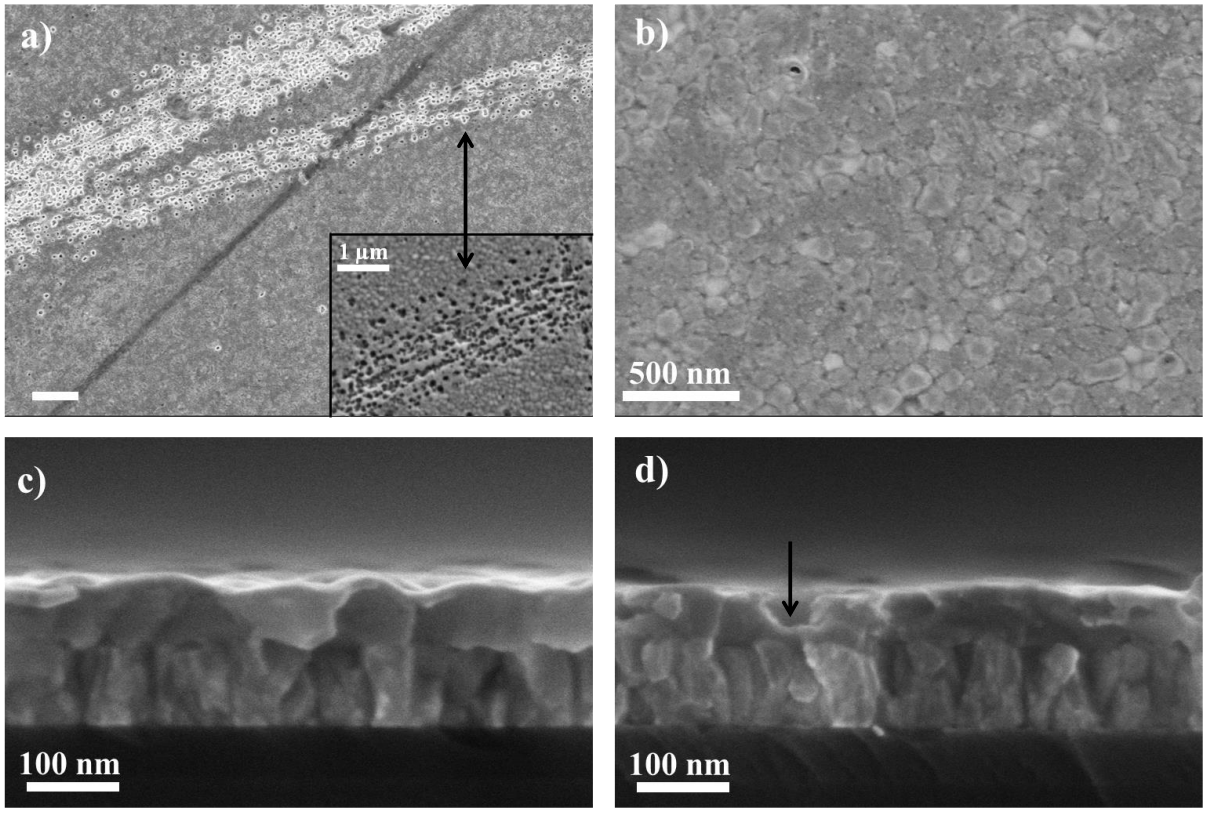

Figure 7: Post-mortem FEG-SEM imaging of ALD-10-TiO_2/Mo:$BiVO_4$ after 3 h of annealing at 450°C, with a), b) surface imaging; and cross-section c) before, d) after PEC performances measurements. The arrows show pores generated in the film.

These results demonstrate the importance of both the thickness and high crystallinity of the TiO_2 layer to improve its passivating property and limit the energy loss caused by recombination phenomena. However, below 15 nm, TiO_2 deposited by ALD requires annealing post-processing, which affects the substrate and doesn't sufficiently improve the efficiency of the

photoanode. Also, a possible alteration of the TiO_2 film deposited by ALD caused by the annealing post-treatment could generate pores that exposed the photoactive $BiVO_4$ underlayer to photocorrosion.

b. TiO_2 deposited by sol-gel / dip-coating

Figure 8 presents the linear voltage sweeps and chronoamperometric measurements of the Dip-1-TiO_2/Mo:$BiVO_4$ with 5 nm TiO_2 passivation layer and Dip-2-TiO_2/Mo:$BiVO_4$ with 3 nm of TiO_2 passivation layer deposited in one dip and two dips, respectively. In both cases, the linear voltage sweeps exhibit quasi-identical photocurrent density at 1.23 V_{RHE} of 0.42 mA cm^{-2} for Dip-1-TiO_2/Mo:$BiVO_4$ and 0.43 mA cm^{-2} for Dip-2-TiO_2/Mo:$BiVO_4$. Compared to the 1.19 mA cm^{-2} for Mo:$BiVO_4$ (110 nm) electrode, the decrease of photocurrent density is only 2.76-times smaller. It is a significant improvement in the limitation of the loss in photocurrent density looking at the important decrease for ALD-10-TiO_2/Mo:$BiVO_4$, 20-times lower than the reference. According to chronoamperometric measurements, the sample containing 3 nm of TiO_2 deposited in two layers (Figure 8.d) shows the best stability, with only one residual recombination peak. Its average photocurrent density value at the plateau corresponds to ~ 0.3 mA cm^{-2}, an improvement of 0.1 mA cm^{-2} compared to the 5 nm thick TiO_2 sample (Figure 8.c).

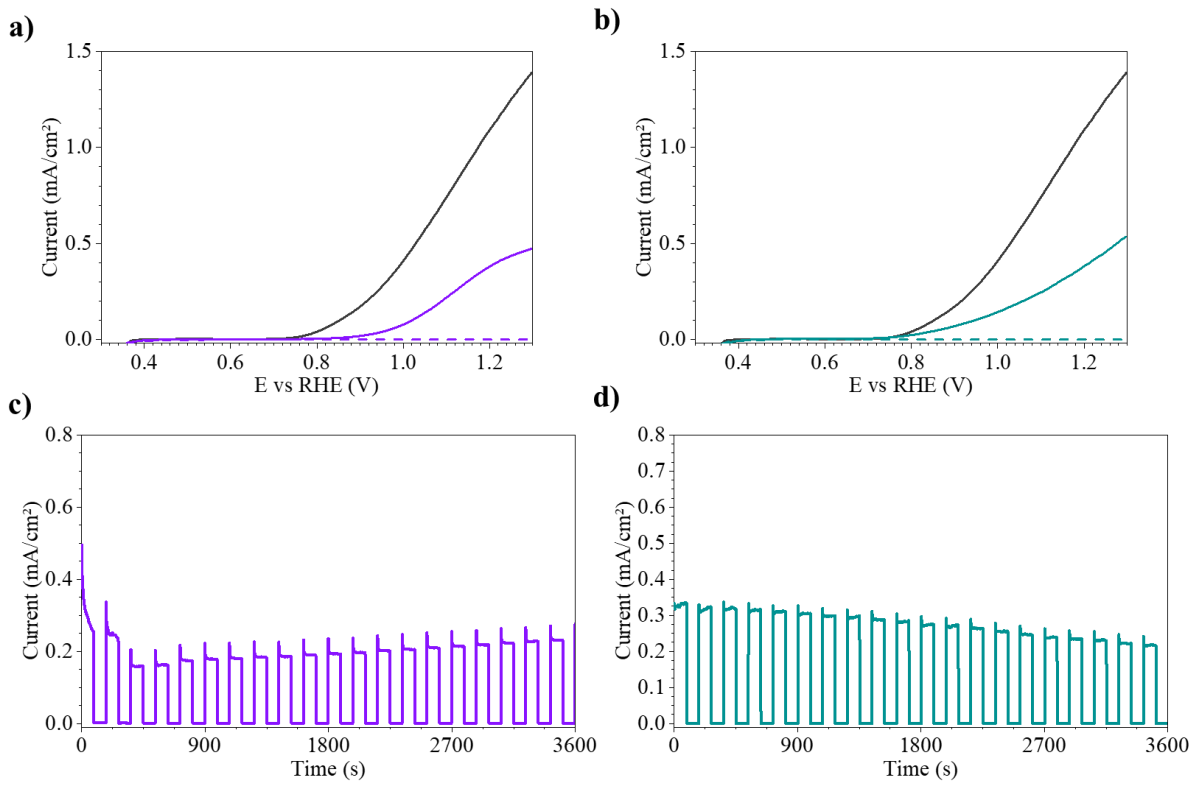

Figure 8: Photoelectrochemical measurements in 1M potassium phosphate buffer (pH 6) under 100 mW cm^{-2}. Linear voltage sweeps measured at Mo:$BiVO_4$ (110 nm) reference photoanode in grey a) Dip-1-TiO_2/Mo:$BiVO_4$ (5 nm) in violet, b) Dip-2-TiO_2/Mo:$BiVO_4$ (3 nm) in blue; Chronoamperometric measurements with chopped on/off irradiation of 90 s during 1 h at 1.23 V_{RHE} on c) Dip-1-TiO_2/Mo:$BiVO_4$ (5 nm) in violet, d) Dip-2-TiO_2/Mo:$BiVO_4$ (3 nm) in blue.

In Figure 9, imaging of the Dip-2-TiO_2/Mo:$BiVO_4$ surface (3 nm) after PEC measurement for2 h 30 ~ 3 h reveals a sharper surface with a darker area in the particle/particle contact region than before PEC testing. Analysis of the cross-section shows a slight reduction in thickness and the presence of a few larger particles on the surface. These could be attributed to the generation of phosphate components. Nevertheless, the film remains dense and free of any photocorrosion induced porosity.

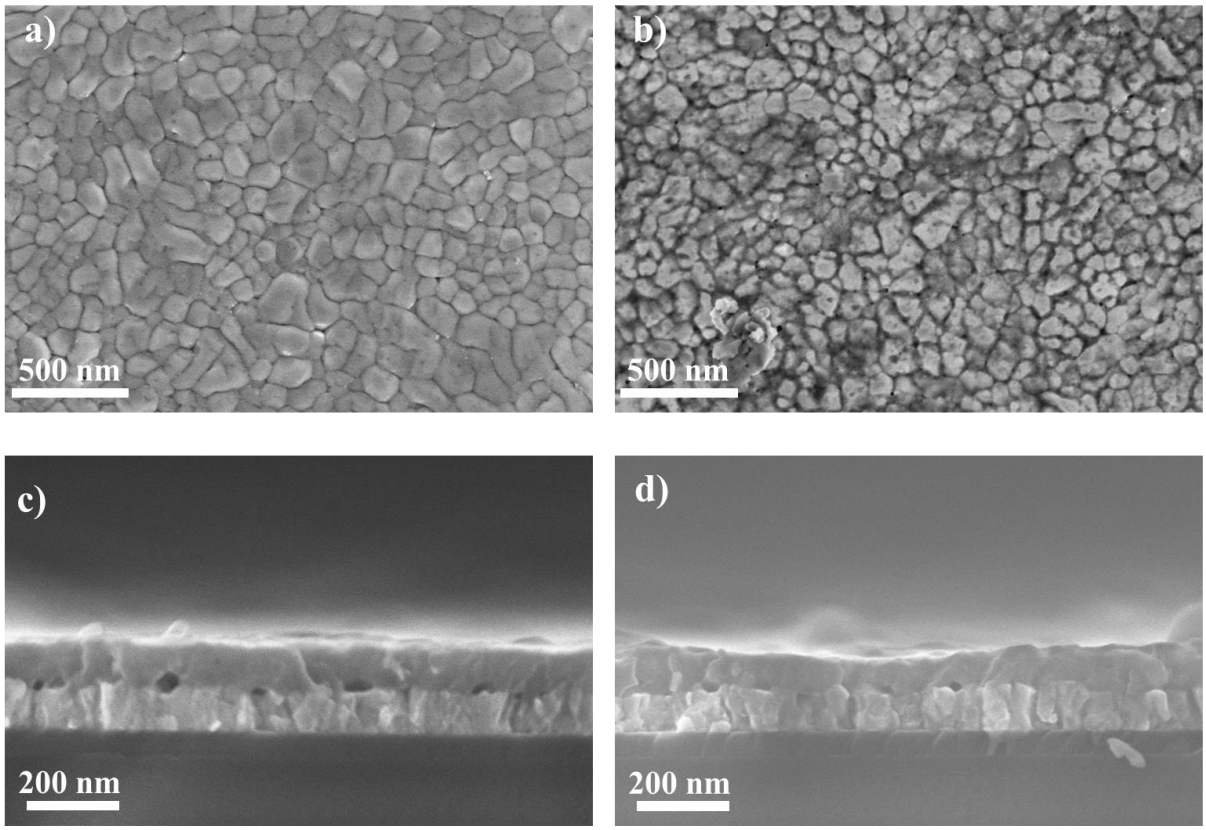

Figure 9: FEG-SEM surface imaging of Dip-2-TiO_2/Mo:$BiVO_4$ a) before PEC measurements b) after PEC measurements; FEG-SEM cross-section imaging of Dip-2-TiO_2/Mo:$BiVO_4$ a) before PEC measurements b) after PEC measurement.

5. Conclusion

To summarize, the PEC performances measured under acidic conditions revealed key parameters for the protection of $BiVO_4$ by TiO_2. Two different processing techniques have been used to synthesize TiO_2, ALD and sol-gel coupled with dip-coating.

Importantly, a highly crystalline TiO_2 layer is needed to protect $BiVO_4$-based photoanodes. However, by ALD, crystalline TiO_2 films are generally obtained at a thickness of 15 nm. At this thickness, the efficiency of OER is extremely low because holes generated from light absorption are mostly blocked at the interface between $BiVO_4$ and TiO_2. The thickness is too wide, allowing only a small number of holes to react with the electrolyte for the OER reaction. Below 15 nm, an annealing post-treatment of at least 2 hours at 450 °C improves crystallinity, but not enough to prevent photocorrosion and side reactions generating porosity in the film. To address this, we have developed an efficient and cost-effective process for depositing TiO_2 protection using sol-gel chemistry and dip-coating. A 3 nm thin TiO_2 layer is easily obtained with good crystallinity in the anatase structure. This layer exhibits a stable photocurrent of ~ 0.3 mA cm^{-2} obtained for 1 hour at 1.23 V_{RHE}. Post-mortem analysis confirms the effective passivation properties of the thin TiO_2 layer deposited by dip-coating, with the absence of porosity and better thickness retention.

6. References

(1) Jiang, C.; Moniz, S. J. A.; Wang, A.; Zhang, T.; Tang, J. Photoelectrochemical Devices for Solar Water Splitting-Materials and Challenges. *Chem. Soc. Rev*. 2017, pp 4645–4660. https://doi.org/10.1039/c6cs00306k.

(2) Amano, F. Photoelectrochemical Oxygen Evolution. In *Solar-to-Chemical Conversion: Photocatalytic and Photoelectrochemical Processes*; Wiley, 2021; pp 163–187. https://doi.org/10.1002/9783527825073.ch7.

(3) Prévot, M. S.; Sivula, K. Photoelectrochemical Tandem Cells for Solar Water Splitting. *Am. Chem. Soc.* **2013**, *117*, 17879–17893. https://doi.org/dx.doi.org/10.1021/jp405291g.

(4) Kim, J. H.; Lee, J. S. Elaborately Modified $BiVO_4$ Photoanodes for Solar Water Splitting. *Advanced Materials*. 2019, pp 1806938 (30)-1806938 (35). https://doi.org/10.1002/adma.201806938.

(5) Tolod, K. R.; Hernández, S.; Russo, N. Recent Advances in the $BiVO_4$ Photocatalyst for Sun-Driven Water Oxidation: Top-Performing Photoanodes and Scale-up Challenges. *Catalysts* **2017**, *7* (1). https://doi.org/10.3390/catal7010013.

(6) Yang, L.; Zhou, H.; Fan, T.; Zhang, D. Semiconductor Photocatalysts for Water Oxidation: Current Status and Challenges. *Physical Chemistry Chemical Physics*. 2014, pp 6810–6826. https://doi.org/10.1039/c4cp00246f.

(7) Park, Y.; Mc Donald, K. J.; Choi, K. S. Progress in Bismuth Vanadate Photoanodes for Use in Solar Water Oxidation. *Chem. Soc. Rev* **2013**, *42* (6), 2321–2337. https://doi.org/10.1039/c2cs35260e.

(8) Rettie, A. J. E.; Lee, H. C.; Marshall, L. G.; Lin, J. F.; Capan, C.; Lindemuth, J.; McCloy, J. S.; Zhou, J.; Bard, A. J.; Mullins, C. B. Combined Charge Carrier Transport and Photoelectrochemical Characterization of $BiVO_4$ Single Crystals: Intrinsic Behavior of a Complex Metal Oxide. *J. Am. Chem. Soc.* **2013**, *135* (30), 11389–11396. https://doi.org/10.1021/ja405550k.

(9) Abdi, F. F.; Van De Krol, R. Nature and Light Dependence of Bulk Recombination in Co-Pi-Catalyzed $BiVO_4$ Photoanodes. *J. Phys. Chem. C* **2012**, *116* (17), 9398–9404. https://doi.org/10.1021/jp3007552.

(10) Tan, H. L.; Amal, R.; Ng, Y. H. Alternative Strategies in Improving the Photocatalytic and Photoelectrochemical Activities of Visible Light-Driven $BiVO_4$: A Review. *J. Mater. Chem. A* **2017**, *5* (32), 16498–16521. https://doi.org/10.1039/c7ta04441k.

(11) Malathi, A.; Madhavan, J.; Ashokkumar, M.; Arunachalam, P. A Review on $BiVO_4$ Photocatalyst: Activity Enhancement Methods for Solar Photocatalytic Applications. *Applied Catalysis A: General*. 2018, pp 47–74. https://doi.org/10.1016/j.apcata.2018.02.010.

(12) Chen, D.; Xie, Z.; Tong, Y.; Huang, Y. Review on $BiVO_4$-Based Photoanodes for Photoelectrochemical Water Oxidation: The Main Influencing Factors. *Energy and Fuels*. 2022, pp 9932–9949. https://doi.org/10.1021/acs.energyfuels.2c02119.

(13) Huang, Z. F.; Pan, L.; Zou, J. J.; Zhang, X.; Wang, L. Nanostructured Bismuth Vanadate-Based Materials for Solar-Energy-Driven Water Oxidation: A Review on Recent Progress. *Nanoscale* **2014**, *6* (23), 14044–14063. https://doi.org/10.1039/c4nr05245e.

(14) Gaikwad, M. A.; Suryawanshi, U. P.; Ghorpade, U. V.; Jang, J. S.; Suryawanshi, M. P.; Kim, J. H. Emerging Surface, Bulk, and Interface Engineering Strategies on $BiVO_4$ for Photoelectrochemical Water Splitting. *Small* **2022**, *18* (10), 1–35. https://doi.org/10.1002/smll.202105084.

(15) Tayebi, M.; Lee, B. K. Recent Advances in $BiVO_4$ Semiconductor Materials for Hydrogen Production Using Photoelectrochemical Water Splitting. *Renew. Sustain. Energy Rev.* **2019**, *111* (May), 332–343. https://doi.org/10.1016/j.rser.2019.05.030.

(16) Siavash Moakhar, R.; Hosseini-Hosseinabad, S. M.; Masudy-Panah, S.; Seza, A.; Jalali, M.; Fallah-Arani, H.; Dabir, F.; Gholipour, S.; Abdi, Y.; Bagheri-Hariri, M.; Riahi-Noori, N.; Lim, Y. F.; Hagfeldt, A.; Saliba, M. Photoelectrochemical Water-Splitting Using CuO-Based Electrodes for Hydrogen Production: A Review. *Advanced Materials*. John Wiley and Sons Inc August 1, 2021, p 2007285. https://doi.org/10.1002/adma.202007285.

(17) Zhang, S.; Rohloff, M.; Kasian, O.; Mingers, A. M.; Mayrhofer, K. J. J.; Fischer, A.; Scheu, C.; Cherevko, S. Dissolution of $BiVO_4$ Photoanodes Revealed by Time-Resolved Measurements under Photoelectrochemical Conditions. *J. Phys. Chem. C* **2019**, *123*, 23410–23418. https://doi.org/10.1021/acs.jpcc.9b07220.

(18) Zhang, S.; Ahmet, I.; Kim, S. H.; Kasian, O.; Mingers, A. M.; Schnell, P.; Kölbach, M.; Lim, J.; Fischer, A.; Mayrhofer, K. J. J.; Cherevko, S.; Gault, B.; Van De Krol, R.; Scheu, C. Different Photostability of $BiVO_4$ in near-PH-Neutral Electrolytes. *ACS Appl. Energy Mater.* **2020**, *3* (10), 9523–9527. https://doi.org/10.1021/acsaem.0c01904.

(19) Walter, M. G.; Warren, E. L.; McKone, J. R.; Boettcher, S. W.; Mi, Q.; Santori, E. A.; Lewis, N. S. Solar Water Splitting Cells. *Chem. Rev.* **2010**, *110* (11), 6446–6473. https://doi.org/10.1021/cr1002326.

(20) Xie, J.; Guo, C.; Yang, P.; Wang, X.; Liu, D.; Li, C. M. Bi-Functional Ferroelectric $BiFeO_3$ Passivated $BiVO_4$ Photoanode for Efficient and Stable Solar Water Oxidation. *Nano Energy* **2017**, *31*, 28–36. https://doi.org/10.1016/j.nanoen.2016.10.048.

(21) Usman, E.; Barzgar Vishlaghi, M.; Kahraman, A.; Solati, N.; Kaya, S. Modifying the Electron-Trapping Process at the $BiVO_4$ Surface States via the TiO_2 Overlayer for Enhanced Water Oxidation. *ACS Appl. Mater. Interfaces* **2021**, *13* (50), 60602–60611. https://doi.org/10.1021/acsami.1c16847.

(22) Wan, X.; Xu, Y.; Wang, X.; Guan, X.; Fu, Y.; Hu, C.; Hu, H.; Rong, N. Atomic Layer Deposition Assisted Surface Passivation on Bismuth Vanadate Photoanodes for Enhanced Solar Water Oxidation. *Appl. Surf. Sci.* **2022**, *573*, 151492. https://doi.org/10.1016/j.apsusc.2021.151492.

(23) Liu, R.; Zheng, Z.; Spurgeon, J.; Yang, X. Enhanced Photoelectrochemical Water-Splitting Performance of Semiconductors by Surface Passivation Layers. *Energy and Environmental Science*. 2014, pp 2504–2517. https://doi.org/10.1039/c4ee00450g.

(24) Zhong, M.; Hisatomi, T.; Kuang, Y.; Zhao, J.; Liu, M.; Iwase, A.; Jia, Q.; Nishiyama, H.; Minegishi, T.; Nakabayashi, M.; Shibata, N.; Niishiro, R.; Katayama, C.; Shibano, H.; Katayama, M.; Kudo, A.; Yamada, T.; Domen, K. Surface Modification of CoOx Loaded $BiVO_4$ Photoanodes with Ultrathin p-Type NiO Layers for Improved Solar Water Oxidation. *J. Am. Chem. Soc.* **2015**, *137* (15), 5053–5060. https://doi.org/10.1021/jacs.5b00256.

(25) Ma, Z.; Song, K.; Wang, L.; Gao, F.; Tang, B.; Hou, H.; Yang, W. $WO_3/BiVO_4$ Type-II Heterojunction Arrays Decorated with Oxygen-Deficient ZnO Passivation Layer A Highly Efficient and Stable Photoanode. *Appl. Mater. Interfaces* **2019**, *11* (1), 889–897. https://doi.org/10.1021/acsami.8b18261.

(26) Pourbaix, M.; Zhang, H.; Pourbaix, A. Presentation of an Atlas of Chemical and Electrochemical Equilibria in the Presence of a Gaseous Phase. *Mater. Sci. Forum* **1997**, *251–254*, 143–148. https://doi.org/10.4028/www.scientific.net/msf.251-254.143.

(27) McDowell, M. T.; Lichterman, M. F.; Spurgeon, J. M.; Hu, S.; Sharp, I. D.; Brunschwig, B. S.; Lewis, N. S. Improved Stability of Polycrystalline Bismuth Vanadate Photoanodes by Use of

Dual-Layer Thin TiO_2/Ni Coatings. *J. Phys. Chem. C* **2014**, *118* (34), 19618–19624. https://doi.org/10.1021/jp506133y.

(28) Lee, D.; Kvit, A.; Choi, K. S. Enabling Solar Water Oxidation by $BiVO_4$ Photoanodes in Basic Media. *Chem. Mater.* **2018**, *30* (14), 4704–4712. https://doi.org/10.1021/.

(29) Sum, J.; Durupthy, O.; Krins, N.; Laberty-Robert, C. Regeneration of Electrocatalyst through Li-Ion Insertion. *J. Electrochem. Soc.* **2022**, *169* (3), 030522. https://doi.org/10.1149/1945-7111/ac5ad4.

(30) Hilliard, S.; Friedrich, D.; Kressman, S.; Strub, H.; Artero, V.; Laberty-Robert, C. Solar-Water-Splitting $BiVO_4$ Thin-Film Photoanodes Prepared By Using a Sol–Gel Dip-Coating Technique. *ChemPhotoChem* **2017**, *1* (6), 273–280. https://doi.org/10.1002/cptc.201700003.

(31) Coutancier, D.; Zhang, S. T.; Bernardini, S.; Fournier, O.; Mathieu-Pennober, T.; Donsanti, F.; Tchernycheva, M.; Foldyna, M.; Schneider, N. ALD of ZnO:Ti: Growth Mechanism and Application as an Efficient Transparent Conductive Oxide in Silicon Nanowire Solar Cells. *ACS Appl. Mater. Interfaces* **2020**, *12*, 21036–21044. https://doi.org/10.1021/acsami.9b22973.

(32) Tauc, J. Optical Properties and Electronic Structure of Amorphous Ge and Si. *Mater. Res. Bull.* **1968**, *3* (1), 37–46. https://doi.org/https://doi.org/10.1016/0025-5408(68)90023-8.

(33) Meng, X.; Wang, X.; Geng, D.; Ozgit-Akgun, C.; Schneider, N.; Elam, J. W. Atomic Layer Deposition for Nanomaterial Synthesis and Functionalization in Energy Technology. *Mater. Horizons* **2017**, *4* (2), 133–154. https://doi.org/10.1039/c6mh00521g.

(34) Favaro, M.; Abdi, F. F.; Lamers, M.; Crumlin, E. J.; Liu, Z.; Van De Krol, R.; Starr, D. E. Light-Induced Surface Reactions at the Bismuth Vanadate/Potassium Phosphate Interface. *J. Phys. Chem. B* **2018**, *122* (2), 801–809. https://doi.org/10.1021/acs.jpcb.7b06942.

Sol-Gel $BiVO_4$ based photoanode with enhanced stability through the deposit of a TiO_2 passivation layer

Supporting Information Chapter II part 2

Table S1: Engagement table for precursor solution of $BiVO_4$ and Mo:$BiVO_4$ photoanode.

Reactant	$BiVO_4$ ~ 60 nm	Mo:$BiVO_4$ ~ 60 nm	Mo:$BiVO_4$ ~ 110 nm
acetylacetone (ACS reagent ≥ 99.0 %)	43.6 mmol	43.6 mmol	130.8 mmol
Acetic acid	9.3 mmol	9.3 mmol	27.9 mmol
bismuth (III) nitrate pentahydrate (ACS reagent ≥ 98.0 %)	0.36 mmol	0.36 mmol	1.08 mmol
vanadium (IV) oxide acetylacetonate	0.36 mmol	0.324 mmol	1.070 mmol
molybdenum (VI) oxide (ACS reagent > 99.0 %)		0.0108 mmol	
molybdenum (VI) dioxide bis(acetylacetone) (ACS reagent ≥ 95.0 %)			0.0107 mmol

Table S2: Dip-coating parameters in function of the synthesis.

parameter	$BiVO_4$ ~ 50 nm	Mo:$BiVO_4$ ~ 50 nm	Mo:$BiVO_4$ ~ 110 nm
V_{out} (mm $s^{-1)}$	0.8 (10 layers)	0.8 (10 layers)	1 (1st layer) 8 (6 layers)
Relative humidity (RH %)	> 3 %	> 3 %	> 5 %

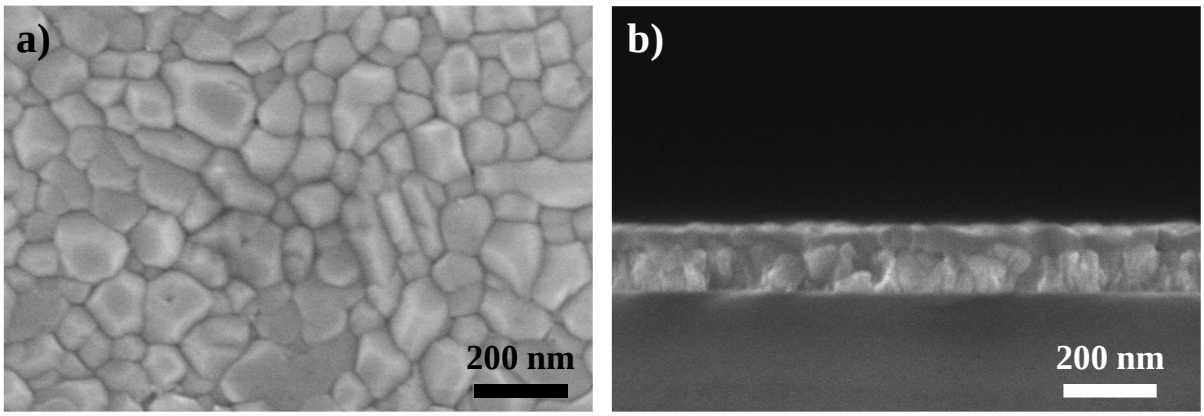

Figure S3: FEG-SEM imaging of a) typical pristine $BiVO_4$ 60 nm surface synthesised by sol-gel/dip-coating process, b) cross-section of pristine $BiVO_4$

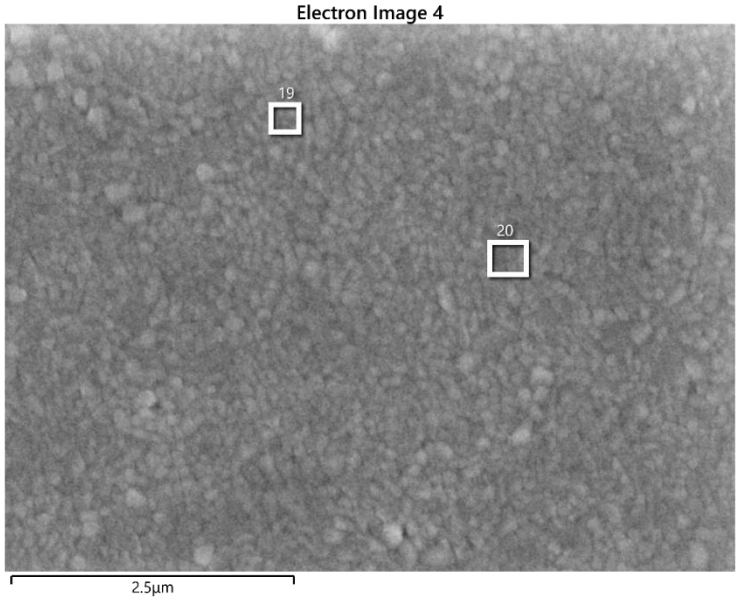

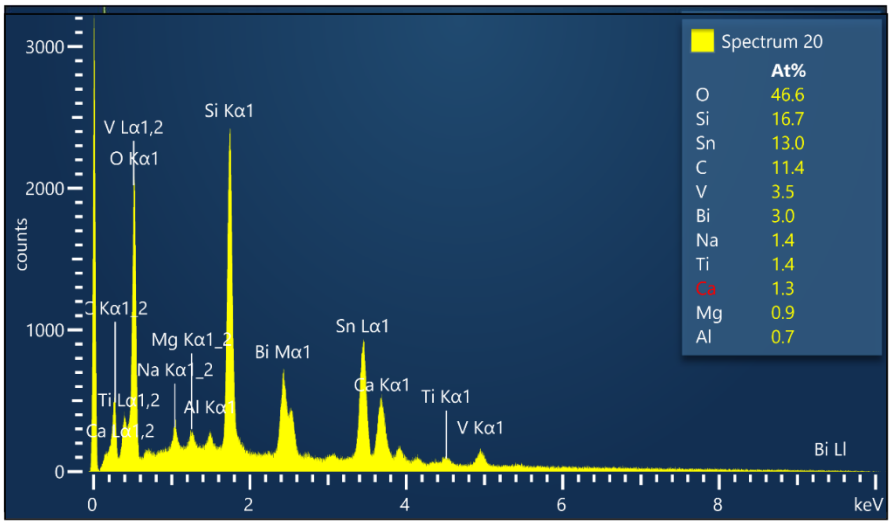

Result Type	Atomic %										
Statistics	C	O	Na	Mg	Al	Si	Ca	**Ti**	**V**	Sn	**Bi**
Max	11.74	48.76	1.57	0.9	0.73	17.56	1.29	**1.46**	**3.58**	13.48	**3.11**
Min	7.85	46.89	1.45	0.89	0.72	17.06	1.2	**1.4**	**3.48**	13.26	**3.01**
Average	9.79	47.83	1.51	0.9	0.73	17.31	1.25	**1.43**	**3.53**	13.37	**3.06**
Standard Deviation	2.75	1.32	0.08	0.01	0.01	0.36	0.06	**0.05**	**0.07**	0.15	**0.07**

Spectrum Label	Spectrum 19	Spectrum 20
C	7.85	11.74
O	48.76	46.89
Na	1.57	1.45
Mg	0.89	0.9
Al	0.73	0.72
Si	17.56	17.06
Ca	1.2	1.29
Ti	**1.46**	**1.4**
V	**3.48**	**3.58**
Sn	13.48	13.26
Bi	**3.01**	**3.11**
Total	100	100

Figure S4: FEG-SEM EDX analysis on $BiVO_4/TIO_2$ 10 nm deposited by ALD. Identification of the atomic percent on two position of the surface spectrum 19 and spectrum 20.

Methodology for band gap determination by ellipsometry

Example of ALD-15-TiO_2/$BiVO_4$

Thickness and Eg can be determined by ellypsometry. The band gap of pure $BiVO_4$ was measured from the extinction coefficient k from the ellipsometry measurement by applying the Tauc-Plot methodology. Models used are the closest of the experimental curves "psy" and "delta". The fitted curves and parameters (MSE, Roughness, Thickness, refractive index n) are detailed below for ALD-15-TiO_2/$BiVO_4$. With the extraction of the "k" parameter for each wavelength we applied a direct Tauc-Plot on the theses value.

With equation (1):

$$hv\ (eV) = \frac{h_{Planck} \times v}{\lambda} \times \frac{1}{e} \qquad (1.a)$$

with: h_{Planck} the constant of Planck (in J.s), v the celerity of light (in nm), λ the wavelength (in nm) and e the elementary charge of a single electron (in Coulombs).

$$hv\ (eV) = \frac{6.626\ e^{34} \times 3\ e^{17}}{\lambda\ (nm)} \times \frac{1}{1.602\ e^{-19}} \qquad (1.b)$$

We transform the wavelength into energy. Then with the formula (3) we obtain an absorbance from the "k" parameter:

$$Abs = \frac{4\ \times \pi \times k}{\lambda\ (nm)} \qquad (2)$$

As $BiVO_4$ is considered a semiconductor with a direct Eg [1] we fitted:

$$(Abs\ \times hv)^2 = f\ (\ hv) \qquad (3)$$

A linear polynomial fit on the linear region of the curves allows us to determine the x-intercept in a typical y = ax + b first-degree polynomial that corresponds to the Eg value.

Nota Bene: For Eg determination from a UV-Visible spectrum, direct Tauc-plot is applied using equations (1.a,b) and (3).

a)

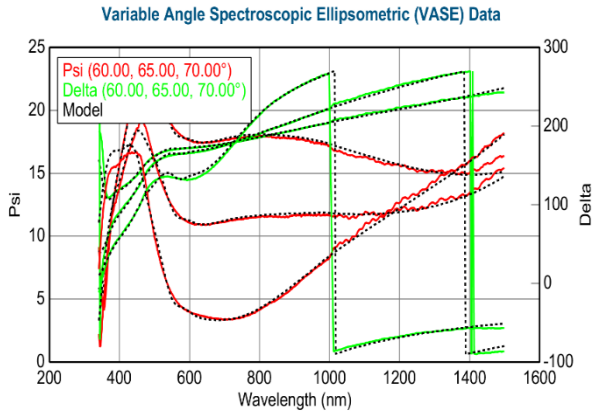

b)

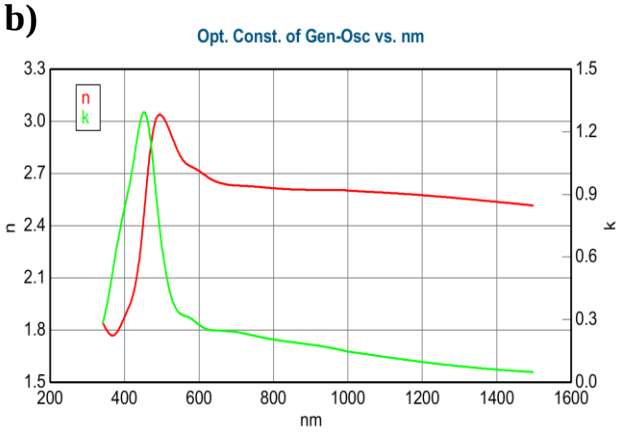

c)

PARAMETER	VALUE	ERROR BAR
MSE	**15.658**	
Thickness # 2 (nm)	**50**	0.075
n of Cauchy Substrate @ 632.8 nm	1.48569	
n sample @ 632.8 nm	2.71	

d)

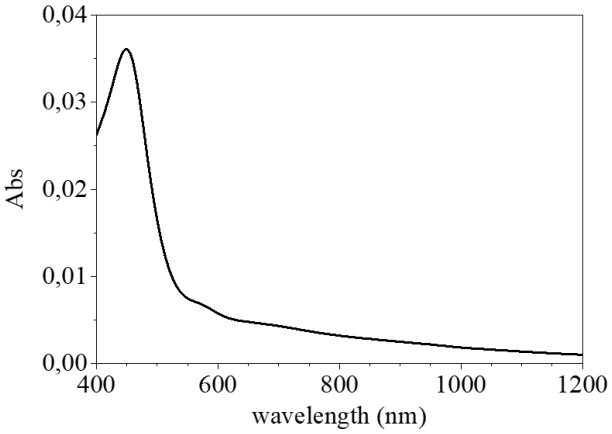

e)

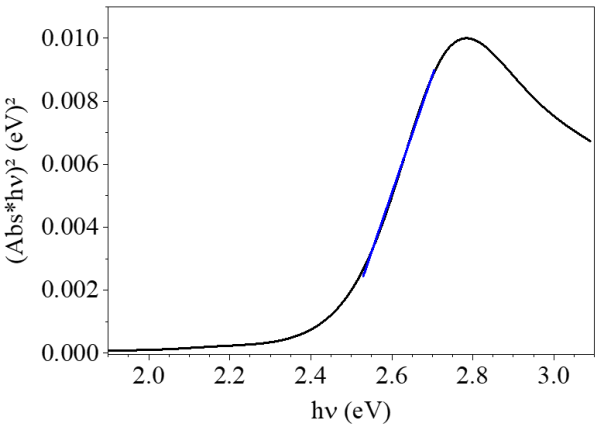

Figure S5: Typical characterization of $BiVO_4/TiO_2$ realised on ALD-15-$TiO_2/BiVO_4$ a) the variable psy and delta measured and the fitting model, b) the refractive "n" and the extinction coefficient "k" in function of the wavelength (nm), c) table regrouping the parameter evaluated, d) Absorbance spectra calculate by ellipsometry, e) ellipsometry bang-gap determination with Tauc-Plot on extinction coefficient k.

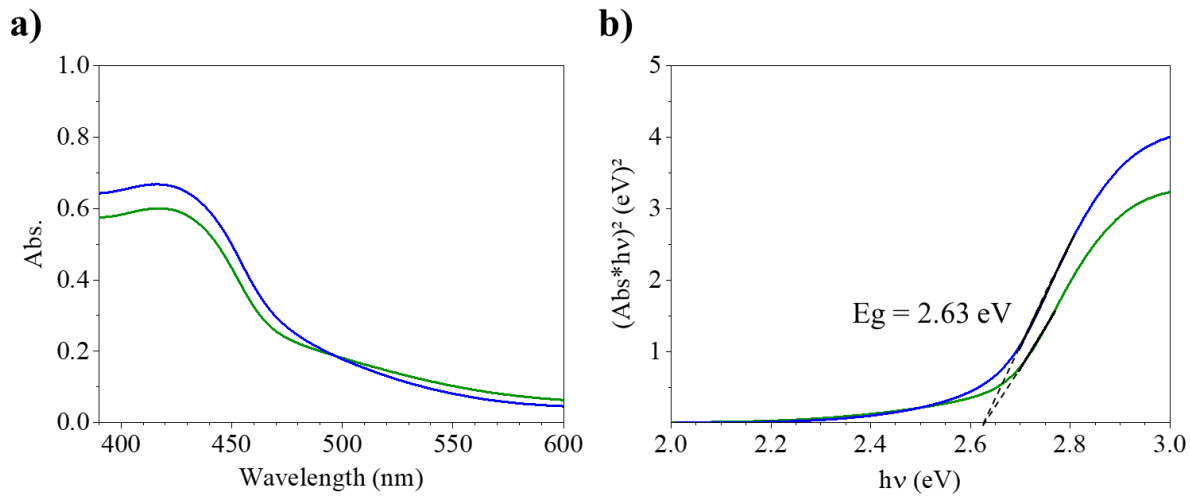

Figure S6: a) UV-Visible absorbance spectrum of $BiVO_4$ (60 nm) in blue and Mo:$BiVO_4$ (60 nm) in green, b) Eg determination by direct Tauc-plot of $BiVO_4$ (60 nm) in blue and Mo:$BiVO_4$ (60 nm) in green.

Table S7: Characterization of by ellipsometry to TiO_2 layers deposited by dip-coating on Silicon substrate, thickness identification.

Approximation : The thickness deposited on Mo:$BiVO_4$ (110 nm) photoanode corresponds to the thickness deposited in the same conditions on Silicon wafers.

Sample	**Si-Dip-1-TiO_2**		**Si-Dip-2-TiO_2**		**Si-Dip-3-TiO_2**	
	1 layer **v = 2.5 mm s^{-1}**		**2 layers** **v = 0.8 mm s^{-1}**		**3 layers** **v = 0.8 mm s^{-1}**	
PARAMETER	**Value**	**Error bar**	**Value**	**Error bar**	**Value**	**Error bar**
MSE	5.704		**0.849**		**1.939**	
Thickness # 2 (nm)	**5**	0.013	**3**	0.002	**5**	0.023
Angle Offset	0.0195	0.003943	-0.00542	0.00076931	6.87	0.027
n of Si_JAW @ 632.8 nm	3.87392		3.87392		-0.00324	0.001641

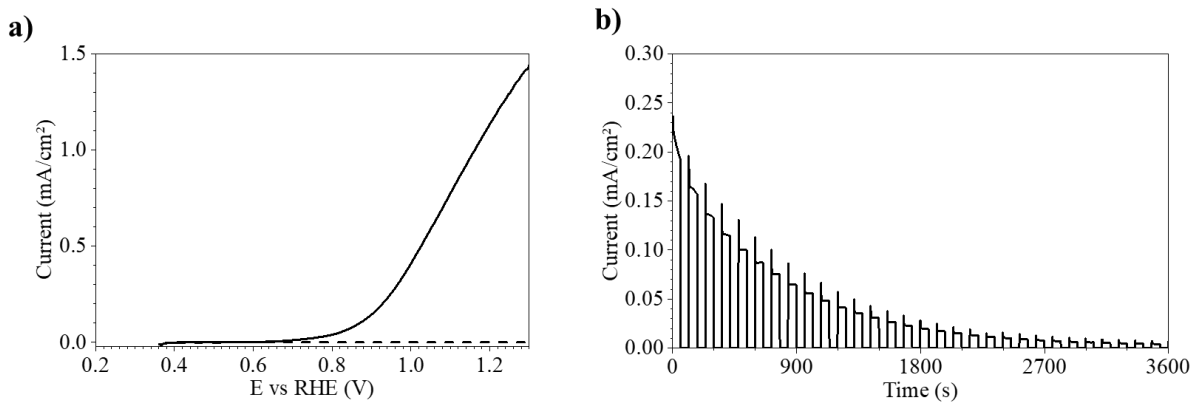

Figure S8: Photoelectrochemical measurements in 1M potassium phosphate buffer (pH 6) under 100 mW/cm2, a) Linear voltage sweeps measured at Mo:$BiVO_4$ (60 nm) and b) Chronoamperometric measurements with chopped on/off irradiation of 90 s during 1 h at 1.23 V_{RHE} at Mo:$BiVO_4$ (60 nm)

References

(1) Walsh, A.; Yan, Y.; Huda, M. N.; Al-Jassim, M. M.; Wei, S. H. Band Edge Electronic Structure of $BiVO_4$: Elucidating the Role of the Bi s and V d Orbitals. *Chem. Mater.* **2009**, *21* (3), 547–551. https://doi.org/10.1021/cm802894z.

CHAPTER III

Hydrothermal synthesis of nano-size $BiVO_4$ nanoparticles and easy heterostructured Mo:$BiVO_4$/V_2O_5 photoanode generation for photoelectrochemical water oxidation in acidic conditions

CHAPTER III

Table of Content

Hydrothermal synthesis of nano-size $BiVO_4$ nanoparticles and easy heterostructured Mo:$BiVO_4$/V_2O_5 photoanode generation for photoelectrochemical water oxidation in acidic conditions

1. Introduction

Photoelectrochemical (PEC) water splitting, is a very interesting way to produce dihydrogen (H_2) sustainably.[1,2] This process absorbs directly the largest renewable resource, solar energy to convert it into chemical fuels by water oxidation reaction at the anode and water reduction at the cathode.[3,4] Despite its potential, the commercialization of PEC-based water-splitting devices composed of a photon-absorbing anode and cathode (photoanode/photocathode) faces challenges.[5] Today, the blocking point relies on the material and design of photoanode because of the significant drops in efficiency when producing dioxygen (O_2).[2,6] Bismuth vanadate metal oxide semiconductor have been put in the light this last decade in the field of PEC water-splitting.[7–9] Its intrinsic capability of solar energy absorption as well as favourable band alignment for water oxidation make it a promising material for an efficient photoanode design.[10,11] Among its three polymorphs, the most interesting form is the monoclinic scheelite structure.[7,12–14] Its lowest band gap (Eg ~ 2.4 eV) and better photocatalytic response give it a theoretical Solar-to-Hydrogen conversion efficiency of ~ 9.2 %. This corresponds to photocurrent density of 7.5 mA cm^{-2}.[7,15,16] Nevertheless, major constraints must be considered for the generation of an efficient $BiVO_4$-based photoanode. Intrinsic hole diffusion length limitation and the necessity to have a conductive substrate reduce the possible type of synthesis.[17] Also, the low electron-hole mobility and low OER kinetic have forced scientists to develop strategies to improve the photocurrent density and minimize the photocharge recombination.[18] These strategies detailed in many reviews can be separated into three main categories: bulk modification (doping, growth orientation), interface modification (heterojunction generation) and surface functionalization (additional catalyst, passivation layer).[1,8,13,19,20]

In this field of application, most synthesis for the formation of $BiVO_4$ films are based on electrodeposition [21], chemical vapour deposition [22], drop-casting [23], spin-coating or dip-coating [24,25].

Dip-coating deposition is a technique well-established in our laboratory. It is known for its low waste production and versatility in the manufacture of a wide range of materials. This includes metallic-oxide coatings derived from sol-gel solutions, as well as biomolecules, polymers, metallic nanoparticles, ceramics, colloids, and hybrid materials like metal-organic frameworks.[26–29] Sol-gel synthesis is a fascinating technology, but its main limitation lies in achieving thicknesses greater than a micron. To overcome this limitation, it is possible to synthesize films from solution or sol containing pre-dispersed nanoparticles.[30–32] In this approach, a prerequisite is to achieve stable suspensions, which requires good control of the size on nanoparticles and their surface chemistry.

$BiVO_4$ (m-s) is the thermodynamic phase and has been synthesized in the literature in a wide variety of particle forms using hydrothermal syntheses. However, the particle sizes obtained are in the micron range.[33] To overcome this limitation, the synthesis condition and the development of new syntheses such as sonochemistry and spray-pyrolysis were studied.[33–37] T. Saison *et al*. synthesized $BiVO_4$ (m-s) square-shaped nanoparticles ranging from 50 to 200 nm at room temperature.[38] These sizes were obtained by controlling the acidity and adding organic molecules to regulate the growth rate and orientation of the particles, based on precipitation in solution mechanisms.[39] Interestingly, this synthesis process enables each $BiVO_4$ polymorph to be isolated as a function of stirring time. However, it took 3 weeks to obtain $BiVO_4$ (m-s) nanoparticles.

To achieve homogeneous films, the nanoparticles must be well dispersed in a solvent in order to avoid sedimentation during film fabrication by dip-coating. This can be limited by Van der Waals interactions, concentration and particle size.[31] The "brick and mortar" approach is a method that has been used to stabilise nanoparticles. Generally used to generate composite materials [40] or high crystalline mesoporous films [41], it can be adapted to the development of heterostructured photoanodes using two different vanadium-based metal oxides in different forms: Mo:$BiVO_4$ nanoparticles and V_2O_5 gel. Firstly, three syntheses were developed build upon the methods developed by T. Saison *et al.* and S. Sun *et al.*, to produce nanoparticles of controlled size and structure.[39,42] We then investigated the stability of colloidal suspensions in various solvents, containing $BiVO_4$ nanoparticles with different structure and size. Unfortunately, this approach did not allow us to fabricate homogeneous films. To overcome this limitation, we have used V_2O_5 gel as a "solvent". This approach was successful in creating a heterostructured photoanode of Mo:$BiVO_4$/V_2O_5 with a type II n-n heterojunction. It can be described as the "brick and mortar" approach with a V_2O_5 gel as the "mortar" for Mo:$BiVO_4$

nanoparticles. Then, the photoelectrochemical properties of Mo:$BiVO_4$/V_2O_5 were evaluated under mildly acidic conditions (pH 6).

2. Controlled size nanoparticles with various composition syntheses

Room temperature synthesis of $BiVO_4$: This synthesis is reproduced from T. Saison et al.[39] Stock solutions S_{Bi}, and S_v with the concentration of Bi and V of 0.2 mol L^{-1} are prepared by dissolving respectively bismuth (III) nitrate pentahydrate ($Bi(NO_3).5H_2O$, ACS reagent ≥ 98. %) in [HNO_3] = 1.5 mol L^{-1}, and sodium metavanadate ($NaVO_3$, ACS reagent ≥ 99.9 %) in Milli-Q water between 50°C to 80°C. 25 mL of this solution is poured into a vial and 0.5 mmol of Xylitol (ACS reagent ≥ 99 %) is added under stirring. Then, 25 mL of S_v cooled at room temperature is poured into the vial and stirred for several days/weeks depending on the desired structure of $BiVO_4$. For complete $BiVO_4$ (m-s) crystallization, the solution is stirred for 12 weeks (91 days). The synthesis will be labelled in the text : *$BiVO_4$-91d*

For the $BiVO_4$ tetragonal zircon (t-z) structure, the solution is stirred for 8 days, labelled *$BiVO_4$-8d.*

Hydrothermal synthesis of $BiVO_4$ with Xylitol ($BiVO_4$-xylitol): The $BiVO_4$ nanoparticles synthesis is adapted from T. Saison *et al.*[39] The protocol is as follows: S_{Bi} solution is prepared by dissolving in a Teflon body 3 mmol of bismuth (III) nitrate pentahydrate ($Bi(NO_3).5H_2O$, ACS reagent ≥ 98. %) in 16 mL of an aqueous acidic solution([HNO_3] = 1.5 mol L^{-1}). Then, 0.2 equivalent of Xylitol (ACS reagent ≥ 99 %) is poured under stirring inside S_{Bi}. S_V solution is prepared by dissolving 3 mmol of sodium metavanadate ($NaVO_3$, ACS reagent ≥ 99.9 %) in 16 mL of milliQ water in a separate vial. After dissolution, S_v is poured in S_{Bi} and stirred for 15 minutes at room temperature. The mixture in the Teflon body is placed in an autoclave and heated at 100 °C for 12 hours in an oven. The synthesized nanoparticles are then separated from the solvent by centrifugation. 6 cycles of washing/centrifugation are realised, half with water and the other half with Ethanol. Between each cycle, the nanoparticles are dispersed ~ 2 min with ultrasound in the colloidal solution using a Hielscher ultrasonicator.

Mo:$BiVO_4$ with Xylitol: Mo:$BiVO_4$ synthesis is similar to the previous one except that S_V is composed of 2.91 mmol of ammonium metavanadate (NH_4VO_3, ACS reagent ≥ 99 %) and

0.09 mmol of ammonium molybdate tetrahydrate ($(NH_4)_6Mo_7O_{24}.4H_2O$, ACS reagent > 99 %) is added to the solution.

Synthesis of $BiVO_4$ with Sodium Oleate ($BiVO_4$-s. oleate): This synthesis is adapted from S. Sun *et al.*[42] In a vial A, S_{Bi} is prepared by dissolving 2 mmol of bismuth (III) nitrate pentahydrate ($Bi(NO_3).5H_2O$, ACS reagent ≥ 98.0 %) in 16 mL of milliQ water at ~ 80 °C and then cooled down to room temperature. Then, 6.5 mmol of sodium oleate (ACS reagent ≥ 82 %) is added under vigorous stirring to S_{Bi}. In a second vial B, S_v is prepared by dissolving 2 mmol of sodium orthovanadate (Na_3VO_4, ACS reagent ≥ 99.9 %) in 16 mL of milliQ water. The S_v solution is transferred in the vial A and the mixture is agitated under vigorous stirring for 1 hour before transferring it into a Teflon body. The Teflon container is finally transferred into an autoclave and heated at 100 °C for 12 hours.

After the first separation of the nanoparticles from the solvent by centrifugation, they are washed and centrifuged 4 times with either hexane or THF depending on the facility of dispersing the nanoparticles and 4 times with ethanol. Between each cycle, the nanoparticles are dispersed in an ultrasound bath for at least 15 min.

Synthesis of V_2O_5 gel: The synthesis of a V_2O_5 gel in water with a vanadium (V) concentration of 0.5 mol L^{-1} is realised following the procedure reported by Durupthy et *al.*[43] The acidification of a 0.5 mol L^{-1} metavanadate solution, initially having a pH close to 8, was carried out using a proton exchange resin (DOWEX 50WX 4–100 mesh). After a complete proton exchange, a clear yellow solution is gradually transformed into a red $V_2O_5 \cdot nH_2O$ gel over a period of approximately 12 hours.

3. Characterization techniques

X-Ray diffraction: X-ray diffractograms were acquired in Bragg–Brentano geometry using a Bruker Discover D8 apparatus, equipped with a Cu anode (1.54 Å) and a LynxEye XE-T detector, over a 2θ range from 5° to 70° with a step size of 0.02°.

X-Ray Fluorescence: Elementary analysis was conducted by X-Ray Fluorescence spectrometer; using WD-XRF Bruker S8 Tiger for powder. For the electrode, X-ray fluorescence measurements are performed on an Epsilon 3XL energy dispersive spectrometer (@Malvern-Panalytical). Bismuth (Lα) and Molybdenum (Kα) are measured with a voltage of 50 kV, an intensity of 6 µA for 300 s, for vanadium (Kα) during 60 s a voltage of 12 kV and an intensity of 25 µA is applied.

UV-Visible spectroscopy: UV-visible light absorption spectra of powders were performed with an Agilent Technologies Cary Series 5000 UV/visible/near-infrared spectrometer using a double beam with an integration sphere. As for the deposited films the classical setup was used with a clean FTO electrode as a reference. The band gap is estimated from UV-vis spectroscopy experiments by applying a direct Tauc-Plot on the UV-visible absorbance of $BiVO_4$.[44,45] following this method: with equation (1):

$$\mathrm{hv\ (eV)} = \frac{\mathrm{h_{Planck}} \times \mathrm{v}}{\lambda} \times \frac{1}{\mathrm{e}} \qquad (1.a)$$

with h_{Planck} the constant of Planck (in J.s), v the celerity of light (in nm), λ the wavelength (in nm) and e the elementary charge of a single electron (in Coulombs).

$$\mathrm{hv\ (eV)} = \frac{6.626\ \mathrm{e}^{34} \times 3\ \mathrm{e}^{17}}{\lambda\ (\mathrm{nm})} \times \frac{1}{1.602\ \mathrm{e}^{-19}} \qquad (1.b)$$

We transform the wavelength into energy. Then with the formula (3), we obtain an absorbance from the "k" parameter:

As $BiVO_4$ is considered a semiconductor with a direct Eg we fitted:

$$(\mathrm{Abs} \times \mathrm{hv})^2 = \mathrm{f}(\mathrm{hv}) \qquad (2)$$

A linear polynomial fit on the linear region of the curves allows us to determine the x-intercept in a typical y = ax + b first-degree polynomial that corresponds to the Eg value.

Transmission Electron Microscopy (TEM): Transmission electron microscopy analyses were performed using a JEOL 2100 PLUs equipped with a LaB_6 electron gun operating at 200 kV. Samples were dispersed by sonication on ethanol and deposited on top of Cu grids covered with a carbon membrane.

FEG-SEM EDX imaging: Field emission gun-scanning electron microscopy (FEG-SEM) was carried out using a Hitachi SU-70 equipped with an Oxford X-Max beam with 50 mm^2 X-Max silicon drift EDS detector with a 50mm^2 tungsten filament operated at 10 – 15 kV.

Photoelectrochemical Performances: The PEC performance of $BiVO_4$ photoanodes was checked with an AMETEK Solartron Analytical Modulab potentiostat coupled with a Newport Xenon lamp in a pH 6 potassium phosphate buffer conducting linear sweep voltammetry (LSV) under AM 1.5 G illumination (100 mW/cm^2) under front side (through the film/ interface) with a reference electrode (E0Ag/AgCl = 0.197 V vs NHE) and a platinum enrolled wire as a counter electrode. A scan rate of 10 mV s^{-1} is used. All current density curves were referenced to the reversible hydrogen electrode (RHE), using the Nernstian relation:

$$V_{RHE} = E\ vs.Ag/AgCl + 0.197 + 0.059 \times pH$$

Chronoamperometry measurement under alternative irradiation was performed using the potentiostatic mode at a fixed potential of 1.23 V_{RHE}. The geometric active area of the $BiVO_4$, working electrode, was defined by Hi-Bond polyamide scotch tape (HB830-19) and measured to be 0.28 cm^2. Electrical contacts were made by conductive copper scotch (3M Scotch 1245) which was adhered directly to the FTO substrate.

4. Nanoparticles synthesized characterization

$BiVO_4$ at room temperature: In figure 1.a, the nanoparticles washed after 8 days of stirring have crystallized in the tetragonal zircon polymorph, which is the less photoactive structure. The nanoparticles absorb wavelengths from 500 nm to 250 nm and exhibit the widest band gap (Eg) of 2.82 eV (Figure 1.b). They are isotropic with spherical shapes and aggregates with a range of size between 10 – 20 nm (Figure 1.c). For the nanoparticles stirred during 12 weeks, they crystallized in the monoclinic scheelite structure (Figure 1.a). They absorb from 530 nm to 250 nm corresponding to an Eg of 2.49 eV (Figure 1.b). In TEM imaging (Figure 1.d), the nanoparticles present a microstructure constituted of square-shaped facetted nanoparticles with some aggregates and a size between 50 to 200 nm.

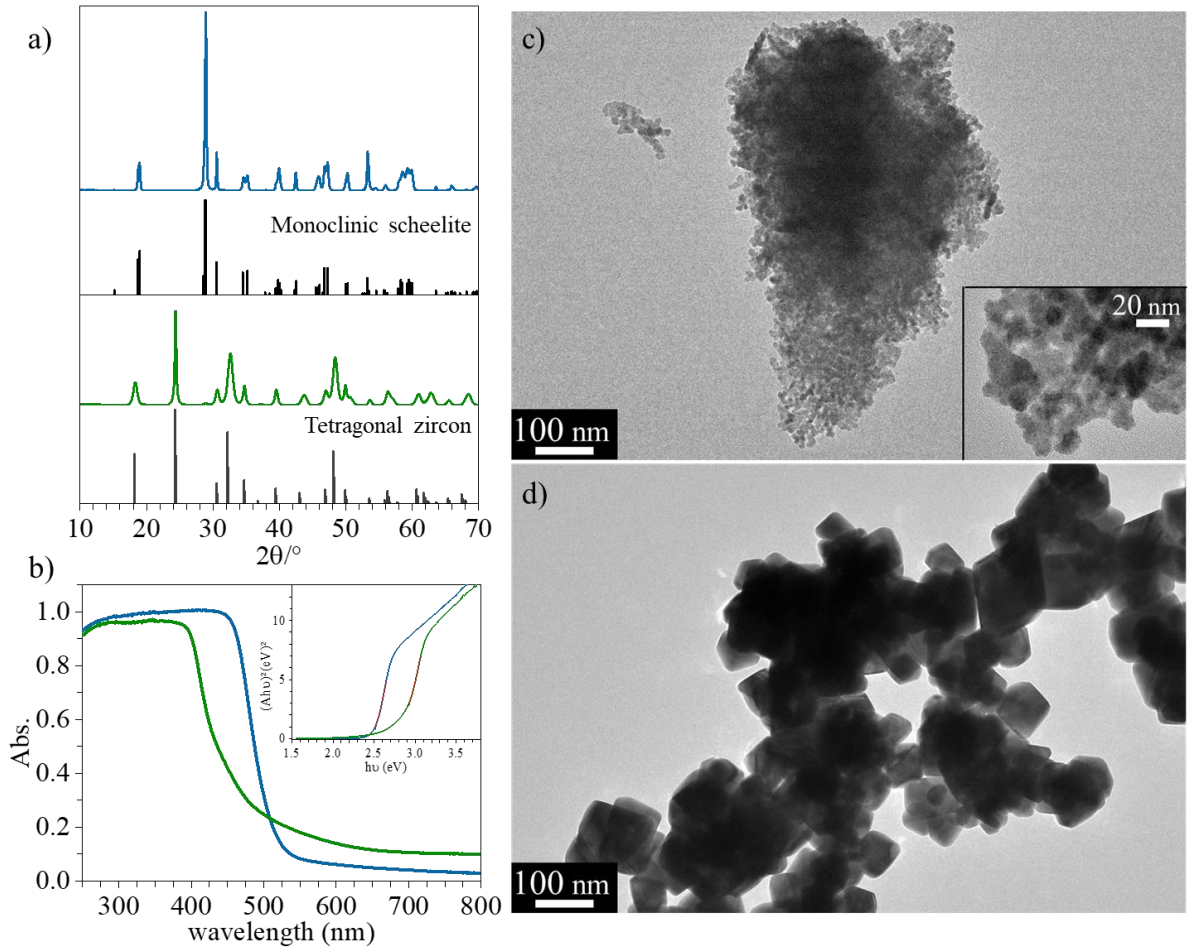

Figure 1: a) XRD patterns of $BiVO_4$-8d (green curve), PDF-00-014-0133 $BiVO_4$ tetragonal zircon (straight grey lines), $BiVO_4$-91d (blue curve), PDF-04-010-5713 $BiVO_4$ monoclinic scheelite (straight black lines); b) UV-Visible absorption spectra and band gap determination of $BiVO_4$-8d (green) and $BiVO_4$-91d (blue); c) TEM imaging of $BiVO_4$-8d d) TEM imaging of $biVO_4$-91d.

$BiVO_4$-xylitol: The nanoparticles of $BiVO_4$-xylitol are crystallized in the unique monoclinic scheelite crystalline structure of $BiVO_4$, which is the .most photoactive polymorph of $BiVO_4$ (Figure 2.a).[14,16,46] The diffraction pattern exhibits the following peaks doublets at 19°, 35° 47°, corresponding to the planes (101) (011), (200) (020), and (204) (024), respectively. TEM imaging has shown well-crystallized nanoparticles with facets (Figure 2.c). Their size varies from 40 to 90 nm for nanoparticles and from 150 to 200 nm for aggregates. The monoclinic scheelite structure is also confirmed with the presence of interferences fringe of (101) or (011) planes (Figure 2.d). In Figure 2.b, the nanoparticles of $BiVO_4$ in a monoclinic scheelite structure absorb from 550 nm to the UV range, then exhibiting a band gap of 2.42 eV.

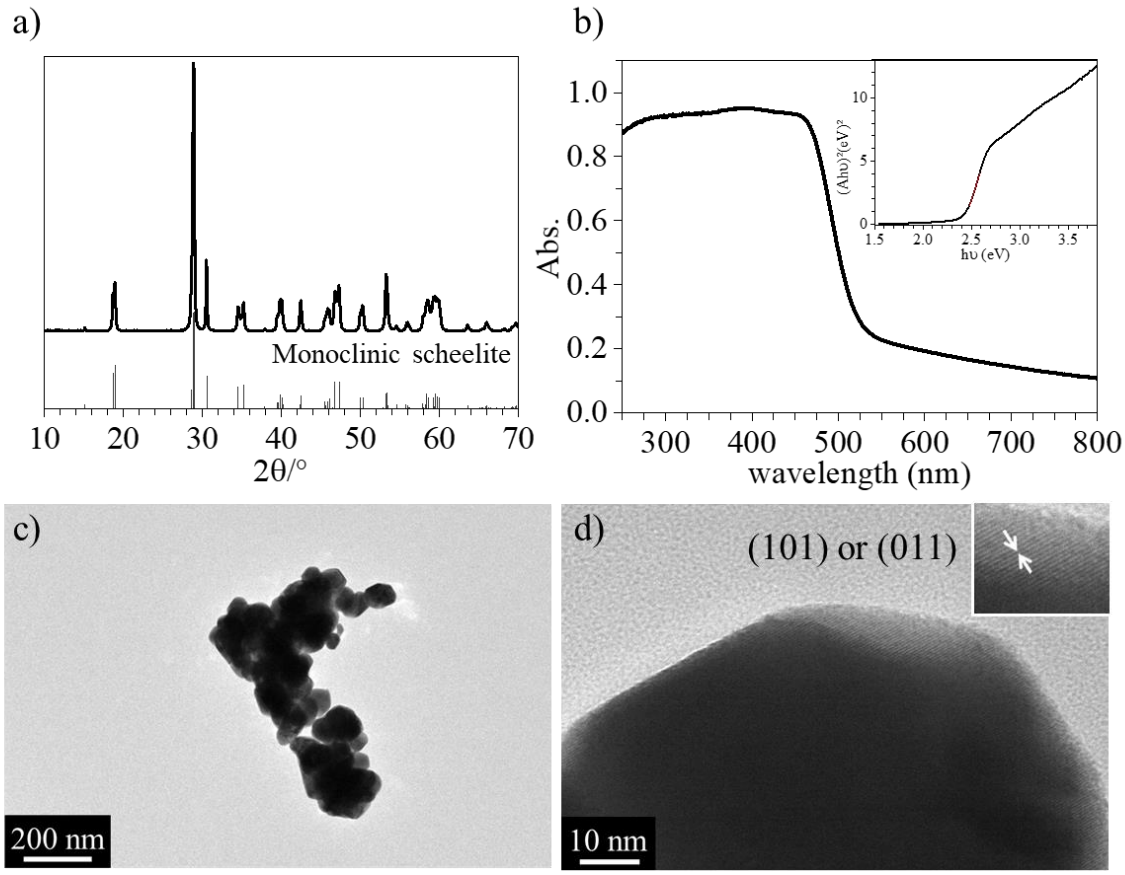

Figure 2: a) XRD patterns of $BiVO_4$-xylitol (curve), PDF-04-010-5713 $BiVO_4$ monoclinic scheelite (straight lines); b) UV-Visible absorption spectra and band gap determination; c) d) TEM imaging

Mo:$BiVO_4$-xylitol: The characterization of Mo:$BiVO_4$-xylitol nanoparticles is presented in Figure 3. The nanoparticles of Mo:$BiVO_4$-xylitol are crystallized in the tetragonal scheelite crystal polymorph (Figure 3.a).These nanoparticles absorb light from 520 nm to 300 nm with an Eg of 2.52 eV, slightly wider than pristine $BiVO_4$ (Figure 2.b). X-ray fluorescence analysis has allowed the identification of Mo 9.42 mol%, V 40.55 mol% and Bi 50.03 mol% in the sample. The detailed concentration of Bi, V, Mo gives the formula $BiV_{0.81}Mo_{0.19}O_4$. TEM analysis in Figure 3.c reveals that the nanoparticles are anisotropic with fewer facets than pristine $BiVO_4$. Interestingly, the nanoparticles' size exhibits a diameter ranging from 15 to 30 nm, with the presence of some aggregates around ~ 100 nm. In Figure 3.d most of the nanoparticles present interference fringes corresponding to the two main plans of $BiVO_4$ (t-s) structure (112) and (101) (marked in yellow) at 19° and 29° in XRD. In comparison to pristine $BiVO_4$, the incorporation of Mo^{6+} during the synthesis affects the growth rate of nanoparticles and slows down the crystalline transition from the tetragonal scheelite to the monoclinic scheelite structure.

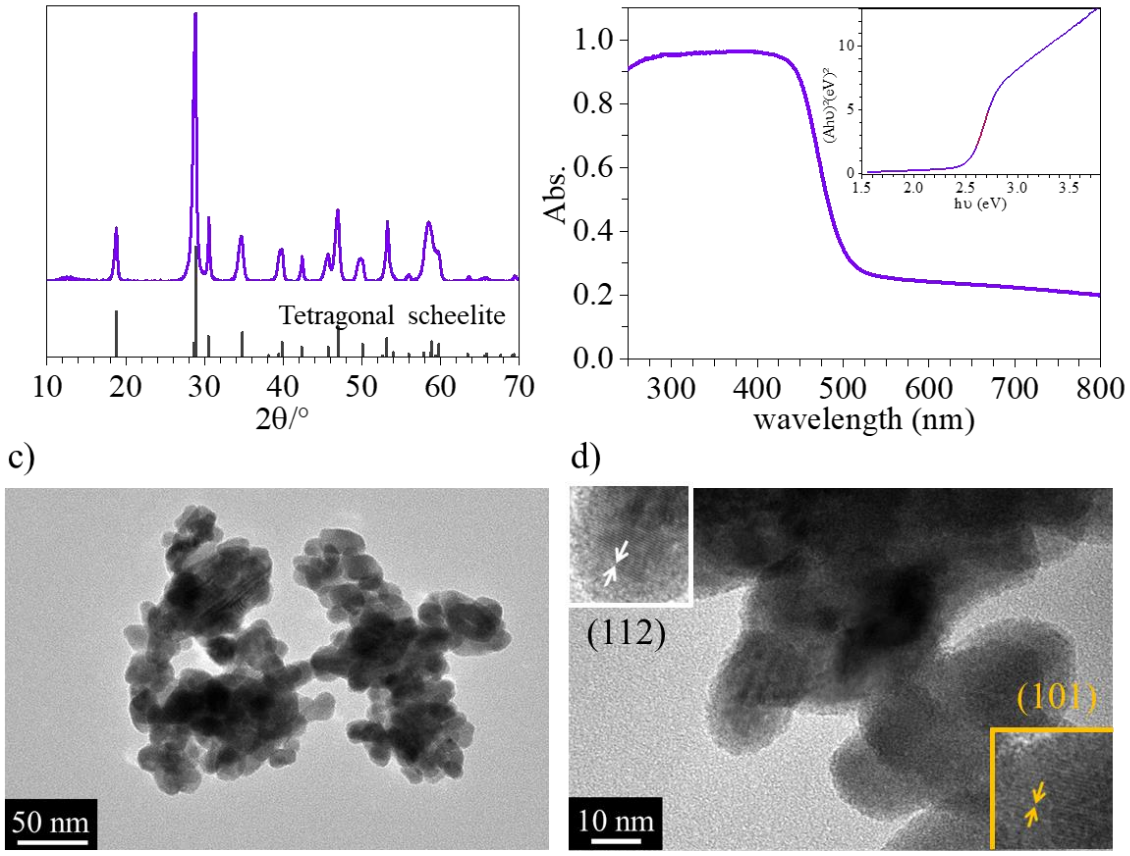

Figure 3: a) XRD patterns of Mo:$BiVO_4$-xylitol (curve), PDF-04-010-5710 $BiVO_4$ tetragonal scheelite (straight lines); b) UV-Visible absorption spectra and band gap determination; c) d) TEM imaging

$BiVO_4$-s. oleate: XRD patterns in Figure 4.a shows broad peaks characteristics of nano-sized particles with amorphous phase. The presence of both the tetragonal zircon peak (112) and tetragonal scheelite peak (112) can be identified at 32.5° and at 28°, respectively. Interestingly, both polymorphs' contributions to solar spectrum absorption are distinguishable in the UV-visible absorbance spectrum (Figure 4.b). Tauc-plot analysis allows the determination of two band gaps: one at 2.33 eV and another at 2.76 eV. In Figure 4.c, the nanoparticles are ovals with a range of size between 3-6 nm. TEM analysis shows that the large amount of sodium oleate organic additive during the synthesis allows good control of the germs' growth and their orientation.

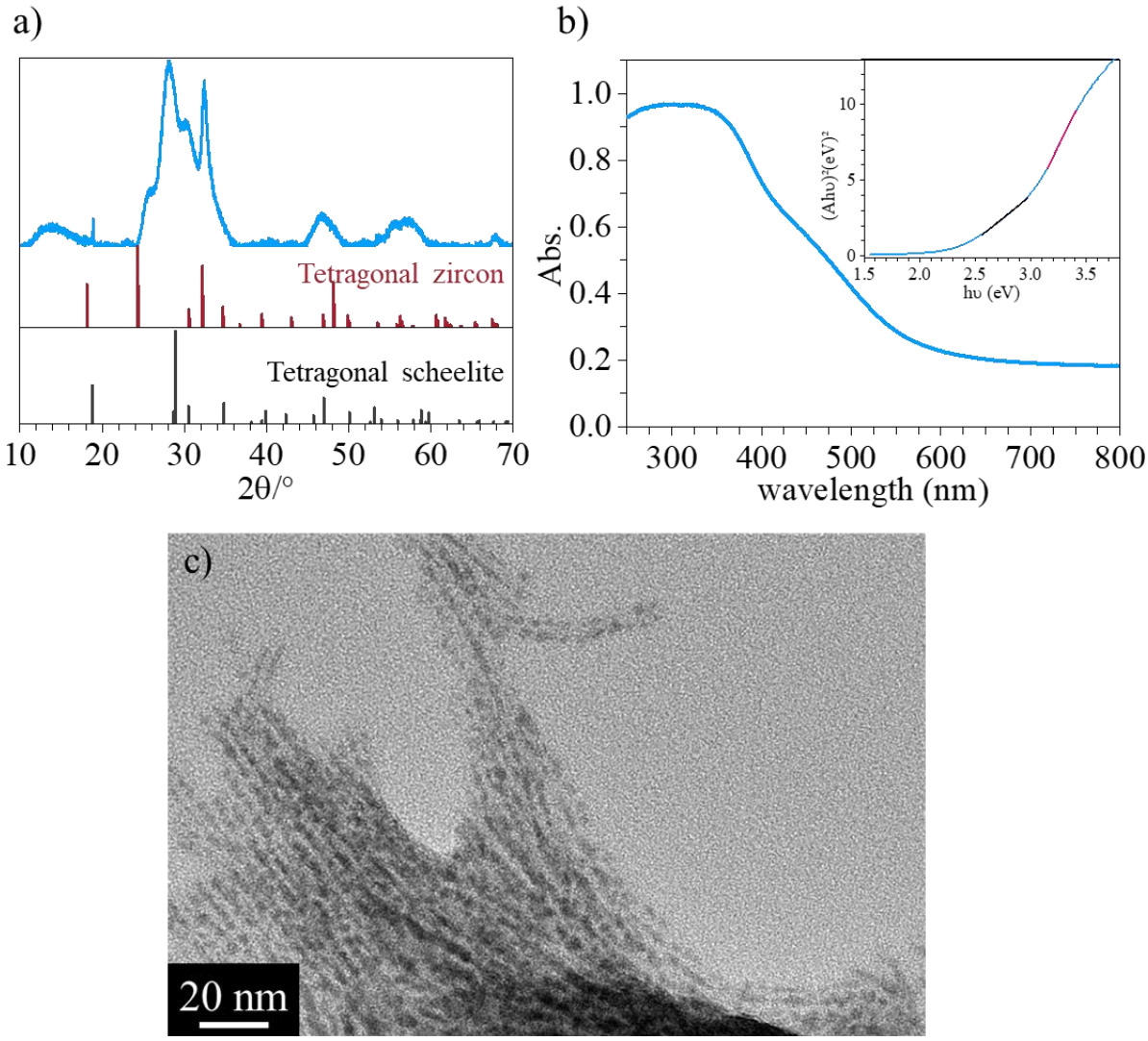

Figure 4: a) XRD of Mo:$BiVO_4$-xylitol (curve), PDF-04-010-5710 $BiVO_4$ tetragonal scheelite (grey), PDF-00-014-0133 tetragonal zircon (red); b) UV-Visible absorption spectra and band gap determination; c) TEM imaging.

5. Electrodes preparation

a. From nanoparticles' colloidal suspensions

To deposit a film of nanoparticles by dip-coating, we set a stability criterion of 15 minutes for the colloidal suspension. To reach this objective, different parameters are studied depending on the nanoparticles used for the deposition process. To study the stability of the nanoparticles, a nanoparticles size analyser using dynamic light scattering (DLS) was employed in a different manner than usual. Indeed, specific parameters were fixed: the attenuator was fixed at 10 or 11, and the measure was made at 2 mm from the vial with a beam angle of 90°. The average count per 30 seconds is measured during 15 minutes. As the solutions are concentrated, particles tend to settle towards the bottom, increasing the number of counts. Indeed, higher concentrations block a portion of the beam for the maximum of particles detection, whereas lower concentrations enable a more accurate particle count. Additionally, colloidal suspension stability was also observed by capturing images at different times.

$BiVO_4$-s.oleate

The first nanoparticles tested are $BiVO_4$-s.oleate, which are the smallest in size. For these tests, we examined two different solvents: absolute ethanol for its ability to drive fast and a mixture of solvent of Milli-Q water/Ethanol with a 50/50 volumetric ratio (v/v). The dispersion chosen for the tests is 4 %w/w and the particles are agitated with an ultrasonic probe (Hielscher) during 15 nm before analysis.

For absolute ethanol, the nanoparticles dispersed in a centrifugation tube, are left next to a ruler and the settling level is noted 10 times as shown in Figure 5.a. From these points, the difference between the measurements of the initial level and during the settlement is evaluated in cm (Δmeas.). It is then plotted as a function of the time to obtain a rate of settlement. The rate is evaluated to be 60 µm s^{-1}, which is equivalent to 3.6 mm min^{-1}. This shows that ethanol is not the ideal solvent to stabilize the nanoparticles in suspension. On the contrary, H_2O/EtOH : 50/50 (v/v) mixtures exhibit efficient stability of the nanoparticles. In Figure 5.b, three replicates were analysed using the particles sizer. Each time, the colloidal suspension undergoes 15 minutes ultrasonic treatment using the Hielscher ultrasonic probe placed within the suspension, followed by the extraction of a sample for analysis using the size analyser. The value of average counts was stable during the 15 minutes and after analysis, the colloidal suspension appears identical as before.

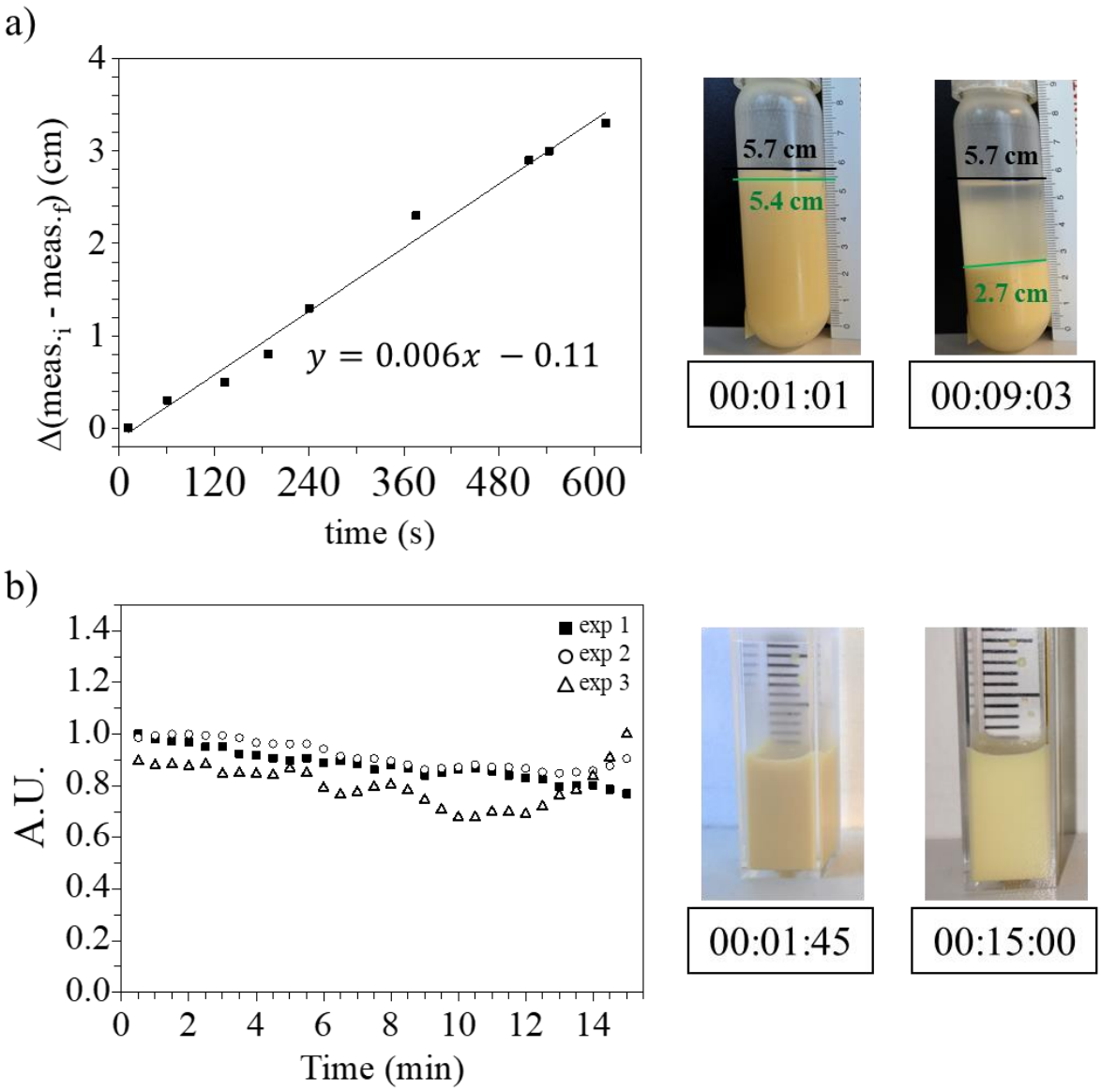

Figure 5: a) Plot of $BiVO_4$-s nanoparticles settling rate using the difference of the initial level at the time "t_0" and level measured at a time "t" in absolute ethanol with 4%w/w ratio; b) average counts each 30 sec of nanoparticles, measured during 15 min in H_2O/EtOH : 50/50 (v/v) with 4%w/w ratio.

After these tests, a new fraction of the synthesis was used to process the dip-coating deposition following the protocol below.

$BiVO_4$-s.oleate dip-coating: $BiVO_4$-s.oleate nanoparticles are dispersed at 10 %w/w in a solvent composed of H_2O/EtOH : 50/50 (v/v). The colloidal dispersion is stirred for 5 min before deposition by dip-coating on the FTO substrate with the following conditions: 3 mm s^{-1} of withdrawal speed and relative humidity (RH) ≤ 10 %). The deposited film on the nonconductive side is removed and the electrode calcined for 1 h at 450 °C in air.

i. $BiVO_4$-s.oleate electrode characterization

The crystalline structure of $BiVO_4$-s.oleate photoanode is more crystalline after heat-treatment of 1 h at 450 °C than that of the pristine nanoparticles (Figure 6a). Interestingly, both the tetragonal zircon and tetragonal scheelite phases (Figure 6.a) are still present but with sharper peaks. SEM analysis indicates that the film does not cover the entire surface of the FTO electrode, as large uncoated areas of FTO are observed making the electrode unsuitable for electrochemical testing (Figure 6.b). As expected, the heat treatment has favoured the growth of the nanoparticles of $BiVO_4$ as their size evolves from 3-6 nm to 50 - 500 nm. This densification at 450 °C reveals the evolution of amorphous to well-crystallized particles, probably promoted by the nanoparticle's arrangement seen in TEM (Figure 4c).

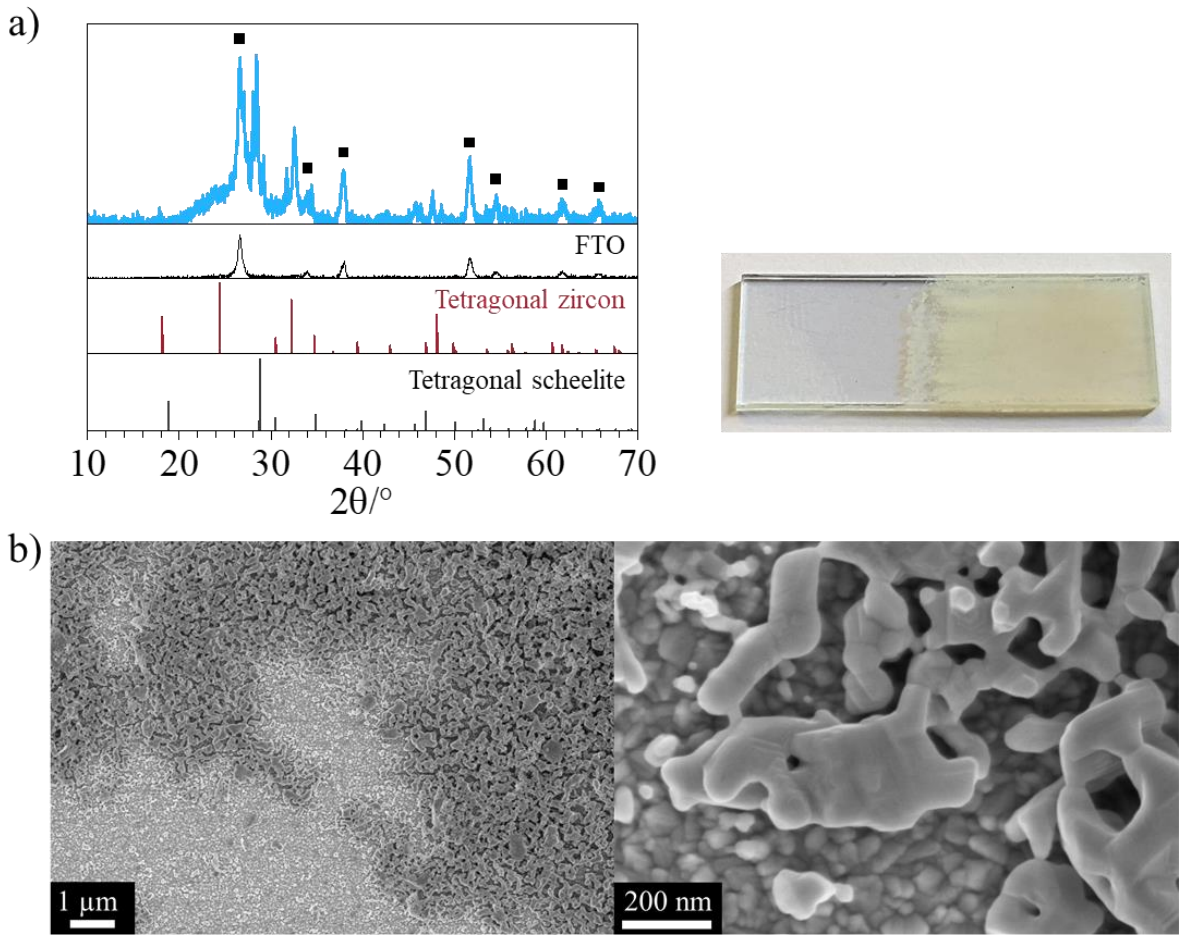

Figure 6: a)XRD of $BiVO_4$-s.oleate photoanode (blue) after calcination, FTO signal (black line and small squares), PDF-00-014-0133 for $BiVO_4$ tetragonal zircon (red), PDF 04-010-5710 for $BiVO_4$ tetragonal scheelite (grey): b) SEM-FEG imaging of $BiVO_4$-s. oleate photoanode surface.

These experiences indicate that one hour of calcination treatment allows good consolidation of the nanoparticles deposited but incomplete conversion to the monoclinic scheelite polymorph. Consequently, we decided to focus our attention on the stabilisation of Mo:$BiVO_4$-xylitol nanoparticles in a colloidal suspension. These nanoparticles have a size between 15 nm to 100 nm for the aggregates and a band gap of 2.52 eV.

Mo:$BiVO_4$-xylitol

To enhance colloidal suspension stability, we employ various strategies for nanoparticle stabilization:

i/ increase surface charge of the nanoparticles by being far from the isoelectric point between pH 4 – 5 [47] that usually favour their precipitation and aggregation;

ii/ test alternative solvents with different viscosity such as ethanol, isopropanol and diethylene glycol

iii/ testing mixture of solvents of various ratio as water/ethanol, water/diethylene glycol.

The best results are presented in Figures 7.a and b. The nanoparticles' surfaces are positively charged by agitation under ultrasounds in water solution at pH = 1 acidified with HNO_3. After centrifugation, they are dispersed at 4 %w/w in a water/ethanol : 50:50 (v:v) (Figure 7.a) or a diethylene glycol/water : 70:30 (v:v) (Figure 7.b) mixed solvent. In triplicated experiments reported in Figure 7.a and b, the dispersion seems stable during the 6 minutes and settles then faster for the 9 lasting minutes. The settling is faster for the nanoparticles dispersed in diethylene glycol/water (Figure 7.b). In Figure 7.a, the slope increases from the first to the last replicate with the total time of ultrasounds. This indicates that the strategies employed are not sufficient to stabilise the particles in a colloidal suspension for 15 minutes.

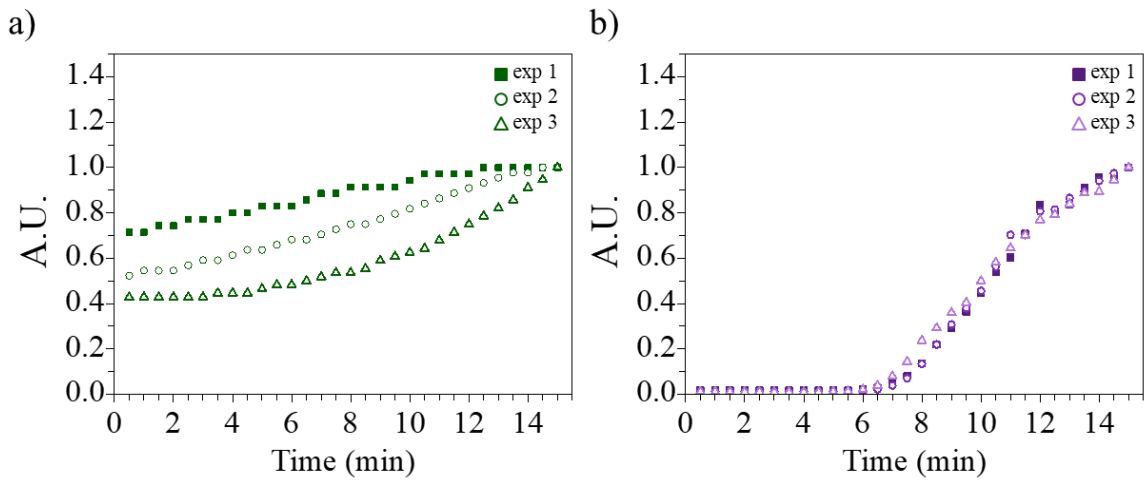

Figure 7: Average counts each 30 sec of Mo:$BiVO_4$-xylitol nanoparticles, measured during 15 min a) in H_2O/EtOH 50/50 (v/v) with 4%w/w ratio b) in diethylene glycol/H_2O : 70/30 (v/v).

b. From V_2O_5 gels

The previous experiments have shown that i/ a homogeneous coating of the nanoparticles with good contact particle/particle at the surface of the electrode substrate was an important constraint, ii/ the strategies tested for Mo:$BiVO_4$ nanoparticles did not provide sufficient stabilization for extended times. Looking at the various strategies applied to improve the efficiency of a $BiVO_4$ photoanode in the literature [1,20], a heterostructured electrode with another metal oxide appeared to be an interesting approach to solve the particle/particle contact and to create a n-n junction. Indeed, V_2O_5 metal oxide can be easily synthesized using proton exchange resins, resulting in a gel-like structure with separated 2D leaflets held together by water. This structure seems to allow the dispersion of Mo:$BiVO_4$ nanoparticles.

The heterostructured Mo:$BiVO_4$/V_2O_5 photoanode is realised following the protocol below:

Mo:$BiVO_4$/V_2O_5 Colloidal suspension: First Mo:$BiVO_4$-xylitol nanoparticles' surfaces are positively charged in a solution with an acidified water solution of $2 < pH < 3$ using HNO_3 0.2 mol l^{-1} to avoid V_2O_5 precipitation which is unstable at $pH > 3$. Then, a colloidal suspension of Mo:$BiVO_4$/V_2O_5 of 14.7 %w/w with V_2O_5 gel considered as the solvent is realised by stirring 0.255 g of Mo:$BiVO_4$ into 1.73 g of V_2O_5 gel.

Prior to the deposition of the mixed Mo:$BiVO_4$/V_2O_5 suspension, a very thin $BiVO_4$ film is achieved by the sol-gel process according to S. Hilliard *et al.* to improve the affinity of the colloidal suspension toward the substrate.[25]

FTO substrate functionalization: Commercial glass of F-doped SnO_2 (FTO) 80 nm/ Glass substrate from (SOLEMS: YSUB/ASAHI120/1) with effective resistivity measured between 200 – 250 Ω is employed as an electrode substrate. FTO substrate is functionalized with a thin layer of $BiVO_4$ deposited by sol-gel chemistry. 0.36 mmol of bismuth (III) nitrate pentahydrate (ACS reagent ≥ 98.0 %) and 0.36 mmol of vanadium (IV) oxide acetylacetonate are dissolved in a mixt solvent of acetylacetone : acetic acid with 4.7:1 ratio using an ultrasonic bath for 10 minutes at 35 °C then left to stir overnight. The film deposition is done the day after the preparation.

Semi-transparent yellow films are produced by dip coating (Ossila Dip-Coater) with the deposition of 3 layers of the precursor solution at RH < 5% with a withdrawal rate of 1 mm s^{-1}, while thermally annealing at 400 °C for 1 – 2 minutes in between each layer depositions. Between each layer, the non-conductive side of the substrate is cleaned before annealing. After the 3 layers of coating the film is finally calcinated 1 h at 450 °C.

Mo:$BiVO_4$/V_2O_5 deposition: After 10 minutes of magnetic stirring, Mo:$BiVO_4$/V_2O_5 mixture is deposited by dip-coating (ACE dip 2.0 from SOLGELWAY Dip-Coater) in a heated chamber at ~ 80 °C, with a withdrawal rate of 0.02 mm s^{-1}. After deposition, the film is cleaned on the nonconductive side and calcinated for 1 h at 450 °C in air.

i. Heterostructured electrode characterization

Mo:$BiVO_4$/V_2O_5 photoanode: XRD pattern of Mo:$BiVO_4$/V_2O_5 photoanode is reported in Figure 8. After the calcination treatment at 450 °C, the crystalline structure of the photoanode is composed of V_2O_5 and $BiVO_4$ nanoparticles in monoclinic and tetragonal scheelite structures, respectively. UV-Vis spectroscopy experiments indicate that the photoanode presents a band gap of 2.21 eV that is attributed to the presence of V_2O_5 in the electrode (Figure 8.b)[48]. The molar ratio of Mo:$BiVO_4$/V_2O_5 has been estimated by X-ray fluorescence with 4.3 mol% for Mo, 77.7 mol% for V and 18.0 mol% for Bi which gives 4.3 atoms of V and 0.24 atoms of Mo for 1 Bi atom. In Figure 8.c,d,e, SEM-FEG imaging of the surface and cross-section allows the identification of the two oxides in the film. Interestingly, Mo:$BiVO_4$ particles (brighter) appear to be surrounded by V_2O_5 (darker), acting then as a cement between the particles. The V_2O_5 particles are elongated and sintered, giving an appearance of stratification. The thickness of the photoanode is 111 ± 15 nm.

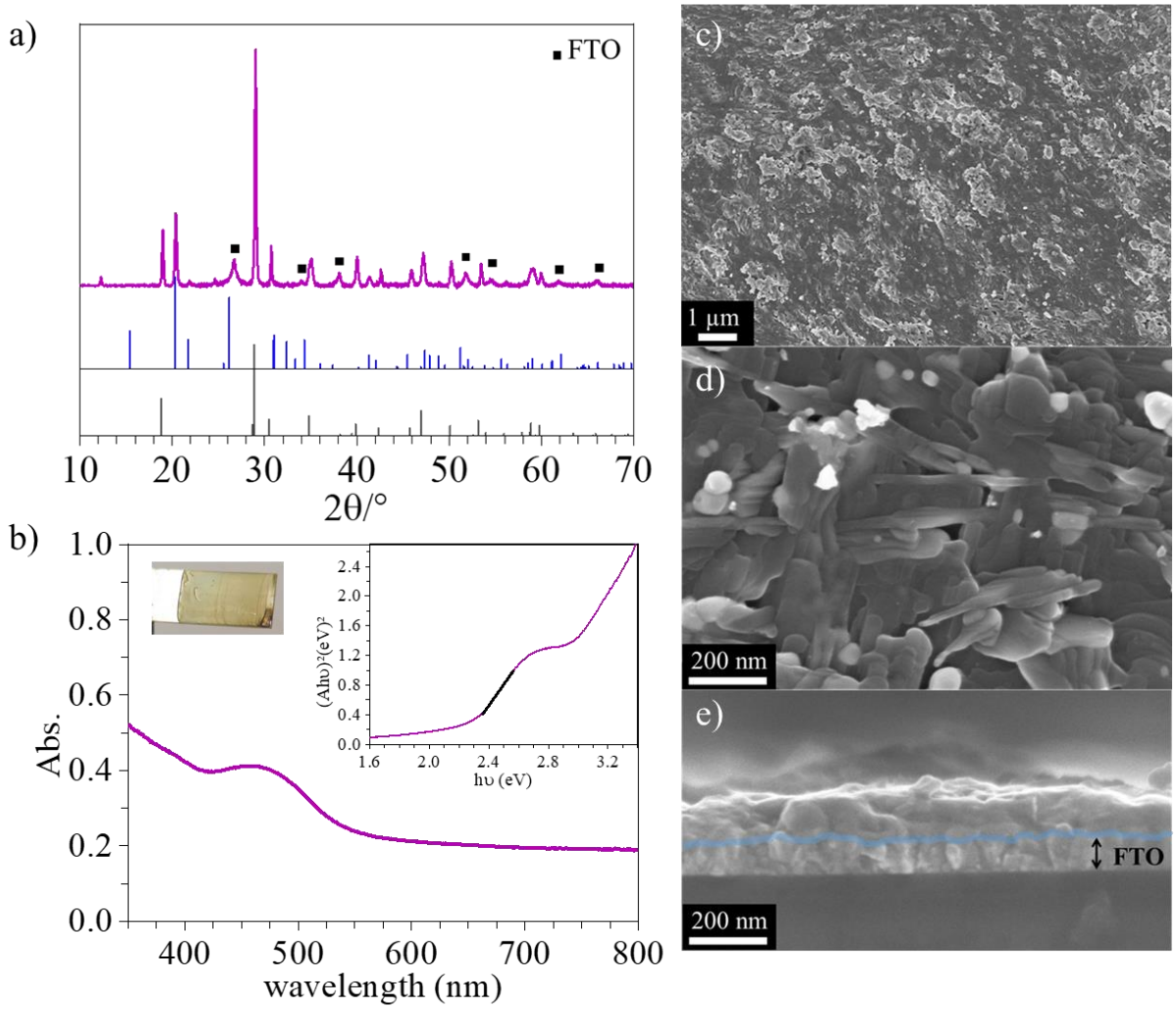

Figure 8: Mo:$BiVO_4$/V_2O_5 photoanode characterization with a) XRD of Mo:$BiVO_4$/V_2O_5 (purple curve), PDF-04-010-5710 $BiVO_4$ tetragonal scheelite (grey), PDF-00-009-0387 V_2O_5 (blue); b) UV-Visible absorption spectra with band gap determination; c) d) surface SEM-FEG imaging; e) cross-section SEM-FEG imaging

ii. Mo:$BiVO_4/V_2O_5$ PEC performances

The photoelectrochemical performances of Mo:$BiVO_4/V_2O_5$ are evaluated by linear sweep voltammetry and chronoamperometry. In Figure 9.a. the linear sweep curves correspond to the photocurrent density measured in the dark and under light in 1 M potassium phosphate buffer (pH 6) under 100 mW cm^{-2} of simulated light. In dark conditions, the photocurrent is inexistent, while under illumination, the first electrons/holes are generated and consumed at an onset potential of 0.6 V_{RHE}. A photocurrent of 0.2 mA cm^{-2} is reached at 1.23 V_{RHE}. The chronoamperometric curve is measured during 2 hours with chopped illumination of 90 s at fixed potential of 1.23 V_{RHE}. It shows a higher photocurrent of 0.4 mA cm^{-2} during the first hour measured at the top of the peak. The photocurrent density at the plateau level is equal to 0.32 mA cm^{-2}. The difference of 0.08 m cm^{-2} is attributed to recombination phenomena occurring at the interface between the holes and the electrolyte. The general decrease in photocurrent (measured at the plateau) over time indicates a loss of the electrode efficiency. This phenomenon is commonly associated with photocorrosion, which is linked to the generation of species that degrade the electrode itself. Nevertheless, these results represent a first study in low acid conditions using standardised conditions. Compared to Yaw *et al.* or T. Andrade *et al.*, no sacrificial agent such as Na_2SO_3 or H_2O_2 is added in the electrolyte to improve the kinetic of holes to react.[49,50] Arunachalam *et al.* designed photoanode composed of V_2O_5@$BiVO_4$ inverse opal heterostructure decorated with NiOOH cocatalyst.[51] They obtained in 0.5 M Na_2SO_4 (pH 6.8) at 1.23 V_{RHE} a photocurrent density of ~ 0.38 mA cm^{-2} without cocatalyst and 1.14 mA cm^{-2} with NiOOH. Our results are very similar to those obtained by Arunachalam's team in more acidic condition that is less favourable for OER.

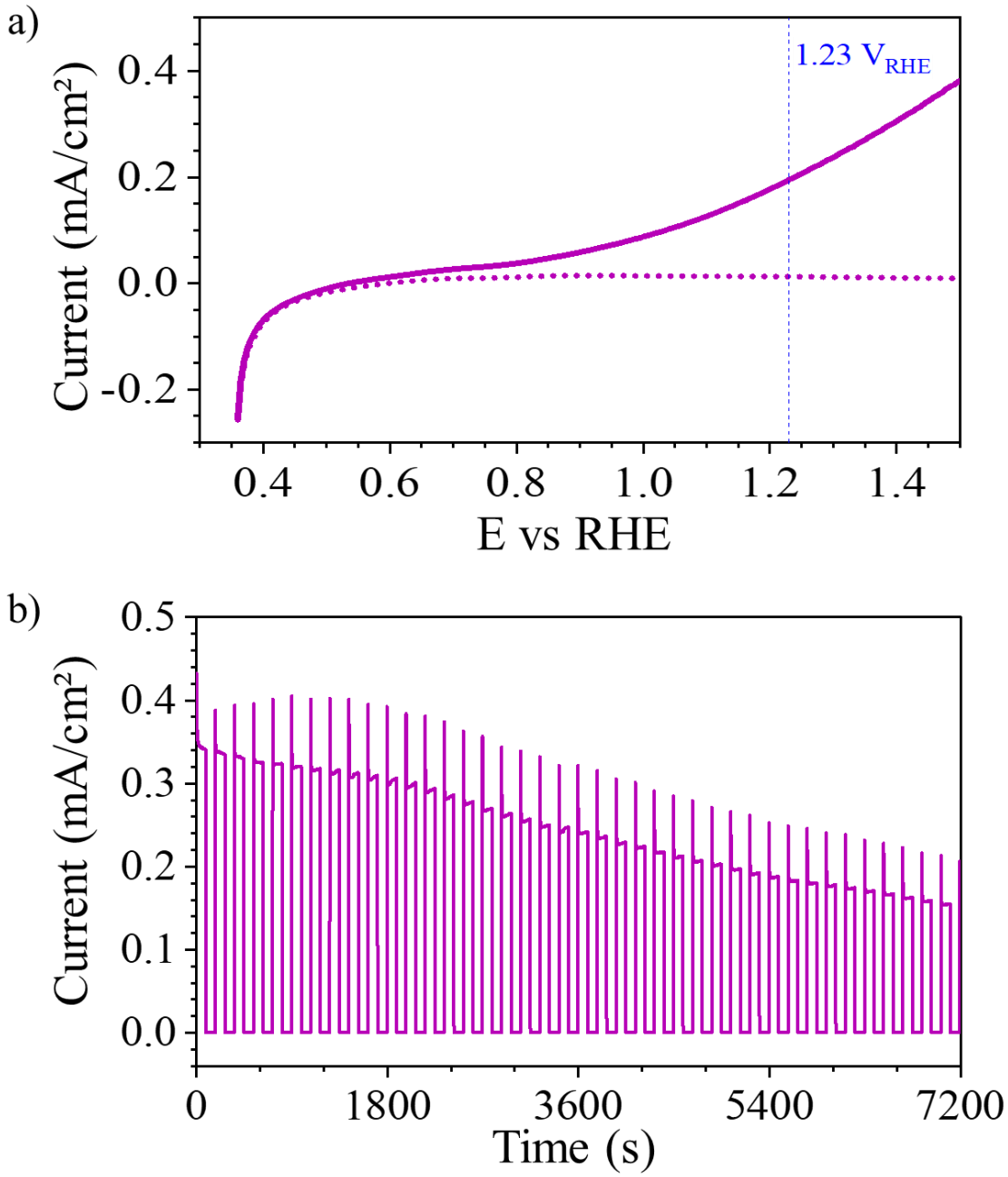

Figure 9: Photoelectrochemical measurements of Mo:$BiVO_4/V_2O_5$ in 1M potassium phosphate buffer (pH 6) under 100 mW cm^{-2} a) Linear voltage sweeps with illumination (lines) and without illumination (dots) b); chronoamperometric measurement with chopped on/off irradiation of 90 s during 2 h at 1.23 V_{RHE}

6. Conclusion

To synthesize thick film of $BiVO_4$ using dip-coating deposition, one solution is to deposit a solution containing $BiVO_4$ nanoparticles dispersed in solvent. To do so, nanoparticles with controlled sizes and structures were synthesized by modifying the temperature of synthesis, the duration, the pH and the amount of complexing agent to generate $BiVO_4$. The smallest nanoparticles ranging from 3 to 6 nm were easily stabilized in H_2O/EtOH : 50/50 (v/v) solvent for 15 minutes and deposited on the FTO substrate. However, this approach revealed two problems: i/ high porosity in the film due to a low contact particle/particle, ii/ incomplete transition to a scheelite structure after calcination. This led to dope $BiVO_4$ with Mo and the use of xylitol to stabilize the Mo:$BiVO_4$-xylitol nanoparticles in the scheelite structure with an Eg of 2.52 eV. Interestingly, with Mo-doping, Mo:$BiVO_4$ nanoparticles have sizes ranging from 15 – 30 nm to 100 nm for aggregates, which is lower than pristine $BiVO_4$-xylitol. A stable colloidal suspension for 15 minutes was not achieved to proceed the film fabrication by dip-coating. Finally, the use of V_2O_5 gel in a "brick and mortar" approach to stabilize the Mo:$BiVO_4$ nanoparticles allowed efficient stabilization of the particles in acidic aqueous media. The dispersion of Mo:$BiVO_4$ in V_2O_5 gel allows the deposition of both metal oxides in one step. The heterostructured photoanode with a type II n-n heterojunction and excellent particle/particle contact is then obtained with the dip-coating process. Photoelectrochemical performance analysis of Mo:$BiVO_4$/V_2O_5 photoanode gave promising results. The photocurrent density of 0.32 mA cm^{-2} obtained at 1.23 V_{RHE} at pH 6, is close to complex microstructure Mo:$BiVO_4$@V_2O_5 reported in literature.[51] From the perspective of durability, and photoelectrochemical improvement, a cocatalyst layer could improve the efficiency increasing the reactivity at the electrode/electrolyte interface.

7. References

(1) Gaikwad, M. A.; Suryawanshi, U. P.; Ghorpade, U. V.; Jang, J. S.; Suryawanshi, M. P.; Kim, J. H. Emerging Surface, Bulk, and Interface Engineering Strategies on $BiVO_4$ for Photoelectrochemical Water Splitting. *Small* **2022**, *18* (10), 1–35. https://doi.org/10.1002/smll.202105084.

(2) Jiang, C.; Moniz, S. J. A.; Wang, A.; Zhang, T.; Tang, J. Photoelectrochemical Devices for Solar Water Splitting-Materials and Challenges. *Chem. Soc. Rev*. 2017, pp 4645–4660. https://doi.org/10.1039/c6cs00306k.

(3) Kumar, M.; Meena, B.; Subramanyam, P.; Suryakala, D.; Subrahmanyam, C. Recent Trends in Photoelectrochemical Water Splitting: The Role of Cocatalysts. *NPG Asia Materials*. 2022. https://doi.org/10.1038/s41427-022-00436-x.

(4) Walter, M. G.; Warren, E. L.; McKone, J. R.; Boettcher, S. W.; Mi, Q.; Santori, E. A.; Lewis, N. S. Solar Water Splitting Cells. *Chem. Rev.* **2010**, *110* (11), 6446–6473. https://doi.org/10.1021/cr1002326.

(5) Amano, F. Photoelectrochemical Oxygen Evolution. In *Solar-to-Chemical Conversion: Photocatalytic and Photoelectrochemical Processes*; Wiley, 2021; pp 163–187. https://doi.org/10.1002/9783527825073.ch7.

(6) Yang, W.; Ramanujam Prabhakar, R.; Tan, J.; Tilley, D. S.; Moon, J. Strategies for Enhancing the Photocurrent, Photovoltage, and Stability of Photoelectrodes for Photoelectrochemical Water Splitting. *Chem. Soc. Rev* **2019**, *48*, 4979–5015. https://doi.org/10.1039/c8cs00997j.

(7) Tolod, K. R.; Hernández, S.; Russo, N. Recent Advances in the $BiVO_4$ Photocatalyst for Sun-Driven Water Oxidation: Top-Performing Photoanodes and Scale-up Challenges. *Catalysts* **2017**, *7* (1). https://doi.org/10.3390/catal7010013.

(8) Tan, H. L.; Amal, R.; Ng, Y. H. Alternative Strategies in Improving the Photocatalytic and Photoelectrochemical Activities of Visible Light-Driven $BiVO_4$: A Review. *J. Mater. Chem. A* **2017**, *5* (32), 16498–16521. https://doi.org/10.1039/c7ta04441k.

(9) Kim, J. H.; Lee, J. S. Elaborately Modified $BiVO_4$ Photoanodes for Solar Water Splitting. *Advanced Materials*. 2019, pp 1806938 (30)-1806938 (35). https://doi.org/10.1002/adma.201806938.

(10) Yabuta, M.; Takeda, A.; Sugimoto, T.; Watanabe, K.; Kudo, A.; Matsumoto, Y. Particle Size Dependence of Carrier Dynamics and Reactivity of Photocatalyst $BiVO_4$ Probed with Single-Particle Transient Absorption Microscopy. *J. Phys. Chem. C* **2017**, *121* (40), 22060–22066. https://doi.org/10.1021/acs.jpcc.7b06230.

(11) Park, Y.; Mc Donald, K. J.; Choi, K. S. Progress in Bismuth Vanadate Photoanodes for Use in Solar Water Oxidation. *Chem. Soc. Rev* **2013**, *42* (6), 2321–2337. https://doi.org/10.1039/c2cs35260e.

(12) Bhattacharya, A. K.; Mallick, K. K.; Hartridge, A. Phase Transition in BiVO4. *Mater. Lett.* **1997**, *30*, 7–13.

(13) Huang, Z. F.; Pan, L.; Zou, J. J.; Zhang, X.; Wang, L. Nanostructured Bismuth Vanadate-Based Materials for Solar-Energy-Driven Water Oxidation: A Review on Recent Progress. *Nanoscale* **2014**, *6* (23), 14044–14063. https://doi.org/10.1039/c4nr05245e.

(14) Tokunaga, S.; Kato, H.; Kudo, A. Selective Preparation of Monoclinic and Tetragonal $BiVO_4$ with Scheelite Structure and Their Photocatalytic Properties. *Chem. Mater.* **2001**, *13* (12), 4624–4628. https://doi.org/10.1021/cm0103390.

(15) Martinez Suarez, C.; Hernández, S.; Russo, N. $BiVO_4$ as Photocatalyst for Solar Fuels Production through Water Splitting: A Short Review. *Appl. Catal. A Gen.* **2015**, *504*, 158–170. https://doi.org/10.1016/j.apcata.2014.11.044.

(16) Kudo, A.; Omori, K.; Kato, H. A Novel Aqueous Process for Preparation of Crystal Form-Controlled and Highly Crystalline $BiVO_4$ Powder from Layered Vanadates at Room Temperature and Its Photocatalytic and Photophysical Properties. *J. Am. Chem. Soc.* **1999**, *121* (49), 11459–11467. https://doi.org/10.1021/ja992541y.

(17) Rettie, A. J. E.; Lee, H. C.; Marshall, L. G.; Lin, J. F.; Capan, C.; Lindemuth, J.; McCloy, J. S.; Zhou, J.; Bard, A. J.; Mullins, C. B. Combined Charge Carrier Transport and Photoelectrochemical Characterization of $BiVO_4$ Single Crystals: Intrinsic Behavior of a Complex Metal Oxide. *J. Am. Chem. Soc.* **2013**, *135* (30), 11389–11396. https://doi.org/10.1021/ja405550k.

(18) Abdi, F. F.; Han, L.; Smets, A. H. M.; Zeman, M.; Dam, B.; Van De Krol, R. Efficient Solar Water Splitting by Enhanced Charge Separation in a Bismuth Vanadate-Silicon Tandem Photoelectrode. *Nat. Commun.* **2013**, *4*. https://doi.org/10.1038/ncomms3195.

(19) Malathi, A.; Madhavan, J.; Ashokkumar, M.; Arunachalam, P. A Review on $BiVO_4$ Photocatalyst: Activity Enhancement Methods for Solar Photocatalytic Applications. *Applied Catalysis A: General*. 2018, pp 47–74. https://doi.org/10.1016/j.apcata.2018.02.010.

(20) Chen, D.; Xie, Z.; Tong, Y.; Huang, Y. Review on $BiVO_4$-Based Photoanodes for Photoelectrochemical Water Oxidation: The Main Influencing Factors. *Energy and Fuels*. 2022, pp 9932–9949. https://doi.org/10.1021/acs.energyfuels.2c02119.

(21) Kim, T. W.; Choi, K. S. SI_Nanoporous $BiVO_4$ Photoanodes with Dual-Layer Oxygen Evolution Catalysts for Solar Water Splitting. *Science (80-.).* **2014**, *343* (6174), 990–994. https://doi.org/10.1126/science.1246913.

(22) Yengantiwar, A.; Palanivel, S.; Archana, P. S.; Ma, Y.; Pan, S.; Gupta, A. Direct Liquid Injection Chemical Vapor Deposition of Molybdenum-Doped Bismuth Vanadate Photoelectrodes for Efficient Solar Water Splitting. *J. Phys. Chem. C* **2017**, *121* (11), 5914–5924. https://doi.org/10.1021/acs.jpcc.6b12710.

(23) Wang, L.; Su, J.; Guo, L. Self-Assembly Synthesis of Monodisperse $BiVO_4$ Nanosphere via a Hybrid Strategy for Photoelectrochemical Water Splitting. *ChemCatChem* **2020**, *12* (20), 5269–5275. https://doi.org/10.1002/cctc.202000975.

(24) Toma, F. M.; Cooper, J. K.; Kunzelmann, V.; McDowell, M. T.; Yu, J.; Larson, D. M.; Borys, N. J.; Abelyan, C.; Beeman, J. W.; Yu, K. M.; Yang, J.; Chen, L.; Shaner, M. R.; Spurgeon, J.; Houle, F. A.; Persson, K. A.; Sharp, I. D. Mechanistic Insights into Chemical and Photochemical Transformations of Bismuth Vanadate Photoanodes. *Nat. Commun.* **2016**, *7* (May), 1–11. https://doi.org/10.1038/ncomms12012.

(25) Hilliard, S.; Friedrich, D.; Kressman, S.; Strub, H.; Artero, V.; Laberty-Robert, C. Solar-Water-Splitting $BiVO_4$ Thin-Film Photoanodes Prepared By Using a Sol–Gel Dip-Coating Technique. *ChemPhotoChem* **2017**, *1* (6), 273–280. https://doi.org/10.1002/cptc.201700003.

(26) Grosso, D. How to Exploit the Full Potential of the Dip-Coating Process to Better Control Film Formation. *J. Mater. Chem.* **2011**, *21* (43), 17033–17038. https://doi.org/10.1039/c1jm12837j.

(27) Faustini, M.; Ceratti, D. R.; Louis, B.; Boudot, M.; Albouy, P. A.; Boissière, C.; Grosso, D. Engineering Functionality Gradients by Dip Coating Process in Acceleration Mode. *ACS Appl. Mater. Interfaces* **2014**, *6* (19), 17102–17110. https://doi.org/10.1021/am504770x.

(28) García Márquez, A.; Demessence, A.; Platero-Prats, A. E.; Heurtaux, D.; Horcajada, P.; Serre, C.; Chang, J. S.; Férey, G.; De La Peña-O'Shea, V. A.; Boissière, C.; Grosso, D.; Sanchez, C. Green Microwave Synthesis of MIL-100(Al, Cr, Fe) Nanoparticles for Thin-Film Elaboration.

Eur. J. Inorg. Chem. **2012**, No. 32, 5165–5174. https://doi.org/10.1002/ejic.201200710.

(29) Faustini, M.; Louis, B.; Albouy, P. A.; Kuemmel, M.; Grosso, D. Preparation of Sol-Gel Films by Dip-Coating in Extreme Conditions. *J. Phys. Chem. C* **2010**, *114* (17), 7637–7645. https://doi.org/10.1021/jp9114755.

(30) Dalstein, O.; Gkaniatsou, E.; Sicard, C.; Sel, O.; Perrot, H.; Serre, C.; Boissière, C.; Faustini, M. Evaporation-Directed Crack-Patterning of Metal–Organic Framework Colloidal Films and Their Application as Photonic Sensors. *Angew. Chemie - Int. Ed.* **2017**, *56*, 14011–14015. https://doi.org/10.1002/anie.201706745.

(31) Berteloot, G.; Daerr, A.; Lequeux, F.; Limat, L. Dip Coating with Colloids and Evaporation. *Chem. Eng. Process. Process Intensif.* **2013**, *68*, 69–73. https://doi.org/10.1016/j.cep.2012.09.001.

(32) Meyniel, L.; Boissière, C.; Krins, N.; Carenco, S. Optical-Quality Thin Films with Tunable Thickness from Stable Colloidal Suspensions of Lanthanide Oxysulfide Nanoplates. *Langmuir* **2023**, *39* (2), 728–738. https://doi.org/10.1021/acs.langmuir.2c02026.

(33) Shang, M.; Wang, W.; Zhou, L.; Sun, S.; Yin, W. Nanosized $BiVO_4$ with High Visible-Light-Induced Photocatalytic Activity: Ultrasonic-Assisted Synthesis and Protective Effect of Surfactant. *J. Jazardous Mater.* **2009**, *172*, 338–344.

(34) Tong, Y.; Zhao, S.; Kang, J.; Shen, J.; Chen, Z.; Wang, B.; Bi, L.; Deng, J. Preparation of Small-Sized $BiVO_4$ Particles with Improved Photocatalytic Performance and Its Photocatalytic Degradation of Doxycycline in Water. *Colloids Surfaces A Physicochem. Eng. Asp.* **2021**, *620*, 126412. https://doi.org/10.1016/j.colsurfa.2021.126412.

(35) Wu, M.; Jing, Q.; Feng, X.; Chen, L. $BiVO_4$ Microstructures with Various Morphologies: Synthesis and Characterization. *Appl. Surf. Sci.* **2018**, *427*, 525–532. https://doi.org/10.1016/j.apsusc.2017.07.299.

(36) Aguilera-Ruiz, E.; Zambrano-Robledo, P.; Vazquez-Arenas, J.; Cruz-Ortiz, B.; Peral, J.; García-Pérez, U. M. Photoactivity of Nanostructured Spheres of $BiVO_4$ Synthesized by Ultrasonic Spray Pyrolysis at Low Temperature. *Mater. Res. Bull.* **2021**, *143*, 111447. https://doi.org/10.1016/j.materresbull.2021.111447.

(37) Ressnig, D.; Kontic, R.; Patzke, G. R. Morphology Control of $BiVO_4$ Photocatalysts: PH Optimization vs. Self-Organization. *Mater. Chem. Phys.* **2012**, *135* (2–3), 457–466. https://doi.org/10.1016/j.matchemphys.2012.05.008.

(38) Saison, T. Oxydes Mixtes de Bismuth Pour La Photocatalyse Dans Le Visible, Université Pierre et Marie Curie - Paris 6, 2011.

(39) Saison, T.; Chemin, N.; Chanéac, C.; Durupthy, O.; Mariey, L.; Maugé, F.; Brezová, V.; Jolivet, J. P. New Insights into $BiVO_4$ Properties as Visible Light Photocatalyst. *J. Phys. Chem. C* **2015**, *119* (23), 12967–12977. https://doi.org/10.1021/acs.jpcc.5b01468.

(40) Arumugam, P.; Xu, H.; Srivastava, S.; M Rotello, V. Mini Review 'Bricks and Mortar' Nanoparticle Self-Assembly Using Polymers. *Polym. Int.* **2007**, *56*, 461–466. https://doi.org/10.1002/pi.

(41) Szeifert, J. M.; Fattakhova-Rohlfing, D.; Georgiadou, D.; Kalousek, V.; Rathouský, J.; Kuang, D.; Wenger, S.; Zakeeraddin, S. M.; Grätzel, M.; Bein, T. Brick and Mortar Strategy for the Formation of Highly Crystalline Mesoporous Titania Films from Nanocrystalline Building Blocks. *Chem. Mater.* **2009**, *21* (7), 1260–1265. https://doi.org/10.1021/cm8029246.

(42) Sun, S.; Wang, W.; Li, D.; Zhang, L.; Jiang, D. Solar Light Driven Pure Water Splitting on Quantum Sized $BiVO_4$ without Any Cocatalyst. *ACS Catal.* **2014**, *4* (10), 3498–3503. https://doi.org/10.1021/cs501076a.

(43) Durupthy, O.; Steunou, N.; Coradin, T.; Maquet, J.; Bonhomme, C.; Livage, J. Influence of PH and Ionic Strength on Vanadium(v) Oxides Formation. From $V_2O_5 \cdot nH_2O$ Gels to Crystalline $NaV_3O_8 \cdot 1.5H_2O$. *J. Mater. Chem.* **2005**, *15* (10), 1090–1098. https://doi.org/10.1039/b414893b.

(44) Walsh, A.; Yan, Y.; Huda, M. N.; Al-Jassim, M. M.; Wei, S. H. Band Edge Electronic Structure of $BiVO_4$: Elucidating the Role of the Bi s and V d Orbitals. *Chem. Mater.* **2009**, *21* (3), 547–551. https://doi.org/10.1021/cm802894z.

(45) Tauc, J. Optical Properties and Electronic Structure of Amorphous Ge and Si. *Mater. Res. Bull.* **1968**, *3* (1), 37–46. https://doi.org/https://doi.org/10.1016/0025-5408(68)90023-8.

(46) Li, G.; Bai, Y.; Zhang, W. F. Difference in Valence Band Top of $BiVO_4$ with Different Crystal Structure. *Mater. Chem. Phys.* **2012**, *136* (2–3), 930–934. https://doi.org/10.1016/j.matchemphys.2012.08.023.

(47) Liu, K.; Chang, Z.; Li, W.; Che, P.; Zhou, H. Preparation, Characterization of Mo, Ag-Loaded $BiVO_4$ and Comparison of Their Degradation of Methylene Blue. *Sci. China Chem.* **2012**, *55* (9), 1770–1775. https://doi.org/10.1007/s11426-012-4525-x.

(48) Schneider, K. Optical Properties and Electronic Structure of V_2O_5, V_2O_3 and VO_2. *J. Mater. Sci. Mater. Electron.* **2020**, *31* (13), 10478–10488. https://doi.org/10.1007/s10854-020-03596-0.

(49) Yaw, C. S.; Ruan, Q.; Tang, J.; Soh, A. K.; Chong, M. N. A Type II N-n Staggered Orthorhombic V_2O_5/Monoclinic Clinobisvanite $BiVO_4$ Heterojunction Photoanode for Photoelectrochemical Water Oxidation: Fabrication, Characterisation and Experimental Validation. *Chem. Eng. J.* **2019**, *364* (January), 177–185. https://doi.org/10.1016/j.cej.2019.01.179.

(50) Andrade, T. S.; Sá, B. A. C.; Oliveira, A. T.; Bruziquesi, C. G. O.; Salomão, P. E. A.; Rodriguez, M.; Nogueira, F. G. E.; Alves de Oliveira, L. C.; Pereira, M. C. W:$BiVO_4$-WO_3-V_2O_5 Heterostructures Increase Light Absorption and Charge Transport in Photoanodes for Water Splitting. *J. Environ. Chem. Eng.* **2022**, *10* (2), 2–8. https://doi.org/10.1016/j.jece.2022.107278.

(51) Arunachalam, M.; Ahn, K. S.; Kang, S. H. Oxygen Evolution NiOOH Catalyst Assisted V_2O_5@$BiVO_4$ Inverse Opal Hetero-Structure for Solar Water Oxidation. *Int. J. Hydrogen Energy* **2019**, *44* (10), 4656–4663. https://doi.org/10.1016/j.ijhydene.2019.01.024.

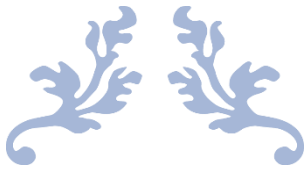

CONCLUSION

Conclusion

The thesis work was positioned in the context of dihydrogen production with a renewable process to get the smallest possible CO_2 footprint. For that, photoelectrochemical (PEC) devices using light and water play a crucial role. H_2 production is favourable in acidic conditions, yet given the wide variety of photoanodes designed for alkaline and neutral conditions, there was a need to develop a photoanode capable of operating in an acidic environment to effectively optimize the performance of these devices. The challenges in these conditions were to design a photoanode that is efficient and stable over time.

We explored two approaches for the synthesis of $BiVO_4$-based photoanodes using the dip-coating deposition technique. We also focussed on three main optimization strategies for the design of an efficient photoanode in an acidic electrolyte buffer (pH 6). The first constrain considered in all the approaches developed is the intrinsic hole-length diffusion limitation in pure $BiVO_4$, which is around 70 – 100 nm. This limitation drove the targeted thickness of a bismuth vanadate dense film deposited on the FTO substrate. However, it affects both the amount of light harvested and the durability of the photoanode against photocorrosion. The main objectives were to get as close as possible to the theoretical 7.5 mA cm^{-2} of $BiVO_4$ and to obtain an electrode that would be stable over time.

The first approach (Chapter II) involves synthesizing the photoanode in a single step using a combination of sol-gel chemistry and the dip-coating deposition technique. This method enables the development of reliable electrodes with high reproducibility and dense films with a thickness of 110 nm. As a part of this approach, two strategies were studied to improve the electrode performances: bulk chemistry modification and surface engineering.

In Chapter II, Part 1, the composition of the $BiVO_4$-based photoanode is modified by the insertion of a Mo^{6+} doping agent. The resulting photoanode exhibits a scheelite structure with a bang-gap of ~ 2.6 eV. Through the appropriate doping amount, the donor density is increased and electron mobility is enhanced. Performing photoelectrochemical measurements in the presence of sulphites, we obtained a higher photocurrent density (3.6 mA cm^{-2}), suggesting that the reaction kinetics of holes with water is still slow on the bismuth vanadate surface. In terms of electrode durability, the presence of sulphites meant that the electrode was very stable over the 5 hours of chronoamperometric analysis. We explained this difference in stability between

OER and sulphites oxidation by an accumulation of holes at the electrode/electrolyte interface due to the slow OER reaction kinetics under acidic conditions. This phenomenon amplifies reactions related to the electrode's photocorrosion. To improve the holes reactivity at the electrode/electrolyte interface, we have modified the surface by electrodepositing a Co-Pi co-catalyst. This has considerably improved the hole transfer efficiency of the photoanode. The new FTO/Mo:$BiVO_4$/Co-Pi photoanode achieved a maximum photocurrent density of 2.4 mA cm^{-2}, twice that of the pristine $BiVO_4$ photoanode at 1.23 V_{RHE} under 100 mW cm^{-2} of illumination. The combination of bulk and surface modifications resulted in a higher photocurrent than the few results reported under acidic conditions. Nevertheless, the obtained value remains far from the theoretical photocurrent density of $BiVO_4$. Conversely, higher photocurrent densities, above 3.5 mA cm^{-2}, have already been achieved under neutral conditions (pH 7). This significant difference demonstrates the substantial impact of the electrolyte on the photoanode's OER efficiency.

Since the pH of the electrolyte buffer directly influences the OER kinetics, it would be interesting to explore further by quantitatively determine the current loss as a function of buffer pH for the same electrode.

Improving the stability of the electrode over time was addressed from the point of view of limiting the accumulation of holes by increasing the kinetics of the OER reaction through the addition of the Co-Pi co-catalyst. It significantly improved the durability of the electrode, since no change in electrode thickness by SEM analysis was observed over time. Nonetheless, some porosity creation is still observed.

To solve the problem of photocorrosion, we enhanced the stability of the electrode with a different strategy, by passivating the surface. We studied the impact of a TiO_2 passivation layer deposited on the $BiVO_4$ photoanode (Chapter II, part II). This metal oxide has been chosen for its stability over a wide range of pH and electrochemical potential. We then examined the influence of TiO_2 passivation layer thickness and crystallinity using two synthesis processes. First, we employed ALD to synthesize 15 nm and 10 nm thick TiO_2 layers. The obtention of well-crystallized TiO_2 synthesized by ALD without annealing post-treatment was limited to a thickness of 15 nm but this thickness almost completely passivated the $BiVO_4$ layer underneath. With a thickness of 10 nm, the ALD deposition method alone did not allow the formation of a crystallized layer. PEC analysis revealed that crystallinity played a critical role on the achievement of a passivation layer. However, with 2 hours of annealing post-treatment on a sample covered with 10 nm of TiO_2, the photocurrent density was twenty-fold times lower than

its reference. Then, we applied a modified Sol-Gel synthesis combined with a dip-coating protocol to synthesize ultrathin TiO_2 films to minimize the decrease in photocurrent density when the surface is passivated. Compared to ALD, this approach is easier to implement and cheaper. A 3 nm thick TiO_2 layer deposited by dip-coating showed the most promising results for passivation. This layer had a stable photocurrent of ~ 0.3 mA cm^{-2} obtained over 1 hour at 1.23 V_{RHE}, which was only 2.76 times less than its reference without the passivation layer. Post-mortem analysis of the surface and cross section by FEG-SEM showed a surface almost identical to that which existed prior to any PEC experiment.

With a better understanding of the critical parameters affecting the passivation properties of a TiO_2 thin film, a synergy could be considered between a TiO_2 passivation layer and a co-catalyst. The balance between efficiency loss and durability gain may still be altered when considering the possibility of adding a co-catalyst on top of the protective layer.

In the context of the work developed in the chapter II, considering a recent innovative approach that involves surface engineering and bulk modification by introducing vacancies in the $BiVO_4$-based photoanode could give intriguing results when implemented in our system. In the review of S. Wang et al. they exposed - ways to generate O vacancies.[1] Chemical reduction with $NaBH_4$, thermal treatment in reduction/inert atmosphere, heteroatom doping with Zn replacing Bi, precursors solution/film treatment, photocharging at room temperature, and electrochemical reduction are all the methods employed to generate the vacancies.[1] They observed that a controlled amount of vacancies in the material enhanced the PEC performance of the photoanode by improving charge carrier's mobility and surface activity. Moreover, to prevent oxidation of the vacancies, thin TiO_2 layer was found efficient after calcination treatment under reduction atmosphere as demonstrate by the work on black-$BiVO_4/TiO_{2-x}$ photoanode.[2] In our system, an annealing post-treatment in a reduction atmosphere of our sol-gel/dip-coated photoanode with TiO_2 could be an interesting way to identify the impacts of O vacancies on the charge carrier mobility as the surface activity.

The second approach presented in Chapter III is quite unusual in the domain of photoelectrodes synthesis. It consisted in a two-step approach with a primarily synthesis of a $BiVO_4$ nanoparticles suspension and then its controlled deposit on an FTO substrate. Unlike the one-step design of the photoanode, this approach allows better control of the structure and size of the nanoparticles constituting the film but require a higher control on the dip-coated suspension.

First, we designed a protocol for synthesizing nanoparticles smaller than 100 nm in order to prepare a colloidal suspension that is stable for 15 minutes, the condition required for deposition by dip-coating. This led to the development of two interesting hydrothermal syntheses. The first synthesis produced nanoparticles with a size ranging from 3 to 6 nm but had a crystalline structure consisting of an amorphous phase, tetragonal zircon, and scheelite polymorphs. The second synthesis involved the doping the photoanode with Mo^{6+} and resulted in the formation of larger nanoparticles with sizes between 15 to 30 nm and aggregates of around 100 nm. These nanoparticles exhibited a crystallized scheelite structure with tetragonal and monoclinic polymorphs and a band-gap of around 2.6 eV.

SEM images of the films obtained from the smallest nanoparticles on the substrate show poor contact between the particles after heat treatment at 450 °C. To overcome this limitation, we decided to explore the brick and mortar approach, using V_2O_5 as solvent and Mo:$BiVO_4$ nanoparticles. Interestingly, this allowed us to create a type II n-n heterojunction with $BiVO_4$, which are known to improve the electron/hole separation as well as the transport of hole or electron within the materials. Our study of the FTO/Mo:$BiVO_4$/V_2O_5 photoanode was the first exploration under acidic conditions of such a heterostructure under standardized illumination conditions, and a photocurrent density of 0.32 $mAcm^{-2}$ at 1.23 V_{RHE} was achieved. These results are similar than a heterojunction realised at pH = 7 by the group of Arunachalam *et al*.[3] However, compared to the doped FTO/Mo:$BiVO_4$ photoanode synthesized in chapter II by sol-gel/dip-coating the photocurrent is still 5.3 times lower. The lower photocurrent could be linked to the large amount of molybdenum inside the $BiVO_4$ nanoparticles as well as an inappropriate ratio of Mo:$BiVO_4$ and V_2O_5.

Previous research has explored the impact of dopant concentration in a $BiVO_4$ photoanode on its PEC performance. At this stage, the primary result in Chapter III can serve as a baseline for comparison, with new photoanode with lower dopant concentration, similar to those obtained in the Chapter II study (between 0.5 at% and 3 at%). Additionally, optimizing the V_2O_5 concentration, when diluted in acidified water, could help determine the most effective heterostructured composition and compare the PEC performance with the one-step sol-gel approach. In complement, a study of the PEC sulphite oxidation into sulphate and an analysis depending of the electrode side illumination could reveal information on the limiting factors affecting the photoanode photocurrent density value.

Because the Mo:$BiVO_4$/V_2O_5 heterostructured photoanode is facilitated in a one step-deposition process, another intriguing experiment could involve creating a photoanode with

multiple junctions. For instance, by introducing a p-type semiconductor as $AgVO_3$, MoS_2 or Cu_2O there is a potential to enhance the separation of electron-hole pairs and avoid recombination.[4–6]

Finally, in each part of the study (Chapter II and III), a heat treatment at 450 °C for 1 hour was necessary to generate $BiVO_4$ photoanode in tetragonal scheelite and monoclinic scheelite polymorph. In this thesis, we gave priority to the surface aspect of FTO-Glass substrate over the electrode stability in order to have the flattest possible FTO layer. This constrained us to use commercial electrodes whose FTO thickness was 80 nm. The thickness limits the temperature and time of exposure of the electrode to heat as previously shown, a prolonged exposure of the electrode to temperatures above 450°C led to an increase in electrode resistance. This was confirmed by punctual measurements of FTO substrate resistivity for different times of calcination.

As a part of a possible future work, to demonstrate a beneficial impact of heat treatment on crystallinity enhancement, a preliminary experiment was conducted with the standard substrate. Two samples were subjected to heating for 1 hour and 3 hours, respectively. This experiment revealed a phase transition to a distinctive monoclinic scheelite phase. These samples, functionalized with Co-Pi co-catalyst and tested in linear sweep voltammetry, showed different signals. With the unique monoclinic polymorph, the photocurrent increases of 0.1 mA cm^{-2} and a cathodic shift to ~ $0.45V_{RHE}$ was observed (Figure annexe A.1). With these promising results, initial attempts to deposit Mo:$BiVO_4$ with the sol-gel approach on new commercial FTO-Glass substrate with thicker but rougher FTO (600 nm, resistance of 7 Ω) enabled us to obtain a first dense film crystallized in the monoclinic scheelite polymorph after 3 h of calcination at 450°C. We measured only a small increase of the resistance of (~ 30 Ω) on the FTO substrate. This first results could allow an improvement of the PEC properties by using a more conductive substrate and could facilitate the use of any strategies requiring heat treatment for several hours.

Taking a wider view, employing $BiVO_4$ as a photoanode for hydrogen (H_2) production within a tandem system alongside a copper-oxide-based photocathode presents considerable challenges. Despite extensive research aimed at enhancing the overall efficiency of the oxygen evolution reaction (OER), the photoelectrochemical (PEC) performance of the photoanodes still falls considerably short of the theoretically predicted photocurrent density. Furthermore, as demonstrated in this thesis, the growing difficulties in effectively oxidizing water molecules under acidic conditions raise the fundamental question of whether it is feasible to design an

autonomous PEC tandem system, or if there exists an intrinsic limit to the experimentally attainable OER photocurrent density in this environment.

In this context, we have identified an unexplored way of improving photocurrent density. This involves combining a photovoltaic cell and a photoanode in a hybrid cell. Ultimately, unbiased water separation is demonstrated, with a high photocurrent density associated with a solar-to-hydrogen conversion efficiency of 5.2% under simulated air mass illumination (AM) 1.5.[7]

(1) Wang, S.; Wang, X.; Liu, B.; Guo, Z.; Ostrikov, K.; Wang, L.; Huang, W. Vacancy Defect Engineering of $BiVO_4$ Photoanodes for Photoelectrochemical Water Splitting. *Nanoscale* **2021**, *13* (43), 17989–18009. https://doi.org/10.1039/d1nr05691c.

(2) Tian, Z.; Zhang, P.; Qin, P.; Sun, D.; Zhang, S.; Guo, X.; Zhao, W.; Zhao, D.; Huang, F. Novel Black $BiVO_4/TiO_{2-x}$ Photoanode with Enhanced Photon Absorption and Charge Separation for Efficient and Stable Solar Water Splitting. *Adv. Energy Mater.* **2019**, *9* (27), 1–8. https://doi.org/10.1002/aenm.201901287.

(3) Arunachalam, M.; Ahn, K. S.; Kang, S. H. Oxygen Evolution NiOOH Catalyst Assisted V_2O_5@$BiVO_4$ Inverse Opal Hetero-Structure for Solar Water Oxidation. *Int. J. Hydrogen Energy* **2019**, *44* (10), 4656–4663. https://doi.org/10.1016/j.ijhydene.2019.01.024.

(4) Gao, L.; Long, X.; Wei, S.; Wang, C.; Wang, T.; Li, F.; Hu, Y.; Ma, J.; Jin, J. Facile Growth of $AgVO_3$ Nanoparticles on Mo-Doped $BiVO_4$ Film for Enhanced Photoelectrochemical Water Oxidation. *Chem. Eng. J.* **2019**, *378*, 122193. https://doi.org/10.1016/j.cej.2019.122193.

(5) Pan, Q.; Zhang, C.; Xiong, Y.; Mi, Q.; Li, D.; Zou, L.; Huang, Q.; Zou, Z.; Yang, H. Boosting Charge Separation and Transfer by Plasmon-Enhanced $MoS_2/BiVO_4$ p-n Heterojunction Composite for Efficient Photoelectrochemical Water Splitting. *ACS Sustain. Chem. Eng.* **2018**, *6* (5), 6378–6387. https://doi.org/10.1021/acssuschemeng.8b00170.

(6) Bai, S.; Liu, J.; Cui, M.; Luo, R.; He, J.; Chen, A. Two-Step Electrodeposition to Fabricate the p-n Heterojunction of a $Cu_2O/BiVO_4$ Photoanode for the Enhancement of Photoelectrochemical Water Splitting. *Dalt. Trans.* **2018**, *47* (19), 6763–6771. https://doi.org/10.1039/c7dt04258b.

(7) Han, L.; Abdi, F. F.; Van De Krol, R.; Liu, R.; Huang, Z.; Lewerenz, H. J.; Dam, B.; Zeman, M.; Smets, A. H. M. Efficient Water-Splitting Device Based on a Bismuth Vanadate Photoanode and Thin-Film Silicon Solar Cells. *ChemSusChem* **2014**, *7* (10), 2832–2838. https://doi.org/10.1002/cssc.201402456.

ANNEXE

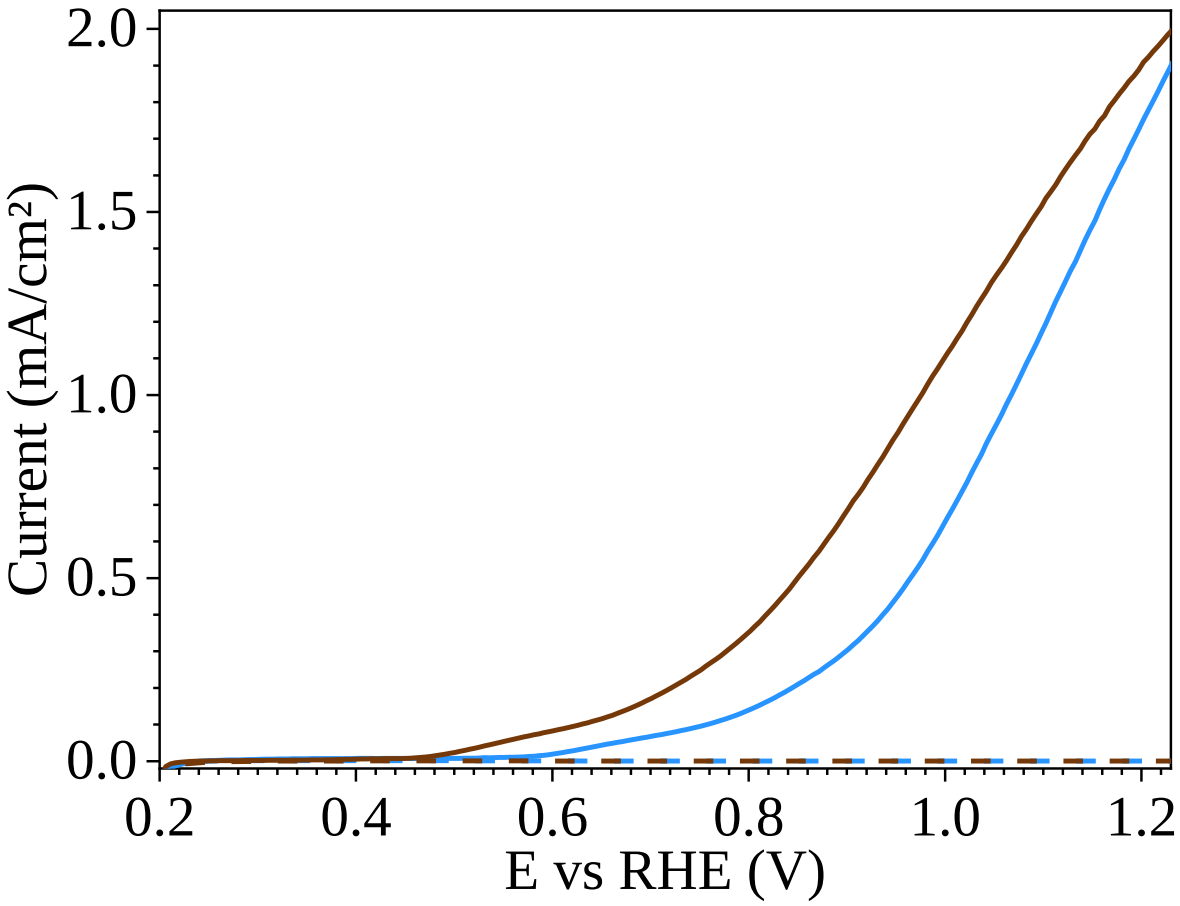

Figure A.1: Photoelectrochemical measurements in 1M potassium phosphate buffer (pH 6) under front simulated illumination at 100 mW cm^{-2}. Linear voltage sweeps of Mo:$BiVO_4$/Co-Pi (5 min) with 1 h calcination at 450 °C for Mo:$BiVO_4$ in blue curve and 3 h calcination at 450 °C for Mo:$BiVO_4$ in brown curve. The dots are measured under dark condition.

Design of heterostructured photoelectrodes for water-splitting

Photoelectrochemical water-splitting is an innovative solution for sustainable dihydrogen production. To create a self-sustaining photoelectrochemical cell capable of performing water electrolysis without the need for external energy input, the development of efficient photoactive materials within a single electrolyte is essential. In this context we have studied bismuth vanadate ($BiVO_4$) semiconductor as promising photoanode for water oxidation in acidic conditions where photocathodes are efficient. However, little research has been carried out into its effectiveness and durability in an acid environment. In this thesis, we studied the performance of this electrode in an acidic environment by developing two approaches to the manufacture of photoanodes based on dip-coating: i\ sol-gel chemistry and ii\ colloidal suspension. To enhance photocurrents and electrode stability, we explored two strategies: modifying the electrode composition by doping it with molybdenum to influence charge transport within the material, and improving surface reactivity by adding a cobalt-phosphate co-catalyst. For the latter, we analysed the charge transfer kinetics with the addition of a co-catalyst and the passivation of the surface with an ultrathin TiO_2 layer, obtained by the sol-gel or ALD process. Finally, we synthesized a $BiVO_4$- V_2O_5 heterojunction based on a 'brick and mortar' approach, in which the size and structure of $BiVO_4$ particles are controlled.

Key words: bismuth vanadate, photoanode, photoelectrochemical water-oxidation (OER)

Conception de photo-électrodes hétérostructurées pour la réaction d'électrolyse de l'eau

La photo-électrolyse de l'eau est une solution innovante pour la production durable de dihydrogène. Pour créer une cellule photoélectrochimique autosuffisante capable de réaliser l'électrolyse de l'eau sans nécessiter d'apport d'énergie externe, le développement de matériaux photo-actifs efficaces au sein d'un unique électrolyte est nécessaire. Dans ce contexte, nous avons étudié le vanadate de bismuth ($BiVO_4$) comme photoanode pour l'oxydation de l'eau dans des conditions acides où l'optimum d'efficacité des photocathodes est atteint. A ce jour, peu de travaux ont porté sur l'efficacité et la durabilité de ces électrodes en conditions acides. Dans cette étude, nous avons exploré deux approches de synthèse de la photoanode par trempage-retrait : i\ la chimie sol-gel et ii\ le dépôt d'une suspension colloïdale. Pour améliorer le photo-courant et la stabilité de l'électrode, nous avons exploré deux stratégies : modifier la structure de $BiVO_4$ en dopant avec du molybdène pour influencer le transport de charge à l'intérieur du matériau, améliorer la réactivité de surface en ajoutant un co-catalyseur cobalt-phosphate. Dans cette dernière approche, nous avons étudié la cinétique de transfert de charge en ajoutant un co-catalyseur à la surface de $BiVO_4$ et la passivation de la surface grâce à une couche ultramince de TiO_2. Enfin, nous avons synthétisé une hétérojonction $BiVO_4$-V_2O_5 en s'inspirant d'une approche de type "brique-mortier", dans laquelle la taille et la structure des particules de $BiVO_4$ sont contrôlées.

Mots clés : vanadate de bismuth, photoanode, oxydation de l'eau photoélectrochimique (REO)